Computational Fluid Dynamics Aided Design of Stirred Liquid-Liquid Extraction Columns

vom Fachbereich Maschinenbau und Verfahrenstechnik der
Technischen Universität Kaiserslautern zur Verleihung
des akademischen Grades

Doktor-Ingenieur (Dr.-Ing.)

genehmigte Dissertation

Dissertation

von

Herrn

Dipl.-Ing. Mark W. Hlawitschka

aus Ludwigshafen am Rhein (Geburtsort)

Tag der mündlichen Prüfung: 21.10.2013

Dekan: Prof. Dr.-Ing. B. Sauer

Prüfungskommission:

Prüfungsvorsitzender: Prof. Dr.-Ing. S. Ripperger

1. Berichterstatter: Prof. Dipl.-Ing. Dr. techn. H.-J. Bart

2. Berichterstatter: Prof. Dr.-Ing. M. Böhle
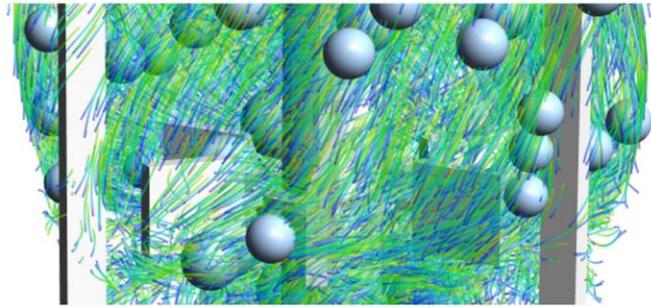
D 386

Computational Fluid Dynamics Aided Design of Stirred Liquid-Liquid Extraction Columns

Mark W. Hlawitschka

2013

Preface

This research work was carried out in a cooperation project with the Department of Separation Science and Technology, the Technomathematics Group, the Computer Graphics and HCI Group of the University of Kaiserslautern and the Fraunhofer ITWM within the research project Multiphysics Modelling and Feature based Visualization (MMV) of the "Center for Computational and Mathematical Modelling" and in close cooperation with the University of Jordan. My work was done at the Department of Separation Science and Technology during the years 2009-2013.

Kaiserslautern, 2013

Mark W. Hlawitschka

Abstract

Aim of this work was the extension and development of a coupled Computational Fluid Dynamics （CFD） and population balance model （PBM） solver to enable a simulation aided design of stirred liquid-liquid extraction columns. The principle idea is to develop a new design methodology based on a CFD-PBM approach and verify it with existing data and correlations. On this basis, the separation performance in any apparatus geometry should be possible to predict without any experimental input. Reliable "experiments in silico" （computer calculations） should give the engineer a valuable and user-friendly tool for early design studies at minimal costs.

The layout of extraction columns is currently based on experimental investigations from miniplant to pilot plant and a scale-up to the industrial scale. The hydrodynamic properties can be varied by geometrical adjustments of the stirrer diameter, the stirrer height, the free cross sectional area of the stator, the compartment height as well as the positioning and the size of additional baffles. The key parameter for the liquid-liquid extraction is the yield which is mainly determined at the in- and outlets of the column. Local phenomena as the swirl structure are influenced by geometry changes. However, these local phenomena are generally neglected in state-of-the are design methodologies due to the complex required measurement techniques. A geometrical optimization of the column therefore still results in costs for validation experiments as assembly and operation of the column, which can be reduced by numerical investigations. The still mainly in academics used simulation based layout of counter-current extraction columns is based at the beginning of this work on one dimensional simulations of extraction columns and first three dimensional simulations. The one dimensional simulations are based on experimental derived, geometrical dependent correlations for the axial backmixing （axial dispersion）, the hold-up, the phase fraction, the droplet sedimentation and the energy dissipation. A combination of these models with droplet population balance modeling resulted in a description of the complex droplet-droplet interactions （droplet size） along the column height. The three dimensional CFD simulations give local information about the flow field （velocity, swirl structure） based on the used numerical mesh corresponding to the real geometry. A coupling of CFD with population balance modeling further provides information about the local droplet size. A backcoupling of the droplet size with the CFD （drag model） results in an enhancement of the local hydrodynamics （e.g. hold-up, dispersed phase velocity）. CFD provided local information about the axial dispersion coefficient of simple geometrical design （e.g. Rotating Disc Contactor （RDC） column）. First simulations of the RDC column using a two dimensional rotational geometry combined with population balance modeling were performed and gave local information about the droplet size for different boundary conditions （rotational speed, different column sizes）.

In this work, two different column types were simulated using an extended OpenSource CFD code. The first was the RDC column, which were mainly used for code development due to its simple geometry. The Kühni DN32 column is equipped with a six-baffled stirring device and flat baffles for disturbing the flow and requires a full three dimensional description. This column type was mainly used for experimental validation of the simulations due to the low required volumetric flow rate. The Kühni DN60 column is similar to the Kühni DN32 column with slight changes to the stirring device (4-baffles) and was used for scale up investigations. For the experimental validation of the hydrodynamics, laser based measurement techniques as Particle Image Velocimetry (PIV) and Laser Induced Fluorescence (LIF) were used. A good agreement between the experimental derived values for velocity, hold-up and energy dissipation, experimentally derived correlations from literature and the simulations with a modified Euler-Euler based OpenSource CFD code could be found. The experimental derived axial dispersion coefficient was further compared to Euler-Lagrange simulations. The experimental derived correlations for the Kühni DN32 in literature fit to the simulated values. Also the axial dispersion coefficient for the dispersed phase satisfied a correlation from literature. However, due to the complexity of the dispersed phase axial dispersion coefficient measurement, the available correlations gave no distinct agreement to each other.

A coupling of the modified Euler-Euler OpenSource CFD code was done with a one group population balance model. The implementation was validated to the analytical solution of the population balance equation for constant breakage and coalescence kernels. A further validation of the population balance transport equation was done by comparing the results of a five compartment section to the results of the commercial CFD code FLUENT using the Quadrature Method of Moments (QMOM).

For the simulation of the droplet-droplet interactions in liquid-liquid extraction columns, several breakage and coalescence models are available in the literature. The models were compared to each other using the one-group population balance model in Matlab which allows the determination of the minimum stable droplet diameter at a certain energy dissipation. Based on this representation, it was possible to determine the parameters for a specific breakage and coalescence model combination which allowed the simulation of a Kühni miniplant column at different rotational speeds. The resulting simulated droplet size was in very good agreement to the experimental derived droplet size from literature. Several column designs of the DN32 were investigated by changing the compartment height and the axial stirrer position. It could be shown that a decrease of the stirrer position increases the phase fraction inside the compartment. At the same time, the droplet size decreases inside the compartment, which allows a higher mass transfer due to a higher available interfacial area. However, the shifting results in an expected earlier flooding of the column due to a compressed flow structure underneath the stirring device.

In a next step, the code was further extended by mass transfer equations based on the two-film theory. Mass transfer coefficient models for the dispersed and continuous phase were investigated for the RDC column design.

A first mass transfer simulation of a full miniplant column was done. The change in concentration was accounted by the mixture density, viscosity and interfacial tension in dependence of the concentration, which affects the calculation of the droplet size. The results of the column simulation were compared to own experimental data of the column. It could be shown that the concentration profile along the column height can be predicted by the presented CFD/population balance/mass transfer code. The droplet size decreases corresponding to the interfacial tension along the column height. Compared to the experimental derived droplet size at the outlet, the simulation is in good agreement.

Besides the occurrence of a mono dispersed droplet size, high breakage may lead to the generation of small satellite droplets and coalescence underneath the stator leads to larger droplets inside the column and hence to a change of the hold-up and of the flooding point. A multi-phase code was extended by the Sectional Quadrature Method of Moment (SQMOM) allowing a modeling of the droplet interactions of bimodal droplet interactions or multimodal distributions. The implementations were in good agreement to the analytical solution. In addition, the simulation of an RDC column section showed the different distribution of the smaller droplets and larger droplets. The smaller droplets tend to follow the continuous phase flow structure and show a higher distribution of inside the column. The larger droplets tend to rise directly through the column and show only a low influence to the continuous phase flow.

The current results strengthen the use of CFD for the layout of liquid-liquid extraction columns in future. The coupling of CFD/PBM and mass transfer using an OpenSource CFD code allows the investigation of computational intensive column designs (e.g. pilot plant columns). Furthermore the coupled code enhances the accuracy of the hydrodynamics simulations and leads to a better understanding of counter-current liquid-liquid extraction columns. The gained correlation were finally used as an input for one dimensional mass transfer simulations, where a perfect fit of the concentration profiles at varied boundary conditions could be obtained. By using the multi-scale approach, the computational time for mass transfer simulations could be reduced to minutes. In future, with increasing computational power, a further extend of the multiphase CFD/SQMOM model including mass transfer equation will provide an efficient tool to model multimodal and multivariate systems as bubble column reactors.

Kurzfassung

Ziel dieser Arbeit war es, ein gekoppeltes Computational Fluid Dynamics (CFD) und Tropfenpopulationsbilanzmodell (PBM), CFD-PBM Modell, zur simulationsgestützten Auslegung von Extraktionskolonnen zu validieren und weiterzuentwickeln. Darauf aufbauend entstand die Idee, die Designmethode weg vom experimentellen Scale-up hin zum numerischen Layout zu bringen und somit eine geometrieunabhängige, prädiktive Auslegung von Extraktionskolonnen ohne zusätzlichen experimentellen Input zu ermöglichen. Dies soll auf Basis eines mit experimentellen Daten und Korrelationen CFD-PBM Ansatzes erreicht werden. Die dadurch ermöglichten virtuellen Experimente sollen dem Ingenieur erste Designstudien unter Aufwendung minimaler Kosten ermöglichen. Ziel ist es zudem, die Eingabe und Analyse der Daten durch eine benutzerfreundliche Eingabemaske sowie durch eine angepasste Visualisierung der Daten zu optimieren.

Die Kolonnenauslegung basiert zurzeit auf Experimenten vom Miniplant- bis hin zum Pilotplant bzw. Industriemaßstab. Die hydrodynamischen Eigenschaften können hierbei durch geometrische Anpassungen des Rührerdurchmessers, der Rührerhöhe, des freien Querschnitts der Statorbleche, der Compartmenthöhe sowie durch die Anordnung der Strombrecher beeinflusst werden. Als Kenngröße der Änderung gilt maßgeblich die Ausbeute, die jedoch meist nur am Ein- und Austritt der Kolonne ermittelt wird. Die lokalen Einflüsse einer geometrischen Anpassung bleiben jedoch bisher aufgrund der komplexen Messtechnik weitestgehend unberücksichtigt. Aus geometrischen Anpassungen resultieren daher vorerst Kosten für die Konstruktion, den Bau der neuen Kolonnengeometrie sowie Kosten für Validierungsexperimente.

Die simulationsgestützte Auslegung von Gegenstromextraktionskolonnen basiert zu Beginn dieser Arbeit auf eindimensionalen Simulationen der Kolonnen sowie auf ersten dreidimensionalen Simulationen einzelner Kolonnensegmente. Erstere basieren auf geometrieabhängigen experimentellen Korrelationen zur axialen Rückvermischung (axiale Dispersion), zum Hold-up, zum Phasenanteil sowie zum Tropfenaufstieg und zur Energiedissipation. Die Verknüpfung der Modelle mit der Tropfenpopulationsbilanzierung ermöglichte eine Berücksichtigung der Tropfen-Tropfeninteraktionen entlang der Kolonnenhöhe und somit eine Verbesserung der modellbehafteten Beschreibung der hydrodynamischen Korrelationen. Die dreidimensionalen CFD Simulationen ermöglichen hierzu geometrieunabhängig Strömungsinformationen, unter anderem über die lokalen Geschwindigkeiten und der Wirbelbildung, zu gewinnen. Eine weitere Kopplung mit der Tropfenpopulationsbilanzmodellierung liefert detaillierte Informationen über die disperse Phase (Tropfen), deren lokale Größe und Fortbewegung. Eine Rückkopplung mit der CFD verbessert zudem die Genauigkeit der hydrodynamischen Größen wie Geschwindigkeit und Hold-up sowie unter Einbeziehung von Stofftransportgleichungen eine Verbesserung des berechneten Wertstoffgehalts. Die CFD ermöglichte daher in der Vergangenheit die Simulation wichtiger

Kenngrößen, wie der axialen Dispersion, am Beispiel einfacher geometrischer Strukturen (z. B. der RDC Kolonne). Kürzlich von Drumm (2010) durchgeführte CFD/PBM Simulationen einer RDC Gegenstromextraktionskolonne unter Ausnutzung der zweidimensional-rotationssymmetrischen Geometrieeigenschaften, ermöglichten es, Informationen über die lokale Tropfengröße bei unterschiedlichen Randbedingungen zu gewinnen.

In dieser Arbeit wurde ein OpenSource CFD-Tool zur Simulation von Extraktionskolonnen vom Miniplant bis zum Pilotplant-Maßstab erweitert und validiert. Hierbei wurden Kolonnen vom Typ RDC und Kühni untersucht. Die Kühni Kolonne besitzt als maßgebliche Geometrie im Gegensatz zur RDC Kolonne mit Scheibenrührer, einen Vier- beziehungsweise Sechsblatt-Rührer und nahe an der Kolonnenwand angebrachte Stromstörer, wodurch eine dreidimensionale Simulation unabdingbar wird. Die Kühni DN32 Kolonne wurde aufgrund ihres geringen Querschnittes und damit einhergehenden geringen Volumenströmen zur messtechnischen Validierung des CFD Codes herangezogen. Zur Scale-up Untersuchung wurde eine Kühni DN60 Kolonne verwendet. Ein numerische Abbildung der Kolonnen erfolgte mittels m4-Skripte, die eine Diskretisierung und Anpassung der Kolonnengeometrie in wenigen Minuten ermöglicht. Der CFD Code wurden mit eigenen experimentellen Daten basierend auf den Lasermesstechniken der Particle Image Velocimetry (PIV) sowie der Laser Induced Fluorescence (LIF) und mit experimentellen und simulativ gewonnenen Daten aus der Literatur zur Fluiddynamik (Turbulenz, Hold-up, axialer Dispersion) validiert. Der CFD Code wurde anschließend um ein Eingruppenpopulationsbilanzmodell erweitert und mit der analytischen Lösung sowie Simulationen mit dem kommerziellen CFD Tool FLUENT unter Benutzung der Quadrature Method of Moments validiert. Basierend auf einem Eingruppenmodell wurde ein adäquates Koaleszenz- und Zerfallsmodell ausgewählt und an experimentelle Daten angepasst. Hierbei ergab sich eine zuverlässige Vorhersage der Tropfengröße bei variierter Drehzahl.

Das Kolonnendesign der Kühni DN32 Kolonne wurde in Hinsicht auf Compartmenthöhe und Rührerposition modifiziert. Es konnte gezeigt werden, dass eine Veränderung der Rührerposition auf ein Drittel der Compartmenthöhe eine Erhöhung des Hold-ups sowie eine Verkleinerung der Tropfengröße bedingt. Dadurch erfolgt gleichzeitig eine Erhöhung des Stofftransports. Hingegen muss durch diese Veränderung mit einem frühzeitigerem Fluten aufgrund der komprimierten Wirbelstruktur gerechnet werden.

Die Verknüpfung des CFD-PBM Codes mit Stoffaustauschmodellen ermöglicht es zudem, den Wertstoffgehalt entlang der Kolonnenhöhe zu ermitteln und deren Rückwirkung auf die Stoffdaten (Dichte, Viskosität und Grenzflächenspannung) mit zu berücksichtigen. In einem ersten Schritt wurden unterschiedliche Stoffaustauschmodelle basierend auf der Zweifilmtheorie miteinander verglichen. Eine erste Simulation einer Miniplant Kolonne wurde durchgeführt und mit eigenen Daten verglichen. Es konnte gezeigt werden, dass die gekoppelte CFD/PBM

Stoffaustauschsimulation das Konzentrationsprofil entlang der Kolonnenhöhe wiedergeben kann. Zusätzlich werden Informationen über die Grenzflächenspannungs-, Dichte- sowie Viskositätsänderung entlang der Kolonnenhöhe gewonnen. Die Tropfengröße zeigte unter Verwendung eines angepassten Koaleszenz- und Zerfallskernels eine gute Übereinstimmung mit den experimentellen Daten.

Zum Abschluss der Arbeit wurde das Eingruppenmodell auf ein Multi-Fluid Populationsbilanzmodell (der SQMOM) erweitert. Dies ermöglicht die Simulation polydisperser Systeme beziehungsweise die Berücksichtigung von Satellitentropfen in der Simulation von Extraktionskolonnen.

Die erzielten Ergebnisse stärken die Verwendung der CFD zur Auslegung von Flüssig-Flüssig Extraktionskolonnen. Insbesondere die Kopplung von Populationsbilanzen und Stoffaustauschmodellen mit einem OpenSource CFD Code ermöglicht die Analyse komplexer und damit rechenintensiver Kolonnendesigns. Der in dieser Arbeit entwickelte gekoppelte Solver ermöglicht es zusätzlich, die Genauigkeit der Hydrodynamik zu erhöhen und somit auch die Prädiktivität der Ausbeute zu verbessern. Die gewonnen bzw. validierten Korrelationen, z.B. zur axialen Dispersion, können zudem in eindimensionale Stofftransportsimulationen einfließen. Durch die Kombination eindimensionaler- und dreidimensionaler Simulationen ergibt sich somit ein leistungsstarkes Auslegungsinstrument.

In Zukunft wird durch die steigende Rechenleistung eine Erweiterung auf multivariate Populationsbilanzen, wie der SQMOM gekoppelt mit Stoffaustauschmodellen, eine Simulation komplexer Systeme mit hoher Genauigkeit ermöglichen. Als Beispiel sind hier reaktive Blasensäulen zu nennen.

List of Publications

Peer-Reviewed Papers

- M. W. Hlawitschka, D. Seiberth, Y. Gao, H.-J. Bart, Populationsbilanzmodellierung – Experimentelle und numerische Untersuchung an Blasensäulen, Chem. Ing. Techn., 85, 7, pp. 1060-1073, 2013. DOI: 10.1002/cite.201200249.

- H. B. Jildeh, M. W. Hlawitschka, M. Attarakih, H.-J. Bart, Solution of Inverse Problem with the One Primary and one Secondary Particle Model (OPOSPM) coupled with Computational Fluid Dynamics (CFD), Procedia Engineering, 42, pp. 1692-1710, 2012. DOI: 10.1016/j.proeng.2012.07.562.

- M.W. Hlawitschka H.-J. Bart, Determination of Local Velocity, Energy Dissipation and Phase Fraction with LIF- and PIV- Measurement in a Kühni miniplant Extraction Column, Chem. Eng. Sci., Volume 69, Issue 1, 13, pp. 138–145, 2012. DOI: 10.1016/j.ces.2011.10.0.019.

- M. Attarakih, M. Jaradat, M. Hlawitschka, H.-J. Bart, J. Kuhnert, Integral Formulation of the Population Balance Equation using the Cumulative QMOM, Computer Aided Chemical Engineering, 29, pp. 81-85, 2011. DOI: 10.1016/B978-0-444-53711-9.500017-1.

- C. Drumm, M. W. Hlawitschka, H.-J. Bart, CFD Simulations and Particle Image Velocimetry in an Industrial Scale Rotating Disc Contactor, AIChE J., 57, 1, pp. 10-26, 2011. DOI: 10.1002/aic.12249.

- H.-J. Bart, M. W. Hlawitschka, M. Mickler, M. Jaradat, S. Didas, F. Chen, H. Hagen, Tropfencluster – Analytik, Simulation und Visualisierung, Chem. Ing. Tech., 83, No. 7, pp. 965-978, 2011. DOI: 10.1002/cite.201100014.

- M.W. Hlawitschka, F. Chen, M. Attarakih, M. Jaradat , J. Kuhnert, M. Mickler, H.-J. Bart, A CFD-Population Balance Model for the Simulation of Kühni Extraction Column, Comput. Aided Chem. Eng., 29, pp. 66-70, 2011. DOI: 10.1016/B978-0-444-53711-9.50014-6.

- C. Drumm, M. Attarakih, M. W. Hlawitschka, H.-J. Bart, One-Group Reduced Population Balance Model for CFD Simulation of a Pilot-Plant Extraction Column, Ind. Eng. Chem. Res., 49 (7), pp 3442-3451, 2010. DOI: 10.1021/ie901411e.

- M. W. Hlawitschka, M. Mickler, C. Drumm, H.-J. Bart, CFD-Simulation der Ein- und Zweiphasenströmung in einer Kühni-Miniplant Extraktionskolonne, Chem. Ing. Tech. 81, No. 8, pp 1075-1076, 2009. DOI: 10.1002/cite.200950166.

Conference Proceedings

- T. Wächtler, A. Klar, M. W. Hlawitschka, H. Jildeh, H. J. Bart, J. Kuhnert, Mean Droplet Size in Stirred Extraction Columns: From 1D Simulation to 3D FPM Approach, 08.11.2013, Young Researchers Symposium, Nachwuchsring des Landesforschungszentrum Center for Mathematical and Computational Modelling (CM²), Kaiserslautern, Germany, 2013.

- M. Attarakih, M. W. Hlawitschka, M. Abu-Khader, S. Al-Zyod, H.-J. Bart, A Hyperbolic Population Balance Model for Dynamic Analysis of Liquid Extraction Columns, Proceedings of the 6th International Conference on Process Systems Engineering (PSE Asia), 25-27 June 2013, Kuala Lumpur, 2013.

- H.-J. Bart, M. W. Hlawitschka, M. M. Attarakih, Mass Transfer and Population Balance Modeling using 3D-CFD, Proc. 5th Population Balance Conference, 11.-13. September 2013, Bangalore.

- H.-J. Bart, M. W. Hlawitschka, Simulationsgestützes Layout von Extraktionskolonnen, Chem. Ing. Techn., 84, 8, p. 1262, 2012. DOI: 10.1002/cite.201250197.

- M. W. Hlawitschka, H.-J. Bart, CFD Simulation of Droplet Size and Mass Transfer inside Stirred Liquid-Liquid Extraction Columns, PSE conference proceeding, Singapore, 2012.

- F. Chen, M. Hlawitschka, H-J. Bart, H. Hagen, Innovative Multiphase Fluid Visualization for Droplet Column Simulations, Proceeding of "First International Symposium on Multiscale Multiphase Process Engineering (MMPE)", Kanazawa, Japan on October 4-7, 2011.

- M. W. Hlawitschka, H.-J Bart, Simulation of a Miniplant Kühni Extraction Column coupled with PBM, Proc. of International Solvent and Extraction Conference 2011, Santiago, Chile, 2011.

- M.W. Hlawitschka, F. Chen, M. Attarakih, M. Jaradat , J. Kuhnert, M. Mickler, H.-J. Bart, A CFD-Population Balance Model for the Simulation of Kühni Extraction Column, Proceeding ESCAPE 21, Chalkidiki – Greece, 2011.

- M. Jaradat, M. Attarakih, M. Hlawitschka and H.-J. Bart, Detailed Mathematical Modelling of Liquid-Liquid Extraction Columns, Proceeding ESCAPE 21, Chalkidiki, Greece, 2011.

- M. W. Hlawitschka, F. Chen, H.-J. Bart, H. Hagen, CFD Simulation und verbesserte Datenauswertung einer Extraktionskolonne vom Typ Kühni, 15.02.2011, Young Researchers Symposium, Nachwuchsring des Landesforschungszentrum Center for Mathematical and Computational Modelling (CM²), Kaiserslautern, Germany.

- M. W. Hlawitschka und H.-J. Bart, Simulation of the Two-Phase Flow in a Stirred Kühni Extraction Miniplant Column, 7th International Conference on Multiphase Flow – ICMF 2010; Tampa; University of Florida; Article-Nr. 1.3.1.

- M. W. Hlawitschka, C. Drumm, H.-J. Bart, Fluiddynamik der Zweiphasenströmung in einer Miniplant-Extraktionskolonne vom Typ Kühni, Fachtagung „Lasermethoden in der

Strömungsmechanik", 17. Fachtagung, 08.-10.09.2009, Erlangen, ISBN 978-3-9805613-5-8.

- M. W. Hlawitschka, M. Mickler, H.-J. Bart, Simulation einer gerührten Miniplant-Extraktionskolonne mit Hilfe eines gekoppelten CFD-Populationsbilanzmodells, Chem. Ing. Techn. 82, 9, 1389-1390, 2010. DOI: 10.1002/cite.201050058.

Table of Contents

List of Tables

List of Figures

List of Symbols

Symbol	Unit	Definition
A	m²	Cross sectional area
a	m²/m³	Specific surface area
c	e.g. mol/l	Tracer concentration
$C_1, C_2, 3, C_4$	-	Model constants
C_d	-	Resistance coefficient
D	m	Column diameter
d	m	Droplet diameter
d_{30}	m	Volumetric droplet diameter
d_{32}	m	Sauter diameter
D_{ax}	m²/s	Axial dispersion
D_R	m	Rotator diameter
D_S	m	Stator diameter
E	kg m²/s²	Energy
f_e	-	Correction factor
g	m/s²	Gravitational acceleration
g	1/s	Breakage frequency
H	m	Column height
h	m³/s	Collision rate
H_c	m	Compartment height
h_v	kg/(ms²)	Pressure loss
k	m/s	Mass transfer coefficient
k_{eff}	S/m	Effective conductivity
L	-	Abscissa
$m*$	-	Distribution coefficient
$\dot{M}$	kg/s	Mass transfer
m_k	-; 1/m; 1/m²; 1/m³	kth-Moment
N	1/s	Revolution speed
n	1/m³	Number density
n	-	Number
n_{dd}	-	Number of daughter droplets
P	W	Energy input
S	m²	Surface of a mesh cell
S	1/(m³/s)	Population balance source term
t	S	Time
u	m/s	Velocity
v_t	m/s	Terminal droplet velocity
Y	-	Concentration
V	m³	Volume
w_i	-	Weight of the distribution
z	m	Spatial coordinate

Greek Symbols

Symbol	Unit	Definition
α	-	Phase fraction
β	m/s	Mass transfer coefficient
Γ	1/s	Breakage frequency
Δ	-	Difference
ε	m²/s³	Energy dissipation
η	kg/(m s)	Dynamic viscosity
λ	-	Coallision efficiency

λ	m	Kolmogorov length scale
v	m²/s	Kinematic viscosity
π	-	Pi
ρ	kg/m³	Density
σ	N/m	Interfacial tension
τ	s	Retention time
$\bar{\bar{\tau}}$	kg/(m s²)	Stress tensor
Φ_x	-	Numerical field
Φ	-	Integral hold-up
φ_d	-	Hold-Up
ω	m³/s	Coalescence rate

Dimensionless Symbols

$Bo = u \cdot L/D_{ax}$	Bodenstein number
$E\ddot{o} = g \cdot d^2 \cdot |\rho_c - \rho_d|/\sigma$	Eötvos number
$Ne = P/(\rho N^3 D_R{}^5)$	Newton number
$Re = u \cdot d/\mu_c$	Reynolds number of a single particle
$Re_R = N \cdot D_R^2/\mu_c$	Reynolds number of an agitator
$Sc_c = \mu_c/D_c$	Schmidt number of the continuous phase
$Sc_d = \mu_d/D_d$	Schmidt number of the dispersed phase
$Sh_c = \beta_c \cdot d/D_c$	Sherwood number of the continuous phase
$Sh_d = \beta_d \cdot d/D_d$	Sherwood number of the dispersed phase
$We = \rho \varepsilon^{2/3} d^{5/3}/\sigma$	Weber number
$We_R = \rho \cdot N^2 \cdot D_R^3/\sigma$	Stirrer Weber umber
$We_p = \rho \cdot N^2 \cdot D_R^2 \cdot d/\sigma$	Particle Weber number

Abbreviations

CFD	Computational fluid dynamics
CM	Classes Method
DN	Diameter nominal
DPBM	Droplet population balance model
MOM	Method of moments
MUSIG	Multiple-Size-Group
OPOSPM	One Primary One Secondary Particle Method
PBE	Population balance equation
PBM	Population balance model
PDF	Probability density function
PIV	Particle Image Velocimetry
QMOM	Quadrature Method of Moments
RDC	Rotating Disc Contactor
rpm	Revolutions per minute
SQMOM	Sectional Quadrature Method of Moments
UDF	User-defined functions

1 Introduction

Liquid-liquid extraction, also called solvent extraction, is a classical unit operation in the field of fluid separations. The process is mainly applied when distillation is impractical and uneconomical to use (e.g. low relative volatility, thermal instable components). For separation, the feed stream (raffinate stream) is brought in contact with an immiscible liquid solvent. The solvent extracts one or more components out of the feed stream. The extracted components are called the solute.

Liquid-liquid extraction is applied in hydrometallurgy, chemical and petroleum industry up to environmental and pharmaceutical engineering and biotechnological applications (Rydberg et al., 1992, Hanson, 1971, Schmidt, 1988, Schmidt, 2006). The rapidly changing economic conditions require a rapid and effective design of columns in order to survive in the market. This means lower product to market times by keeping or even increasing the efficiency to be on business against the competitors. The uncertain economy and the need of new products have also resulted in shorter product life cycles. Therefore, the development of new layout strategies and extraction processes is of central importance to fulfil the new industrial and economic requirements. The layout of extraction columns is still based on laboratory experiments. These are performed to determine the liquid-liquid equilibrium, the liquid properties such as densities, viscosities and interfacial tensions and to consolidate the choice of solvent. A broad knowledge base of liquid-liquid properties can significantly reduce the first layout step. In addition to the determination of the liquid-liquid properties, first bench experiments using the a small section of the real column geometry can be performed to determine the single and swarm behaviour. Miniplant and pilot plant experiments are used to optimize the extraction parameters for scale-up to the industrial scale (Figure 1.1). Even today, pilot plant experiments are an inevitable preliminary to full scale design for any new process, especially for new liquids with changing properties along the column height. The pilot plant experiments thereby cause most of the costs for layout due to the increased investment costs for safety, construction and operation of the column. The continuous improvement of the miniplant technology and the numerical models to describe the complex behaviour of the liquid-liquid interactions inside the column was a first step to reduce the experimental effort for the scale-up process.
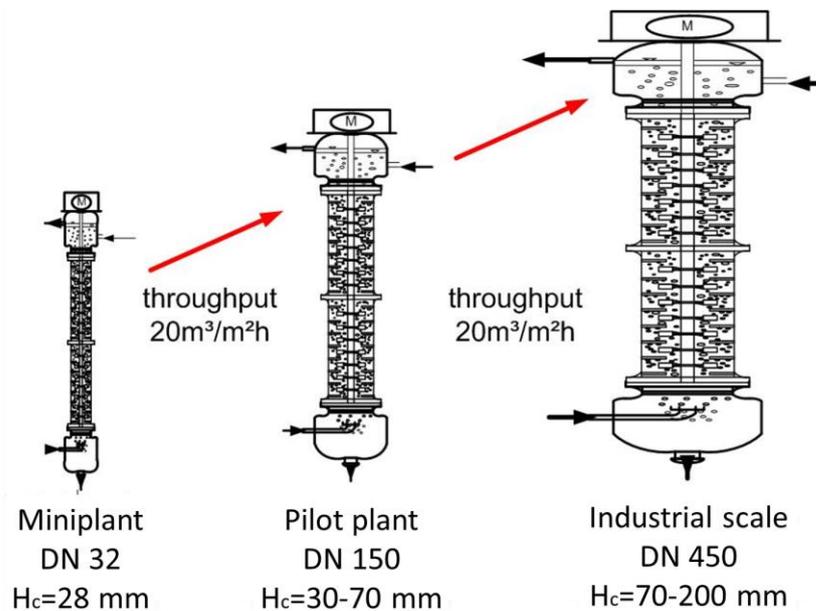
Figure 1.1: Scale up process from miniplant to industrial scale.

The numerical layout of extraction column was mainly based on short-cut methods combined with simplified flow models. The complex droplet-droplet interactions as droplet coalescence and breakage were neglected in this early stage. A promising and validated approach to account the complex interactions in the numerical layout is the bivariate droplet population balance model (Attarakih et al., 2008), which is able to describe the hold-up, droplet size distribution and concentration against the column height. A variety of parameters or correlations, e.g. for axial dispersion, breakage and coalescence and droplet velocity, has to be determined experimentally in advance for every column design. A step forward is the simulation of liquid-liquid extraction columns using a combined computational fluid dynamics (CFD)-population balance solver, which is able to predict the complex flow structure. Initial work was done by Drumm (2010) for the axial symmetrical RDC column.

In this work, the results of Drumm (2010) were transferred to a full three dimensional test case of a Kühni column. The used numerical codes were transferred to an OpenSource environment and extended by new models, especially to describe the influence of mass transfer. For layout purposes, a validation of CFD and PBM to model the hydrodynamics, e.g. the hold-up, the energy dissipation and the droplet size, is essential. Due to this, particle image velocimetry measurements were performed to validate the flow field and energy dissipation in this work. The axial dispersion coefficient obtained from own experiment is compared to simulations using the Euler-Lagrange method. Mass transfer equations combined with population balance modelling for the layout of liquid-liquid extraction columns are new to literature for the investigation of liquid-liquid extraction columns. Mass transfer equations were implemented and compared against

literature and own experimental data. Finally, the visualization techniques for Euler-Euler flows were improved to get a better representation of the local phenomena.

1.1   Layout of Extraction Columns - State of the Art

The extraction column layout typically starts with a definition of the extraction task (e.g. feed stream, purity, throughput, costs) followed by the choice of an adequate solvent. The solvent should have a low toxicity, should be recoverable and may be available at the plant site. In lab experiments, the density, viscosity, interfacial tension and wetting behaviour has to be determined. The characteristics about the coalescence and breakage behaviour can be determined by batch extraction tests (shake-out tests). An appropriate column design (packed, pulsed or stirred column) has to be determined either by knowledge or by the column geometry limits. Single droplet and swarm experiments give information about the droplet swarm behaviour. A verification of the selected solvent and column will be done in miniplant and pilot plant scale to verify the influences of droplet movement, droplet interaction (breakage and coalescence), energy input (stirrer, pulsation) and mass transfer, which cannot be described satisfactorily by existing models. The pilot plant column will be further scaled-up to the industrial scale.

Experimental mass transfer studies for liquid-liquid extraction columns were done by Zamponi (1996) and Garthe (2006). Zamponi (1996) investigated a Kühni DN150 column. Garthe (2006) investigated the mass transfer experimentally in a stirred DN80 column with different internals (RDC, Kühni), where he applied the two-film theory to model mass transfer. Steinmetz (2007) investigated the mass transfer in a Kühni miniplant column and compared the results to the ones obtained from a Kühni DN150 column. Garthe (2006) compared several mass transfer coefficient models to each other based and to single droplet experiments.

The mass transfer is reflected by the concentration of the transition component in each phase. In general, mass transfer is described by the two-film theory (Lewis & Whitman, 1924).

1.2   Aim of the Work

The scale-up of agitated extraction columns from miniplant to industrial scale is still a challenging task due to the complex interactions of the phases. Pilot plant column experiments in columns with diameters ranging from 60 mm up to 150 mm are still used to ensure the results from the miniplant experiments. However, pilot plant experiments become costly, especially when the solvent or the feed is expensive. In addition, tons of waste can further increase the amount of investment costs. The scale-up costs can be significantly reduced by performing the scale-up step with computational fluid dynamics simulations in combination with population balance modelling and mass transfer equations. In addition, the simulations offer a deeper knowledge of the local hydrodynamics and an investigation of different column layouts is possible without the construction

of new column sites. First simulations using the commercial CFD code FLUENT combined with population balance were performed by Drumm（2010）for a small section of an RDC column, where the computational time could be further reduced by using a two-dimensional axial symmetrical mesh. In this study, the focus is placed on the Kühni miniplant column. The Kühni column has in contrast to the RDC column, baffled stirrers and stream breakers along the column, which only allows simulations using a three dimensional framework. Investigations of the different coalescence and breakage kernels are required to find suitable model constants. Mass transfer equations should be added to the CFD solver to account for the concentration change along the column height and to describe the change in physical properties of the two phases. In a last step, the mass transfer equations should be coupled with population balance equations to account for the changes in breakage and coalescence rate due to the concentration change.

Mass transfer correlations were mainly introduced for the simulation of liquid-liquid extraction columns in a one dimensional framework, as ReDrop（Kalem et al., 2011）, LLECMOD（Jaradat et al., 2012）and PPBLAB（Attarakih et al., 2012）. The obtained results concerning the concentration profiles were encouraging. However, the one dimensional modelling still requires a numerous of geometrical dependent correlations.

1.3   CFD Simulations for the Investigation of Extraction Columns

CFD simulations have been used intensively in the field of chemical engineering and the number of publications is still increasing（Figure 1.2）. The investigations of stirred liquid-liquid extraction columns started in 1993 with a publication of Weiss & Bart describing the simulation of a segment of an RDC column with the CFD code Fire. Rieger et al.（1996）simulated a DN150 RDC column at low hold-up and employed the Euler-Euler model to predict the two-phase flow structure. A validation of the velocity field was performed with LDA-measurements at several points. Fei et al.（2000）investigated the single phase flow in stirred liquid-liquid extraction columns. The residence time distribution was numerically and experimentally investigated by Modes & Bart in（2001）and recently by Gurker & Marr（2009）. The two phase flow field was simulated by Vikhansky & Kraft（2004）and You & Xiao（2005）. Ghaniyari-Benis et al.（2009）simulated an RDC column using the Euler-Euler approach. At the beginning of this project in the year 2009, the focus was mainly on the hydrodynamics and less on the droplet-droplet interaction and mass transfer. Drumm（2010）implemented and applied several population balance models（QMOM, DQMOM, SQMOM）for the simulation of the droplet interactions in an RDC column. Due to the high computational time of these models, there was a need for efficient and fast population balance models to allow coupled CFD-PBM simulations in a three dimensional framework and simulations requiring a high number of computational cells.
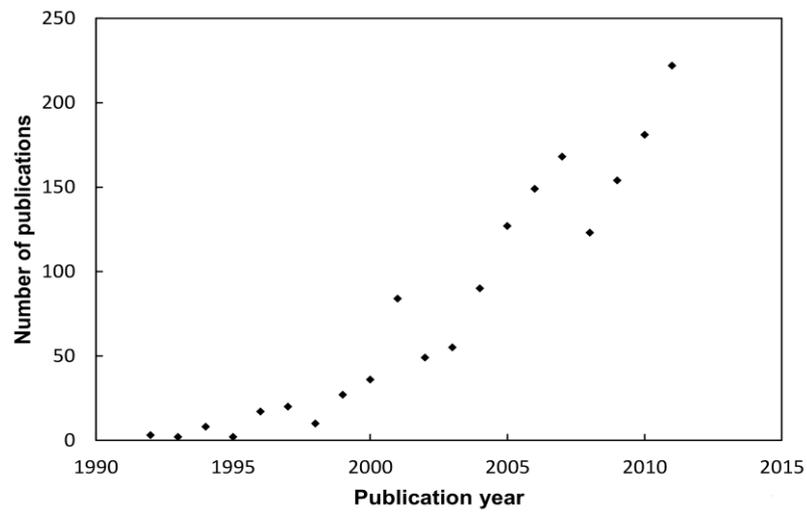
Figure 1.2: Number of publications in Chemical Engineering   Journal containing the words Computational Fluid Dynamics.

2 Computational Fluid Dynamics

Computational Fluid Dynamics （CFD） has become a widely adopted methodology for solving complex fluid flow problems in fluid mechanics and heat transfer, but also has become an important tool in chemical and process engineering. In the face of increasing industrial competitiveness （Tu et al., 2007） and sustainability, the industry is forced to reduce the time-to-market, accounting in addition a more energy efficient, safer and flexible process design with reduced emissions compared to the actual design. Especially when it comes to new and improved process designs, CFD can help to investigate different design possibilities and to reduce, for example, recirculation zones, which lower the final efficiency of the process.

2.1   Simulation Setup

For the prediction of the flow-, heat- and concentration distribution, several mathematical models exist, which can be solved numerically. One the one hand, for solving the numerical equations, several commercial CFD codes are available that include a graphical user interface （GUI） for a user friendly setup of the simulations. Commercial CFD codes are for example Ansys workbench, including Ansys CFX and FLUENT, but also StarCCM+ and Flow3D. On the other hand, there is a huge activity around open-source CFD codes, where the OpenSource Tool OpenFOAM has an outstanding role in the academic area. OpenFOAM provides a principle collection of single phase and two-phase solvers which has the advantage of full access to the source code and therefore can be easily modified and extended by using the programming language C++. However, OpenFOAM does not provide a graphical user interface. After the decision for a suitable simulation program, the flow problem has to be modelled, beginning by the preprocessing and ending by the post processing of the numerical simulation. The principle structure of the flow modelling is shown in Fig. 2.2 and can be divided in four main steps, the problem description, the preprocessing, the simulation and postprocessing. These steps will be further explained in the following sections, while the steps may not only be linear. An iterative process will help to overcome challenges concerning stability and accuracy of the simulation and the final result.
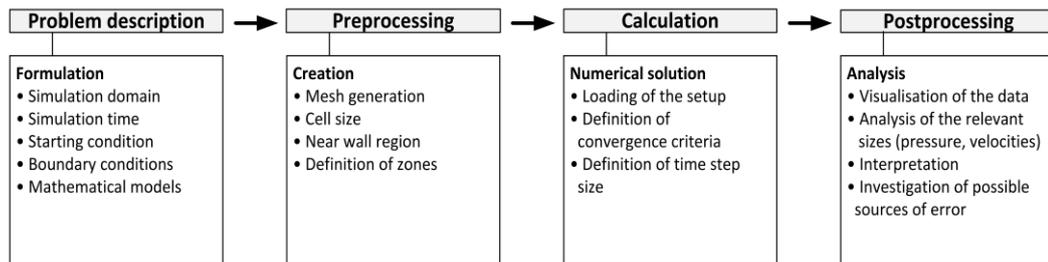
Figure 2.1: **Illustration of the workflow starting with a problem description up to the postprocessing step, in which the simulated data is analysed.**

2.2   Problem Description

In a first step, the principle problem has to be defined. The reasons of using CFD in the process engineering field are based on a reduction of experimental costs and the possibility to improve a current process layout or even support an ongoing design process. In comparison to experimental investigations, the CFD simulation is on the one hand able to describe a flow problem in detail, while on the other hand, the CFD requires numerical models (e.g. drag coefficient), which must be derived experimentally.

2.3   Preprocessing

The preprocessing starts with the creation of a representative flow region of the respective physical domain. The flow region itself, also known as computational domain, is discretized into a finite number of mesh cells. The higher the resolution of the generated mesh is, the better is the approximation to the real object and the simulation result. Especially near hard edges and curved boundaries, a higher resolution is needed to approximate the real geometry. The flow region can be imported in most cases from computer aided design (CAD) software to the simulation software. In most cases, the geometry has to be simplified by e.g. removing small parts as screws and small edges, to keep the number of generated mesh cells low. Another possibility is the generation of the mesh using a specialized preprocessor program such as GAMBIT. A pure description of the mesh can be done using the preprocessor blockMesh, which is part of the OpenFOAM tool, by defining points, edges, faces and volumes.
The mesh can be characterized depending on the cell form in structured and unstructured meshes (Figure 2.2). Structured meshes have a regular topology and consist of a single cell type. The neighbouring cells can be easily counted without additional computation by the indices i=1..N in 1-D, (i,j) in 2-D and (i,j,k) in 3-D. As cell types, mainly rectangular cells and seldom triangular cells are used in 2-D. In a 3-D domain, hexahedron cells, prisms, pyramid cells or tetrahedron cells may be applied (Figure 2.3). Unstructured meshes are more flexible and easier

to use than structured meshes. Due to the complexity of the unstructured mesh, the neighbouring information has to be stored explicitly or has to be calculated during the simulation, which results in a higher computational effort.
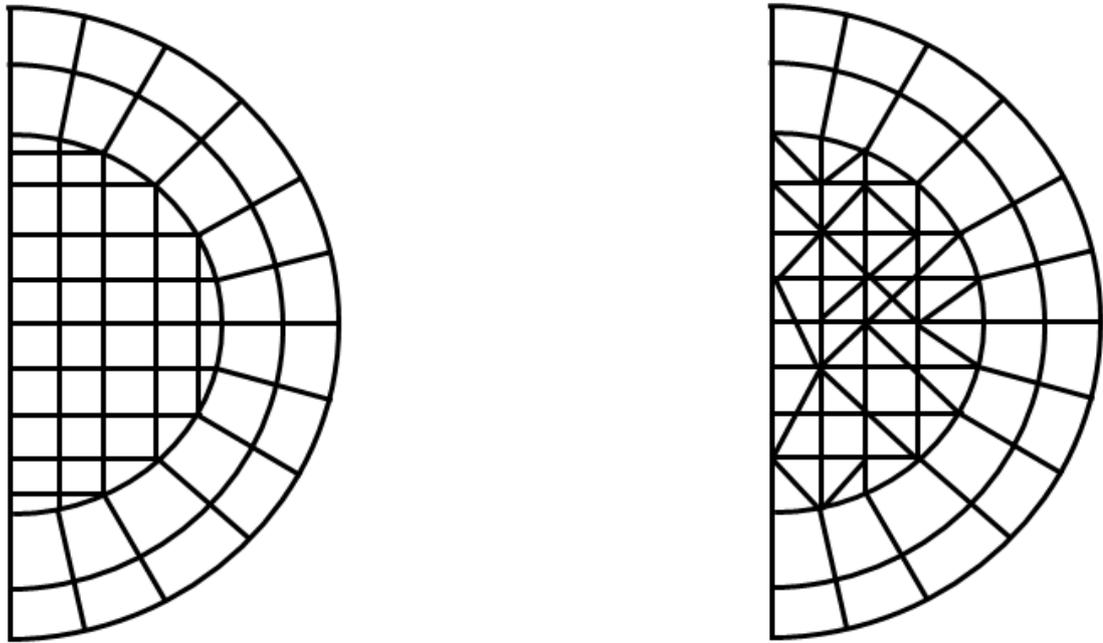
Figure 2.2: Mesh with structured wall parallel boundary: inner structured mesh (left), unstructured mesh (right) (Paschedag, 2004).
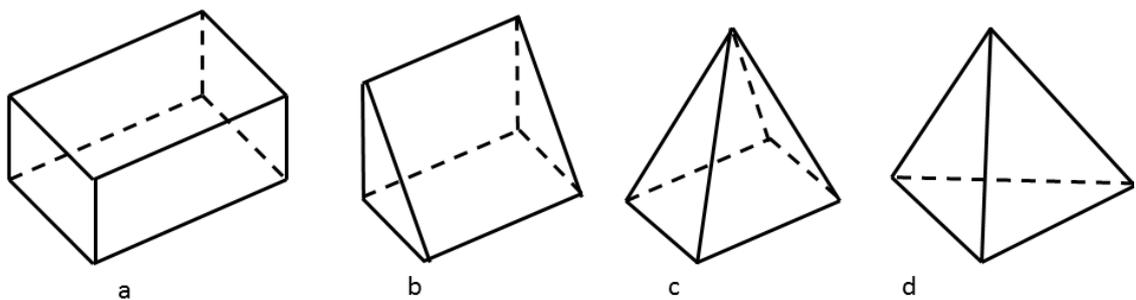
Figure 2.3: Common used cell types: a) hexahedron, b) prism, c) pyramid d) tetrahedron (Paschedag, 2004).

2.4   Calculation – Basic Theory

Several codes are available for the simulation of multiphase flow problems. Among them are the Euler-Euler approach and the Euler-Lagrange approach. The numerical effort and validity of the result depends thereby on the chosen boundary conditions and mathematical solvers. In the following, the basic CFD code is described, starting from the single phase simulation to the multiphase solvers.

2.4.1   Mass Conservation

The conservation law states, that mass can neither be created nor destroyed. Considering a control volume V in Figure 2.4, the fluid flow moves through the control volume and across a second control surface. The rate of change of mass within the control volume is equivalent to the mass flux across the surface:

$$\frac{d}{dt}\int_V \rho dV = \int_S \rho \mathbf{V} \cdot \mathbf{n} dS \qquad (\,2.1)$$

Following the Gauss divergence theorem, the volume integral of the divergence of the vector-function $\mathbf{V}$ is equal to the total flux of $\mathbf{V}$ across the surface S.

$$\int_V div\rho \mathbf{V} dV = \int_S \rho \mathbf{V} \cdot \mathbf{n} dS \qquad (\,2.2)$$

A combination of these two equations results in:

$$\int_V \left[\frac{d\rho}{dt} + div(\rho \mathbf{V})\right] dV = 0 \qquad (\,2.3)$$

Due to the applicability of this equation to any size of volume, it can be written in partial form:

$$\frac{d\rho}{dt} + div(\rho \mathbf{V}) = 0 \qquad (\,2.4)$$

The equation is also known as the mass conservation equation for single phase flow.
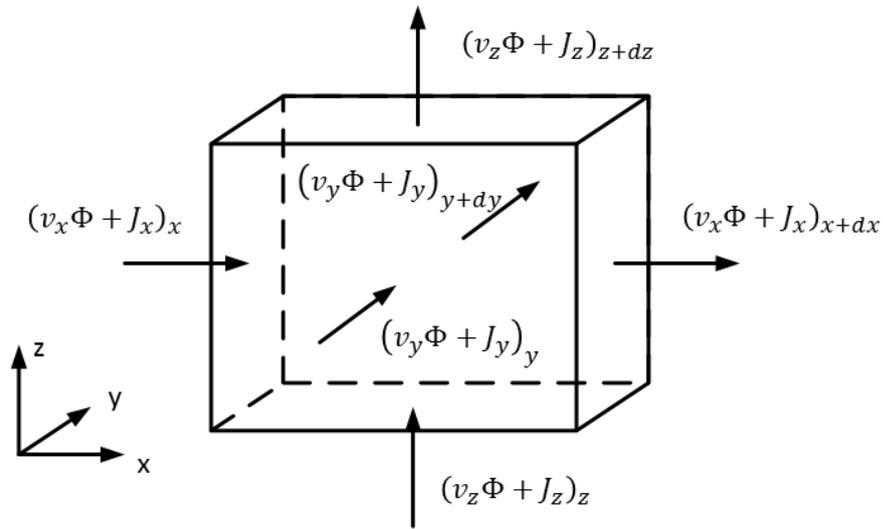
Figure 2.4:   Schematic representation of a control volume.

2.4.2   Momentum Equation

The momentum equation is based on the conservation of the field ϕ (velocity in x, y, z direction), where the first term in Eqn. 2.5 denotes the rate of change of a field Φ_x per unit volume and the second one the second to fourth term represents the in- and outflow of Φ_x of the unit volume.

$$\frac{d\rho\Phi_x}{dt} + \frac{d\rho u\Phi_x}{dx} + \frac{d\rho v\Phi_x}{dy} + \frac{d\rho w\Phi_x}{dz} = 0 \qquad (2.5)$$

On the right hand side of the equation, the interacting forces need to be considered such as pressure p, the stress tensor $\bar{\bar{\tau}}$ and the gravitational body force $\vec{g}$ and forces $\vec{F}$ that arise from the interaction of the continuous with the dispersed phase. In addition, $\vec{F}$ describes all the model dependent user defined sources. Hence, the momentum equation for the velocity field $\vec{u}$ is given by:

$$\frac{d\rho\vec{u}}{dt} + \nabla \cdot (\rho\vec{u}\vec{u}) = -\nabla p + \nabla \cdot (\bar{\bar{\tau}}) + \rho\vec{g} + \vec{F} \qquad (2.6)$$

The stress tensor $\bar{\bar{\tau}}$ is calculated by the molecular viscosity μ, the unit tensor I and the effect of volume dilation, given by the second term on the right hand side:

$$\bar{\bar{\tau}} = \mu\left[(\nabla\vec{u} + \vec{u}^T) - \frac{2}{3}\nabla \cdot \vec{u}I\right] \qquad (2.7)$$

2.4.3 Energy Equation

The energy transport plays only a minor role in liquid-liquid extraction columns and can be neglected in most cases. The equation is also based on the local acceleration term and the advection term on the left hand side, where the terms on the right hand side represent the energy transfer due to conduction, species diffusion and viscous dissipation:

$$\frac{\partial(\rho E)}{dt} + \nabla \cdot \left(\vec{u}(\rho E + p) \right) = \nabla \left(k_{eff} \nabla \text{T} - \sum_j h_j \vec{J}_j + \left(\bar{\bar{\tau}}_{eff} \right) \cdot \vec{u} \right) + S_h \qquad \textbf{(2.8)}$$

Hereby, $\vec{J}_j$ is the diffusion flux of species j and the source S_h includes the heat of chemical reaction and any other defined volumetric heat sources. k_{eff} is the effective conductivity:

$$k_{eff} = k + k_t \qquad \textbf{(2.9)}$$

where k_t is the turbulent thermal conductivity.

2.4.4 Multiphase Modelling

In nature as well as in process engineering systems, particulate systems are widely spread and can be simulated using two-phase or multi-fluid models. In the chemical industry, the two phase flow occurs for example in distillation, absorption, evaporation, condensation, separators and extraction processes. The flow itself can be categorized by its components (gas-liquid, liquid-liquid, gas-solid and liquid-solid flow) and by the flow regime, which ranges from slug flow, free surface flow, sedimentation, fluidized bed, slurry flow to bubbly, droplet and particle laden flow. For the numerical calculation of multiphase flow systems, the Euler-Euler approaches and the Euler-Lagrange approach are available. Hence, the Eulerian approach is typically used for the continuous phase. The dispersed phase may be either described by the discrete approach in the Lagrangian framework or corresponding to the continuous phase in an Eulerian framework. In the Lagrangian framework, the discrete phase is described by a finite number of particles. At low concentration, the effect of the dispersed phase on the continuous phase may be neglected, resulting in a one-way coupling of the phases. A two-way coupling, where the influence of the phases to each other is accounted, is required at higher phase fraction and particle diameters. Hereby, the continuous and dispersed phase hydrodynamics have to be determined simultaneously. Multiphase flows with free surfaces can be simulated using interface-tracking methods or interface-capturing methods, as applied in the volume of fluid (VOF) method, that was firstly introduced by Hirt & Nichols (1981). (Tu et al., 2007)

2.4.4.1. Euler-Euler Approach

In the Euler-Euler approach, the different occurring phases are treated mathematically as interpenetrating continua. In the commercial code FLUENT for example, three different Euler-Euler multiphase models are implemented. The mixture model, the Eulerian model and the volume of fluid (VOF) model.

2.4.4.2. The Eulerian Model

The Eulerian model solves a set of momentum and continuity equations for each phase. The phases are coupled through the pressure and interphase exchange coefficients (e.g. the drag term). The model is the most recommended model (FLUENT, 2005) for simulating liquid dispersed phase flows with phase fractions exceeding 10%. It was also used by several authors simulating the liquid-liquid flow in extraction columns (Drumm, 2010) and will also be used in this work. In the Euerian model, the continuity and mass conservation equation are solved for each phase. The continuity equation for the continuous phase is represented by:

$$\frac{\partial(\alpha_c \rho_c)}{dt} + \nabla \cdot (\alpha_c \rho_c \vec{u}_c) = S \qquad (2.10)$$

The phase fraction of the continuous phase in this equation is represented by α_c, the density of the continuous phase is ρ_c and the velocity of the continuous phase is u_c. The moment conservation equation is given by:

$$\frac{\partial(\alpha_c \rho_c \vec{u}_l)}{dt} + \nabla\big(\rho_c \vec{u}_{c,i} \vec{u}_{c,j}\big) = -\alpha_l \nabla p + \alpha_c \rho_c \vec{g}_i + \alpha_c \nabla \bar{\bar{\tau}} + \vec{F} \qquad (2.11)$$

The sum of the volume fractions of the continuous phase α_c and dispersed phase α_d in each computational cell is equal to one:

$$\alpha_c + \alpha_d = 1 \qquad (2.12)$$

In accordance to the work of Drumm (2010) and the work of Wang & Mao (2005), the dominant interphase interaction is the drag force that is described as:

$$F_{c,i} = -F_{d,i} = \frac{3\rho_c \alpha_c \alpha_d C_d |\vec{u}_d - \vec{u}_c| (u_{d,i} - u_{c,i})}{4d} \qquad (2.13)$$

where C_d is calculated with the model of Schiller & Naumann (1935):

$$C_d = \begin{cases} 24(1 + 0.15Re^{0.687})/Re & Re \leq 1000 \\ 0.44 & Re > 1000, \end{cases} \qquad\qquad \textbf{(2.14)}$$

where the Reynolds number Re is defined as

$$Re = \frac{\rho_c|\vec{u}_d - \vec{u}_c|d}{\mu_c}. \qquad\qquad \textbf{(2.15)}$$

2.4.4.3. The Volume of Fluid Model

The VOF model is using a single set of momentum equation, which is shared by the fluids and the volume fraction, and is tracked throughout the computational domain. The VOF model uses a surface-tracking technique to capture the interface between two or more immiscible fluids. Hence, the main applications for this model include free-surface flows, filling, sloshing or the motion of bubbles or drops in liquids. The VOF model is also used to simulate the breakup of jets by accounting the surface tension. It is often applied to the simulation of free surfaces as single or multiple droplets (less than 10 droplets). For example Tomiyama et al. (1993) investigated a single bubble in a stagnant liquid and in a linear shear flow, whereas 16 cells were used in diameter to represent the droplet size.

2.4.4.4. The Mixture Model

The mixture model is a multiphase model, based on the treatment of the phases as interpenetrating continua. The momentum equation is solved for mass-averaged mixture velocity. The dispersed phase is accounted by relative velocities. The application of the model ranges from bubbly flow to slurry flow: e.g. particle-laden flows with low loading, bubbly flows, sedimentation and cyclone separators (FLUENT, 2005).

2.4.4.5. The Euler-Lagrange Approach

The Euler-Lagrange approach treats the continuous phase as a continuum, which means that the movement is calculated in fixed control volumes. The dispersed phase instead is represented by a large number of particles, where a differential equation is solved for space, force and momentum in a moving grid. A fundamental assumption is, that the dispersed phase only should occupies a low volume fraction (up to 10%, FLUENT, 2005), where the mass fraction may exceed this value. Hence, the model is appropriate for the modelling of spray dryers, coal and liquid fuel combustion, and some particle-laden flows, but it fails for the modelling of liquid-liquid mixtures and fluidized beds. Due to its unique ability of tracking a finite number of particles, it can be used for modelling fluid parameters such as retention time. The trajectory of a discrete

phase particle is determined by the Lagrangian method by integrating the force balance on the particle. In Cartesian coordinates, the force balance is equal to the forces acting on the particle and the particle inertia.

$$\frac{du_p}{dt} = F_D\big(u - u_p\big) + \frac{g_x(\rho_p - \rho)}{\rho_p} + F_x + F_p g, \qquad (2.16)$$

where $F_D(u - u_p)$ represents the drag force per unit particle mass:

$$F_D = \frac{18\mu}{\rho_p d_p^2}\frac{C_d Re}{24} \qquad (2.17)$$

In this equation, u is the fluid phase velocity and u_p is the particle velocity. The molecular viscosity of the fluid is μ. The densities ρ and ρ_p describe the densities of the fluid and particle representatively. The relative Reynolds number of the particle is defined as:

$$Re = \frac{\rho|u_p - u\ |d_p}{\mu_c} \qquad (2.18)$$

C_d is the drag coefficient, which can e.g. be taken from the equation of e.g. Schiller & Naumann (1935) or Morsi & Alexander (1972). The virtual mass force F_x describes the acceleration of the fluid surrounding particle:

$$F_x = \frac{1}{2}\frac{\rho}{\rho_p}\frac{d}{dt}\big(u - u_p\big) \qquad (2.19)$$

The virtual mass force is important, when the densities of the continuum and particle differ ($\rho > \rho_p$). An additional force F_{pg} arises due to the pressure gradient in the fluid:

$$F_{pg} = \left(\frac{\rho}{\rho_p}\right)u_p\frac{\partial u}{\partial x} \qquad (2.20)$$

2.4.5 Particle Method

Particle methods, as the Finite Pointset Method (FPM), are based on a Lagrangian description of the continuous phase and dispersed phases. The main advantage compared to classical methods is, that the FPM method does not require a time consuming geometrical mesh generation. This becomes especially dominant for complex or moving cases, where classical solvers require high computational costs to establish and maintain these grids (Ataki, 2006). The fluid information's as density and velocity are carried by free positioned particles, that are moving with the fluid flow during the simulations.

2.4.6   Turbulence Models

RANS-turbulence models are generally used for the simulation of industrial applications due to an efficient and sufficient resolution of the turbulence. The large eddy simulations (LES) and direct numerical simulations (DNS) instead are used to resolve the details of the turbulent fluctuations and require higher computational resources compared to the RANS models. Due to the increased computational resources and the need of more precise characterization of the flow, LES and DNS become more and more important also in the field of industrial applications. The hydrodynamics in liquid-liquid extraction columns instead, require a long time to reach steady state (e.g. due to accumulation of the dispersed phase). Therefore efficient modelling of the turbulence becomes more important than a detailed modelling of the fluctuations. Hence, here only the RANS-turbulence models will be described.

2.4.7   Two-Equation Models

The contribution of turbulence to the averaged (mean) flow is accounted by two additional transport equations. Representatives of this group are the standard k-ε model, the k-ε realizable model and the Reynolds Stress Model (RSM).
The semi-empirical standard k-ε model (Launder & Spalding, 1974) is widely applied and validated for most kinds of industrially relevant flows (Tu et al., 2007). Nevertheless, the model fails when it comes to highly curved flows. The model transport equation for the turbulent kinetic energy is given as:

$$\frac{\partial}{\partial t}(\rho k) + \frac{\partial}{\partial x_j}(\rho k u_i) = \frac{\partial}{\partial x_j}\left[\left(\mu + \frac{\mu_t}{\sigma_k}\right)\frac{\partial k}{\partial x_j}\right] + P_k + P_b - \rho \ \varepsilon - Y_M + S_k \qquad \textbf{(2.21)}$$

The transport equation for the turbulent energy dissipation instead is derived from physical reasons (FLUENT, 2005):

$$\frac{\partial}{\partial t}(\varepsilon\rho) + \frac{\partial}{\partial x_j}(\rho\varepsilon u_i) = \frac{\partial}{\partial x_j}\left[\left(\mu + \frac{\mu}{\sigma_\varepsilon}\right)\frac{\partial\varepsilon}{\partial x_j}\right] + C_{1\varepsilon}\frac{\varepsilon}{k}(P_k + C_{3\varepsilon}P_b) -$$
$$C_{2\varepsilon}\rho \ \frac{\varepsilon^2}{k} + S_\varepsilon, \qquad \textbf{(2.22)}$$

where the turbulent viscosity in this equation is modelled as:

$$\mu_t = \rho C_\mu \frac{k^2}{\varepsilon} \qquad \textbf{(2.23)}$$

The generation of turbulent kinetic energy is derived from the mean rate-of-strain tensor:

$$P_k = -\rho \overline{u_i' u_j^j} \frac{\partial u_j}{\partial x_i} \qquad (2.24)$$

The effect of buoyancy is accounted by:

$$P_b = \beta g_i \frac{\mu_t}{Pr_t} \frac{\partial T}{\partial x_i} \qquad (2.25)$$

The model constants, which also have been applied in this work, are given as:

$$C_{1\varepsilon} = 1.44, \ \ C_{2\varepsilon} = 1.92, \ \ C_\mu = 0.09, \ \ \sigma_k = 1.0 \ \ \text{and} \ \ \sigma_\varepsilon = 1.3.$$

Improvements have been made to overcome the weaknesses of the standard $k\text{-}\varepsilon$ model, which led to the development of the realizable $k\text{-}\varepsilon$ model.

2.4.7.1. The $k\text{-}\varepsilon$ Realizable Model:

In comparison to the standard $k\text{-}\varepsilon$ model, the realizable $k\text{-}\varepsilon$ model is able to overcome the model based anomaly when it comes to the modelling of a round jet flow due to an enhanced description of the energy dissipation transport equation.

$$\frac{\partial}{\partial t}(\rho k) + \frac{\partial}{\partial x_j}(\rho k u_i) = \frac{\partial}{\partial x_j}\left[\left(\mu + \frac{\mu_t}{\sigma_k}\right)\frac{\partial k}{\partial x_j}\right] + P_k + P_b - \rho \ \varepsilon - Y_M + S_k \qquad (2.26)$$

$$\begin{aligned}
\frac{\partial}{\partial t}(\varepsilon\rho) + \frac{\partial}{\partial x_j}(\rho\varepsilon u_i) \\
= \frac{\partial}{\partial x_j}\left[\left(\mu + \frac{\mu}{\sigma_\varepsilon}\right)\frac{\partial \varepsilon}{\partial x_j}\right] + \rho C_1 S_\varepsilon - \rho C_2 \frac{\varepsilon^2}{k + \sqrt{\nu\varepsilon}} \\
+ C_{1\varepsilon}\frac{\varepsilon}{k}C_{3\varepsilon}P_b + S_\varepsilon
\end{aligned} \qquad (2.27)$$

where

$$C_1 = max\left[0.43, \frac{\eta}{\eta+5}\right], \eta = S\frac{k}{\varepsilon}, S = \sqrt{2S_{ij}S_{ij}} \qquad (2.28)$$

P_k and P_b are calculated in the same way as in the standard $k - \varepsilon$ model. The turbulent viscosity is also calculated in the same manner, where the constant C_μ was replaced by a variable capturing the inertial sub layer of equilibrium boundary layers as well as the homogeneous shear flow:

$$\mu_t = \rho C_\mu \frac{k^2}{\varepsilon}$$

(2.29)

where

$$C_\mu = \frac{1}{A_0 + A_s \frac{kU^*}{\varepsilon}}$$

(2.30)

$$U^* \equiv \sqrt{S_{ij}S_{ij} + \widetilde{\Omega}_{ij}\widetilde{\Omega}_{ij}}$$

(2.31)

$$\begin{aligned}
\widetilde{\Omega}_{ij} &= \Omega_{ij} - 2\varepsilon_{ijk}\omega_k \\
\Omega_{ij} &= \overline{\Omega_{ij}} - \varepsilon_{ijk}\omega_k
\end{aligned}$$

(2.32)

Ω_{ij} is the mean rate of rotation tensor in a rotating reference frame. The angular velocity is described by ω_k. The model constants are described by:

$$A_0 = 4.04 \ \text{and} \ A_s = \sqrt{6}\cos\phi$$

(2.33)

with

$$\phi = \frac{1}{3}\cos^{-1}\left(\sqrt{6}W\right), W = \frac{S_{ij}S_{jk}S_{ki}}{\tilde{S}^3}, \tilde{S}^3 = \sqrt{S_{ij}S_{ij}}, S_{ij} = \frac{1}{2}\left(\frac{\partial u_j}{\partial x_i} + \frac{\partial u_i}{\partial x_j}\right).$$

(2.34)

The used model constants are:

$$C_{1\varepsilon} = 1.44, \ C_2 = 1.9, \ \sigma_k = 1.0 \ \text{and} \ \sigma_\varepsilon = 1.2.$$

2.4.7.2. The Re-Normalisation Group (RNG)-Model

The RNG model uses a modified turbulent dissipation equation to account for smaller scales of motion.

$$\frac{\partial}{\partial t}(\varepsilon\rho) + \frac{\partial}{\partial x_j}(\rho\varepsilon u_i) = \frac{\partial}{\partial x_j}\left[\left(\mu + \frac{\mu}{\sigma_\varepsilon}\right)\frac{\partial\varepsilon}{\partial x_j}\right] + C_{1\varepsilon}\frac{\varepsilon}{k}P_k - C_{2\varepsilon}^*\rho \ \frac{\varepsilon^2}{k} + S_\varepsilon$$

(2.35)

where

$$C_{2\varepsilon}^* = C_{2\varepsilon} + \frac{C_\mu\eta^3(1 - \eta/\eta_0)}{1 + \beta\eta^3}$$

(2.36)

with $\eta = Sk/\varepsilon$ and $S = \left(2S_{ij}S_{ij}\right)^{1/2}$. The typical used constants for the RNG differ from the standard k-ε model and are given by Yakhot et al. (1991) and Tu et al. (2007):

$$C_\mu = 0.0845, \ \sigma_k = 0.718, \ \sigma_\varepsilon = 0.718, \ C_{1\varepsilon} = 1.42, \ C_{2\varepsilon} = 1.68, \ \eta_0 = 4.38, \ \beta = 0.012$$

2.4.8 Simple Algorithm

The Simple-Algorithm (Semi-Implicit Method for Pressure-Linkage Equations) was developed by Patankar & Spalding (1972) for an effective coupling between pressure and velocity field. The pressure field is calculated based on a guess and correct iterative approach to guarantee mass conservation. It is used for implicit type algorithms of steady and unsteady solutions. Derivations of the algorithm are the SIMPLEC (SIMPLE-Consistent) algorithm by van Doormal & Raithby (Yeoh & Tu, 2009).

2.4.9 PISO Algorithm

The PISO algorithm (Pressure-Implicit with Splitting of Operators), developed in 1985 by Issa, is a further extension of the SIMPLE algorithm. The algorithm was developed for non-iterative computation of compressible unsteady flows (Yeoh & Tu, 2009). Adaptions to the PISO algorithm made it applicable for iterative solution of steady-state problems. Also this algorithm caters on the iterative solution of the pressure in the conservation equation. Besides the implicit correction steps existing in the SIMPLE algorithm, a second explicit correction step is used for the velocity field. However, this correction step is seldom and is also not implemented in the OpenFOAM algorithm. The main differences between the PISO and the simple algorithm are: first, that no under relaxation is applied and second, that the momentum correction is applied more than once.

2.5   Postprocessing

In the postprocessing, the simulation data is visualized as vectors, contour plots, or streamlines (Figure 2.5). For a better visualization, especially of three dimensional cases, point probes, line plots, slices, or iso-surfaces can be used (Johnson & Hansen, 2005). However, for particulate flow simulations using the Eulerian simulation, the visualization possibilities of the droplets are still limited by slices or spheres which do not represent the amount and location of particles.

| Slice: Visualization of the phase fraction | Iso−surfaces of the phase fraction | Streamlines of the dispersed velocity field | Vectors of the dispersed velocity field |
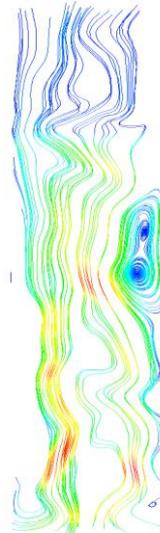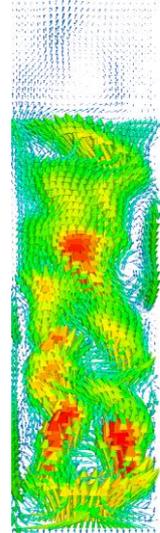
Figure 2.5:   Different visualization possibilities for the hydrodynamics of a rectangular bubble column.

3 Population Balance Equation

In unstable particular systems, the particles tend to grow and to coalesce and break-up due to the shear forces in the flow field. This leads to a widespread particle size distribution, where each particle size moves with its own velocity. Hence, a description of the particle interactions is required to obtain a good numerical approximation of the real system. Hulburt & Katz (1964) and Valentas & Amundson (1966) were among the first who introduced population balance methods for the description of particulate systems in chemical process engineering. The population balance itself is based on a number density function $n\,(\vec{x}, r, t)$ transported with time t in terms of the external coordinate $\vec{x}$ as the spatial position and the internal coordinates r as the droplet volume. Ramkrishna (2000) expressed the population balance equation by a number density balance:

$$\frac{\partial}{\partial t} n + \nabla_x \dot{X} n + \nabla_r \dot{R} n = h \qquad (3.1)$$

Hereby, $\dot{X}$ and $\dot{R}$ are the velocities for the external and internal coordinates. The generation and extinction of particles are described by h. In CFD, the external and internal velocities are replaced by the local calculated velocity, which is given by $\vec{u}$ and number density is often described in terms of the droplet volume as internal coordinate.

$$\frac{\partial}{\partial t} n(V, t) + \nabla \cdot [\vec{u} n(V, t)] = S(V, t) \qquad (3.2)$$

The source term $S(V, t)$ describes the particle interactions and consists in general of four terms, two for breakage (b) and two for coalescence (c):

$$S(V, t) = B^c(V, t) - D^c(V, t) + B^b(V, t) - D^b(V, t) \qquad (3.3)$$

B and D thereby represent the birth and death rates of droplets. Several models were developed over the years to describe the coalescence and breakage of particles beginning with Valentas et al. (1966) and Valentas & Amundson (1966), where the occurrence of breakage is mainly a function of the turbulent energy dissipation. A brief description of breakage models based on the energy for liquid-liquid systems can be found in Steinmetz (2007) and Maaß et al. (2007).

The transport equation for the number density function can be written for the internal coordinate of the particle volume including the integral formulation of coalescence and breakage as:

$$\frac{\partial}{\partial t}[n(V,t)] + \nabla \cdot [\vec{u}n(V,t)] + \nabla_v \cdot [G_v n(V,t)]$$

$$= \frac{1}{2}\int_0^V a(V-V',t)n(V',t)dV'$$

$$- \int_0^\infty a(V,V')n(V,t)n(V',t)dV' \qquad (3.4)$$

$$+ \int_{\Omega_v} \frac{g(V')\beta(V|V'')n(V',t)dV'}{-g(V)n(V,t)}$$

3.1   Solution Methods of the PBM

3.1.1   Monte-Carlo methods

The Monte-Carlo method describes a number of numerical methods using random numbers for the simulation or approximation of different mathematical problems. The methods are applied e.g. in computer sciences for path tracing, in engineering for wind energy yield analysis, in physical sciences for the description of the dynamics of chemical molecules and the solution of population balance equations. Thereby, the dispersed phase is given by finite particles representing the particle size distribution. The interactions as collisions, coalescence and breakage are described by Monte Carlo stochastic simulations（Sommerfeld, 2001, Vikhansky & Kraft, 2004）. An increased number of particles increases the accuracy of the size distribution and of the simulation result.

3.1.2   Discrete Methods

In the discrete method, the particle distribution is discretized into a finite number of size intervals, typically more than 30（Hounslow et al., 1988）. In addition, the applied integration methods for the source term are discretized. Batterham et al.（1981）applied an alternative technique, where the distribution is discretized based on the geometrical sequence：

$$\frac{v^{i+1}}{v^i} = 2 \qquad (3.5)$$

Batterham et al.（1981）used a numerical method for aggregation, which could conserve the mass, but lacks by the description of the total particle number and volume（Batterham et al., 1981, Hounslow et al., 1988）. Hounslow et al.（1988）used a stepwise uniform number density distribution and introduced four interaction mechanisms to account for the particle interactions, two

for coalescence and two for breakage to conserve the number of particles. The mass conservation was reached by the introduction of a correction factor. Litster & Hounslow（1995）used a generalized form of Hounslow's discretization. Also, Hill & Ng（1995）developed a similar technique, which was still limited to pure breakage. In the fixed pivot technique（Kumar & Ramkrishna, 1996）new particles are reassigned to a neighbouring pivot. In comparison to analytical solutions, Kumar & Ramkrishna found over predictions of the large particles, when aggregation was taken into account. To overcome this problem, the method was extended to account for the pivot location within each interval class, resulting in the moving pivot technique（Kumar & Ramkrishna, 1996）, which gives more accurate predictions compared to the fixed pivot technique（Nopens & Vanrolleghem, 2006）.

3.1.3   Moment Based Methods

The Method of Moments（MOM）was introduced by Hulburt & Katz（1964）. The method is based on the solution of the population balance equation through the moments of the particle size distribution（PSD）（Marchisio et al., 2003）. The kth moment can be determined as follows:

$$m_k(x,t) = \int_0^\infty n(L,x,t)L^k dL \qquad (3.6)$$

The MOM is able to track the PSD by a few lower-order moments, whereas the original particle distribution is destroyed. Closure of the source terms is only possible for constant aggregation and size-independent growth. The closure constraints are overcome through the Quadrature Method of Moments（QMOM）.

3.1.4   Quadrature Method of Moments

The Quadrature Method of Moments is based on the MOM and was proposed by McGraw（1997）. The method found its application in the work of Marchisio et al.（2003）to model aggregation and breakage processes. In the QMOM, the shape of the distribution is destroyed and replaced by a set of its moments. The rth moment is given by the integration of the population number density function and commonly solved by the quadrature approximation:

$$m_k(x,t) = \int_0^\infty n(L,x,t)L^k dL = \sum_{i=1}^N w_i L_i^k \qquad (3.7)$$

It could be shown by Drumm（2010）that four moments are sufficient to describe the Sauter diameter for liquid-liquid systems.

3.1.5 Sectional Quadrature Method of Moments

The SQMOM was invented by Attarakih et al. (2009) and is based on primary and secondary particle concept. The primary particles (sections) are responsible for the distribution reconstruction and the secondary particles are responsible for accounting breakage and coalescence. In comparison to the QMOM, the SQMOM has the following main advantages:

- SQMOM is able to reconstruct the distribution:
  A better reconstruction of the distribution is achieved by an increase of primary particles.
- The product difference algorithm is no longer needed due to an analytical solution of the weights and abscissas.
- Problem of ill-conditioning is reduced (only two abscissas).
- Convergence can be enhanced by increasing the number of primary particles.

The SQMOM uses the two-equal weight quadrature derived by the zero, first and third moment:

$$L_{1,2}^i(t) = m_1^i \mp \frac{1}{\sqrt{3}} \sqrt{\frac{m_3^i}{m_1^i} - (m_1^i)^2} \qquad (3.8)$$

$$w_{1,2}^i(t) = \frac{1}{2} m_0^i \qquad (3.9)$$

The moments in this equations are normalized with respect to the zero moment (number of particles) in accordance to the publication of Drumm (2010). For the case of two primary particles and two secondary particles, eight moments transport equations are solved (i=0,1,2,3,4,5,6,7):

$$\alpha_i \rho_d \frac{\partial}{\partial t}(m_k^{<i>}) + \alpha_i \rho_d \nabla(u_d m_k^{<i>}) = \alpha_i \rho_d S_k^{<i>} \qquad (3.10)$$

The source terms for birth and death describe the movement between the sections and are given for the case of two primary and two secondary particles as:

$$B^{C_k^i} = \sum_{k=1}^{i \cdot N_{sp}} \sum_{j=1}^{i \cdot N_{sp}} \left(1 - \frac{1}{2} \partial_{k,j}\right) w_j^{<i>} w_k^{<i>} \cdot \left(L_j^{<i>3} + L_k^{<i>3}\right)^{k/3} \cdot a\left(L_j^{<i>}, L_k^{<i>}\right)$$

$$D^{C_k^i} = \sum_{k=1}^{N_{sp}} w_j^{<i>} \cdot L_j^{<i>} \cdot \sum_{m=1}^{N_{sp}} \left(a\left(L_j^{<i>}, L_k^{<i>}\right) w_1^{<m>} + a\left(L_j^{<i>}, L_k^{<i>}\right) w_2^{<m>}\right) \qquad (3.11)$$

$$B^{B^i}_{k} = \sum_{m=1}^{N_{pp}} \sum_{j=1}^{N_{sp}} L_j^{<m>k} \cdot w_j^{<m>} \cdot g\left(L_j^m\right) \cdot \int_{d_{i-1/2}}^{\min\left(d_{i+\frac{1}{2}}, d_j^{<i>}\right)} L^k \beta\left(L \middle| L_j^{<m>}\right) \partial L$$

$$D^{B^i}_{k} = \sum_{j=1}^{N_{sp}} w_j^{<i>} \cdot L_j^{<i>} \cdot g\left(L_j^{<i>}\right)$$

3.1.6   The One Primary and One Secondary Particle Methods (OPOSPM)

The One Primary One Secondary Particle Method (OPOSPM) by Attarakih et al. (2009) is the simplest case of the SQMOM with one primary and one secondary particle. The droplet diameter in each cell is calculated with the use of the volumetric diameter

$$d_{30} = \sqrt[3]{\frac{6V}{\pi N_d}} = \sqrt[3]{\frac{m_3}{m_0}} \tag{3.12}$$

where N_d and α_d are the total number and volume concentrations that are related to the zeroth (m_0) and third (m_3) moments of the distribution. Since the third moment corresponds to the continuity equation of the dispersed phase, only the zeroth moment has to be considered additionally as a user defined scalar in the CFD calculation. The OPOSPM was implemented as "User Defined Functions" in FLUENT by Drumm et al. (2010), where only one additional transport equation in form of a user defined scalar transport equation had to be added. The population balance equation is generally written in terms of a number concentration function given here by the zeroth moment (m_0):

$$\frac{\partial}{\partial t}\left(\rho_d m_0\right) + \nabla\left(u_d(d_{30})\rho_d m_0\right) = \rho_d S \tag{3.13}$$

The droplet size as well as the source term was solved by Drumm et al. (2010), using a normalized zeroth moment ($m_{0;norm} = m_0 \cdot m_3$), which leaded to a stabilized solution, especially at the beginning of the simulation. For the OpenFOAM simulations in this work, the zeroth moment is used instead of the normalized moment, which was possible, especially due to a better access to the boundary conditions. The droplet distribution is represented by a single droplet, which is calculated based on the volumetric diameter d_{30}. The coalescence of droplets is represented by two equal daughter droplets, reducing the computational effort further. The droplet breakage is based on the representative diameter in each cell. A coupling of the newly obtained diameter by the drag term leads to a two way-coupling of the hydrodynamics and the population balance equation.

3.1.7   Cumulative Quadrature Method of Moments

The Cumulative Quadrature Method of Moments is a new integral formulation to couple the QMOM and the evolving particle size (Attarakih et al., 2011). The CQMOM is able to conserve the particle distribution itself by tracking the cumulative continuous moments. The basic idea is based on a given set of low-order cumulative moments of $\omega(x)$ as the non-negative integrable function on the interval [a,b]:

$$\mu_r = \int_{a=0}^{x} \varsigma^r \omega(\varsigma) du, \quad r \in [0, 2N_q - 1] \tag{3.14}$$

In this equation, ς represents the nodes (diameters) between 0 and x. The transport equation for the cumulative moment is then given as:

$$\frac{D}{Dt}\left(\alpha_i \rho_{d_0} \mu_r\right) + \nabla(\alpha_i u_d(d)\mu_r) = \alpha_i \rho_d r \sum_{j=1}^{N_q} \varsigma^{r-1} G(\zeta)\omega(\zeta)\lambda + \alpha_i \rho_d S \tag{3.15}$$

A detailed description of the source term is given in (Attarakih et al., 2011). The main advantage of this model is, that a full conservation of the cumulative droplet size distribution is obtained. In comparison to the SQMOM, the CQMOM requires a higher number of transport equations to account for bivariate distributions. However, the CQMOM allows a reconstruction of the cumulative droplet size distribution for continuous droplet size distributions with a lower number of transport equations.

3.2   Determination of the Moments from Measurements

The droplet sizes and number of droplets entering a column are represented by the droplet size distribution. For the momentum based calculations, the droplet size distribution is represented by a set of integral values, the moments of the distribution. The moments are calculated based on a number density distribution:

$$m_{k,r} = \int_{x_{min}}^{x_{max}} x^k \cdot q_r(x)dx = \sum \bar{x}^k \cdot \delta Q_r(x) \tag{3.16}$$

Hence, the Sauter diameter is given by the third moment to the second moment.

$$d_{32} = \frac{m_3}{m_2} \tag{3.17}$$

4 Coalescence and Breakage

Liquid-liquid dispersed phase systems are characterized by the droplet size, droplet volume and droplet number. These parameters describe the total interfacial area and influence the mass transfer between the phases. The droplet specific parameters are subject to a continuous change due to breakage and coalescence of the droplets. For liquid-liquid extraction columns, a better understanding of the coalescence and breakage phenomena leads to a better prediction of the droplet size inside a single compartment and of the droplet size along the column height. In the past 50 years, several techniques were developed to gain a better understanding especially of the coalescence phenomena (Simon, 2004). On the one hand, the experimental derived models depend on the average energy dissipation, inner and outer geometrical data as the column diameter, compartment height or stirrer diameter and system data as total flow rate. On the other hand, models were developed based on pure liquid data (e.g. density, viscosity, interfacial tension) and the local energy dissipation causing breakage and coalescence. For the CFD simulations, only the second class of equations is reliable due to the local resolution of the energy dissipation. Among the most common models, which are also used in this work, are the coalescence models from:

- Coulaloglou & Tavlarides (1977)
- Prince & Blanch (1990)
- Luo & Svendsen (1996)

and the breakage models from:

- Coulaloglou & Tavlarides (1977).
- Luo & Svendsen (1996)
- Martínez-Bazán et al. (1999a, 1999b)
- Andersson & Andersson (2006)

4.1 Coalescence Models

4.1.1 Coulaloglou & Tavlarides (1977)

The model of Coulaloglou & Tavlarides (1977) is validated against measurements in a turbulent vessel. Coalescence between droplets occurs due to the collision of droplets and a sufficient contact time that film drainage, film rupture and finally the coalescence of the droplets can take place. The coalescence model assumes a collision rate proportional to the collision

times. The collision rate is based on the kinetic theory of gases for colliding molecules and on a locally isotropic flow field.

$$h(d_1, d_2) = C_3 \frac{\varepsilon^{1/3}}{1 + \alpha} (d_1 + d_2)^2 \left(d_1^{\ 2/3} + d_2^{\ 2/3}\right)^{1/2} \qquad (\ 4.1)$$

The constant C_3 accounts for corrections of the energy dissipation and mean square fluctuation velocities of the droplets and is given as $2.32 \cdot 10E-6$. The collision efficiency accounts for the processes taking place after the first contact. The film thickness at initial contact of the drops is lumped into a parameter C_4 and is given as $1.2 \cdot 10E-9$:

$$\lambda(d_1, d_2) = exp\left(-C_4 \frac{\mu_c \rho_c \varepsilon}{\sigma^2} \left(\frac{d_1 d_2}{d_1 + d_2}\right)^4\right) \qquad (\ 4.2)$$

4.1.2   Prince and Blanch

The coalescence rate in the model of Prince & Blanch (1990) is based on pure turbulent collision, while the buoyancy drive and laminar shear collisions were neglected (Drumm et al., 2009). The collision efficiency is based on the relative film thickness h_0 to the critical film thickness h_c.

$$h(d_1, d_2) = 0.089\pi(d_1 + d_2)^2 \varepsilon^{1/3} \left(d_1^{\ 2/3} + d_2^{\ 2/3}\right)^{1/2} \qquad (\ 4.3)$$

$$\lambda(d_1, d_2) = exp\left(-\frac{\left(d_1 d_2 / \left(4(d_1 + d_2)\right)\right)^{5/6} \rho_c^{1/2} \varepsilon^{1/3}}{4\sigma^{1/2}} ln\left(\frac{h_0}{h_c}\right)\right) \qquad (\ 4.4)$$

4.1.3   Luo & Svendsen

The model of Luo & Svendsen (1996) contains no directly adjustable parameters as the previous models. The coalescence frequency in the model is similar to the one of Prince & Blanch (1990). The coalescence term is based on the kinetic gas theory and is given by:

$$h(d_1, d_2) = \frac{\pi}{4}(d_1 + d_2)^2 \beta^{0.5} \varepsilon^{1/3} \left(d_1^{\ 2/3} + d_2^{\ 2/3}\right)^{1/2} \qquad (\ 4.5)$$

$$\lambda(d_1, d_2) = exp\left(-C_1 \frac{[0.75(1 + \xi^2)(1 + \xi^3)]^{1/2}}{\left(\frac{\rho_d}{\rho_c} + \gamma\right)^{1/2} (1 + \xi)^3} We^{1/2}\right) \qquad (\ 4.6)$$

4.2   Breakage Models

4.2.1   Coulaloglou & Tavlarides (1977)

The breakage model of Coulaloglou & Tavlarides (1977) is based on a drop breakup in a locally isotropic field and takes into account the influence of local pressure fluctuations and the breakup time of critically deformed drop. The model is valid for droplets within the inertial sub range eddies and consists of two terms: The breakage time and the fraction of droplets breaking up.

$$g(d) = C_1 \cdot \frac{\varepsilon^{1/3}}{d^{2/3}(1+\alpha)} exp\left(-\frac{C_2 \sigma (1+\alpha)^2}{\rho_d \varepsilon^{2/3} d^{5/3}}\right) \tag{4.7}$$

The dimensionless constants are given as $C_1 = 0.336$ and $C_2 = 0.106$ in Coulaloglou & Tavlarides (1977).

4.2.2   Luo & Svendsen (1996)

The breakage function is based on arriving eddies to the surface of the droplets. The breakage frequency is calculated for a droplet of size d as

$$g(d) = 0.923 \cdot (1+\alpha) \left(\frac{\varepsilon}{d^2}\right)^{1/3} \int_0^{0.5} \int_\xi^1 \frac{(1+\xi)^2}{\xi^{11/3}} exp\left(-\frac{12 c_f \sigma}{\beta \rho_c \varepsilon^{2/3} d^{5/3} \xi^{11/3}}\right) d\xi df_v$$

$$c_f = f_v^{2/3} + (1-f_v)^{2/3} - 1$$

$$f_v = \frac{d_2^3}{d_1^3} \tag{4.8}$$

4.2.3   Martínez-Bazán et al. (1999a, 1999b)

The model of Martínez-Bazán et al. (1999a, 1999b), is based on purely kinematic ideas. The surface of the particle has to be deformed by turbulent stresses.

$$g(d) = \frac{K\sqrt{\beta_0 (\varepsilon d)^{2/3} - 12(\sigma/(\rho d))}}{d} \tag{4.9}$$

K is an adjustable parameter in the original model where Drumm (2010) used a value of 1. The fluctuations between two points separated in a characteristic distance d is described by the use of the constant β_0 (Batchelor, 1956).

$$\delta u^2(d) = \beta_0(\varepsilon d)^{2/3} \qquad\qquad\qquad \text{(4.10)}$$

β_0 is described as a relation between the Kolmogorov constant C and the gamma function of $1/3$.

$$\beta_0 = \frac{9}{5}\Gamma\left(\frac{1}{3}\right)C = 4.82C. \qquad\qquad\qquad \text{(4.11)}$$

The Kolmogorov constant, used by Martínez-Bazán et al. (1999a, 1999b), is C=1.70, which is in the range of literature data given by Yeung & Zhou (1997). With that estimation, the critical diameter is determined by:

$$d_c = \left(12\sigma/(\beta_0\rho)\right)^{3/5}\varepsilon^{-2/5}. \qquad\qquad\qquad \text{(4.12)}$$

4.2.4   Andersson & Andersson (2006)

The model of Andersson and Andersson (2006) was developed to describe the breakup of fluid particles in a turbulent flow. Therefore, a new model for the interaction frequency of the fluid particles and the turbulent eddies was introduced. The breakup rate is given by:

$$g(d) = \int_{d_0}^{10d_0} \omega_s(d_0,\lambda)P(d_0,\lambda)d\lambda \qquad\qquad\qquad \text{(4.13)}$$

where the interaction frequency is given by:

$$\omega_s = \frac{c_a\pi d_0^3\varepsilon^{1/3}}{6\lambda^{14/3}} \qquad\qquad\qquad \text{(4.14)}$$

The constant c_a is taken from Luo & Svendsen (1996) and was determined to 0.822. The probability of an eddy breaking up a fluid particle of size d is given by

$$P(d_0,\lambda) = \int_{\chi_{min}}^{\infty} \varphi(\chi)d\chi \qquad\qquad\qquad \text{(4.15)}$$

where $\varphi(\chi)$ describes the normalized energy distribution with χ defined as the ratio of the eddy viscosity to the average eddy viscosity. Compared to the previous described models, the model of Andersson & Andersson (2006) shows the highest breakage probability to equal sized droplets.

5 Hydrodynamics

5.1 Hold-up

Besides the knowledge of the hydrodynamics and droplet size, a deep knowledge about the dispersed phase hold-up ϕ is required for the layout of liquid-liquid extraction columns. On the one hand, the hold-up defines in combination with the droplet size the interfacial area between the phases, which is available for mass transfer. On the other hand, a high mass transfer thereby leads to a change in hold-up and therefore to a change in the interfacial area due to droplet growth and droplet shrinkage. In addition, the hold-up changes the local hydrodynamics due to swarm effects and accumulation.

The hold-up in single compartments is also used for the calculation of the hydrodynamics in one-dimensional models. The slip velocity between the phases in counter-current columns for example is defined by:

$$V_{slip} = \frac{V_d}{\phi} + \frac{V_c}{1-\phi} \qquad (5.1)$$

A correlation for the hold-up is given by Kumar & Hartland (1995), which is suitable for rotated columns as well as for pulsed, packed and spray columns:

$$\phi = \left[0.27 + \left\{\frac{\varepsilon}{g}\left(\frac{\rho_c}{g\sigma}\right)^{\frac{1}{4}}\right\}^{0.78}\right]\left[V_d\left(\frac{\rho_c}{g\sigma}\right)^{\frac{1}{4}}\right]^{0.87} \cdot$$

$$exp\left[3.34V_c\left(\frac{\rho_c}{g\sigma}\right)^{1/4}\right]\left(\frac{\Delta\rho}{\rho_c}\right)^{-0.58}\left(\frac{\mu_d}{\mu_c}\right)^{0.18}C_\Gamma e^{n_6}\left[l\left(\frac{\rho_c g}{\sigma}\right)^{1/2}\right]^{-0.39} \qquad (5.2)$$

The parameter e is defined by the ratio of the free cross sectional area. For rotating columns, this is given by the ratio of the stator opening D_s to the column diameter D_c:

$$e = \left(\frac{D_s}{D_c}\right)^2 \qquad (5.3)$$

In addition, the parameter C_Γ depends on the column geometry and is given in Table 1. The value of n_6 is set to -1 for Kühni and packed columns and zero for other rotating columns. Kumar & Hartland (1995) could reproduce hold-up measurements of different column types with a relative error of 29%. However, the equation only predicts the hold-up as an average value for the whole column. A change in droplet size along the column height and therefore a change

of the hold-up along the column height is not accounted for as it is done in modern population balance models (Steinmetz, 2007).

Table 1: **Parameters for the determination of the hold-up inside extraction columns using the correlation of Kumar & Hartland (1995).**

	RDC	Kühni	Wirz	Pulsed	Packed	Spray
C_Γ	$(D_R/H)^{0.62}$	2.27	5.13	153.2	2.43	1.32

5.2 Droplet Sedimentation Velocity

The fluid dynamic behaviour of the existing two phase flow is determined on the one hand by the energy input and by the geometrical design. On the other hand, the hydrodynamics of the dispersed phase are determined by the droplet sedimentation velocity, which is mainly influenced by the density difference between the liquid phases. For the numerical calculation, a correct description of the droplet velocity compared to literature data must be assured. Based on investigations of different liquid-liquid systems, several phenomenological and empirical correlations (Table 2) were obtained and are discussed in Steinmetz (2007), Clift et al. (1978) and Brauer (1971).

Table 2: **Common used droplet rise velocity correlations in literature (Steinmetz, 2007)**

Author	Droplet velocity		Validity
Stokes (1851)	$$v_t(d) = \left(\frac{4dg\Delta\rho}{3\rho_c C_d}\right)^{0.5} \quad C_d = \frac{24}{Re_d}$$	**(5.4)**	Rigid sphere, $Re_d < 1$
Misek (1974)	$$v_t(d) = 0.249 \cdot d \cdot \left(\frac{g^2\Delta\rho^2}{\rho_c\eta_c}\right)^{1/3}$$	**(5.5)**	Rigid sphere, empirical correlation
Oseen (1910)	$$v_t(d) = \frac{d}{4.2} \cdot \left(\frac{g\Delta\rho}{\rho_c}\right)^{2/3} \left(\frac{\rho_c}{\eta_c}\right)^{1/3}$$	**(5.6)**	Rigid sphere
Vignes (1965)	$$v_t(d) = \frac{d}{4.2} \cdot \left(\frac{g\Delta\rho}{\rho_c}\right)^{2/3} \left(\frac{\rho_c}{\eta_c}\right)^{1/3} \left(1 - \frac{E\ddot{o}}{6}\right)$$	**(5.7)**	Circulating droplets
Klee & Treybal (1956)	$v_t(d) = 38.3 \cdot \rho_c^{-0.45}\Delta\rho^{0.58}\eta_c^{-0.11}d^{0.7} \; for: d < d_{crit.}$ $v_t(d) = 17.6 \cdot \rho_c^{-0.55}\Delta\rho^{0.28}\eta_c^{-0.1}\sigma^{0.18} \; for: d < d_{crit.}$ $d_{crit.} = 0.3 \cdot \rho_c^{0.14}\Delta\rho^{-0.43}\eta_c^{0.3}\sigma^{0.24}$	**(5.8)**	Circulating and oscillating droplets
Grace et al. (1976)	$$v_t(d) = \frac{\eta_c}{d\rho_c}Mo^{-0.149}(J - 0.857)$$ $$J = \begin{cases} 0.94H^{0.757} \; for: 2 < H < 59.3 \\ 3.42H^{0.441} \; for: H > 59.3 \end{cases}$$ $$H = \frac{4}{3}E\ddot{o} \cdot Mo^{-0.149}\left(\frac{\eta_c}{\eta_{water}}\right)$$	**(5.9)**	Empirical correlation for rigid and oscillating droplets in contaminated systems

Clift et al. (1978) describe the occurrence of different droplet forms in dependence of the Reynolds number, the Eötvös number and the Morton number, where the first one describes the flow regime and the second and third one together describe the form based on the fluid properties in the gravitational field. Small droplets are considered to have a spherical shape with a rigid surface. Viscous forces are more important than inertia forces (Clift et al., 1978). An increase in droplet size leads to a higher droplet velocity and the beginning of a surface flow inducing an inner circulation to the droplets. The inner circulation reduces the droplet resistance and improves the mass transfer due to a continuous transport of fluid elements with lower concentration to the interface, when a mass transfer direction from continuous to disperse phase is considered. With a further increase of droplet volume, the droplets deform to an ellipsoidal shape and the droplets follow a wobbling motion (Clift et al., 1978). Larger droplets form spherical caps or ellipsoid-caps.

In extraction columns, the typical droplet size is between 1 and 4 mm (Steinmetz, 2007) and can be considered as rigid spheres. Larger droplets are influenced by the column wall and reduce the droplet rise velocity (Clift et al., 1978, Henschke et al., 2000). A critical diameter ratio of droplet size to column size of 1:6 reduces the free droplet rise velocity to 70% (Chhabra & Bangun, 1997). For smaller droplets, the resulting velocity is about 95% of the free rising velocity (Steinmetz, 2007).

For the layout of stirred liquid-liquid extraction column, Steinmetz (2007) specifies the equation of Grace et al. (1976) for the determination of the sedimentation velocity, which also is in good agreement with experimental data from Modes (2000), Schmidt (2006), Garthe (2006), Steinmetz (2007) (Figure 5.1).
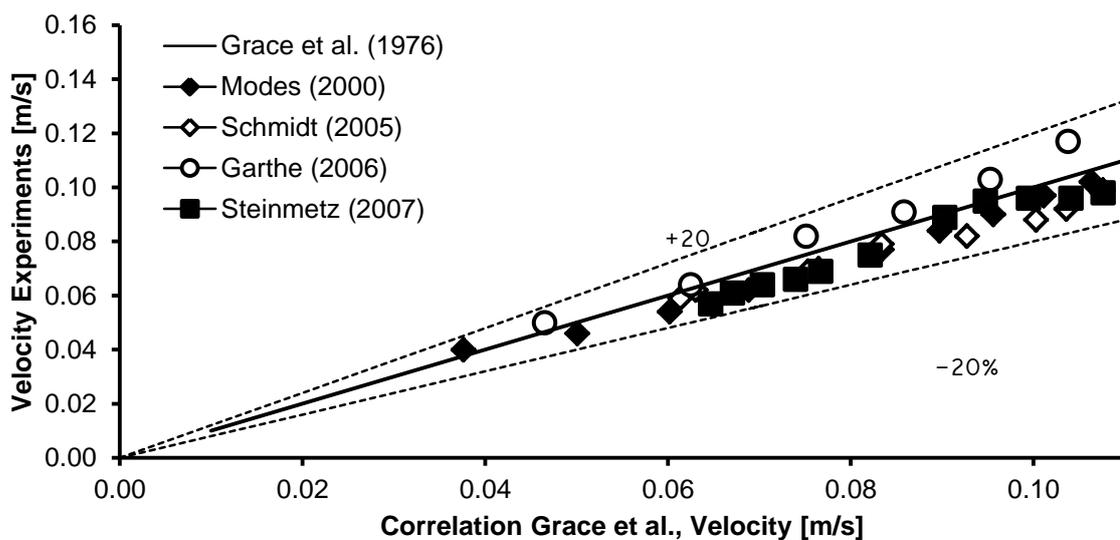
Figure 5.1:   **Parity plot of the experimental droplet velocity to the droplet velocity correlation of Grace et al. (1976) for the system of water/toluene.**

Recently, the focus is based on a numerical description using CFD simulations to describe the shape of the droplets and the droplet rise velocity (Deshpande & Zimmermann, 2006, Petera & Weatherley, 2001, Watanabe & Ebihara, 2003, Waheed et al., 2004, Dijkhuizen et al., 2005, Bertakis et al., 2010, Bäumler et al., 2010). But, the CFD is still based on the investigation of inherently "clean" systems (Bäumler et al., 2010).

5.3   Axial Dispersion

The efficiency of liquid-liquid extraction columns is not only influenced by the grade of extraction and mass transfer resistance but also by deviations from the ideal plug flow leading to mixing in axial direction (Figure 5.3). In liquid-liquid extraction columns, the axial dispersion is caused by several mixing effects, which are described by Pratt & Hanson (1982):

- Transport of the continuous phase with the droplets and against the main flow direction.
- Backmixing of the continuous phase in the wake of the droplet swarms.
- Backtransport of the continuous phase due to the generation of the double vortex structure in agitated columns.
- A droplet velocity distribution of the different sized droplets caused by breakage and coalescence.
- Channelling of the liquids due to the geometry of the column (e.g. around the stator rings).

Especially the first three points, characterized by a backward mixing, lead to a reduction of the concentration difference and reduce the column efficiency. Also forward mixing, as occurs due to coalescence, leads to a decrease of the specific surface and a decrease in contact time of the phases due to a higher droplet rise velocity. The effect of axial dispersion on the concentration transition component concentration profile in the continuous and dispersed phase is shown in Figure 5.2. The axial dispersion induces a jump of the concentration profiles at the inlet of the light and heavy phase resulting in a reduced true driving force between the phases.

A description of the backmixing effects is done by the axial dispersion model, which is based on the 1. Fick's law:

$$J = -D_{ax} \cdot \frac{dc_A}{z} \qquad\qquad (5.10)$$

J is the diffusion flow density in z direction and D_{ax} is the dispersion coefficient in axial direction. From the derivation of the 1. Fick's law, the 2. Fick's law can be obtained:

$$\frac{dc}{dt} = -D_{ax} \cdot \frac{d^2 c_A}{dz^2}$$

(5.11)
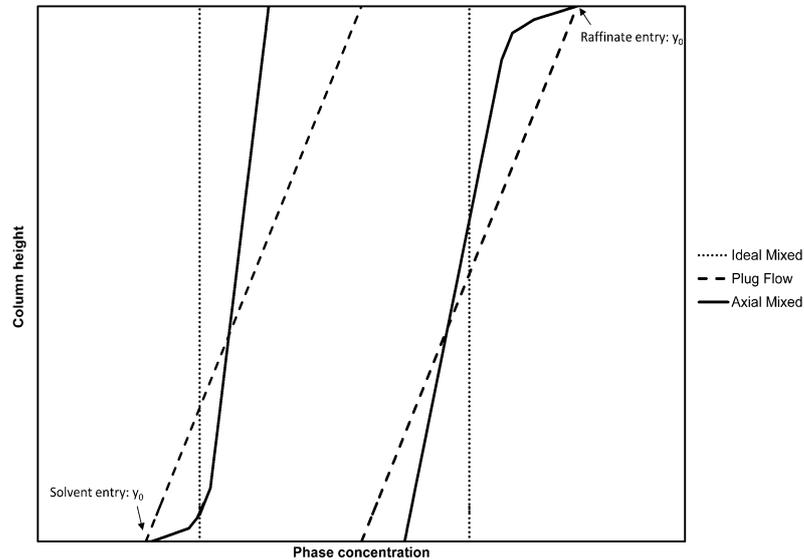
Figure 5.2:   The effect of axial dispersion on the concentration profile of the transition component in the continuous and dispersed phase (Misek & Rod, 1971)

In an open system, the axial dispersion coefficient at the boundaries（inlet and outlet）of the system corresponds to the one inside the system. In a closed system, the axial dispersion coefficient at the inlet differs from the one inside the system. Considering a pipe flow, the concentration transport by axial dispersion is superposed by the convective transport along the main flow direction（Figure 5.3）.
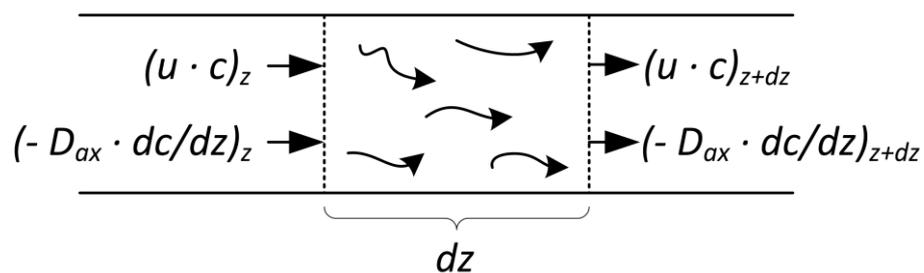
Figure 5.3:   Axial dispersion in a pipe.

From the balance around the system, the concentration transport is described by:

$$\frac{\partial c}{\partial t} = D_{ax} \frac{\partial^2 c}{\partial z^2} - u \frac{\partial c}{\partial z}$$

(5.12)

In the normalized form, the balance is given by the normalized concentration C, the normalized retention time θ and the normalized coordinate Z:

$$\frac{\partial C}{\partial \Theta} = \frac{1}{Bo} \frac{\partial^2 C}{\partial Z^2} - u \frac{\partial C}{\partial Z} \tag{5.13}$$

Instead of the axial dispersion, the Bodenstein number Bo was introduced as dimensional number:

$$Bo = \frac{uL}{D_{ax}}, \tag{5.14}$$

where u is the velocity, L the length of the column and D_{ax} is the axial dispersion coefficient. Taking this equation, two idealized limiting cases are possible:

- ideal stirred tank: $D_{ax} \rightarrow 1$ and Bo $\rightarrow 0$
- ideal flow tube: $D_{ax} \rightarrow 0$ and Bo $\rightarrow 1$

The axial dispersion coefficient is experimentally determined by measuring the response concentration profile of an added tracer downstream the column. Feller (1968) published an analytical solution for an ideal impulse function of the tracer at the inlet:

$$c(t) = \frac{\tau}{2 \cdot t} \cdot \left[\frac{Bo \cdot \tau}{\pi \cdot t} \right]^{1/2} exp\left[-\frac{Bo \cdot \tau}{4 \cdot t} \left(1 - \frac{t}{\tau}\right)^2 \right] \tag{5.15}$$

An earlier solution is described by Levenspiel & Smith (1957):

$$c(t) = \frac{1}{2} \cdot \left[\frac{Bo \cdot \tau}{\pi \cdot t} \right]^{1/2} exp\left[-\frac{Bo \cdot \tau}{4 \cdot t} \left(1 - \frac{t}{\tau}\right)^2 \right] \tag{5.16}$$

Both solutions lead to similar solutions for $Bo \gg 10$ (Krizan, 1987).

5.3.1   Backmixing Continuous Phase

Several experimentally derived correlations were obtained over the years to describe and determine the axial dispersion coefficient based on geometrical and operational boundary conditions. However, the one dimensional description of the flow makes the correlations prone to changes in flow conditions e.g. due to geometrical changes in the stirrer geometry during scale-up. Bauer (1976), for example, derived a correlation including different compartment heights:

$$D_{ax,c} = u_c H_c \cdot (0.5 + q) \tag{5.17}$$

The backmixing parameter q is derived from the stirrer diameter d_r, the stirring speed n and the continuous phase velocity u_c:

$$q = C \cdot \frac{d_R \cdot n}{u_c} \qquad\qquad (5.18)$$

Miyauchi et al. (1966) gives the following equation based on the assumption of isotropic turbulence and the geometrical constraints:

$$D_{ax.c} = H_c \cdot \left[C_1 + C_2 \cdot \varphi \cdot (\frac{D_C}{H_c})^{C_3} \cdot \frac{Re_R^{0,83}}{Re_c} \right]$$

where the parameters $C_1 - C_3$ are given in Table 3 for the RDC and Kühni column.

Table 3: Coefficients to determine the axial dispersion coefficient based on the equation of Bauer (1976).

Author	Column type	Norm diameter [mm]	C_1	C_2	C_3
Miyauchi et al. (1966)	RDC	150	0.176	0.0817	0.5
Bauer (1976)	Kühni	150	0.325	0.118	0.33

Several authors published a similar equation for the axial dispersion coefficient for a Kühni column:

$$D_{ax,c} = u_c \cdot H_c \left(C_1 + C_2 \cdot \left(\frac{D_R N}{u_c} \right) \cdot C_3 \right) \qquad\qquad (5.19)$$

The constants were adapted to experiments and are shown in Table 4.

Table 4: Experimentally derived constants for the axial dispersion coefficient in Kühni columns.

Author	Column type	Norm diameter [mm]	C_1	C_2	C_3
Breysee et al.(1983)	Kühni	150, 600, 800	0.14	0.046	φ
Bauer & Widmer (1977)	Kühni	150	0.176	0.0817	$\varphi \cdot \frac{d_R}{d_K} \cdot \left[\frac{d_K}{H_C} \right]^{1/3}$
Steiner (1988)	Kühni	150	0.188	0.0267	$\varphi^{0.5}$
Kolb(2005)	Kühni	32	0.203	0.031	$\varphi^{0.5}$
Steinmetz(2007)	Kühni	32	0.203	0.031	φ
Steinmetz(2007)	Kühni	32	0.14	0.093	φ
Steinmetz(2007)	Kühni	150	0.118	0.0264	φ

5.3.2   Axial Dispersion of the Dispersed Phase

The dispersed phase axial dispersion coefficient depends in addition to the geometry of the column on the droplet size distribution. Coalescence and breakage along the column height may influence the axial dispersion in each compartment. Stermerding et al. (1963) observed a higher dispersed phase axial dispersion coefficient compared to the continuous phase coefficient resulting from a higher deviation of the droplet size, which causes a higher spreading of the residence time distribution. A higher rotational speed leads to a smaller droplet size distribution and lower droplet rise velocities and hence to lower axial dispersion coefficients. The coefficients of each phase are approaching with increasing speed (Figure 5.4) (Gourdon et al., 1994). The available axial dispersion coefficient correlations for the dispersed phase are shown in Table 5.
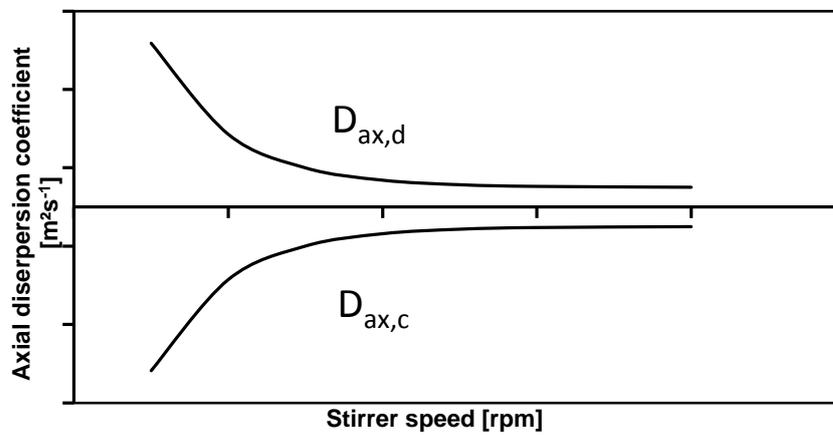
Figure 5.4:   Theoretical axial dispersion coefficient in extraction column for different stirrer speeds (Gourdon et al., 1994).

Table 5: Axial dispersion coefficients for the dispersed phase.

Author	Column type	Norm diameter [mm]	Equation
Bibaud & Treybal (1966)	Oldshue-Rushton	150	$\frac{1}{Bo} = 3.93 \cdot 10^{-8} \left(\frac{\rho_c d_s^3 N^2}{\sigma}\right)^{1.54} \left(\frac{\rho_c}{\Delta\rho}\right)^{4.18} \left(\frac{\rho_c d_s^2 N}{\eta_c}\right)^{0.61}$
Rod (1968)	RDC		$\frac{1}{Bo} = 0.7 + 0.006 \frac{d_R N}{u_d}$
Bauer (1976)	ARD	150	$\frac{1}{Bo} = 0.092 + 1.9 \cdot 10^{-8} Re_R^{1.7} Re_D^{-0.7}$
Steinmetz (2007)	Kühni	32	$\frac{1}{Bo} = 0.056 + 1.19 \cdot 10^{-2} \left(\frac{d_R N}{u_d}\right)^{3.45}$

5.4 Flow Regimes

The flow in the extraction column is composed of a pipe flow and a superimposed vortex structure flow generated by the stirrer. For later validation of a Lagrangian solver for the determination of the axial dispersion coefficient, a single pipe flow is investigated and compared to the following analytical equations. The velocity profile in pipes is characterized by the laminar and turbulent flow regime. The transition from laminar to turbulent flow in pipes is defined by the Reynolds number (2315<Re<10000) (Lohrengel, 2007, Baerns et al., 2006). At Re<2315, a stable laminar flow develops inside the pipe where the highest velocity is found in the central axis of the pipe (Kalide, 1990):

$$u_{max} = \frac{h_v}{16 \cdot \nu \cdot L} \cdot d^2 \qquad (5.20)$$

The parabolic velocity profile decreases to the pipe wall and can be described for the laminar case by:

$$u_{x,lam.} = \frac{h_v}{4 \cdot \nu \cdot L} \cdot (R^2 - r^2), \qquad (5.21)$$

The pressure loss in pipes h_v is influenced by the pipe length, the cross sectional area, the roughness of the pipe and by the fluidic parameters as viscosity and density and can be calculated by the Darcy-Weisbach equation (Weisbach, 1845):

$$h_v = \frac{p_1 - p_2}{\rho} + g \cdot \Delta z = \lambda \cdot \frac{l}{d} \cdot \frac{u^2}{2}, \qquad (5.22)$$

where p_1 is the pressure at the inlet and p_2 is the pressure in a distance l to p_1. The friction number λ for a laminar flow in pipes can be determined following the law of Hagen-Poiseuille:

$$\lambda = \frac{64}{Re} \qquad (5.23)$$

For turbulent flows, the friction number depends in addition on the roughness of the pipe wall. Following the velocity profile from the pipe wall to the centre axis, the velocity increases rapidly close to the wall where to the middle of the pipe, the velocity only slightly increases. The maximum velocity reaches values of 1.25 of the average velocity (Schade & Kunz, 1989). Following Nikuradse (1933), the turbulent velocity profile can be calculated by:

$$u_{x,turb.} = \left(1 - \left(\frac{r}{R}\right)\right)^n \cdot u_{max} \qquad (5.24)$$

The friction number for the turbulent case in a pipe can be calculated by (Nikuradse, 1933):

$$\lambda = \frac{1}{\left(2 \cdot log\left(\frac{d}{k}\right) + 1.138\right)^2}$$

(5.25)

The exponent n and the friction factor k are dependent on the Reynolds number (Table 6).

Table 6: Exponent n and friction factor k in dependence of the Re-number (Sigloch, 2007).

Re	$4 \cdot 10^3$	$2.3 \cdot 10^4$	$1.1 \cdot 10^5$	$1.1 \cdot 10^6$	$(2- 3.2) \cdot 10^6$
N	1/6	1/6.6	1/7	1/8.8	1/10
K	0.791	0.807	0.817	0.85	0.865

5.5   Flow Regimes in Stirred Tanks

The stirring inside the columns leads to a generation of a specific flow pattern and the generation of a normal- and shear stress field, which is required for a homogenization of the liquids and concentrations as well as a dispersion of the droplets (Stieß, 1995). Different stirring types are available for extraction columns ranging from simple rotating discs to the complex Kühni turbine stirrer. Based on the principle flow patterns, the stirrer types are characterized by their axial, radial or tangential flow generation. The principle flow patterns in a stirred compartment is shown in Figure 5.5.
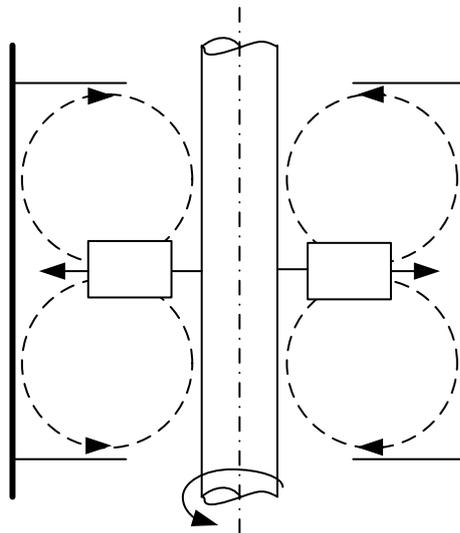
Figure 5.5:   Flow structure in a single compartment (Goldmann, 1986).

The flow structure and energy input depend in addition to the stirrer type and stirrer form on the internals as baffles and stators of the column. The turbulent energy input is responsible for the generation of the interfacial area between the phases and is enhanced by droplet breakup and

reduced by droplet coalescence. Breakup is thereby limited by a minimum rotational speed corresponding to the minimum energy input. The breakup also depends on the column geometry and the liquid properties as density, viscosity, interfacial tension and hold-up (Coulaloglou & Tavlarides, 1977, Simon, 2004). The average energy dissipation can be obtained by the use of the Newton number Ne, the rotational speed n, the stirrer diameter D_R and the compartment volume V:

$$\bar{\varepsilon} = \frac{P}{V \cdot \rho} = \frac{Ne \cdot n^3 \cdot D_R^5}{V} \qquad (5.26)$$

The Newton number is a function of the Reynolds number and stirrer geometry and becomes constant in a turbulent flow regime. In general, the transition from laminar to turbulent flow in stirred tanks is characterized by a Re-number range (Paul et al., 2004):

$$Re = \frac{\rho N D_R^{\,2}}{\nu} = 10 \ldots 10^4 \qquad (5.27)$$

5.6   Mass Transfer

The mass transfer determines the efficiency of the liquid-liquid extraction column and is characterized by diffusion processes as well as by convective transport mechanism in the interior and near surrounding regions of the droplet. A change in density of the phases due to mass transfer influences in addition the hydrodynamics. For example, a higher density difference leads to higher relative velocities of the droplets and the entrainment of small droplets is reduced (Fischer, 1973). Hence, the phase fraction of the dispersed phase is reduced inside the column. However, a direct dependency on the change in density difference to the droplet size could not be found for the test system iso-octane/water by Fischer (1973). Also a change in viscosity and interfacial tension along the column height may change the breakage and coalescence behaviour of the droplets and influence the hydrodynamics especially of the dispersed phase. The interfacial tension is also responsible for the stability of the droplets and the droplet form. A low interfacial tension leads to a loss of the form stability and hence to deviations from the drag coefficient and again to influences on the hydrodynamics.

In liquid-liquid extraction, a solute is transferred from one liquid solvent to another across a boundary (Backhurst et al., 1999). The mass transfer on each side of the interface is the same, there no mass accumulates at the interface. The rate of it depends on the physical properties of the two liquid phases as interfacial area and concentration difference. Especially the stirred columns are designed to improve the specific interfacial area between the two phases by promoting breakage of the dispersed phase due to the energy input. In literature, different

mechanism are available to describe the mass transfer between two phases. The mass transfer rates are controlled, according to the two-film theory (Lewis & Whitman, 1924), shown in Figure 5.6, by the resistance in the continuous and dispersed phase. The resistance at the interface is suggested to be zero. Turbulence, which is existing in the bulk phase, is going to die out close to the interface. On both sides of the interface, thin laminar boundary layers with a linear concentration profile exists. This model, original generated for adsorption, was also introduced by Kumar (1985) for modelling the mass transfer in liquid-liquid extraction columns. The mass transfer from the dispersed to the continuous phase is thereby described by:

$$\dot{M} = a \cdot \rho_d \cdot \beta_d \cdot (y_b - y_{if}) = a \cdot \rho_c \cdot \beta_c (x_{if} - x_b) \qquad (5.28)$$

In this equation, the specific interfacial area is given by a, the density of the dispersed phase by β_d and the density by ρ_d. The concentration inside the droplet is given by y_b and the concentration at the interface by y_{if}. The density of the continuous phase is ρ_c and the concentration at the interface and in the bulk is given by x_{if} and x_b respectively (see Figure 5.6). The concentration at the interface can be determined by the concentration in the bulk phase and the distribution coefficient, which results in:

$$y_{if} = m \cdot x_b \qquad (5.29)$$

and

$$x_{if} = \frac{y_b}{m}. \qquad (5.30)$$

Hence, the mass transfer rate can be described only by the bulk concentration of each phase:

$$\dot{M} = a \cdot \rho_d \cdot \beta_{od} \cdot (m \cdot x_b - y_b) = a \cdot \rho_c \cdot \beta_{oc} \left(x_b - \frac{y_b}{m}\right), \qquad (5.31)$$

where β_{od} is the overall dispersed phase mass transfer coefficient and β_{oc} is the overall continuous phase mass transfer coefficient. The interfacial area a is calculated based on the Eulerian calculation with the droplet size d and the phase fraction:

$$a = \frac{6 \cdot \alpha}{d} \qquad (5.32)$$

The distribution coefficient can be assumed in a small range as a constant, where especially for industrial systems, a non-ideality can be observed. The penetration theory, proposed by Higbie (1935), describes a mass transfer, where fresh material is transported by eddies to the interphase. Thies is depicted in Figure 5.7 and results in an unsteady state of mass transfer for

a period of time. Fluid elements having the concentration of the bulk are transported to the phase boundary interface by turbulence. During the contact of the fluid element with the phase boundary interface, a non-steady diffusion process occurs. After the constant contact time Δt, the fluid element is transported again into the bulk of the continuous phase. The retention time of the fluid element is for each element identical. The penetration is often used to describe mass transfer in liquid films, bubbles and droplets (Mersmann, 1986). Danckwerts' (1951) surface renewal theory is based on the theory of Higbie. In addition, he considers, that eddies range into the interface from the continuous phase and renew the interface with fresh fluid.
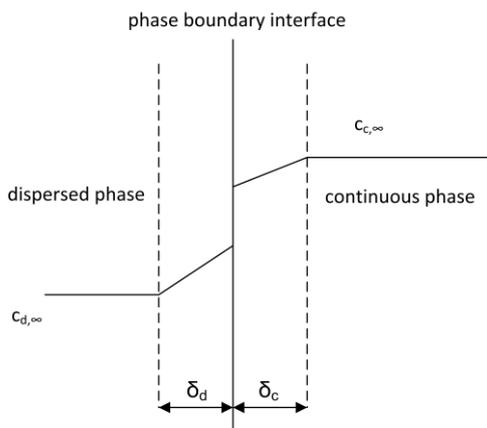
Figure 5.6: Film theory.   **Figure 5.7: Penetration theory (Higbie, 1935)**
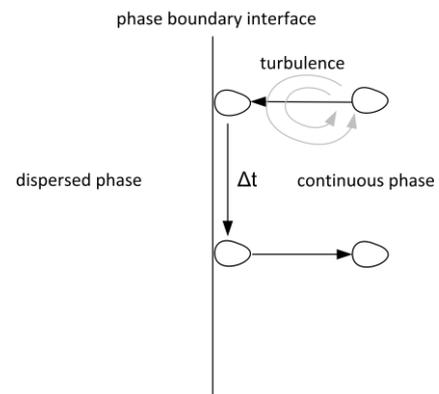
5.7   Mass Transfer Coefficients

The overall mass transfer coefficients β_{od} and β_{oc} can be calculated by the knowledge of the individual mass transfer coefficients β_d and β_c (Garthe, 2006):

$$\frac{1}{\beta_{od}\cdot\rho_d} = \frac{1}{\beta_d\cdot\rho_d} + \frac{m}{\beta_c\cdot\rho_c} \text{ and } \frac{1}{\beta_{oc}\cdot\rho_c} = \frac{1}{\beta_c\cdot\rho_c} + \frac{1}{\beta_d\cdot\rho_d m} \tag{5.33}$$

The mass transfer rate is mainly influenced by the droplet velocity, form and state. Three main states could be determined for liquid-liquid droplets (Clift et al., 1978):

- Rigid droplets: Small droplets at moderate Reynolds number (low relative velocity) and average to high surface tension. Diffusion controlled mass transfer.
- Circulating droplets: Rigid droplets with an internally circulating current. Convection controlled mass transfer. Mainly at low viscosities of the dispersed phase compared to the continuous phase (Fischer, 1973).

- Oscillating droplets: Large droplets. The droplet shape changes periodically. Convection controlled mass transfer. Due to the energy input and low droplet sizes in extraction columns, oscillating droplets are seldom.

Several equations for the individual mass transfer coefficients were developed in the past. The best-known correlations are described in the following sections for the dispersed phase and continuous phase.

5.7.1   Individual Mass Transfer Coefficient in the Dispersed Phase

Newmans (1931) description of the mass transfer is the basis for many other models. It is based on the assumption of rigid droplets. A simplified form of the model is given in Steinmetz (2007):

$$k_d = 0.083 \cdot \frac{d}{t_e} + 6.58 \frac{D_d}{d}$$

(5.34)

Kronig & Brink (1950) describe the mass transfer of a single falling droplet under the influence of gravity. The viscous forces between the fluids arising from the droplet movement lead to circulation currents in the droplets and a higher mass transfer compared stagnant droplets. It could be shown, that the mass transfer increases by a factor of 2.5 in comparison to simple diffusion as it was given by Newman, which results in a higher 2nd term:

$$k_d = 0.079 \cdot \frac{d}{t_e} + 17.66 \frac{D_d}{d}$$

(5.35)

The model of Handlos & Baron(1957) was developed for rigid droplets in the range of 2.5 to 5 mm and is one of the most commonly used models for the layout of liquid-liquid extraction columns (Schmidt, 2006). It is based on the viscosity of the two liquids:

$$k_d = 0.00375 \cdot \frac{u_0}{1 + \nu_d/\nu_c}$$

(5.36)

where u_0 is the terminal velocity of a free rising droplet, ν_d is the viscosity of the dispersed phase and ν_c is the viscosity of the continuous phase. Kumar & Hartland (1999) developed an empirical correlation based on the measurements of 21 groups of investigators.

$$k_d = \frac{D_d}{d_p} \cdot Sh_d \quad \text{mit } Sh_d = 17,7 + \frac{3,19 \cdot 10^{-3} \left(Re_p Sc_d^{1/3} \right)^{1,7}}{1 + 1,43 \cdot 10^{-2} \left(Re_p Sc_d^{1/3} \right)^{0,7}} \left(\frac{\rho_d}{\rho_c} \right)^{2/3} \times$$

(5.37)

$$\frac{1}{1+(\eta_d/\eta_c)^{2/3}}$$

where Sc_d and Re_p are:

$$Sc_d = \frac{\eta_d}{D_d\rho_d} \text{ and } Re_p = \frac{\rho_c \cdot \text{u} \cdot d_p}{\eta_c} \tag{5.38}$$

where κ is the viscosity ratio of the dispersed phase and the continuous phase. Pilhofer & Mewes（1979）developed an empirical model, which is similar to the one developed by Handlos & Baron（1957）:

$$k_d = 0.002\frac{u_0}{1 + v_d/v_c} \tag{5.39}$$

An empirical model for circulating droplets is given by Laddha （1974）:

$$k_d = 0.023\frac{u_0}{Sc_d^{0.5}} \tag{5.40}$$

The dispersed phase mass transfer coefficients are compared in Figure 5.8 for a droplet size of 3 mm for the test system toluene/acetone/water. The mass transfer coefficients show a linear dependency on the relative velocity of the droplets to the surrounding liquid. The highest mass transfer coefficient for a 3 mm droplet size is observed from the model of Handlos & Baron （1957）followed by the model of Kumar & Hartland （1999）, Laddha （1974）and Pilhofer & Mewes （1979）.
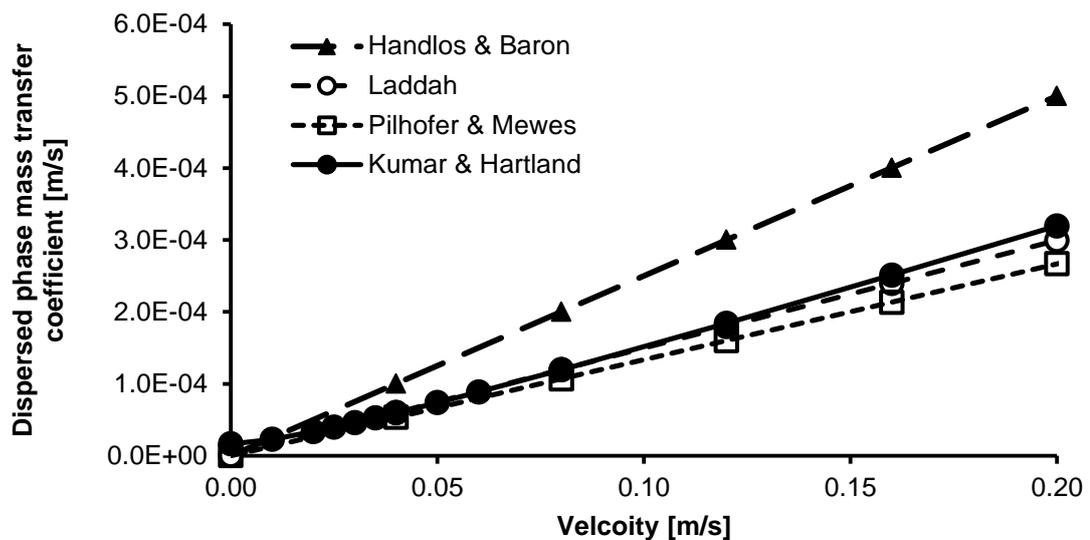
Figure 5.8:   Dispersed phase mass transfer coefficient.

5.7.2   Individual Mass Transfer Coefficient in the Continuous Phase

A theoretical model for the mass transfer coefficient in the continuous phase for droplets under the influence of gravity is given by Kronig & Brink (1950). Internal circulation is considered based on the Hadamard streamlines.

$$k_c = \frac{D_c}{d}\left(0.6\sqrt{Re_p \cdot Sc}\right)$$
(5.41)

A correlation for rigid droplets is given by Garner & Tayeban (1960) for the range of 8<Re<800:

$$k_c = \frac{D_c}{d}\left(2 + 0.67\sqrt{Re_p \cdot Sc}\right)$$
(5.42)

An empirical correlation for circulating droplets is given by Treybal (1963) accounting the swarm effect by the phase fraction α_d:

$$k_c = \frac{D_c}{d}\left(0.725 Re_p^{0.57} Sc_c^{0.42}(1 - \alpha_d)\right)$$
(5.43)

A correlation for oscillating droplets is given by Clift et al. (1978):

$$k_c = 1.2 D_c^{0.5}\left[\frac{48\sigma}{\pi^2 d^3(2\rho_c + 3\rho_d)}\right]^{0.25}$$
(5.44)

For the transition of spherical droplets to droplets with a moving interface, the correlation of Heertjes et al. (1954) was frequently used in literature (Schmidt, 2006).

$$k_c = 0.83 \cdot \sqrt{\frac{D_c \cdot u_r}{d}}$$
(5.45)

Slater (1994) describes a correlation for contaminated droplets:

$$k_c = \frac{D_c}{d}\frac{2}{\pi^{1/2}} \cdot \sqrt{c_{slater}\sqrt{Pe}}$$
(5.46)

The model of Kumar & Hartland (1999) is based on the correlation of Steiner (1988) for rigid droplets and for the transition to oscillating droplets, the correlation is based on the work of Clift et al. (1978). Based on 600 experimental data, the error of the equation was found to be in the range of 24.5%.

$$k_c = \frac{D_c}{d_p} \cdot \frac{Sh_{c,\infty} \cdot a + Sh_{c,rigid}}{1+a} \qquad \text{with} \qquad Sh_{c,\infty} = 50 + \frac{2}{\pi^{0,5}} \cdot Pe_c^{0,5} \qquad \text{and}$$

$$Pe_c = \frac{d_p \cdot w_p}{D_c}$$

(5.47)

where $Sh_{c,rigid}$ and a are defined as:

$$Sh_{c,rigid} = 2,43 + 0,775 \cdot Re_p^{0,5} \cdot Sc_c^{1/3} + 0,0103 \cdot Re_p \cdot Sc_c^{1/3}$$

(5.48)

$$a = 5,26 \cdot 10^{-2} Re_p^{\frac{1}{3}+6,59 \cdot 10^{-2} Re_p^{1/4}} \times Sc_c^{1/3} \left(\frac{w_p \eta_c}{\sigma}\right)^{1/3} \frac{1}{1+(\eta_d/\eta_c)^{1,1}}$$

(5.49)

A comparison of the most commonly used models is shown in Figure 5.9 for a droplet size of 3 mm considering the test system toluene/acetone/water. The highest mass transfer coefficient can be observed from the model of Kumar & Hartland (1999) for high relative velocities. The model of Heertjes et al. (1954) shows the second highest mass transfer coefficient for high relative velocities (>0.08 m/s) and the highest mass transfer coefficients for lower values. The models are followed by the mass transfer coefficient models of Garner & Tayeban (1960) and the model of Kronig & Brink (1950).
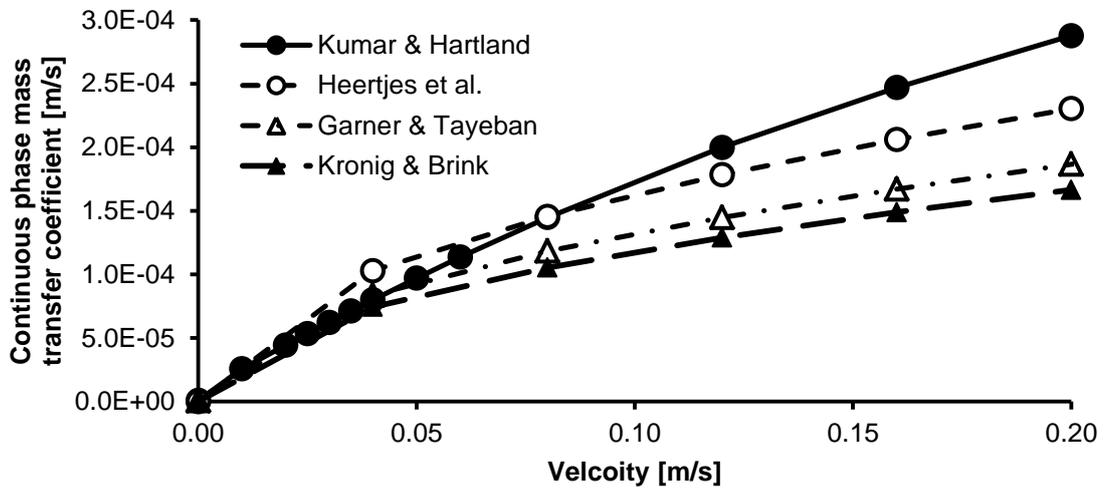
Figure 5.9: Continuous phase mass transfer coefficients vs. relative velocity of the droplets.

5.7.3 Overall Mass Transfer Coefficient

Based on the individual mass transfer coefficients, the overall mass transfer coefficient can be calculated using Eqn. 5.33. Several mass transfer coefficient combinations were investigated (Figure 5.10), where the combination of the individual mass transfer coefficient from Handlos

and Baron and Kronig and Brink showed the highest overall coefficient for a droplet size of 3 mm and low velocities (<0.12 m/s) for the test system toluene/acetone/water. At higher velocities, the model of Kumar & Hartland shows even higher values. The two model combinations are followed by the model combination of Heertjes et al. and Pilhofer & Mewes and the model of combination of Garner & Tayeban and Kronig and Brink. The model combination of Kronig & Brink and Pilhofer & Mewes shows the lowest overall mass transfer coefficients.

Garthe (2006) compared experimentally derived overall mass transfer coefficients of single toluene droplets for both mass transfer directions to the described correlations. For a mass transfer direction from dispersed to continuous phase, the eruptions at the interface are ranging deep into the bulk phase and are stronger in the bulk phase than in the droplet phase (Qi, 1992). Therefore, continuous phase with lower concentration is transported to the interface promoting the mass transfer (Garthe, 2006). A mass transfer from the continuous phase to dispersed phase leads to a stronger eruption in the droplet phase, where the effect is reduced due to Marangoni convection inside the droplet. For a mass transfer direction from dispersed phase to the continuous phase Garthe (2006) found the best agreement of his measurements to the model of Kumar & Hartland (1999). For a reversed mass transfer direction, he observed the agreement to the best overall mass transfer coefficient calculated using the models of Kronig & Brink (1950) for dispersed and continuous phase mass transfer coefficient for a droplet size between 2.5 to 3.0 mm.
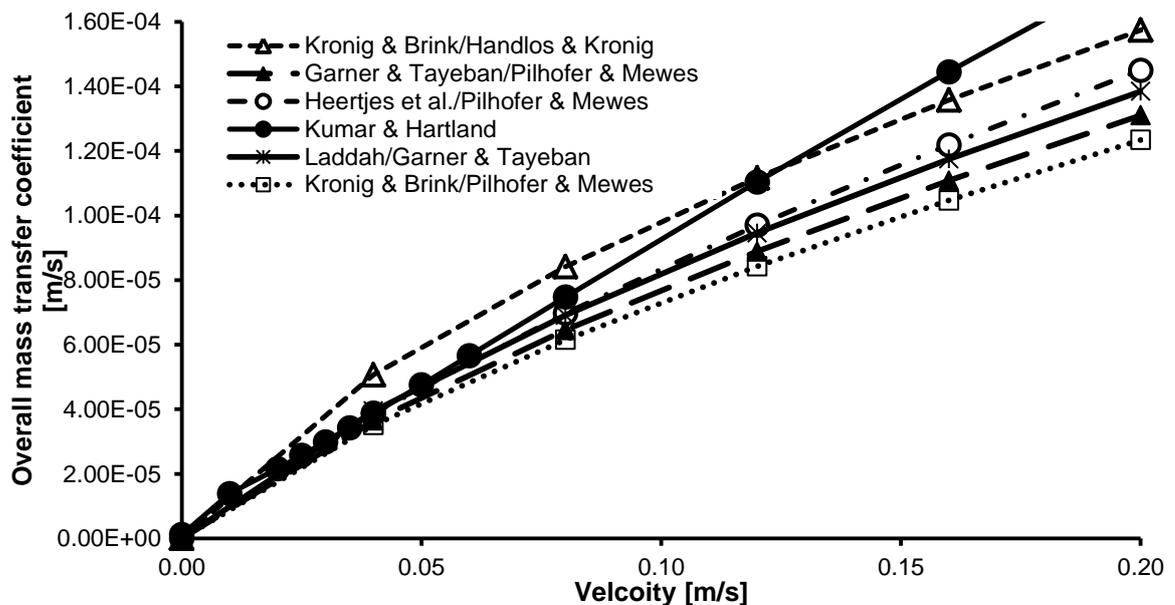
Figure 5.10: **Overall mass transfer coefficient for different individual mass transfer combinations.**

5.7.4   Selection of Solvent

Solvents are the key component for a successful separation of the liquid mixture components and must provide higher separation factors than those attainable with distillation. Influencing factors of the separation factors and the choice of the solvent are（Sattler, 1988）:

- Distribution coefficient: Indicates the ratio of the concentration of solute in the extract to the one in the raffinate and should be as large as possible.
- Selectivity: The solvent should provide a high selectivity against the solute which should be extracted.
- Separability: Large differences in boiling points of the solvent and the extract allow a feasible recovery of the solvent.
- Low viscosity: High viscosities counteract the hydrodynamics and mass transfer conditions.
- Low vapour pressure: Reduces losses during storage and operation.
- Appropriate surface tension.
- Chemical reactivity: The solvent should be chemically stable and inert to other components of the system.
- No corrosivity, no safety and environmental problematic properties.
- Availability and costs: Low costs of the solvent ensure low operational costs.

5.7.5   Selection of Dispersed Phase

The selection of the continuous and dispersed phase may influence the mass transfer efficiency and hydrodynamics boundaries of the column operation. Several empirical rules were designed in the last years, which can also be contradictory to the previous ones. In general, mass transfer should be from the continuous to the dispersed phase. For an increase of the interfacial area and turbulence, the phase with the higher throughput should be dispersed. In this context, the phase with a smaller surface tension should be dispersed. The phase with the lower viscosity should be chosen as continuous phase. Due to safety reasons and a lower hold-up of the dispersed phase, the more expensive, explosive and toxic phase should be dispersed. In column extractors, the phase with the lower viscosity（lower flow resistance）is generally chosen as the continuous phase. Also note that the phase with the higher flow rate can be dispersed to create more interfacial area and turbulence. This is accomplished by selecting an appropriate material of construction with the desired wetting characteristics. In general, aqueous phases wet metal surfaces and organic phases wet non-metallic surfaces. Change in flows and physical properties along the length of extractor should also be considered. Choosing a continuous phase

is generally not available in batch processes, as the larger liquid phase usually becomes the continuous phase. (Sattler, 1988)

5.8   Standard Test Systems for the Investigation of Mass Transfer

The European Federation of Chemical Engineering (EFCE) Working Party on "Distillation, Absorption and Extraction" recommends the use of standard test systems to provide a comparable basis for the investigations of liquid-liquid equipment and the ongoing liquid-liquid hydrodynamics. Three systems are recommended for the investigation of liquid-liquid mass transfer experiments concerning extraction. The system with the highest interfacial tension, which will be used in this study for mass transfer investigations, is water/acetone/toluene. The second system is water/acetone/butyl acetate and the third system with low interfacial tension is water/succinic acid/n-butanol.

5.8.1   Distribution Coefficient for Toluene/Acetone/Water

The distribution coefficient for the system toluene/acetone/water is given by the EFCE in Mísek et al. (1984), Henschke (2003) and Garthe (2006). The distribution coefficient depends on the weight fraction of acetone in water. A good agreement could be found between the experimental values of Garthe (2006) to the experimental correlation of Henschke (2003) depicted Figure 5.11, where the deviation between the EFCE data and Garthe (2006) is above 20% for low concentrations (1.5-wt%). For higher concentrations of 8-wt% acetone in water, the data showed a better agreement to each other. In conclusion, for mass transfer calculations based on the film theory, a detailed and exact knowledge of the mass transfer coefficient is necessary to achieve a high accuracy of the simulation result.
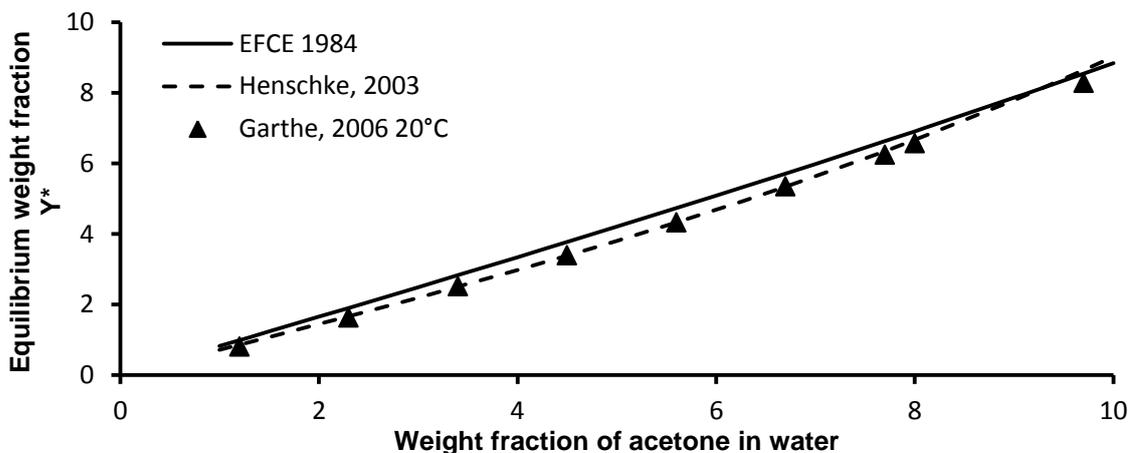
Figure 5.11: Measured distribution coefficient for the system toluene/acetone/water compared to literature data.

6   Experiments

6.1   Single Droplet and Swarm Experiments

Single and swarm experiments can give an indication about the droplet coalescence and breakage behaviour in liquid-liquid extraction columns. In the following, the droplet breakage is investigated using single droplets and swarm droplets in a test rig suggested by Steinmetz (2007) (Figure 6.1). A section of a Kühni miniplant column is mounted between two larger sized inflow and outflow zones. The droplets are generated by a distributor and rise through the column segment. Afterwards, the droplets separate due to the increased column diameter, which inhibits droplet coalescence in this region due to an increased droplet-droplet distance. The rising droplets are recorded by an infrared light-camera system which is connected to a PC. The droplets accumulate at the top of the column and coalesce forming a continuous liquid. The continuous water phase is introduced at the top of the column and leaves the column at the bottom leading to a counter-current flow of the continuous and dispersed phase.

1 Dispersed phase vessel
2 Personal computer
3 IR camera
4 IR light source
5 High speed camera
6 Twin component nozzle
7 Motor
8 Overflow
9 Continuous phase vessel
10 Continuous phase pump
11 Continupous phase pump (nozzle)
12 Dosimat (dispersed phase)
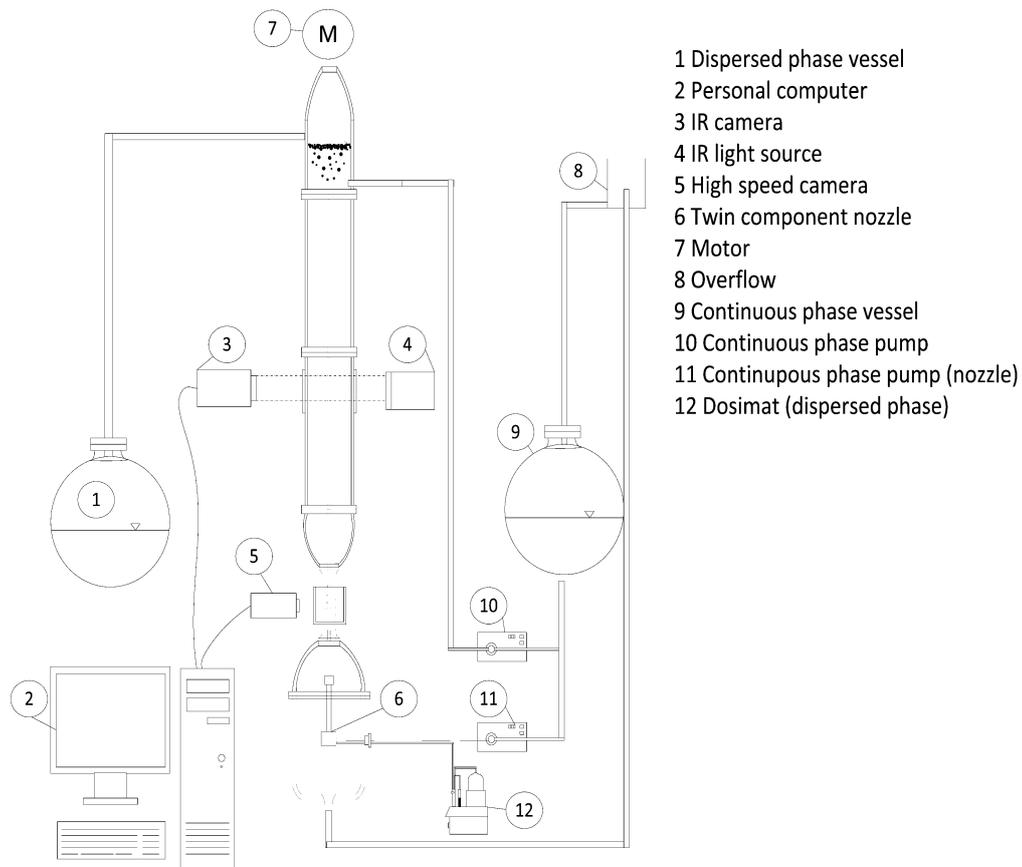
Figure 6.1:   Experimental setup for the determination of single droplet breakage.

6.2   Single Droplet Experiments

Single droplet experiments were carried out to gain information about the number of daughter droplets generated by a single breakage event. Droplets with a diameter of 2.6 mm were generated and the breakage behaviour of the droplets were studied by the use of a high speed camera. It could be observed, that with increased rotational speed of the stirrer, the breakage probability increased (Table 7). At 250 rpm, multiple breakage events of a single droplet in a compartment occurred with higher frequency. The droplets thereby mainly breakup in two equal-sized droplets. At higher stirring speed, also the generation up to three daughter droplets could be observed where a smaller satellite droplet was generated.

Table 7: Results of the single droplet experiments using n-butyl acetate as dispersed phase and water as continuous phase.

Stirring speed [rpm]	Breakage probability	Breakage probability for multiple breakage of a single droplet in a single compartment	Average number of daughter droplets
200	0.25	0	2.2
225	0.30	0	2.1
250	0.38	0.23	3.1
275	0.60	0.30	3.1

6.3   Initial Droplet Size

In liquid-liquid extraction columns, one phase is dispersed by perforated plates, nozzles or single tubes into another liquid. The generated initial droplet size influences the mass transfer and the hydrodynamics in the first few compartments until stable droplet sizes are obtained along the column height due to breakage and coalescence. At low velocities, the droplet detaches from the nozzle, when the gravitational forces overcome the tension forces (Kumar & Hartland, 1983). At higher velocities, droplet formations occur due to jet breakup.

A general correlation for the drop formation using multiple nozzles (distributors) was found by Kumar & Hartland (1983) which was also recommended by Steinmetz (2007) for the layout of liquid-liquid extraction columns:

$$d_{32} = d_{nozzle} E\ddot{o}^{-C_1} \left\{ 2.13 \left(\frac{\Delta\rho}{\rho_d} \right)^{0.67} + \exp(-C_2 \cdot Fr) \right\} \; for \; E\ddot{o} < 0.4, We < 8.64 \qquad \textbf{(6.1)}$$

and

$$d_{32} = d_{nozzle} E\ddot{o}^{-0.42} \{ 1.24 + \exp(-Fr^{0.42}) \} \; for \; E\ddot{o} \geq 0.4, We < 8.64 \qquad \textbf{(6.2)}$$

The parameters in the correlation C_1 and C_2 are given by Kumar & Hartland (1983) with values of 0.4 and 0.13, respectively. The parameters had to be adapted slightly in this work to describe the experimental data of Steinmetz (2007) using the system of toluene/water and to own experimental data using a system of n-butyl acetate/water. For the system of toluene/water, the parameters were found to be $C_1 = 0.38$ and $C_2 = 0.15$. For the system of n-butyl acetate/water, the parameter set was $C_1 = 0.33$ and $C_2 = 0.15$. In general, surfactants may lead to a deviation from the initial measured droplet size. A standardized equipment in combination with a droplet size data base may help to indicate liquid-liquid property changes by the measured initial droplet size.
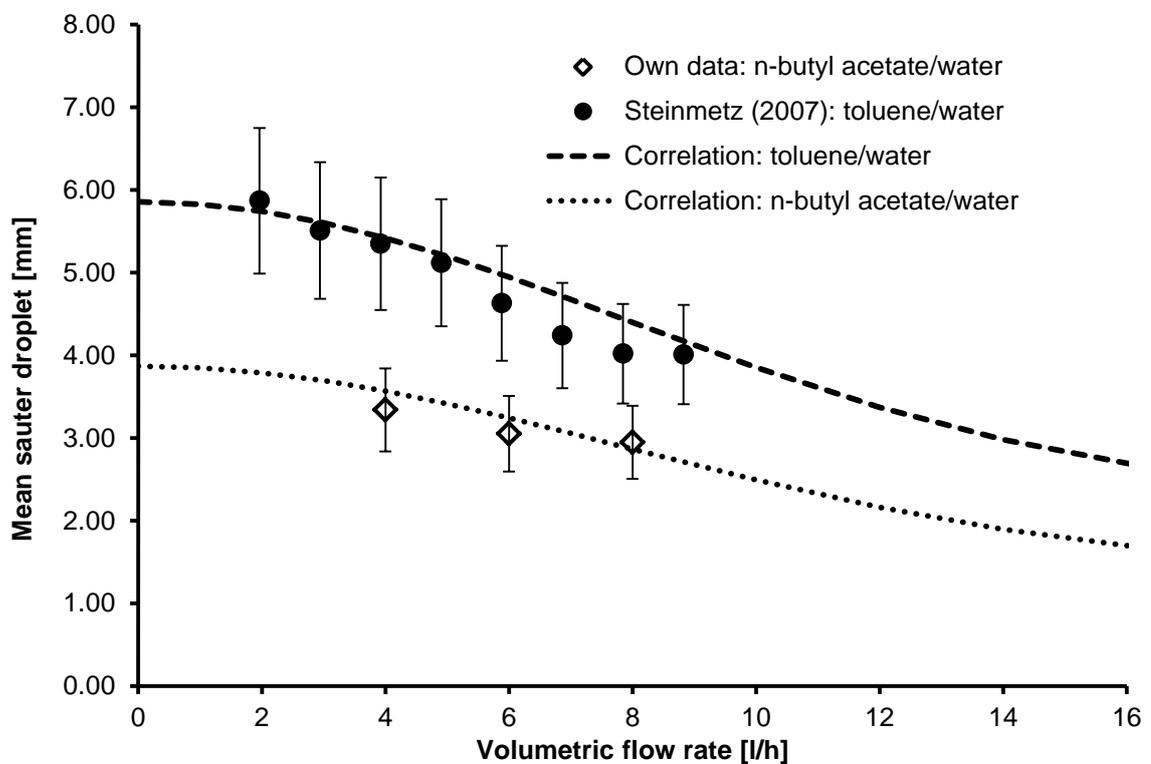
Figure 6.2:   Initial droplet size in dependence of the volumetric flow rate compared to the correlation of Kumar & Hartland (1983).

6.4   Swarm Experiments for the Determination of the Droplet Size

Swarm experiments were carried out using the EFCE test systems of toluene/water as a system with high interfacial tension and n-butyl acetate/water as a system with low interfacial tension. Due to the fact, that most coalescence and breakage models were developed for gas-liquid systems, an air-water system is used as reference to investigate the different behaviour of liquid-liquid systems to gas-liquid systems. Figure 6.3 shows the development of the average air particle size compared to the average n-butyl-acetate droplet size at different rotational speeds in

a five compartment section of the Kühni miniplant column. It can be observed, that with increasing rotational speed, the particle size of both systems drops. The liquid-liquid systems show a higher influence on the rotational speed and the droplet size decreases down to the system limits of the measurement system of one millimetre. Instead, the air system shows only a slight decrease. From optical impression, the air bubbles show a higher coalescence rate and a lower breakage rate, which results from a better stabilization of the air bubble after an energy impact (contact with the stirrer tip) due to the higher interfacial tension. Nevertheless, the density difference of the air-liquid system is higher than the liquid-liquid system resulting in a lower retention time of the bubbles inside the compartments.
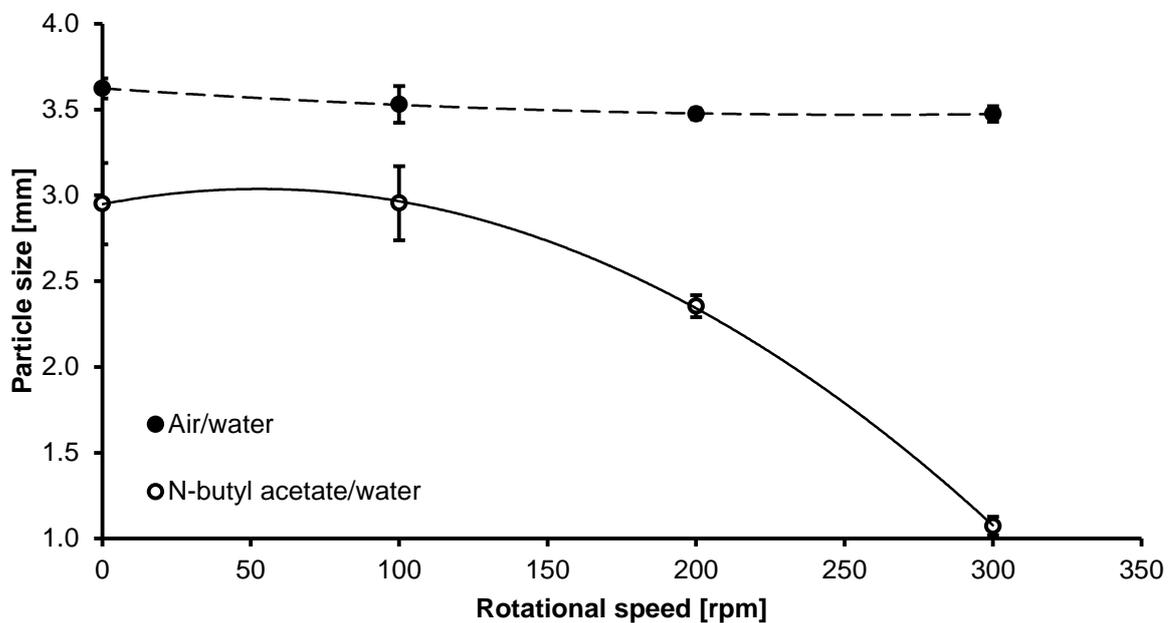
Figure 6.3:   Particle size in dependence on the rotational speed.

6.4.1   Dependency of the Droplet Size on the Flowrate

The residence time of the droplets is influenced by the density difference between the droplets, by the rotational speed of the stirrer and by the volumetric flow rate of each phase. Besides the rotational speed, the ratio of the dispersed and continuous phase flow influences the phase fraction inside the column and hence the rate of droplet collision. Swarm experiments at different volumetric flow rates at constant rotational speed were conducted in the presented five compartment section of a Kühni miniplant column. The results are shown in Figure 6.4. The measured droplet size distributions at the outlet of the column show only a slight deviation to each other and lie in the range of measurement uncertainties. It can be concluded, that the

droplet size mainly depends on the rotational speed of the stirrer and only shows a slight dependence on the volumetric flow rate. However, higher dispersed phase flow rates, especially flow rates close to the flooding point, may result in larger droplet sizes (Fischer, 1973) or when systems with higher coalescence rates are used.
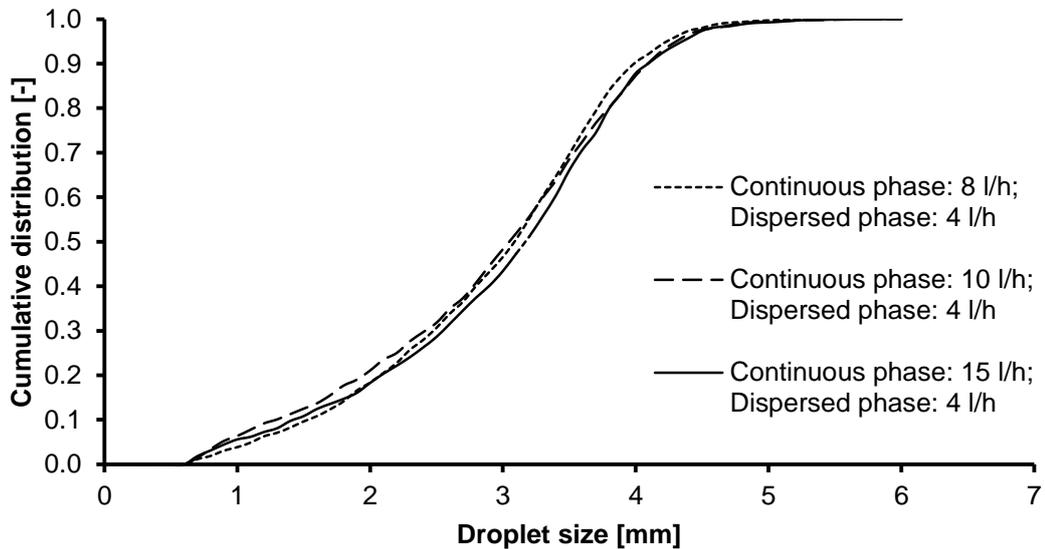
Figure 6.4: **Droplet size distribution of butyl acetate droplets in water in dependency of the volumetric flow rate at 100 rpm.**

6.5   Hydrodynamics in a Miniplant column

The hydrodynamics in the Kühni miniplant column are determined using optical measurement techniques. Optical measurement techniques are, in comparison to classical measurement techniques, non-intrusive and hence do not influence the flow field. The main optical measurement systems are the particle image velocimetry (PIV), the laser induced fluorescence (LIF), the laser induced incandescence and the laser doppler velocimetry or phase doppler interferometry.

6.5.1   Particle Image Velocimetry

The motion of fluids of homogeneous and optically transparent media is not visible directly. The fluid has to be marked by small particles or a dye, to make the flow structure visible. One of the most successful non-intrusive measurement techniques has become the particle image velocimetry. Compared to single-point methods, as the laser Doppler anemometry and the hot-wire anemometry, PIV is able to track the interested flow field at once by measuring the displacement of small particles in short time intervals. The tracer particles need to have

approximately the same density than the surrounding fluid and need to be small in size to follow the motion of the fluid. In addition, the tracer should have no influence to the fluid flow characteristics. The principle setup of a PIV system is shown in Figure 6.5. A thin laser sheet, generated from a pulsed light source, illuminates the tracer particles, which are usually dotted with fluorescence. The light scattered from the particles will be recorded by a camera, usually a charge-coupled device (CCD) camera. By the use of a second camera, stereoscopic imaging is obtained, that allows the measurement of the axial, tangential and radial component of the flow velocity within the laser sheet. The recorded double-images are processed by a personal computer. The postprocessing consists of a cross-correlation of the first and second double image in small subdomains, depending on the velocity of the particles, particle concentration, size and resolution of the image. The cross-correlation may be followed by several correction steps to filter outliers (false predicted vectors).

PIV systems also found their way into the field of process engineering to investigate the fluid flow structures and turbulence. Especially in the application field of liquid-liquid extraction columns, PIV systems were used by Kolb (2005), Steinmetz (2007) and Drumm (2010). Kolb investigated the flow field in a today outdated Kühni miniplant column design. Steinmetz used the PIV system to determine the energy dissipation in an up-to-date design of the Kühni miniplant column. Drumm studied the flow field and energy dissipation in different scales of an RDC column.

1 Laser
2 Mirror
3 Beam expander
4 Cylindrical lens
5 Measuring area
6 CCD-camera
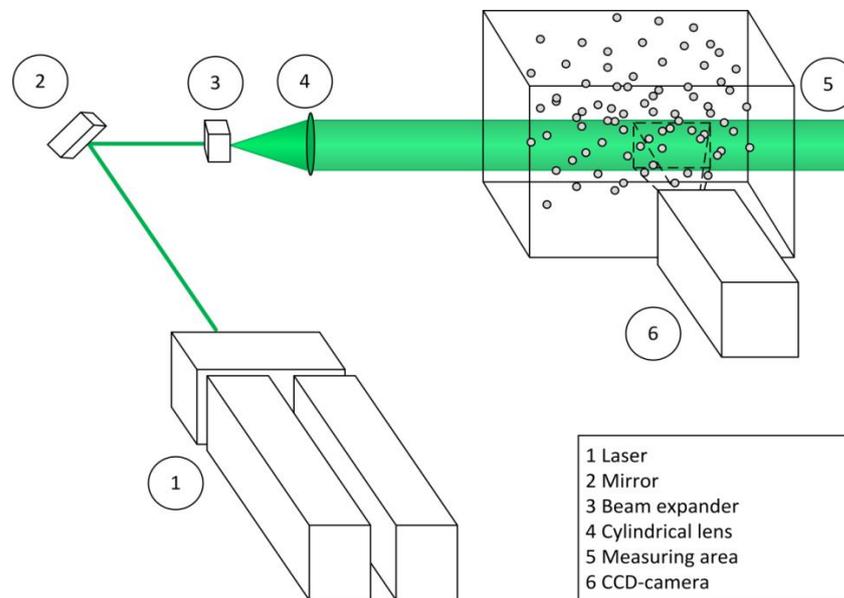
Figure 6.5:   Schematic setup of a PIV measurement system using a single camera.

6.6   Velocity Measurements

6.6.1   Setup of the Velocity Measurement

The hydrodynamics inside a single compartment of a Kühni miniplant column was investigated using a 2-D ILA (Intelligent Laser Applications GmbH, ILA) PIV system. The installation of a second camera in an angle to the present one to allow 3-D velocity measurements would induce further errors due to the sharp curvature of the Kühni miniplant column wall. The investigated column consisted of two glass segments, each containing eight compartments. For the laser measurements, the fourth compartment of the second glass segment was investigated. The internals were coated black to reduce reflections of the laser from the internals with a two-component paint (Bricapox 2K Epoxy-Primer EP-351 and 2K Expoxy hardener). The paint showed a good resistance against the solvents toluene and butyl-acetate in preliminary experiments. An optical planar and transparent plexiglass box filled with water is mounted around the measurement area to reduce refraction of the laser hitting the cylindrical column wall. Hollow glass spheres from Dantec Dynamics with a diameter of 10 µm are used as tracer particles. A collimator spreads the Nd-YAG laser and forms a light sheet in the center of the column. A CCD camera with a spatial resolution of 1280x1024 pixel is positioned perpendicular to the laser sheet. The velocity field is only determined in radial and axial direction due to the use of the 2-D PIV system. The time average velocity field is calculated by averaging the time dependent velocity fields obtained by the cross-correlation of the double images. For cross correlation, an interrogation size of 32x32 pixels was used.

6.6.2   Results of the Velocity Measurement

The measured velocity field inside a Kühni miniplant column at 300 rpm is shown in Figure 6.6. Corresponding to the description of Goldmann 1986 depicted in Figure 5.5, two vortexes are formed, one above the stirrer and one below the stirrer. The highest velocity can be observed at the stirrer tip and decreases to the column wall. In addition, the fluid is accelerated by the axial suction effect of the stirrer close to the shaft. A further description of the influence of different flow rates to the velocity field is given in Hlawitschka & Bart (2012a), where it could be shown, that an unequal flow rate of the dispersed to the continuous phase leads to a deviation of the swirl structure. This effect is enhanced by low stirring speeds.
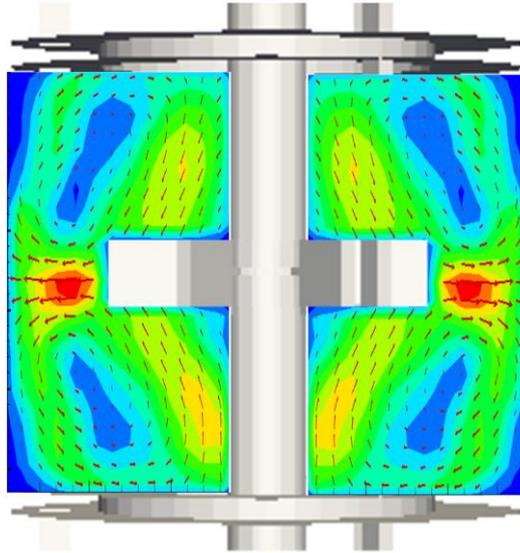
Figure 6.6:   **Velocity field at 300 rpm using a CaCl$_2$-solution (30 wt-%) as liquid.**

6.7   Energy Dissipation Calculation

The turbulent energy dissipation can be calculated based on the turbulent fluctuation velocities u_i (Steinmetz, 2007, Drumm, 2010), obtained by a single cross-correlation, and the local average of the velocity over $\bar{u}$ time:

$$u_i' = u_i - \bar{u} \tag{6.3}$$

Based on this fluctuation velocity, the energy dissipation can be calculated:

$$\varepsilon = \nu \left(2 \left(\frac{\partial u_r'}{\partial r} \right)^2 + 2 \left(\frac{\partial u_z'}{\partial z} \right)^2 + 3 \left(\frac{\partial u_r'}{\partial z} \right)^2 + 3 \left(\frac{\partial u_z'}{\partial r} \right)^2 + 2 \left(\frac{\partial u_r'}{\partial z} \frac{\partial u_z'}{\partial r} \right)^2 \right) \tag{6.4}$$

However, the energy dissipation calculation depends on the local resolution of the PIV system, which should be in the range of the Kolmogorov length scale:

$$\eta = \left(\frac{\nu^3}{\varepsilon} \right)^{0.25} = \text{ PIV resolution} \tag{6.5}$$

In cases of a PIV system having a larger resolution then the Kolmogorov length scale, Alekseenko et al. (2007) proposed a correction algorithm based on the Pao energy spectrum. The real energy dissipation hence results from the measured energy dissipation divided by a correction factor f_e:

$$\varepsilon_{real} = \frac{\varepsilon_{PIV}}{f_e}$$

(6.6)

6.7.1   Results of the Energy Dissipation Determination

In the us

ed Kühni miniplant column, two vortexes are generated by the stirrer, one above and one underneath the stirring device. The highest velocity is observed at the stirrer tip and decreases along the column wall until the liquid is accelerated again by the stirrer. Also, the highest energy dissipation can be seen at the stirrer tip, the region of the highest shear rate. In general, the energy dissipation increases with increased rotational speed, which was correlated by Kumar and Hartland (1995, 1996) for mechanically agitated columns. The energy dissipation is given by:

$$\bar{\varepsilon} = \frac{4 \cdot P}{\pi \cdot D_c^2 \cdot H_c \rho_c}$$

(6.7)

The power input per unit mass P is a function of the geometry dependent power number N_p and the stirrer Reynolds number.

$$P = N_p N^3 D_r{}^5$$

(6.8)

For a rotating disc contactor, the power number is given by:

$$N_p = \frac{C_5}{Re_R} + C_6 \left[\frac{1000 + 1.2 Re_R^{m_2}}{1000 + 3.2 Re_R^{m_2}} \right]^{m_3}$$

(6.9)

with

$C_5 = 109.36$ $C_6 = 0.74$ $m_2 = 0.72$ $m_3 = 3.30$

The corresponding power number for a Kühni column is given by Kumar & Hartland (1995, 1996):

$$N_p = 1.08 + \frac{10.94}{Re_R^{0.5}} + \frac{257.37}{Re_R^{1.5}}$$

(6.10)

An extension to the model of Kumar & Hartland (1995, 1996) was done by Gomes et al. (2006) accounting for the density changes of the mixture:

$$\bar{\varepsilon} = \frac{4 \cdot P}{\pi \cdot D_c^2 \cdot H_c (\rho_c \cdot (1 - \alpha) + \rho_d \alpha)}$$

(6.11)

Steinmetz (2007) used PIV measurements to correlate the average energy dissipation and describes the following correlation:

$$\bar{\varepsilon} = c_1 \cdot v \cdot \left(\frac{B_R}{D_R}\right)^{2/3} \cdot \left[\frac{(\pi \cdot D_R \cdot N)}{D \cdot H_c}\right] \tag{6.12}$$

For the Kühni miniplant column with a compartment height of 28 mm, he used a constant factor of 570 for a pure water system without any flow rate. The correlation of Steinmetz (2007) and the correlation of Kumar & Hartland (1996) are compared to own measurements of the Kühni miniplant column using a system of $CaCl_2$/water-n-butyl acetate in Figure 6.7. A good agreement between the measured data and the correlation of Kumar & Hartland (1996) can be seen up to a rotational speed of 200 rpm. The measured value at 300 rpm lies above the correlation. The correlation of Steinmetz (2007) leads to an overproduction of the energy dissipation and therefore, it is not suitable for the used system.
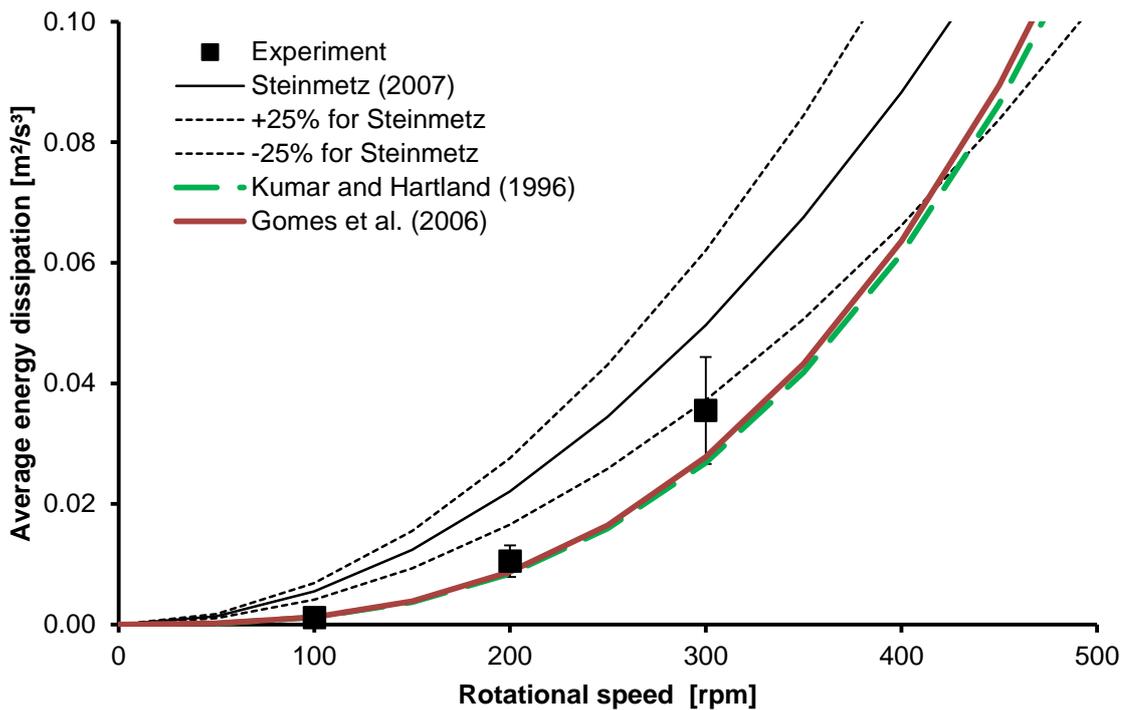
Figure 6.7: Comparison between measured energy dissipation and correlations by Steinmetz (2007), Gomes (2006) and Kumar and Hartland (1996).

6.8   Local Phase Fraction Determination

In Eulerian flow simulation, the dispersed phase is treated as interpenetrating continua, where the positions and the size of the droplets are represented by the stochastically local phase fraction. The local phase fraction can be measured using the radiation method, the conductivity probe, capacitance probe, optical probe and a hot-wire anemometer. With the exception of the radiation method, the probes influence the local velocity field and hence the local phase fraction. The LIF allows a non-intrusive measurement of the local phase fraction by using an iso-optical test system Hlawitschka & Bart (2012a) and was earlier successfully applied by Liu et al. (2005) to investigate the phase inversion in a stirred vessel.

Rhodamine 6G is used to illuminate the dispersed phase when it passes the laser light sheet. The surrounding continuous phase stays black as can be seen in Figure 6.8. A postprocessing of the LIF images to black and white images allows a better discrimination of the dispersed and continuous phase. From the LIF images and black & white images, first information about the droplet movement, for example the rise of an accumulated droplet from the stator underneath the compartment, can be visualized. In a last step, an averaging of the images leads to an average representation of the local phase fraction. Therefore, an average of 400 single figures was required to reach a steady state value of the phase fraction. Especially fluctuations occurring due to droplet rise from the stator and accumulations underneath the stator may influence the calculated average phase fraction result. The reproducibility of the results however is in the deviation range of 30%. From the measurements it could be optically observed that single droplets may accumulate underneath the stator ring. For an integral observation of the phase fraction in the whole compartment, the occupied volume of these accumulated droplets must be recognized as a single occurrence.

LIF image   Black & white   Average
                              conversion
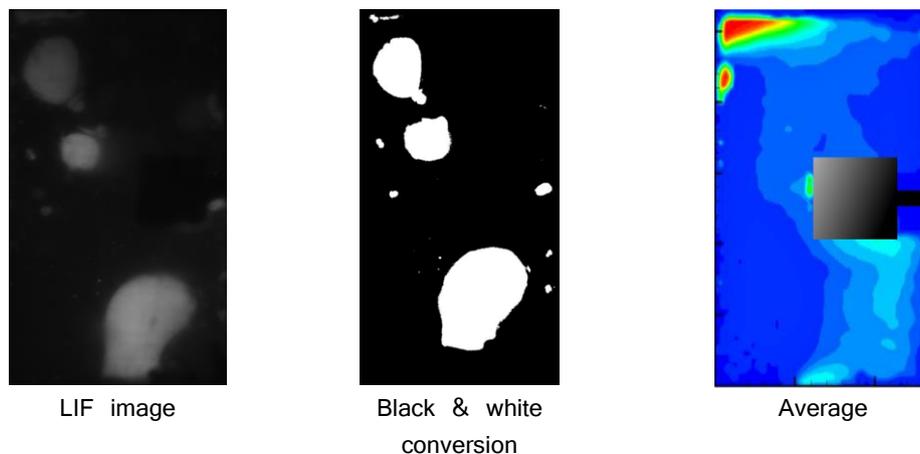
Figure 6.8:   LIF measurement for the determination of the local phase fraction. 15 m³/m²/h continuous phase and 10 m³/m²/h dispersed phase at 100 rpm (Hlawitschka & Bart, 2012a).

For the iso-optical test system of water/CaCl$_2$-n-butyl acetate, the phase fraction was determined for different rotational speeds and the results are compared to the correlation of Kumar & Hartland (1996) in Figure 6.9. An increased rotational speed leads to an increase in phase fraction, which results from a higher distribution of the droplets inside the compartment. The obtained results are in the range of the correlation given by Kumar & Hartland (1996).
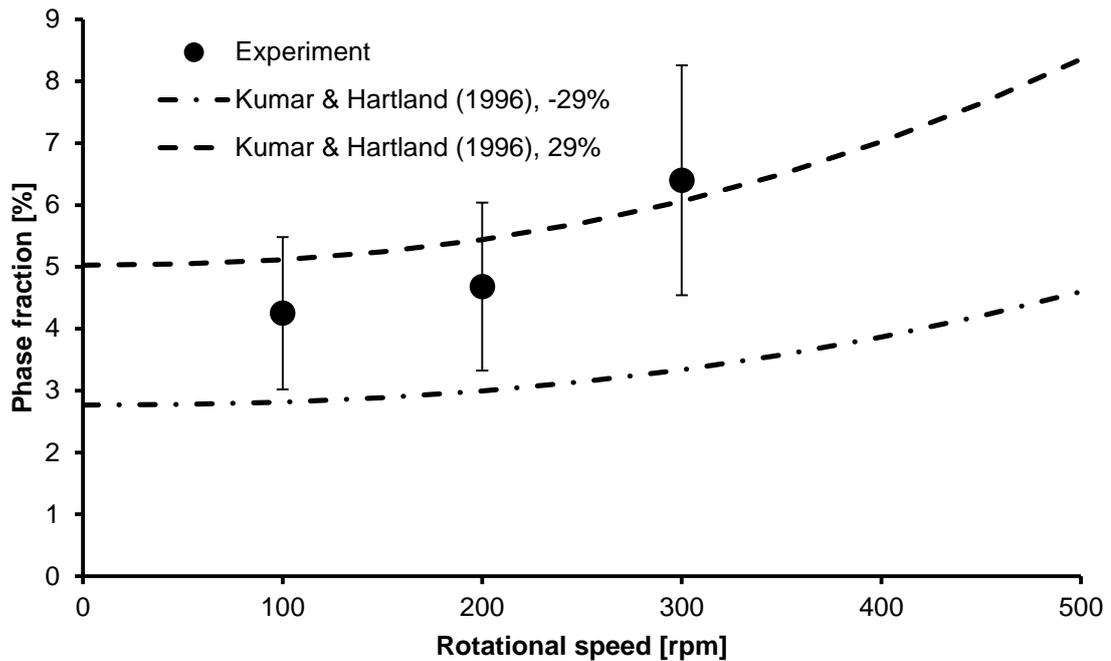
Figure 6.9: **Comparison of the experimental derived phase fraction to the correlation of Kumar & Hartland (1996).**

6.9   Mass transfer in Kühni Extraction Columns

The mass transfer in a Kühni miniplant DN32 column and a Kühni DN60 column was investigated experimentally to obtain a validation base for the later in this work implemented mass transfer correlations. The dimensions of the columns are given in Table 8. The principle setup of the extraction column is shown in Figure 6.10 for the DN32 column. The inlet of the dispersed phase is at the column bottom, where the continuous phase enters the column at the top. The concentration profile is measured at the in- and outlets of each phase and at five positions along the column height. The droplet size is measured at the column top using a high speed camera (Vosskühler, HCC-1000).

Table 8:   Main dimensions of the miniplant extraction and Kühni DN60 column.

	Kühni miniplant		Kühni DN60	
Compartment height	28	mm	40	mm
Column diameter	32	mm	60	mm
Number of compartments	40	–	45	–
Number of agitator blades	6	–	4	–
Agitator diameter	20	mm	40	mm
Shaft diameter	5	mm	10	mm
Agitator blade height	4.5	mm	8.1	mm
Agitator blade diameter	5	mm	9.1	mm
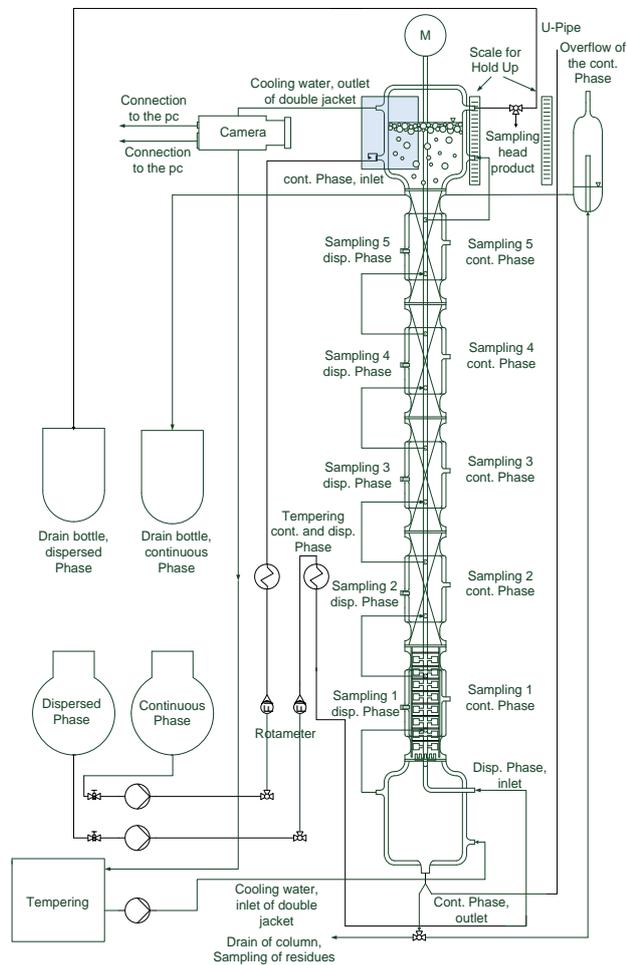
Figure 6.10: Experimental setup for the determination of the outlet droplet size and the concentration profile along the column height.

6.9.1   Distribution Coefficient

Besides the concentration, the mass transfer along the column height is influenced by the distribution of acetone in the used system of toluene/water. Therefore, the distribution coefficient was determined at 25°C previous to the experiments and is compared in Figure 6.11 to the literature data and to the result of the simulation tool PPBLAB, which is based on the UniQUAC model. A distribution coefficient of 0.809 and 0.855 is determined experimentally for the used system and is in good agreement with the published literature data of the EFCE data published in Míšek et al. (1984), Henschke (2003) and Garthe (2006). In the following simulation parts, the distribution coefficient as recommended by the EFCE a value of 0.843 is used.
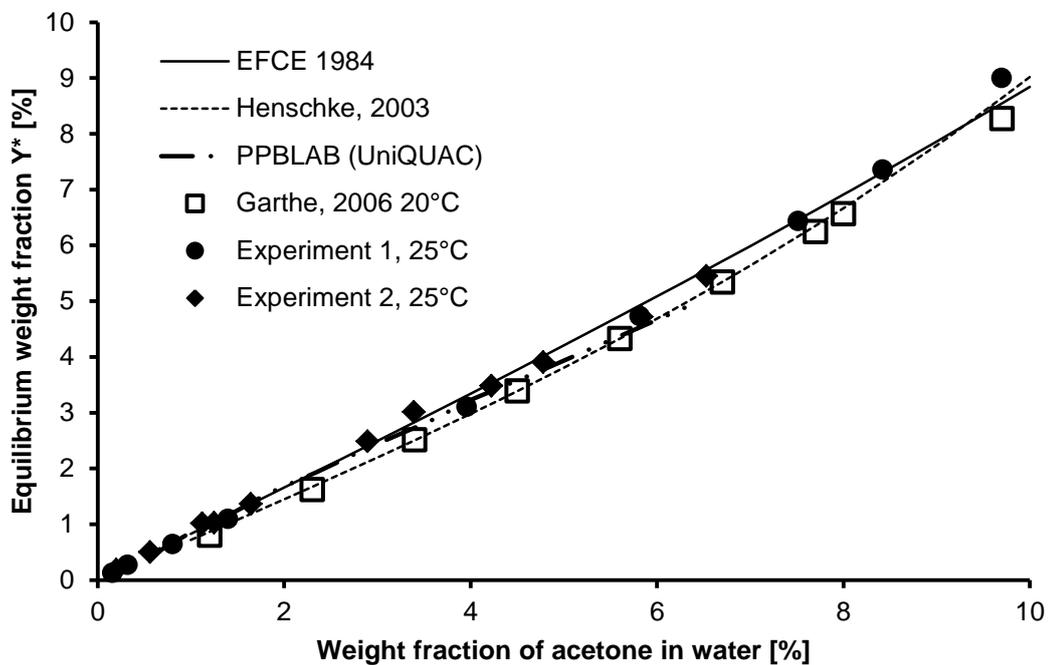
Figure 6.11: Measured equilibrium weight fraction in comparison to literature data.

6.10   Transient Measurements

A transient measurement was performed to investigate the hydrodynamics behaviour of the column. After 25 minutes, the acetone concentration along the column height reaches steady state (Figure 6.12). Fluctuations occur from the frequent sampling. For the reduction of the fluctuations and relevant data for later comparison with CFD simulations, for each boundary condition (flow rate, stirrer speed), at least two measurements were performed.
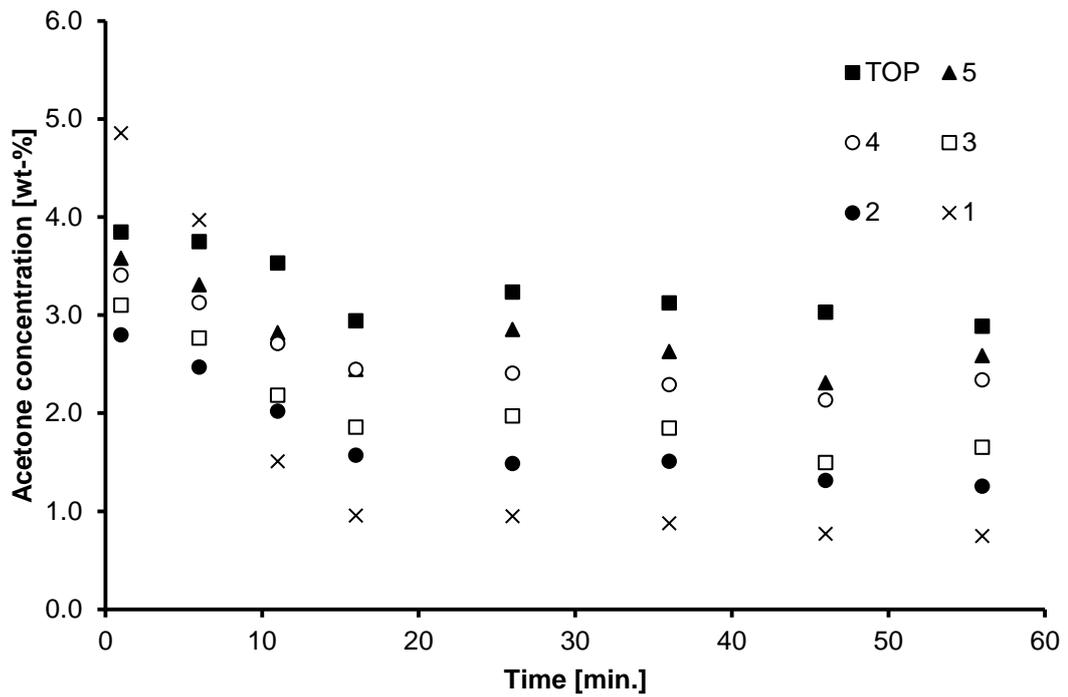
Figure 6.12: Acetone concentration profile in the dispersed phase at volumetric flow rate of 6l/h dispersed phase and 5 l/h continuous phase at 200 rpm stirring speed.

6.11   Steady State Concentration Measurements

The concentration of both phases is measured along the column height. The column is operated for 40 minutes to ensure, that the process reaches steady state. In addition to the concentration profile, the droplet size is measured at the column outlet and the hold-up is determined. In Figure 6.13, the single measurements of the acetone concentration in the continuous phase is depicted, where the samplings were averaged over time to obtain the concentration profile along the column height（Figure 6.14）.
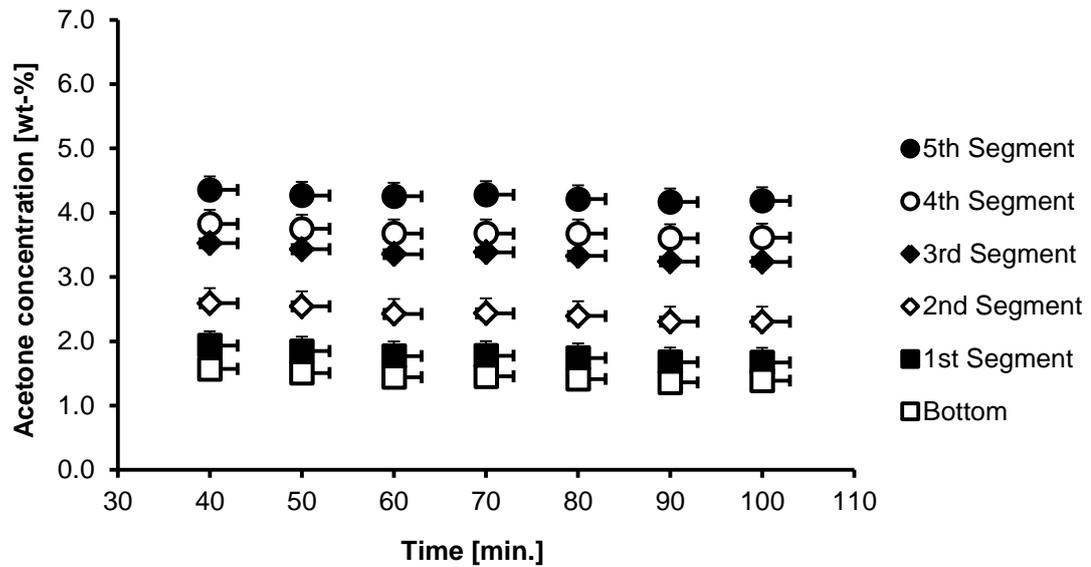
Figure 6.13: Measured acetone concentration in the continuous phase over time for a flow rate of 6 l/h dispersed phase and 5 l/h continuous phase at 250 rpm in the Kühni miniplant column.
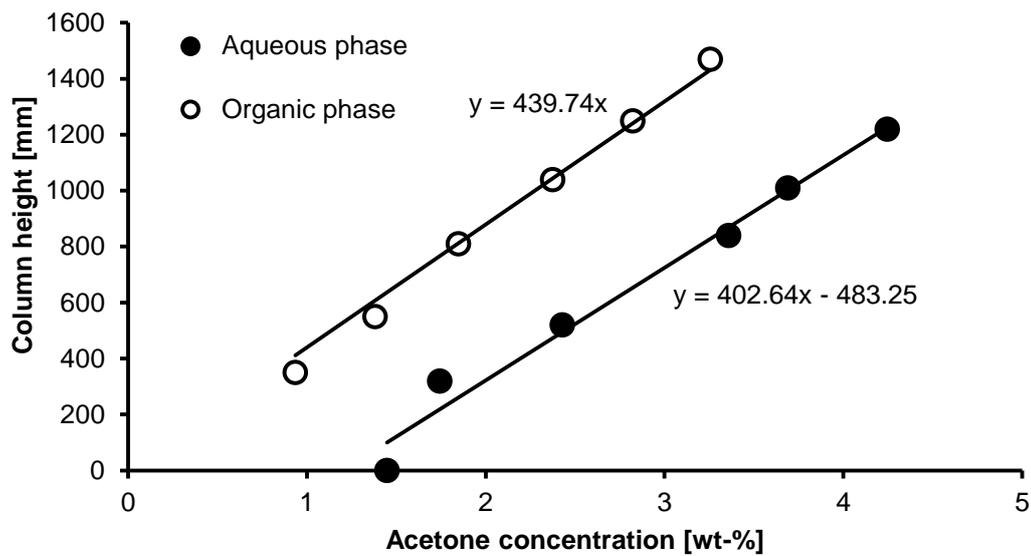
Figure 6.14: Experimental derived acetone concentration in the dispersed and continuous phase along the column height of a Kühni miniplant column.

6.12 Axial Dispersion Coefficient

The axial dispersion coefficient is determined for the DN32 and DN60 Kühni column using transient tracer measurements described by Langmuir (1908) ad Danckwerts (1953). The used system is water for the single phase axial dispersion coefficient measurements and toluene/water for the two phase axial dispersion coefficient measurement. Potassium chloride is used as tracer

in a concentration of 0.1 mol/l. The tracer is injected into the column and the concentration is measured at two positions downstream the column (Bauer, 1976, Aufderheide, 1985, Garthe, 2006). The results were recorded using LabView. The resulting plots were analysed using the Matlab optimization toolbox (Figure 6.15).
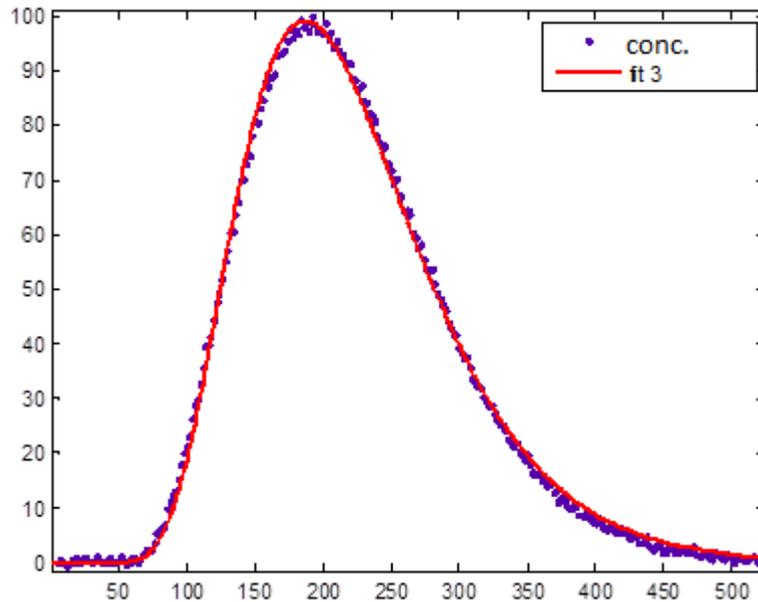
Figure 6.15: Curve fitting: (4l/h,100rpm: $Bo = 16.6$, $\tau = 198.9$, $A = 86.04$).

The results of the axial dispersion measurement for 6 l/h single phase flow (water) are shown for varied rotation speeds in Figure 6.16. The axial dispersion increases with an increased rotational speed. In comparison to literature correlations, the model of Breysee et al. (1983) and Steiner (1988) fits best to the experimental results. However, Garthe (2006) comments that the determination of axial dispersion coefficients is a contentious issue, there total radial mixing is not given in all extractors. Especially in the use with single phase flow, a high flow rate of the continuous phase leads to deviations of the swirl structure (Hlawitschka & Bart, 2012a) and hence to deviations in the axial dispersion coefficient determination. In general, the axial dispersion coefficient increases with increased flow rate.
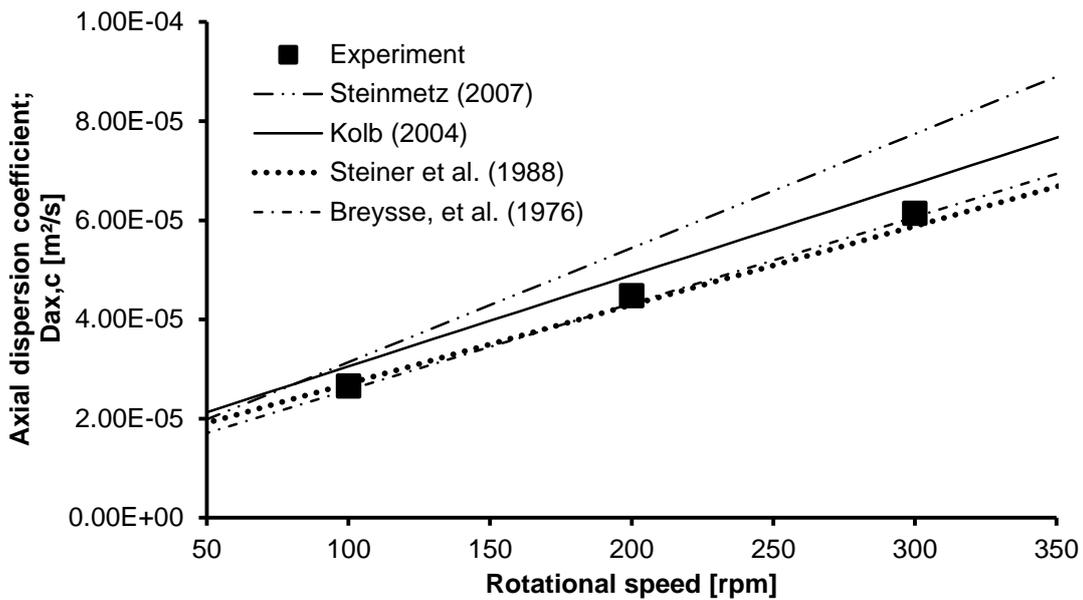
Figure 6.16: Measured Axial dispersion coefficient of the continuous phase at a flow rate of 8 l/h compared to correlations in literature.

6.12.1   Continuous Phase Dispersion Coefficient in a Two Phase Flow

In comparison to the previous experiment, the axial dispersion is measured while the column was operated at two phase flow. Due to the occurrence of flooding at high rotational speeds, the measurements were only performed up to 225 rpm. The dispersed phase leads to a change of the continuous phase hydrodynamics resulting in a change of the continuous phase axial dispersion coefficient (Figure 6.17). In comparison to the single phase axial dispersion coefficient, an linear increase can only be seen for a flow rate of 4 l/h per phase. With an increased flow rate, the axial dispersion coefficient drops from 100 rpm to 200 rpm and then starts to increase again. However, the resulting axial dispersion is heavily influenced by local hydrodynamic effects as droplet relief from the stator plates. Compared to the single phase measurements (Figure 6.18), the axial dispersion coefficients of the two-phase system lies above the single phase dispersion coefficients.
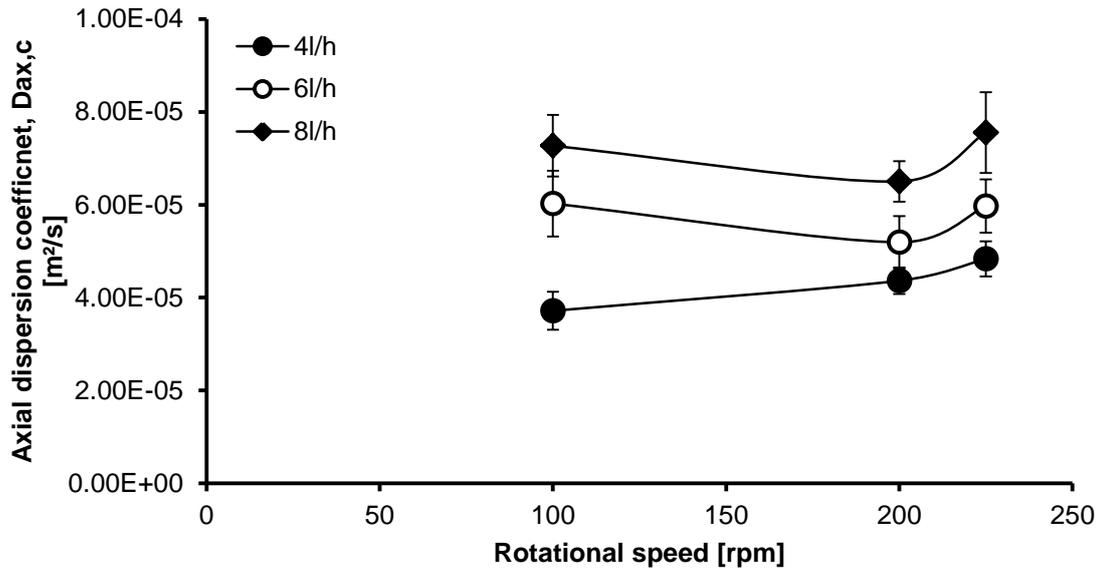
Figure 6.17: Continuous phase dispersion coefficient for two phase flow of water/toluene in a Kühni miniplant column. Volumetric flow rate for each phase.
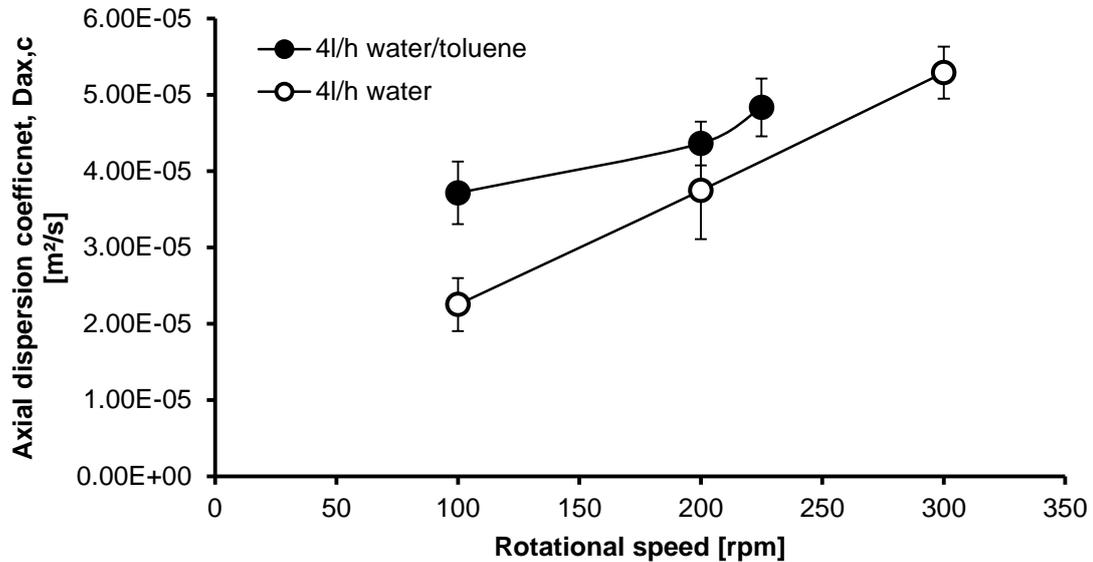
Figure 6.18: Comparison of the continuous phase axial dispersion coefficient determined in single phase water flow and in a counter‑current two phase operation of the Kühni miniplant column.

7 Simulations

OpenFOAM as an OpenSource CFD tool box offers full access to the CFD code without having license costs. Compared to the commercial CFD code FLUENT, the basic solvers are mainly extended by the user group and need to be checked and validated prior to the use. In OpenFOAM, several Euler-Euler models similar to the one used in FLUENT exist, which can be employed for the simulation of liquid-liquid extraction columns. Among them are the solver bubbleFoam, the twoPhaseEulerFoam which are part of the OpenFOAM toolbox and the twoPhaseEulerPimpleFoam solver, which is published by the user community. The latter is derived from the twoPhaseEulerFoam solver and shows an increased stability due to under relaxation and an ensured convergence of all equations at each time step achieved by the adoption of the PIMPLE (PISO/SIMPLE) algorithm instead of the PISO algorithm.

7.1 Liquid-Liquid Extraction Column Module for OpenFOAM®

The mesh generation of liquid-liquid extraction column and the setup of simulations require a deep knowledge of meshing and CFD. A graphical user interface (GUI) was created using Qt4 (see student thesis: Hagelauer, 2011), which is a gui abstraction library developed by Trolltech. The layout of the program was continuously enhanced and now allows the mesh generation of three different column types (RDC, Kühni and QVF). The layout of the column can be modified using the graphical user interface. The adjustable parameters are (Figure 7.1):

- Column diameter
- Compartment height
- Stator height
- Free cross-sectional area of the stator

- Rotor diameter
- Axial rotor position
- Inlet and outlet zone height
- Location of the baffles

Besides the setup of the column geometry, the GUI enables the user to specify the liquid-liquid properties and the boundary conditions as velocities, phase fraction, droplet size, rotating speed and population balance model and constants. The user can specify an existing solver or an own modified solver using a table box to start the simulation.
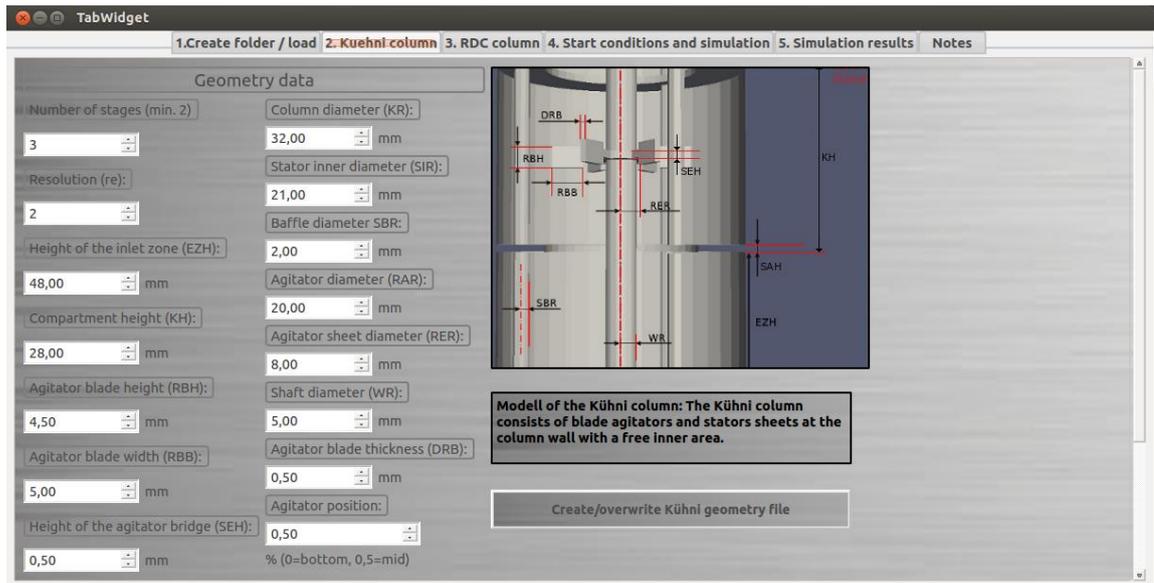
Figure 7.1:   Toolbox for simulation setup written in qt4. The depicted window shows the Kühni column setup with its adjustable parameter options.

7.1.1   Mesh Generation

The column design is based on repeating sections （compartments）, where the number of compartments will be given by the required efficiency of the column. A flexible and fast meshing of different column designs is required to allow a study of different geometrical designs and heights of the columns.

The mesh is created from the inside of the column to the outside of the column. Hexagonal meshes of column were generated by defining a vertex at each cutting point of the geometry. The vertices are connected by lines and curves which are used as the principle edges for a hexagonal block in Figure 7.2 （left）. The red line indicates the shaft, the dark blue line and purple line represent the stirrer blade, the yellow line describes the outer boundary of the MRF zone and the green line is responsible for the inner stator diameter. Each block is filled with a hexagonal mesh shown in Figure 7.2 （right）. Four different meshes were generated to account for the different geometries of the Kühni miniplant column, the Kühni DN60 column, the QVF column and the RDC column （Figure 7.3）. The vertices itself were defined by variables using m4 scripts, which allows a variation of the geometry within minutes.
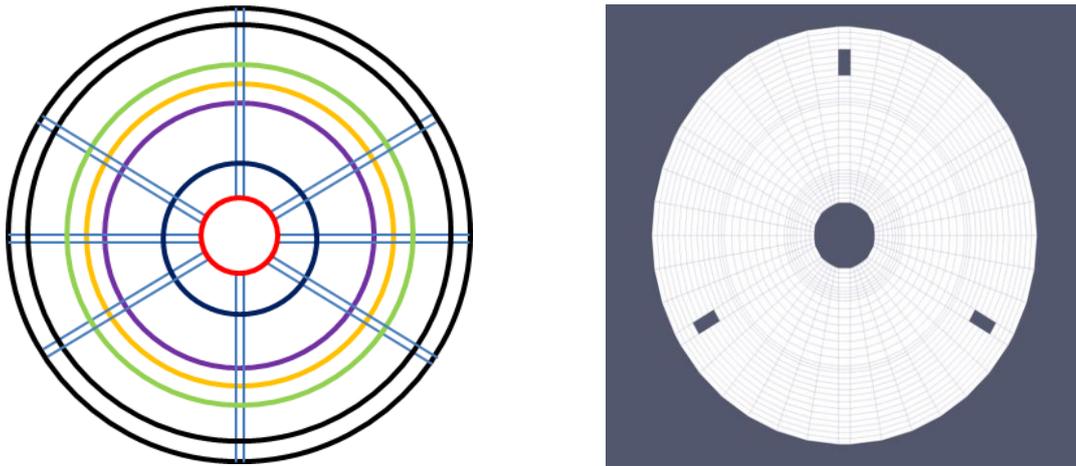
Figure 7.2: Principle intersection lines for mesh construction (left) and final mesh of a Kühni miniplant column (right).

| Kühni miniplant | Kühni DN60 | QVF DN50 | RDC DN 150 |
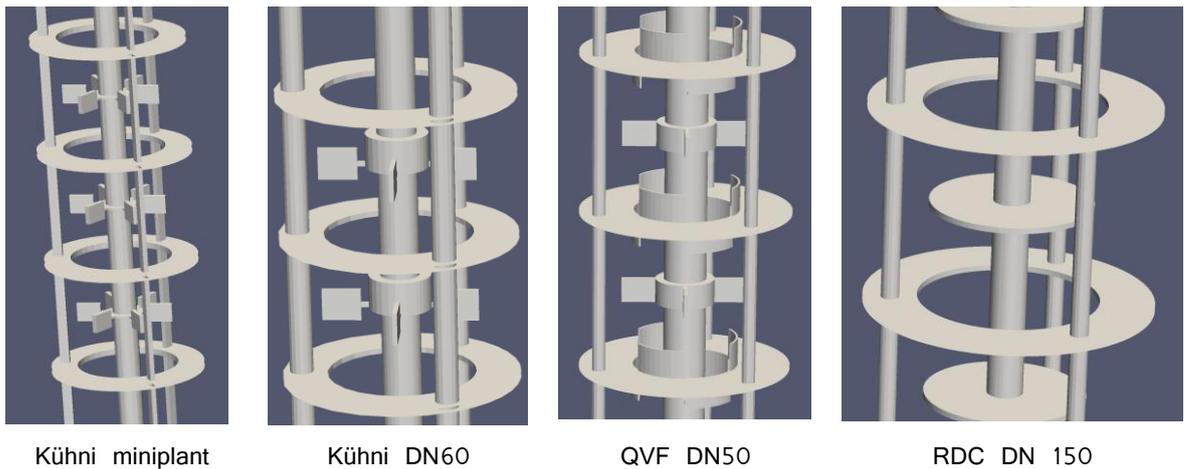
Figure 7.3: Generated geometries using the available m4 scripts.

The use of hexagonal blocks throughout the whole mesh enables the user to enhance the quality of the mesh by automatic mesh refinement. As an example, the mesh is refined based on the energy dissipation using the own extended solver MRFtwoPhaseEulerPimpleFoam_Energy, which includes the dynamic mesh library of OpenFOAM. The mesh is refined in a range of 0.01 m²/s³ up to an energy dissipation of 0.5 m²/s³ using five buffer layers and a maximum refinement of 3 per cell. A result of the refinement is shown in Figure 7.4. It shows the refined mesh around the moving parts (stirrer and shaft) as well as the outflow region of the stirrer to the column wall.
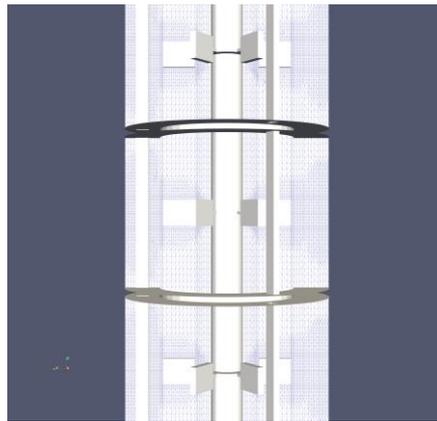
Figure 7.4: **Refined mesh of the Kühni miniplant column using automated mesh refinement.**

7.2 Two Phase Flow Simulations

The evaluation of the transient and steady state behaviour in different apparatuses（stirred and pulsed columns）is done by local flow analysis with particle image velocimetry（PIV）respectively by optical image analysis（Drumm & Bart, 2006）. The iso-optical test system of water/glycerine for the continuous phase and n-heptane as dispersed phase, which was used by Drumm & Bart（2006）is also applied in this study. In a first step, the used solver is compared to PIV measurements and FLUENT simulations of an RDC column. The volume flow rate is set in agreement to the setup of Drumm & Bart（2006）to 200 l/h aqueous phase and 100 l/h organic phases, while the stirrer revolution is set to 150 rpm. The predicted flow field is in good agreement compared to PIV measurements（Figure 7.5）.

PIV-Drumm and Bart (2006)
CFD-Fluent-Drumm and Bart (2006)
CFD-OpenFOAM
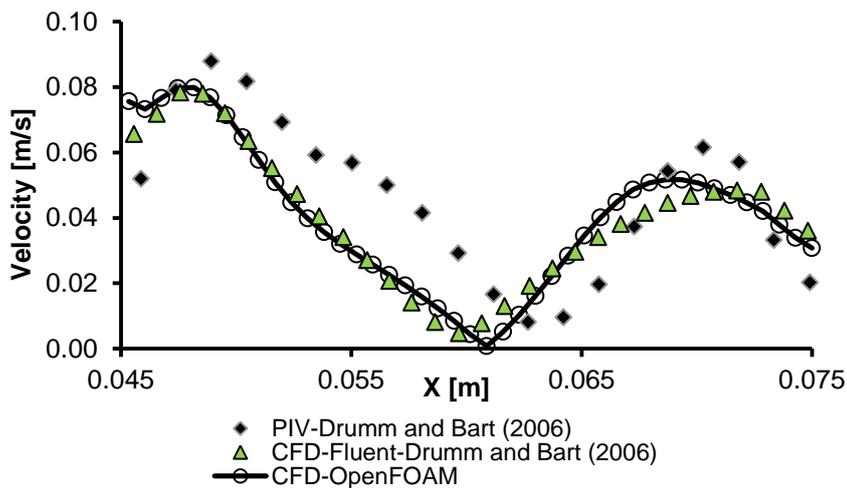
Figure 7.5: **Simulated velocity profile from stirrer tip to column wall (left) for RDC column design (right).**

A further comparison of the flow structure obtained by OpenFOAM simulation to the FLUENT simulations obtained by Durmm & Bart （2006） shows a good prediction of the vortex generation and location （Figure 7.6）.
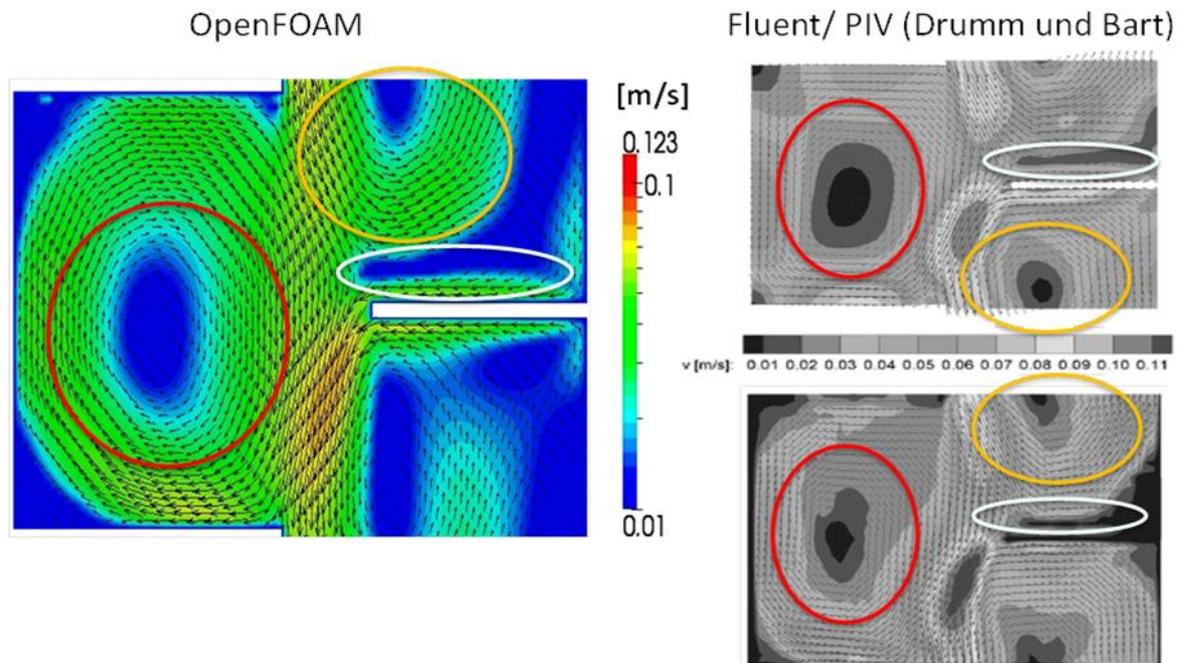
Figure 7.6:   Velocity profiles of the simulated RDC DN150 column compared to a FLUENT simulation by Durmm & Bart (2006) and to his PIV measurement.

7.2.1   Kühni Geometry

The non-rotational Kühni geometry can be simulated using the Moving Reference Frame （MRF） or the General Grid Interface （GGI）. In the first case, the rotor is fixed and the rotation is induced by source terms which accelerate the fluid. In the case of the general grid interface, the mesh around the rotor moves with each time step. To avoid especially influences of the mesh change to the energy dissipation, the MRF case is chosen for the simulation of the Kühni miniplant column, keeping in mind, that the specific effects of rotator stator interactions may not be accounted.

The simulated velocity profile of the shaft to the column wall at two millimeters above the stirrer is compared to the own measured PIV velocity profile and to own FLUENT simulations in Figure 7.7. Also here, a good agreement between the simulated profile and the measured profile can be observed, which allows a further use and extension of the solver.
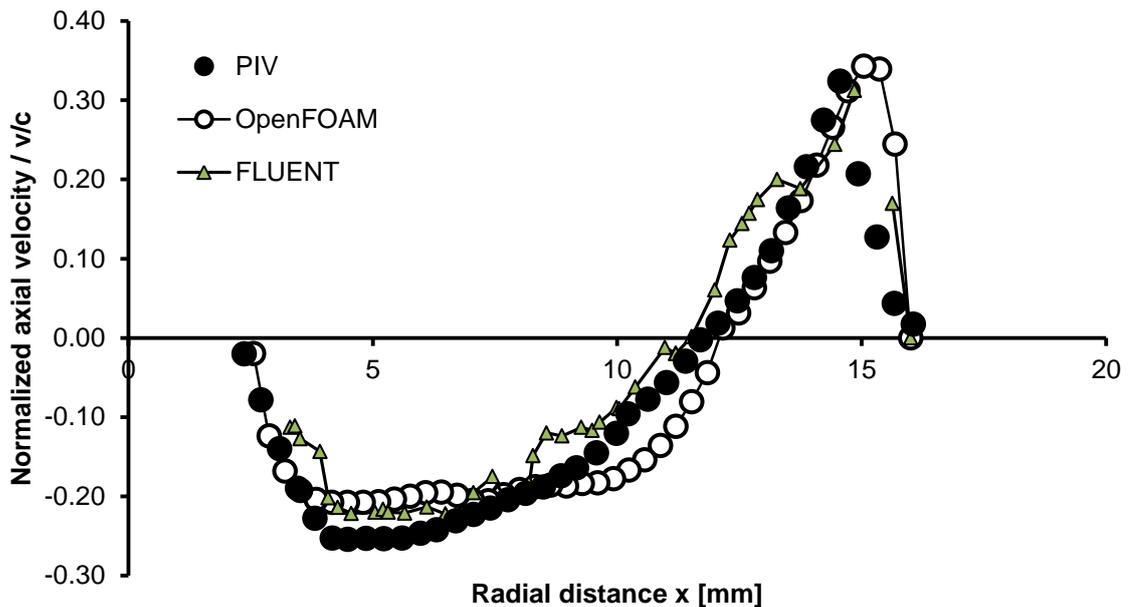
Figure 7.7: **Measured normalized velocity profile compared to the simulated velocity profile using OpenFOAM and FLUENT at 2 mm above the stirrer level.**

7.3   Turbulent Energy Dissipation

The CFD is able to calculate the local turbulent energy dissipation. Due to the still existing energy dissipation equation parameters, a validation of the calculated turbulent energy dissipation is still inevitable. The energy dissipation at an iso-value of 0.005 m²/s³ for the single phase case and a rotational speed of 100 rpm is shown in Figure 7.8. The highest energy dissipation is observed at the stirrer blades and in the extension of the stirrer blade at the column wall. The average energy dissipation is compared to literature values in Figure 7.9. A good agreement between the correlation of Kumar & Hartland (1996) and our own simulation could be found. Compared to the experimental derived correlation of Steinmetz (2007), a deviation can be observed. In addition, the results are compared to the average energy dissipation obtained from FLUENT simulations, which follow the trend of the OpenFOAM results. Especially for higher rotational speed, a slight deviation can be seen between the simulation tools resulting from slight differences in the generated meshes.

In addition, the simulated and experimentally obtained results of Drumm (2010) are compared to the energy dissipation equation for an RDC column given by Kumar & Hartland (1996) in Figure 7.10. Also in this case, a good agreement between the experimental results, the simulations using the standard k-ε-model and the correlation can be observed, which indicates the appropriate use of the k-ε-model for further investigations of stirred columns in combination with population balance modelling.
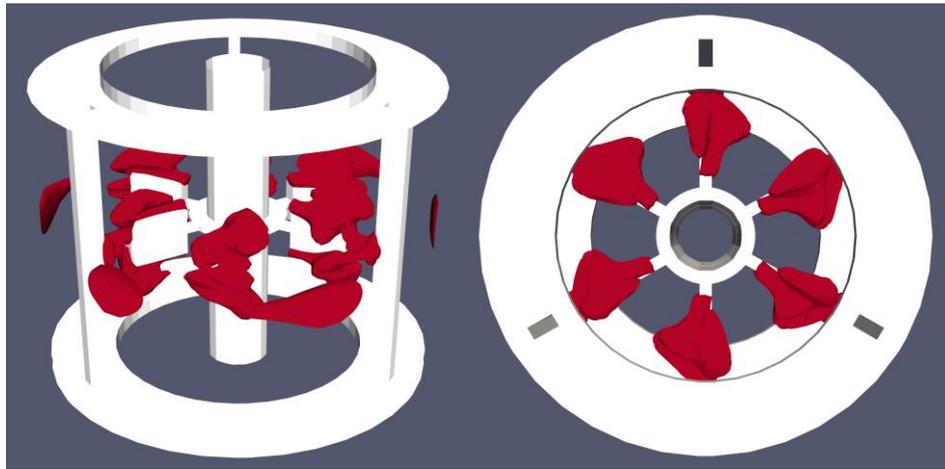
Figure 7.8: Iso−value plot of the energy dissipation=0.005 m²/s³ for a rotational speed of 100 rpm.
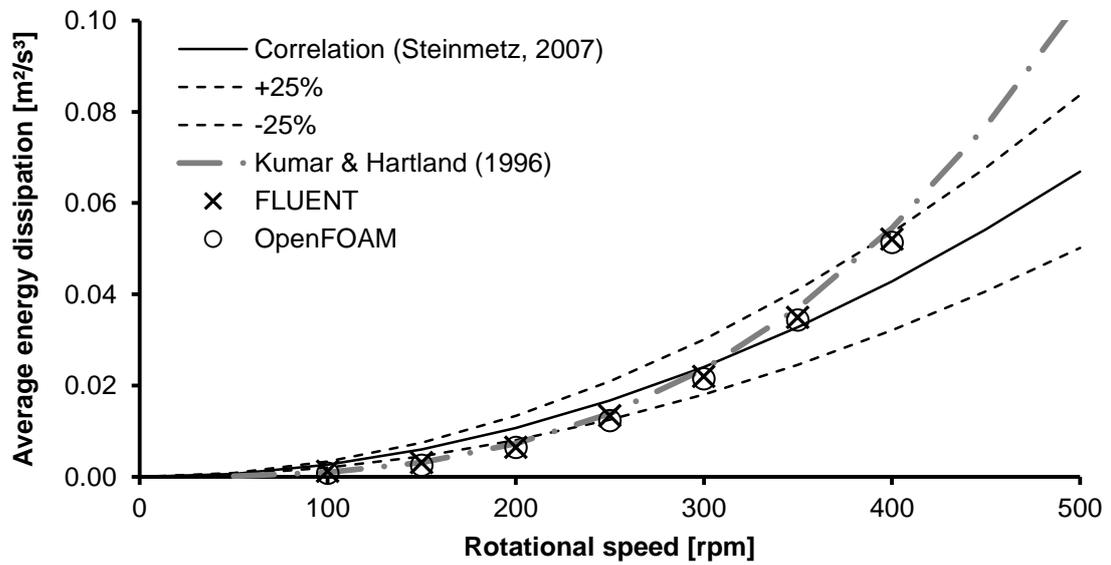
Figure 7.9: Comparison of the simulated average energy dissipation in a single compartment to the experimentally derived correlation of Steinmetz (2007).
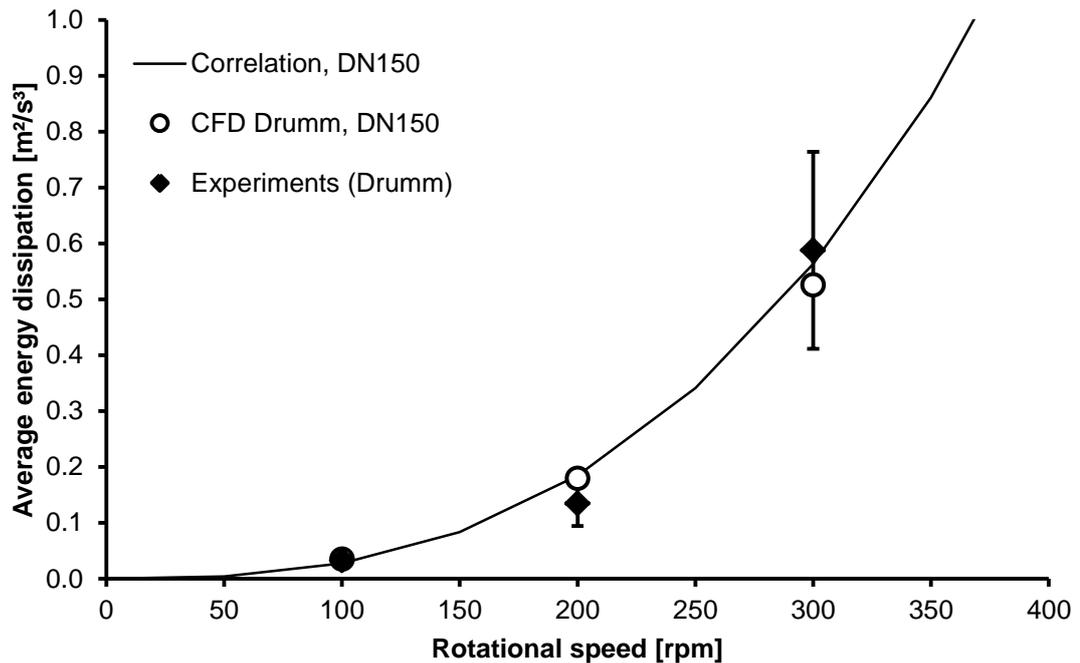
Figure 7.10: Comparison of the simulated average energy dissipation in a single compartment of an RDC DN150 column to the correlation of Kumar and Hartland (1996) and to experimental data derived from Drumm (2010).

7.4   Simulation of the Droplet Velocity

The free rising droplet velocity is based on the implemented drag term correlation. Drumm (2010) showed a good agreement between the FLUENT simulations and experiments using the drag term of Schiller & Naumann (1935). The correlation of Grace et al. (1976) could predict the experimental data of different authors in good agreement and is used to validate the numerical results. The simulated droplet velocity increases with increasing droplet size (Figure 7.11), which corresponds to the experimental results of Grace et al. (1976). The simulated droplet velocity for a droplet size of 1.5 mm droplet is 0.054 m/s and nearly doubles to a value of 0.1 m/s at a droplet size of 3.5 mm. Due to the low hold-up inside the column, the flow rate shows only a low influence on the droplet velocity in the given range of droplet sizes and flow rates.
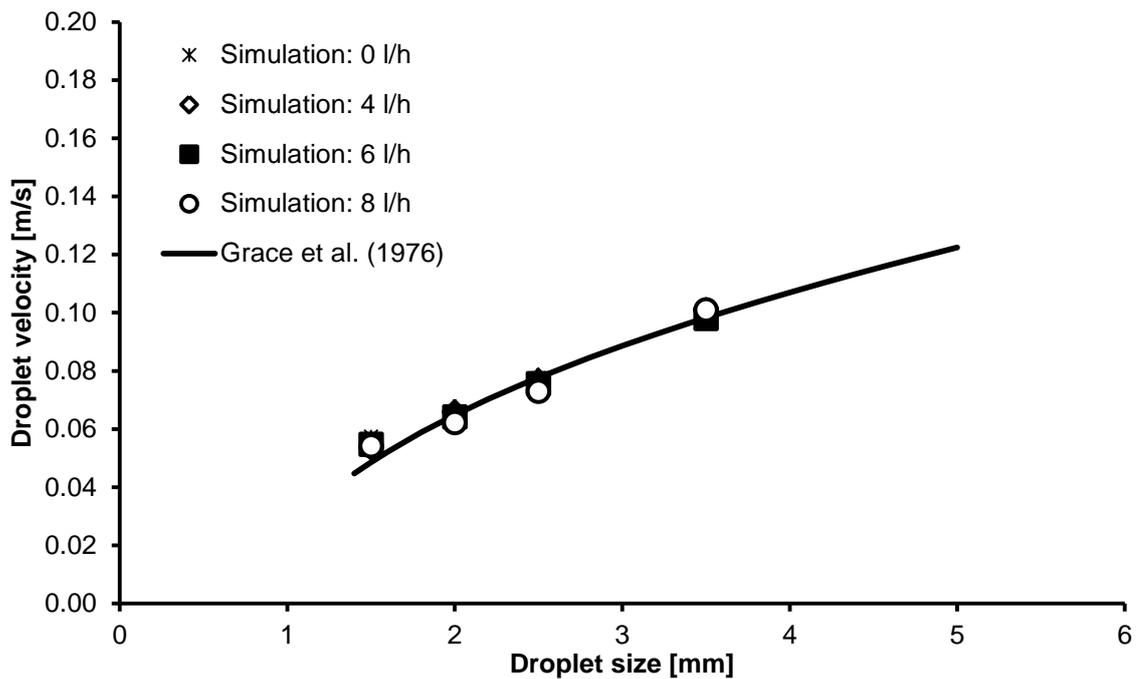
Figure 7.11: Simulated droplet velocity in comparison to an empirical correlation.

7.5 Phase Fraction

The phase fraction was measured experimentally using laser induced fluorescence (LIF) for the iso-optical systems water/$CaCl_2$-n-butyl acetate and for the system of water/glycerine/n-heptane for changing flow rates and varied rotational speeds. Here, the results of the second system are compared to the average phase fraction obtained from the adequate simulations (Figure 7.12). The droplet size in the simulations is reduced accordingly to the experimental observations from 2.5 mm at a rotational speed of 100 rpm to a droplet size of 1 mm at 300 rpm (flooding limit). The simulated phase fraction results in slightly lower values than the measured values. Compared to the correlation of Kumar & Hartland (1995), the CFD is able to describe the increase in phase fraction due to higher rotational speed and lower droplet size.
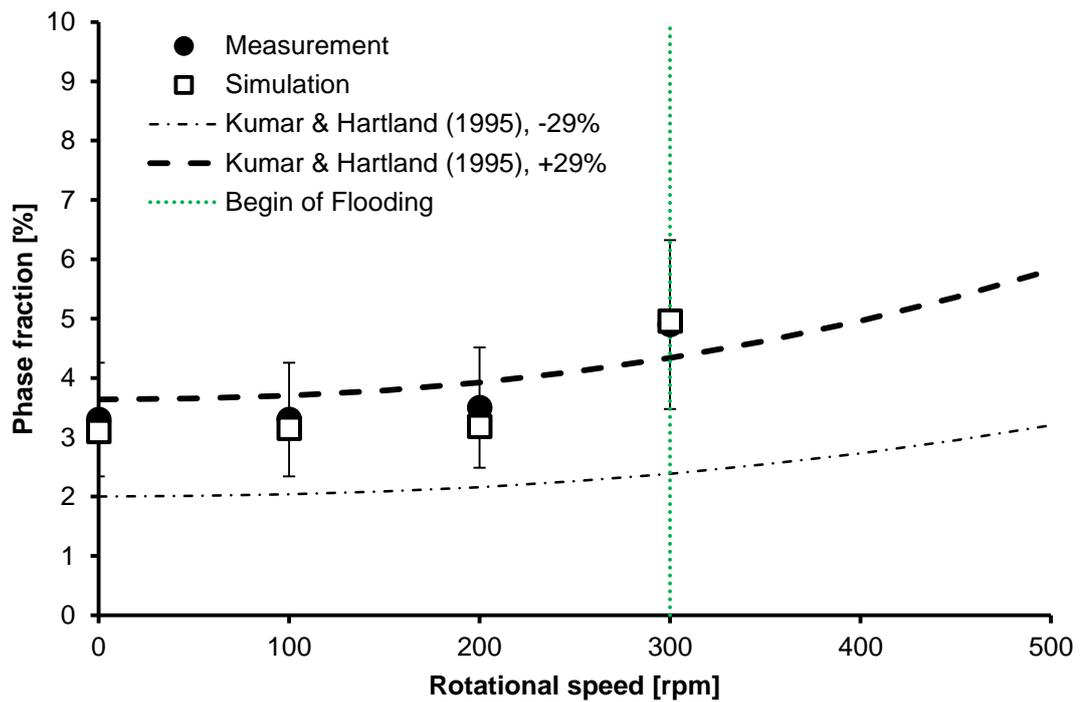
Figure 7.12: Simulated phase fraction in comparison to the measured phase fraction using LIF.

7.6   Simulation of the Axial Dispersion

Backmixing and local non-ideals influence the residence time of the liquids in the extraction column. The local simulated Euler-Euler flow field was compared to PIV measurements in the previous sections, where a good agreement between both could be found. Additional tracer simulations allow a further investigation of the flow field, the retention time and axial dispersion. For this purpose, a Lagrangian solver is derived based on the icoCouplekinematicParcelFoam solver contributed with the OpenFOAM standard solvers, which is able to simulate the particle movement based on an Eulerian based steady state solution. As test case for the newly derived solver, the flow field inside a DN25 pipe is simulated using the solver MRFtwoPhaseEulerPimpleFoam for a laminar test case at Re=500 (Figure 7.13) and turbulent test case at Re=15 000 (Figure 7.14), followed by the particle simulation. The boundary conditions for the simulation are given in Table 9.

Table 9: Laminar and turbulent boundary conditions for the Lagrangian solver validation.

Flow regime	Re-number [-]	Pipe Diameter [m]	Viscosity [m^2/s]	Velocity [m/s]	Particle number [-]
Laminar	500	0.0272	$1 \cdot 10^{-6}$	0.01838	146
Turbulent	15000	0.0272	$1 \cdot 10^{-6}$	0.55147	146

The Lagrangian particle simulation results are compared to the analytical velocity profile solution of Nikuradse (1933), where the first particles in flow direction correspond to the velocity profile distribution in the pipe (Figure 7.13) for the laminar case. Also the turbulent velocity profile fits to the particle movement (Figure 7.14).
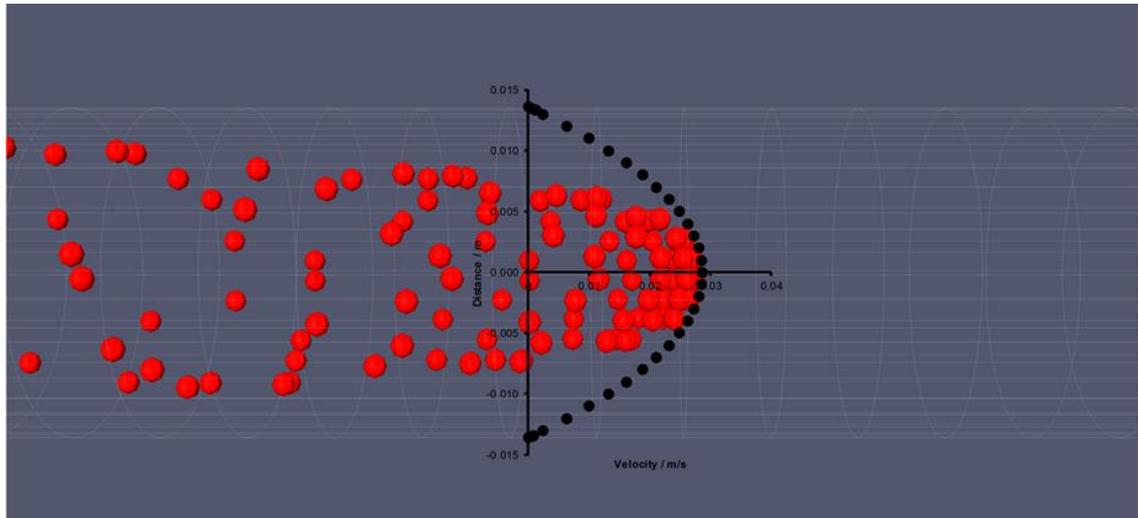
Figure 7.13: Visualization of the simulated laminar flow in a pipe by Lagrangian particles at Re=500 compared to the analytical velocity profile.
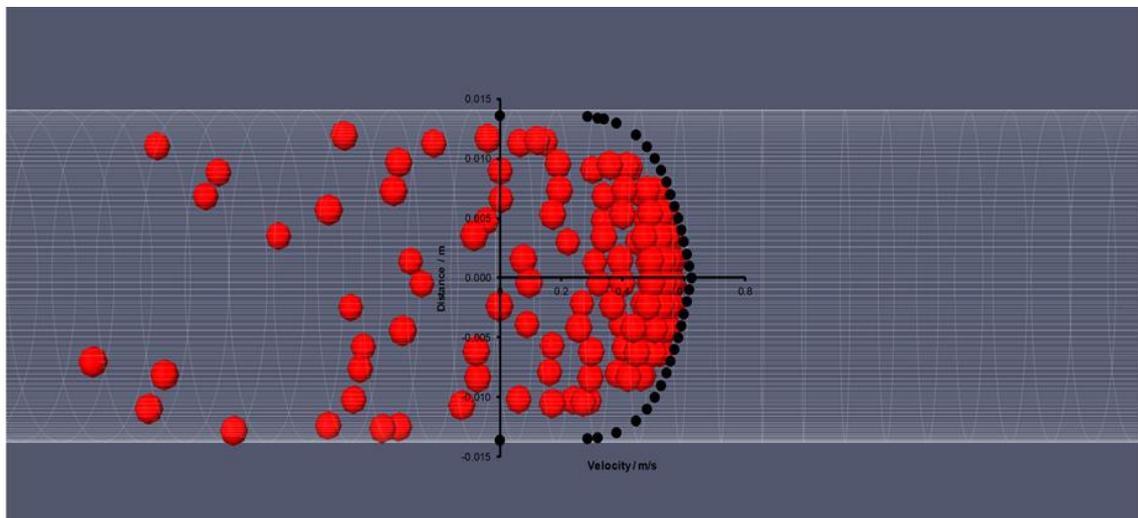
Figure 7.14: Visualization of the simulated turbulent flow in a pipe by Lagrangian particles at Re=15 000 compared to the analytical velocity profile.

Based on steady state single phase Euler and two-phase Euler-Euler simulations of an eight compartment section of a Kühni miniplant column, the axial dispersion coefficient is determined using the Euler-Lagrange method. In a first set of simulations, the axial dispersion coefficient is

determined for the single phase flow of the continuous phase （water） at different rotational speeds of the stirrer. Particles were injected at the stirrer level of the topmost compartment to determine the axial dispersion coefficient of the continuous phase （Figure 7.15）.
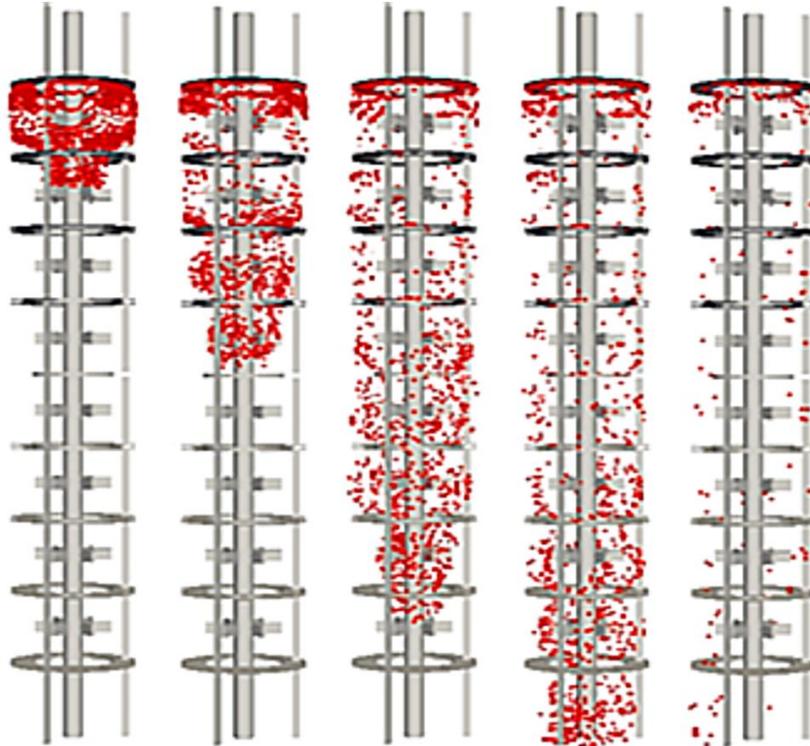
Figure 7.15: Particle flow for the determination of the continuous phase axial dispersion coefficient at a flow rate of 8 l/h and 300 rpm.

The results of the axial dispersion coefficient simulations for the Kühni miniplant column are compared to the experimental values in Figure 7.16. The simulated values using OpenFOAM follow the measured axial dispersion coefficients, where the values obtained by the FLUENT simulations show a slight under prediction. Compared to the available correlations, the best agreement could be found to the model of Breysee et al. （1983）. However, the axial dispersion coefficient of the continuous phase depends on the flow rate and on the influence of the dispersed phase. Therefore, the axial dispersion coefficient of the continuous phase considering a two-phase flow is shown in Figure 7.17. With increased flow rates of the dispersed and continuous phase, the axial dispersion increases. The dispersed phase axial dispersion coefficient is determined by injecting particles at the stirrer level of the lowest compartment. The density of the injected particles were fitted to the dispersed phase density. The particles follow the dispersed phase velocity and leave the column at the top Figure 7.18. In comparison to the available axial dispersion coefficient correlations for the dispersed phase, the model of Bauer （1976） shows the

best agreement to the simulation data, where the model of Rod （1968） and Steinmetz （2007）

show a high deviation.
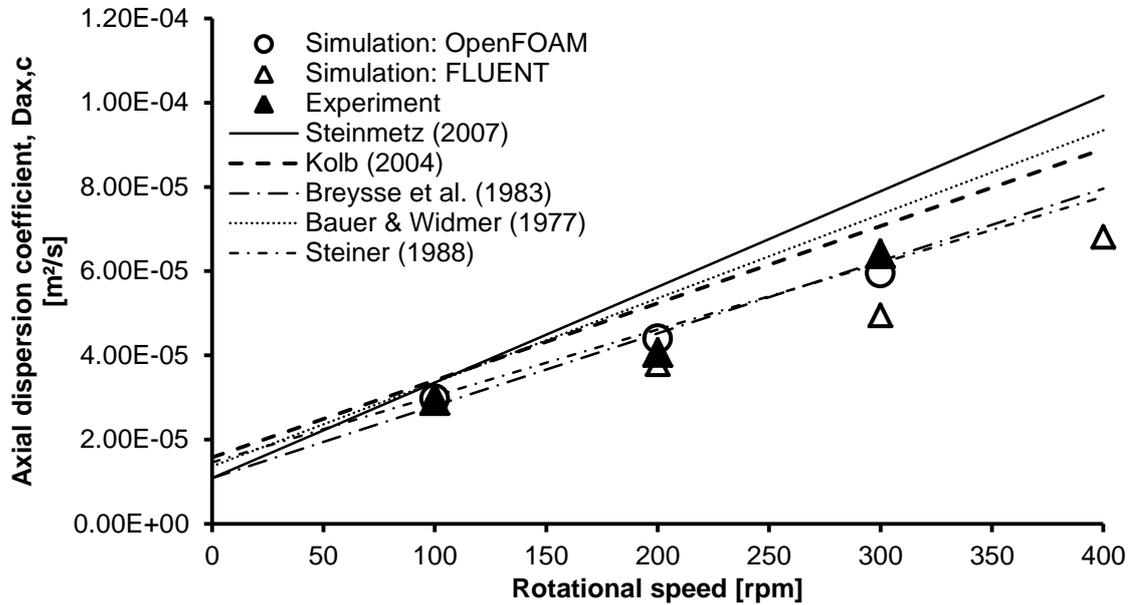
Figure 7.16: Axial dispersion coefficient of the continuous phase in a Kühni miniplant column at single phase flow of 8 l/h.
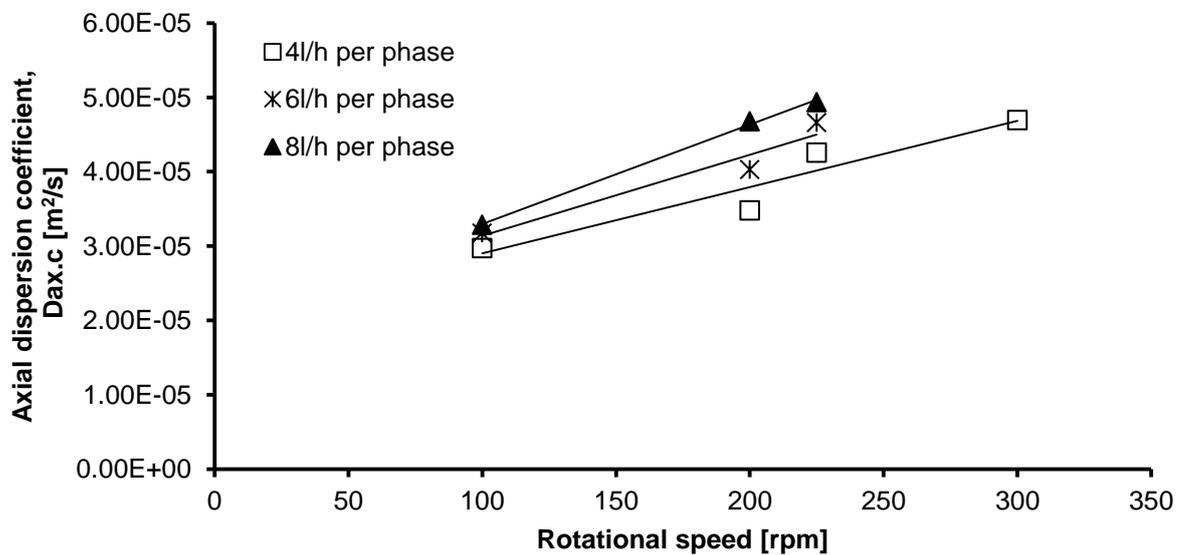
Figure 7.17: Axial dispersion coefficient of the continuous phase in a Kühni miniplant column considering a two-phase flow.
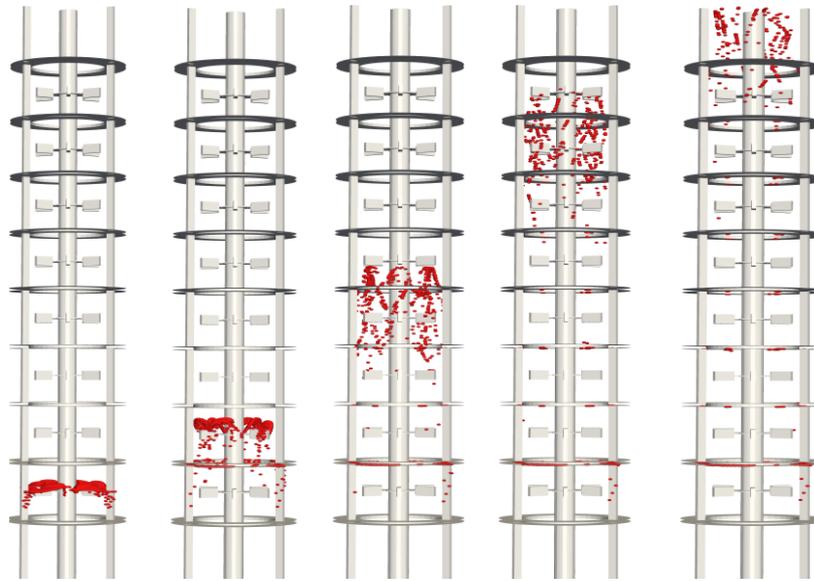
Figure 7.18: Particle flow for the determination of the dispersed phase axial dispersion coefficient at a flow rate of 8 l/h for each phase and 3.8 mm droplets at 100 rpm.
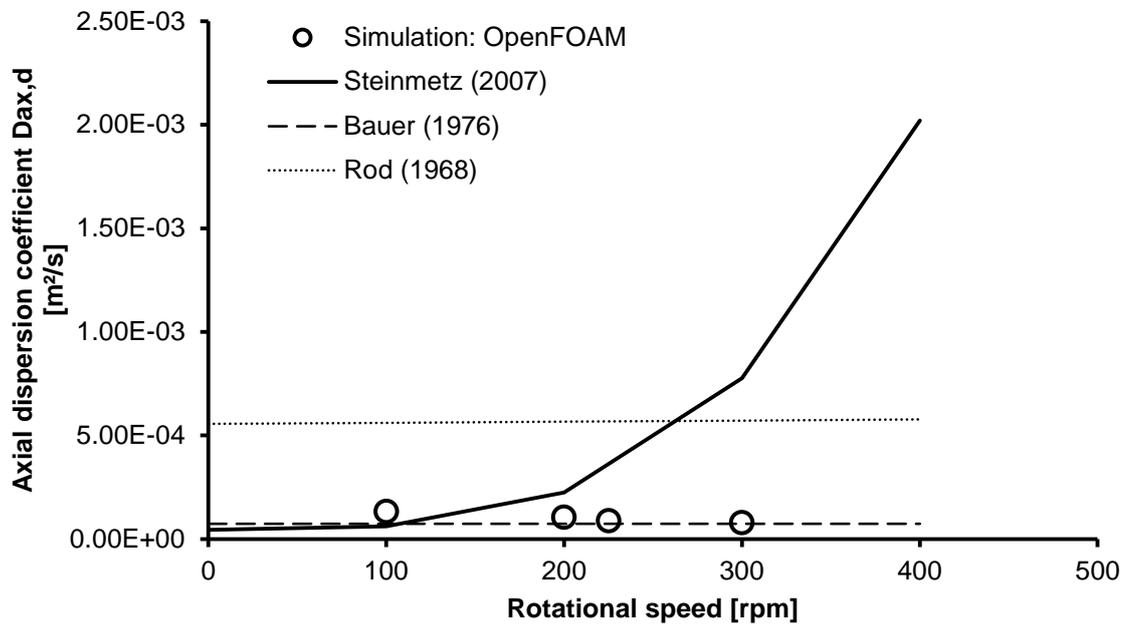
Figure 7.19: Axial dispersion coefficient of the dispersed phase in a Kühni miniplant column considering a two‑phase flow at 4 l/h per phase.

In addition, the axial dispersion coefficient of a Kühni DN60 column is determined (Figure 7.20). Regarding the accuracy of the measured data, the simulated results could predict the axial dispersion of the continuous phase. The obtained values show in addition a good agreement to the correlation of Breysee et al. (1983). The dispersed phase axial dispersion coefficient of the DN60 column is shown in Figure 7.21. The simulated axial dispersion coefficient is higher than the ones predicted for the DN32 column, which can be referred to geometrical changes of the stirrer design. In addition, a higher accumulation of dispersed phase underneath the stator, which was also observed from measurements, leads to backward mixing and a higher retention time of droplets inside the compartment. The agreement between the simulated results and the literature correlations is only given, by adjusting the constant parameters e.g. for the correlation of Bauer (1976):

$$\frac{1}{Bo} = 0.28 + 1.9 \cdot 10^{-8} Re_R^{1.7} Re_D^{-0.7} \qquad (7.1)$$
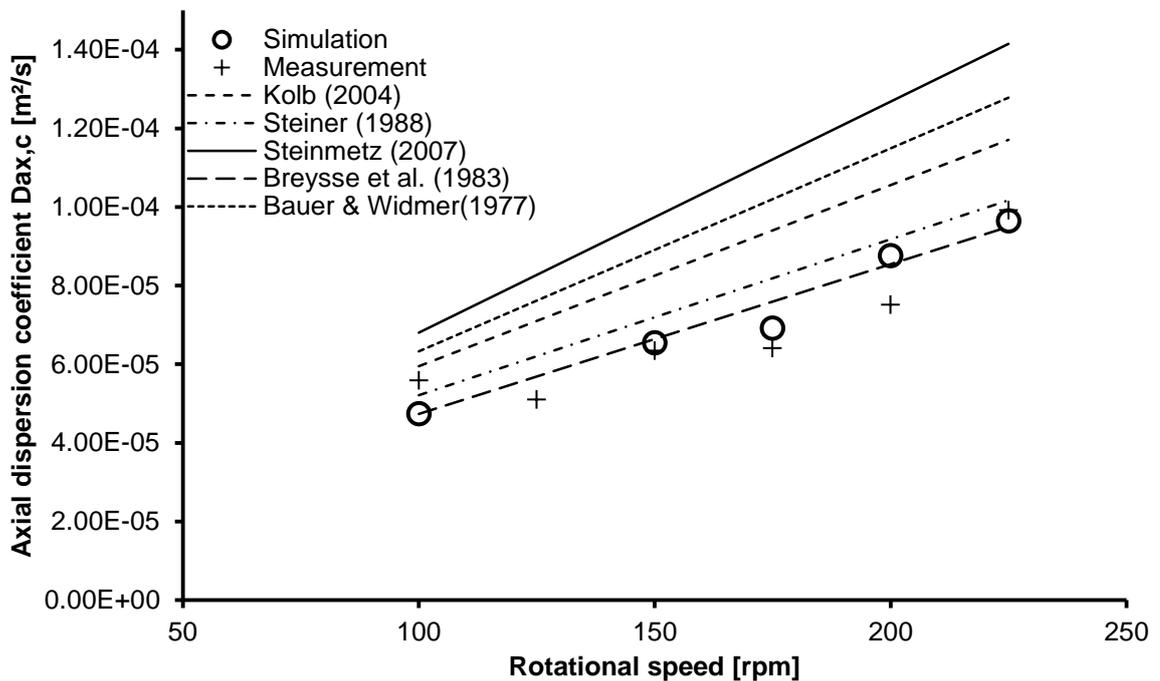
Figure 7.20: Axial dispersion coefficient of the continuous phase in a Kühni DN60 column (H$_c$=40 mm) at single phase flow of 16.5 l/h.
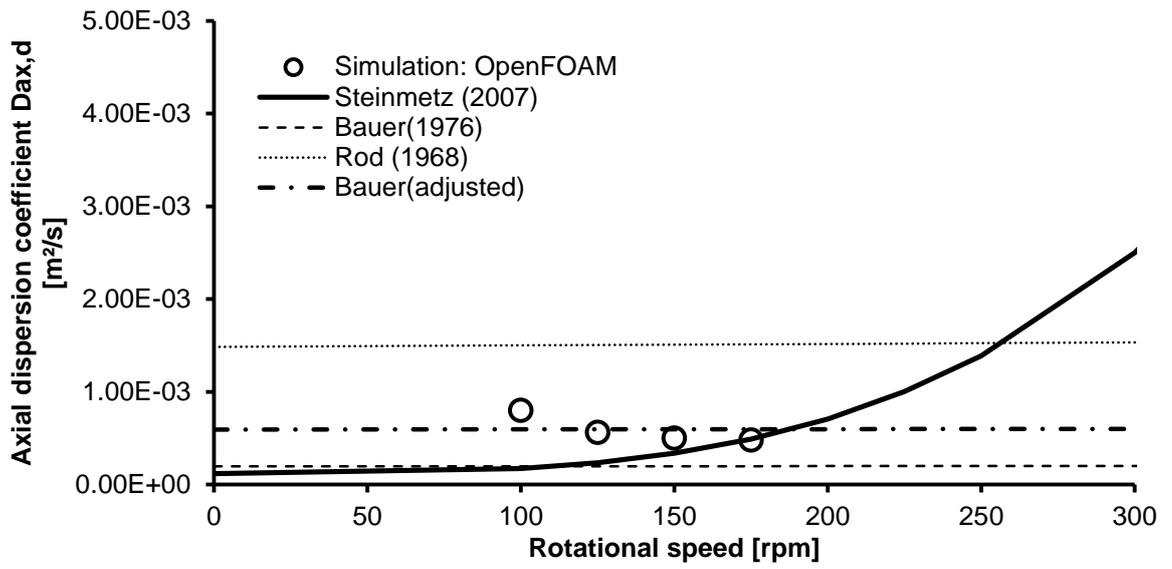
Figure 7.21: Axial dispersion coefficient of the dispersed phase in a Kühni DN60 column (H$_c$=40 mm) at 17.5 l/h continuous phase and 21.02 l/h dispersed phase.

7.7   Population Balance Equation Implementation

The hydrodynamics simulation is directly linked (two-way coupling) with the PPBM using the One Primary One Secondary Particle Method (OPOSPM) (Drumm et al., 2010). This one group PBM is derived from the Sectional Quadrature Method of Moments (SQMOM) developed by Attarakih et al. (2009). It is a moment based approach being very fast and stable from a computational point of view allowing the simulation of complex cases.

7.7.1   OPOSPM

The general implementation of the one group model is based on a single additional moment transport equation for the zeroth moment, which represents the transport of the total number of droplets per volume (Drumm et al., 2010):

$$\frac{\partial \alpha m_0}{\partial t} + \nabla \cdot \left(\alpha m_0 U_\varphi \right) = \alpha S \tag{7.2}$$

The source term S is studied in Attarakih et al. (2009) and is given by:

$$S = [n_{dd}(d_{30}) - 1]g(d_{30})m_0 - \frac{1}{2}a(d_{30}, d_{30})m_0^2 \tag{7.3}$$

Based on these additional equations to the hydrodynamics calculations, the volumetric droplet size can be calculated:

$$d_{30} = \sqrt[3]{\frac{m_3}{m_0}} = \sqrt[3]{\frac{6\alpha}{\pi m_0}} \tag{7.4}$$

As a test case, a rectangular mesh is generated, with a cell size of 20x20x1. The velocities were set to zero and a zero gradient boundary condition was chosen for the pressure. The initial phase fraction of the dispersed phase is set to 0.05 and the droplet size is set to 2 mm. A constant breakage rate of $g(d_{30})$ =0.2 1/s is set as the only source term for the number balance. The under-relaxation factors were set to 1. The results of CFD/PBM code are compared to the analytical solution of a stirred tank with binary breakage:

$$N = N_0 e^{0.2 \cdot t} \tag{7.5}$$

The CFD/PBM simulation perfectly fits to the analytical solution (Figure 7.22). Also the simulation at a constant breakage rate of 0.2 1/s and a constant coalescence rate of 1E-8 (m³/s) in Figure 7.23 fits to the analytical solution of:

$$N = 2(\frac{g(d)}{a(d,d)})N_0 \left[N_0 + 2 \left(\frac{g(d)}{a(d,d)} \right) e^{-g(d)t} - N_0 e^{-g(d)t} \right]^{-1}$$ (7.6)
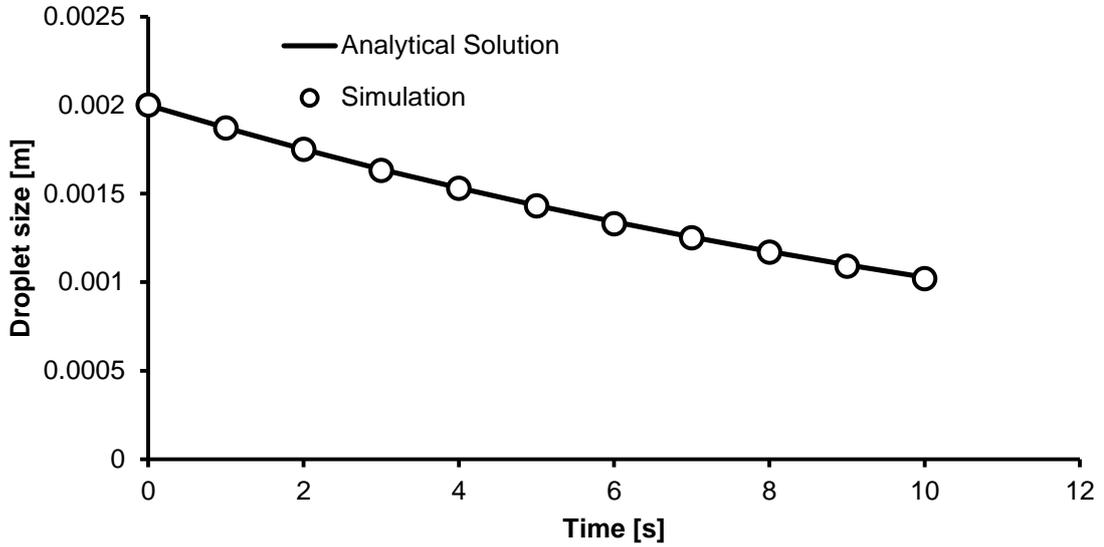
Figure 7.22: Comparison of the calculated droplet size between the analytical solution and the CFD simulation at a constant breakage rate of 0.2 1/s.
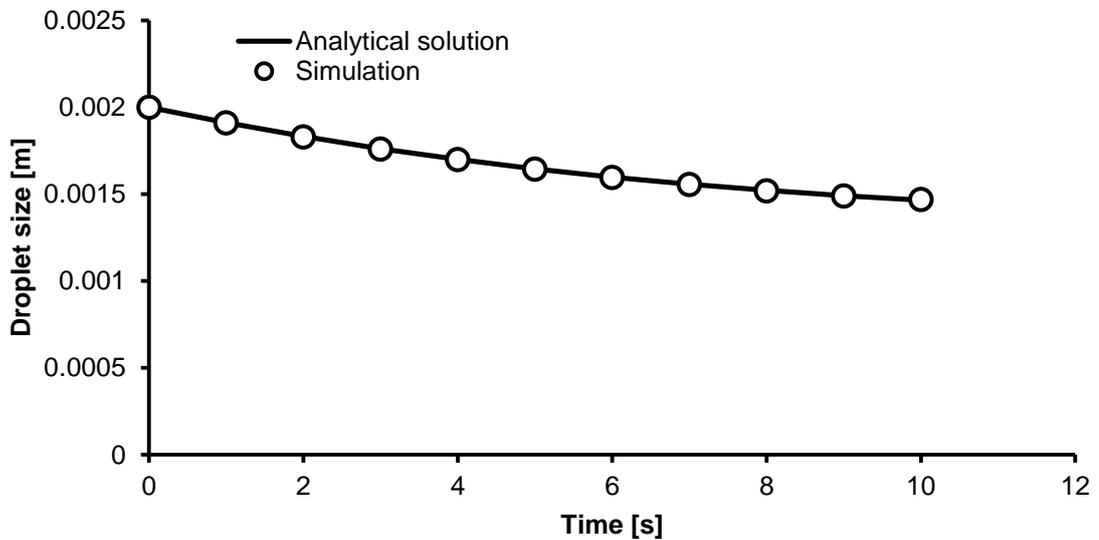
Figure 7.23: Comparison of the calculated droplet size between the analytical solution and the CFD simulation at a constant breakage rate of 0.2 1/s and a coalescence rate of 1E-8 m^3/s.

The implemented population balance model is further compared to the commercial CFD code FLUENT using the available QMOM. The under relaxation factors were set to 0.9 for the velocity, phase fraction and number balance equation and for the pressure equation, it was set to 0.3. In Figure 7.24, the result of the droplet size simulations using a constant breakage kernel

of 0.2 1/s is shown. In this five compartment section of an RDC column, the dispersed phase inlet was set at the bottom, whereas the heavier continuous phase enters the column at the top leading to a counter-current flow of the phases. The droplet size decreases in both cases from a droplet diameter of 2.66 mm to a droplet diameter of 1.90 mm in the OpenFOAM/OPOSPM simulation and to 1.88 mm in the FLUENT/QMOM simulation. In Figure 7.25, the results including an additional coalescence of 1.0E-8 m³/s is depicted. The droplet size slightly decreases to 2.38 mm in the FLUENT simulation and 2.34 in the OpenFOAM simulation. The deviation in the simulated droplet size at the outlet can be traced back to the accumulation of dispersed phase underneath the stirrer and stator ring and therefore different retention times of the droplets inside the column.
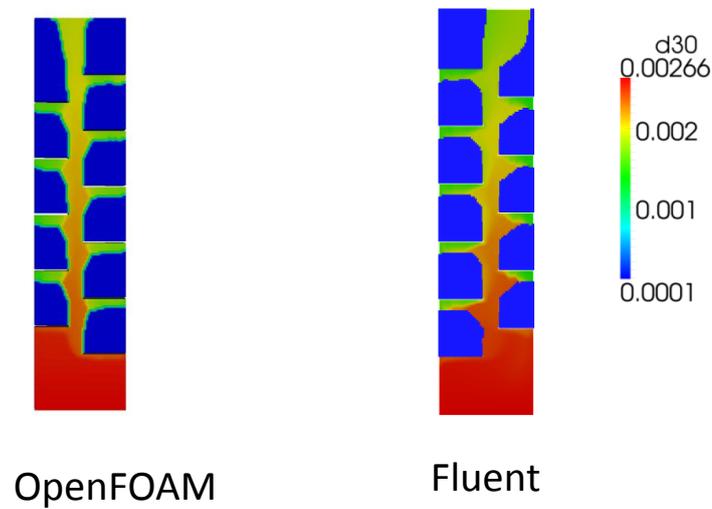
Figure 7.24: Droplet size in meter using a constant breakage kernel of 0.2 1/s.
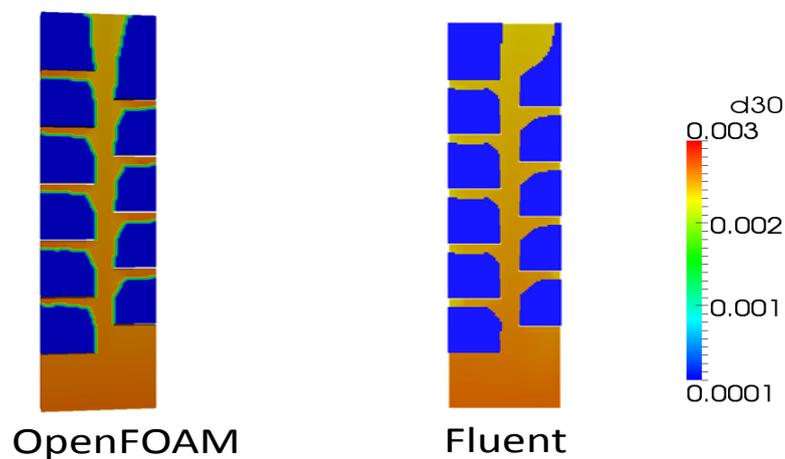
Figure 7.25: Droplet size in meter using a constant breakage kernel of 0.2 1/s and a coalescence kernel of 1.0E-8 m³/s.

7.7.2   Coalescence and Breakage Models

Several coalescence and breakage kernels were developed over the years including adjustable parameters to fit the model to the properties of the liquids and to the geometrical design of the investigated column. The presented OPOSPM allows the investigation of the breakage and coalescence terms in dependence of energy dissipation and droplet size. However, binary droplet coalescence is only accounted for equal sized droplets due to the mentioned model limitations of the one group model. But, in advance of the simulation, breakage or coalescence events predicted by the models can be visually investigated.

7.7.2.1. Breakage

The breakup rate $g(d)$ of each model is shown for the system of n-butyl acetate in Figure 7.26. The results are based on a phase fraction of 5%. The model of Coulaloglou & Tavlarides (1977) shows for the droplet sizes between 1 mm and 10 mm, as they occur in counter-current liquid-liquid extraction columns, a tendency to higher breakage for small droplets and high energy input. Only for smaller droplets, the breakage frequency shows the expected trend to higher breakage for larger droplets and high energy dissipation. The model of Luo & Svendsen (1996) predicts the highest breakage frequency for large droplets and high energy input. The model of Andersson & Andersson (2006) shows a similar shape of the breakage frequency over the droplet size and energy dissipation resulting in the highest breakage frequency for large droplets and high energy dissipation. The model of Martínez-Bazán et al. (1999a,b) includes a square root term and therefore a zone without breakage. This zone is enclosed by a borderline of beginning breakage defined by the minimum stable droplet size at given energy input. A rapid increase in the breakage rate is formed from this limit, which finds its maximum for large droplets and small energy dissipation.
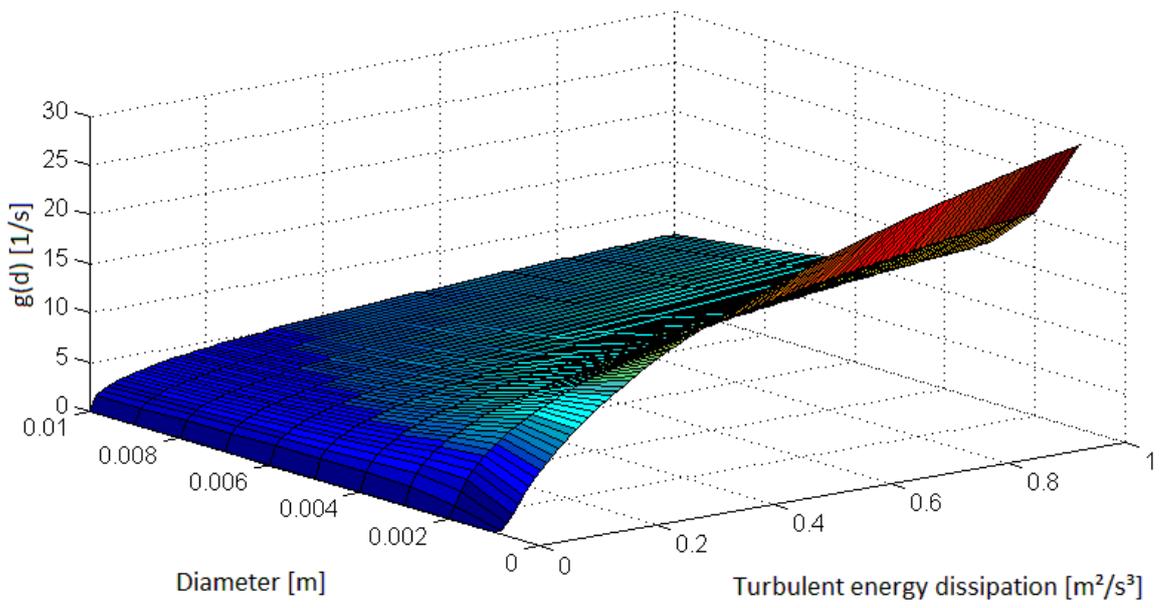
a) Coulaloglou & Tavlarides (d>0.001)
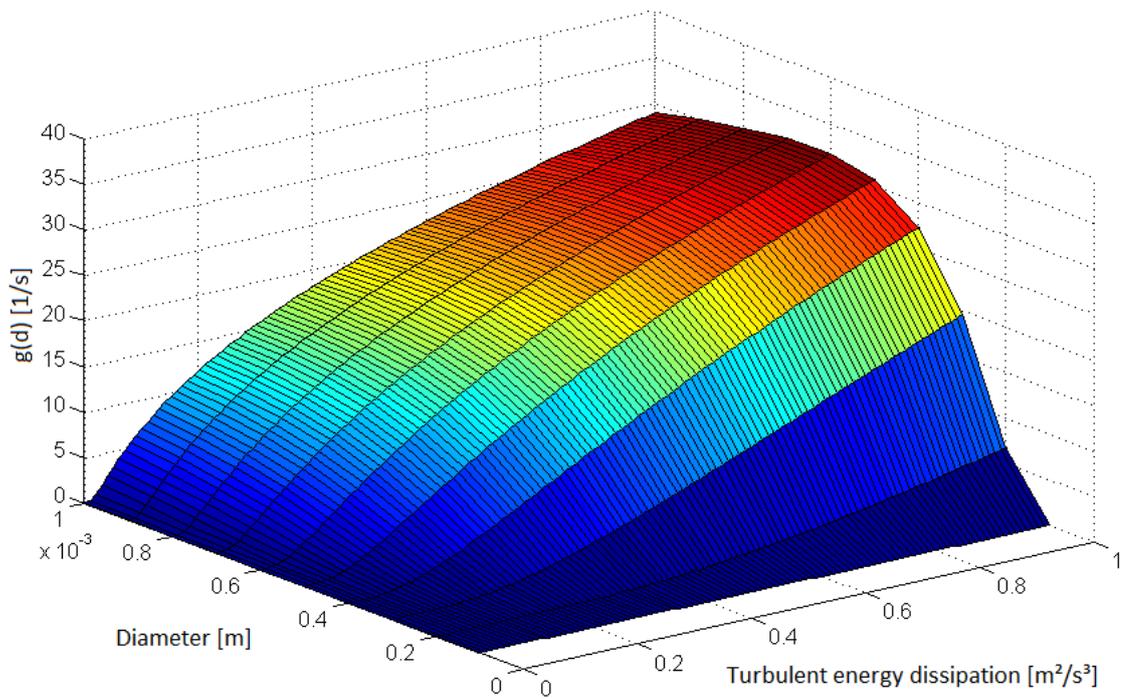
b) Coulaloglou & Tavlarides (d<0.001)
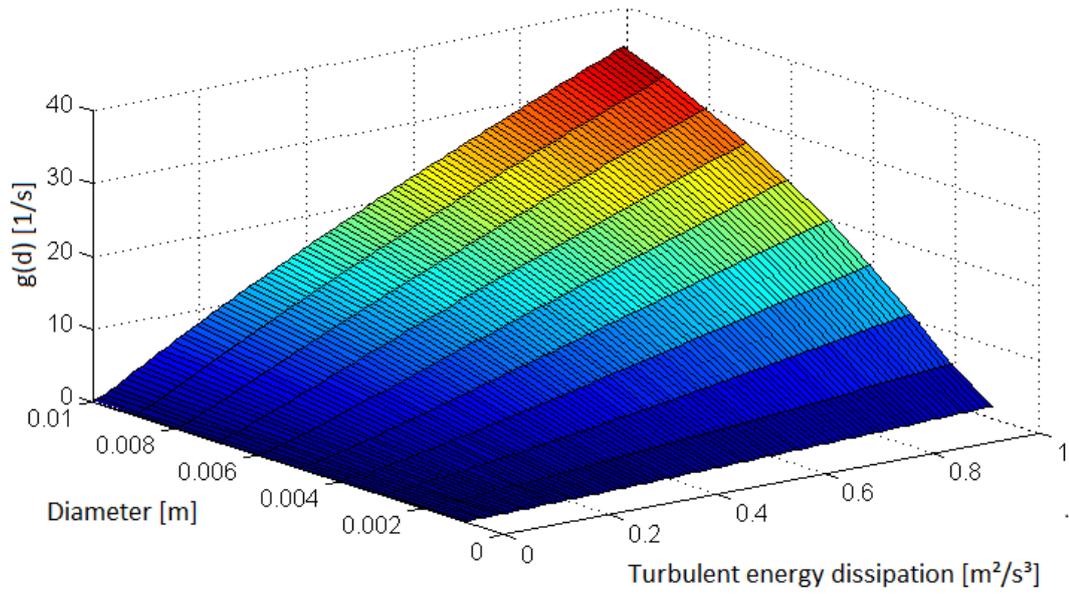
c) **Luo & Svendsen**
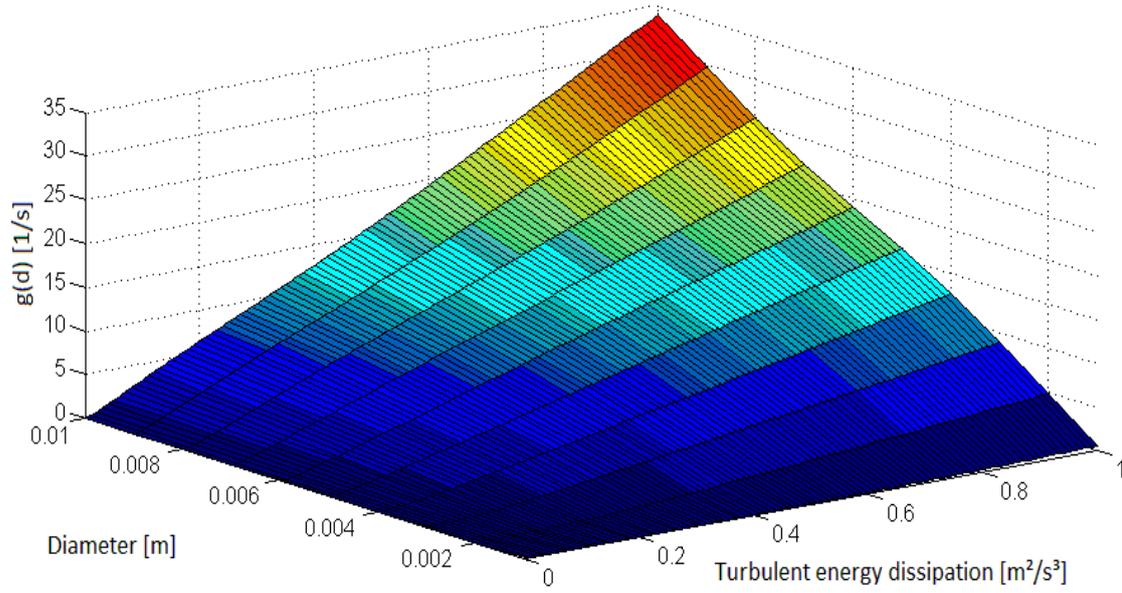
d) **Andersson & Andersson**
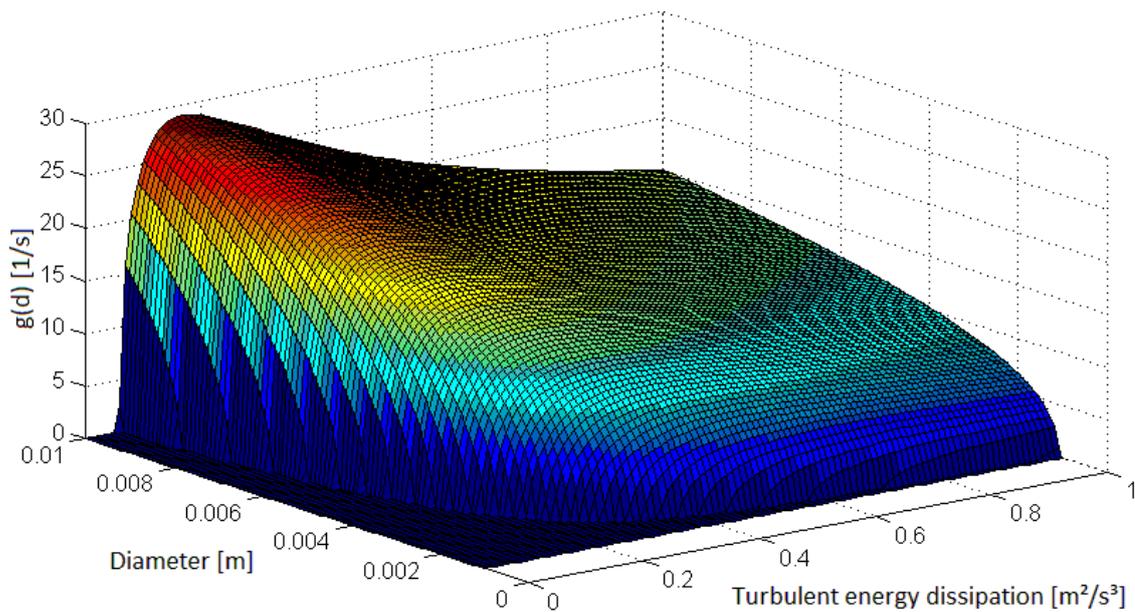
e) Martínez-Bazán et al.

Figure 7.26: Breakage rates in dependency of the turbulent energy dissipation and the particle diameter.

7.7.2.2. Coalescence

The coalescence frequency is determined for the same boundary conditions of 5% dispersed phase fraction and the system of n-butyl acetate/water. The coalescence kernel of Coulaloglou & Tavlarides (1977) is in the range of $2.7 \cdot 10^{-10}$ m³/s for energy dissipations of 1 m²/s³ and droplets of 10 mm diameter. The model of Luo & Svendsen (1996) also predicts the highest value for large droplets and high energy dissipation. Nevertheless, the maximum is in the range of $1.2 \cdot 10^{-4}$ m³/s. The model of Prince & Blanch (1990) shows a similar shape to the both presented models. However, the maximum value is slightly lower ($3.3 \cdot 10^{-5}$ m³/s) than the model of Luo & Svendsen, where the model of Prince and Blanch depends on the film thickness and critical film thickness. For both values, there is a wide range of values given in literature. The highest deviation among the models can be seen from the model of Coulaloglou & Tavlarides (1977) to the other models using the original suggested model constants. By adjusting these constants, the model can be fitted closer to the other coalescence models.
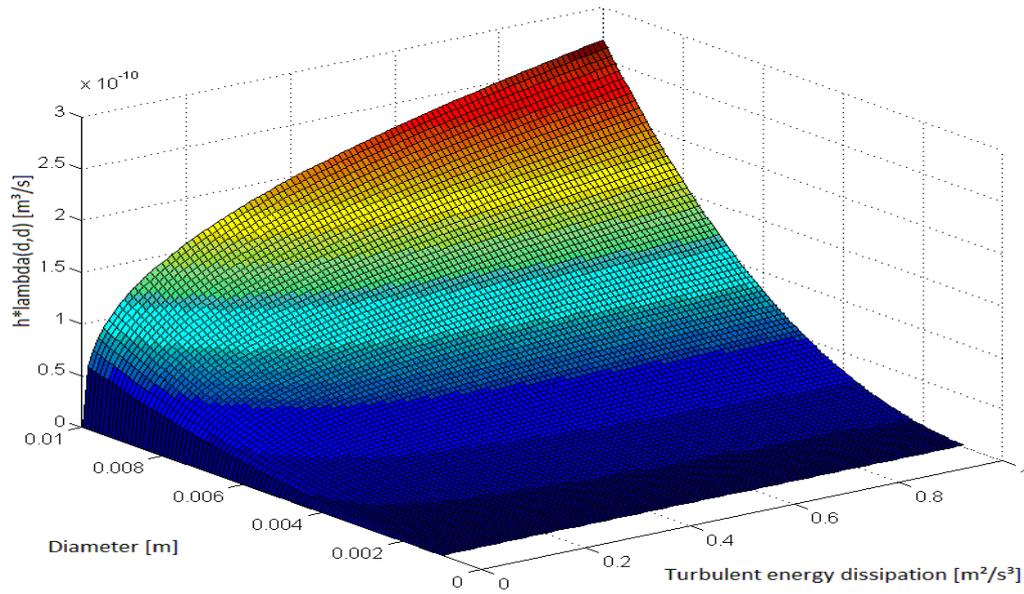
a) Coulaloglou & Tavlarides (d>0.001)
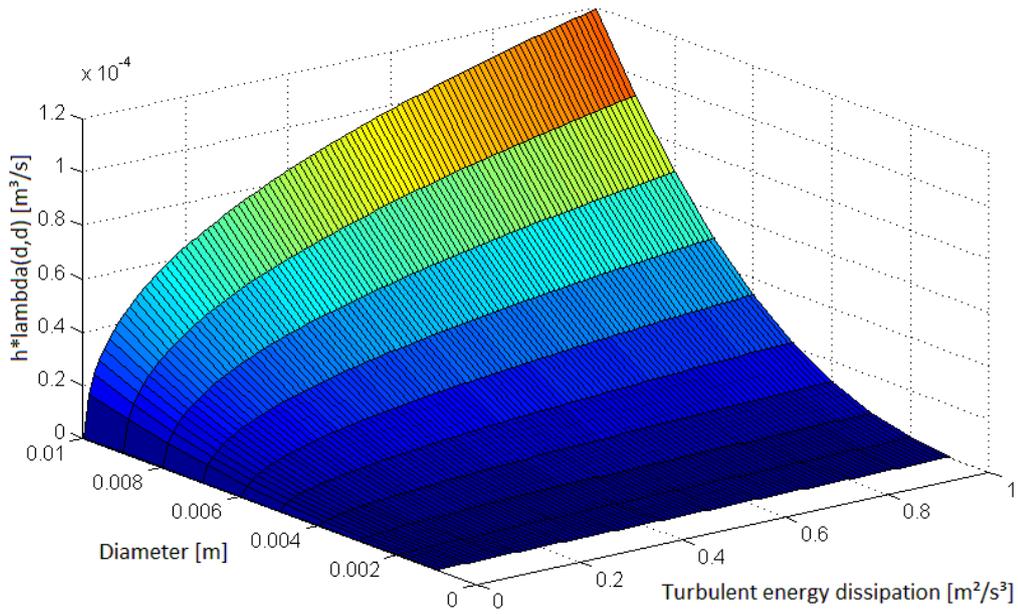
b) Luo & Svendsen
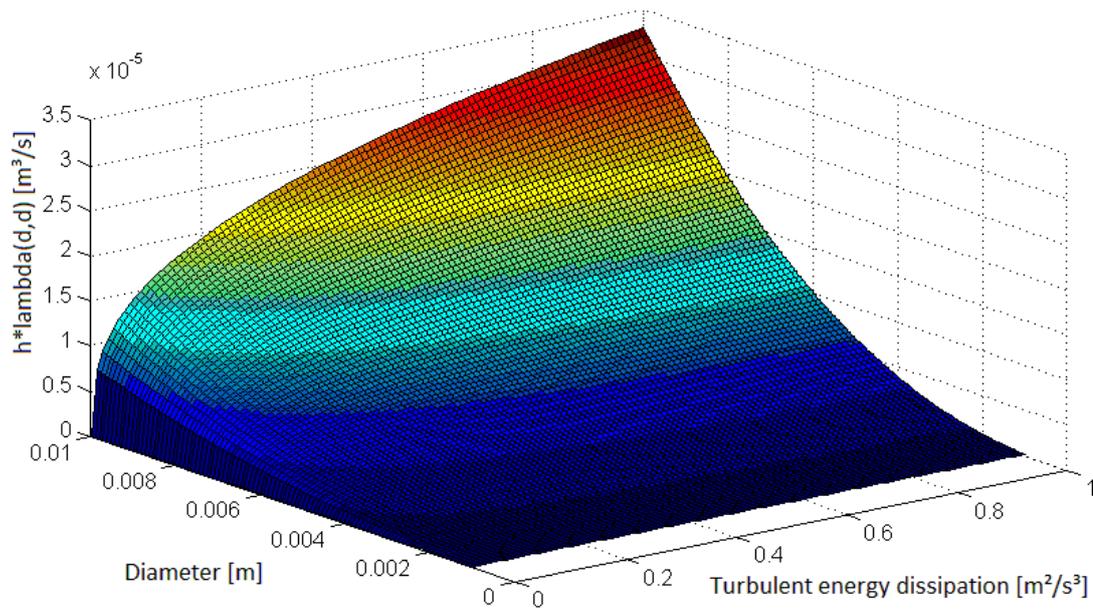
c) Prince & Blanch

Figure 7.27: Coalescence kernel in dependency of the turbulent energy dissipation and the particle diameter.

7.7.2.3. Source term

The source term indicates the total loss and gain of droplets due to coalescence and breakage. A negative source term thereby describes a region with dominant coalescence and a positive source term indicates a region with dominant breakage. The resulting source term of the coalescence and breakage models are given in Figure 7.28. In the case of Coulaloglou & Tavlarides (1977), the breakage occurs only for small droplets. However, due to the simplifications of the one group model, coalescence only occurs between equally sized droplets. The model of Luo & Svendsen (1996) predicts a decrease in coalescence at small droplet sizes which can also be observed by the mixed model. However, the mixed model, consisting of the breakage term from Martínez-Bazán et al. (1999a,b) and the coalescence term of Prince & Blanch (1990), also predicts a region with droplet breakage at a droplet size around 3 mm and an energy dissipation between 0.2 m²/s³ up to 0.4 m²/s³.
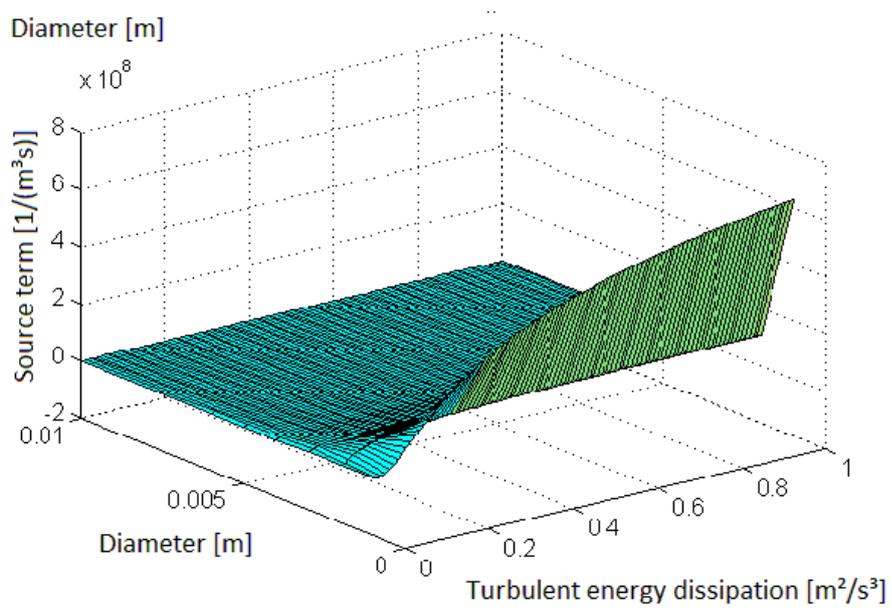
a) Coulaloglou & Tavlarides (d>0.001)
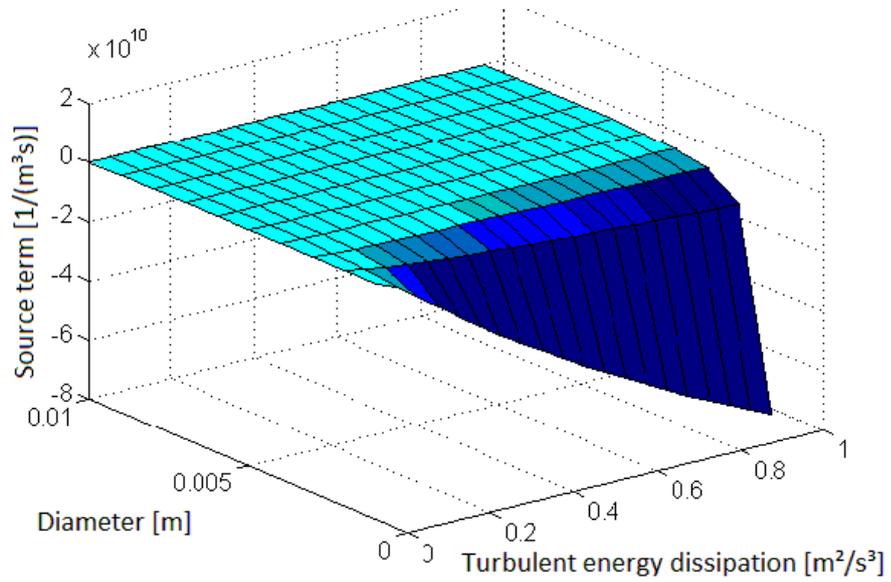
b) Luo & Svendsen
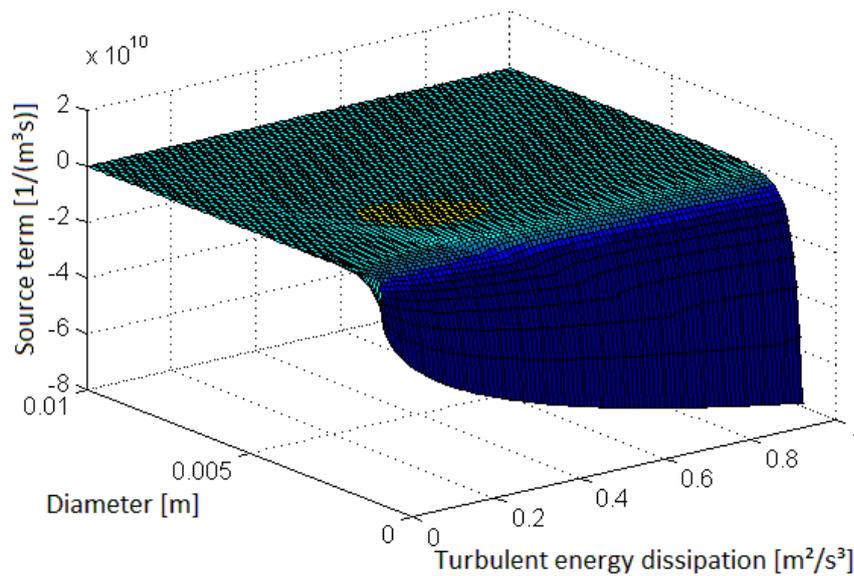
c) Martínez-Bazán, et al. & Prince & Blanch

Figure 7.28: Source terms in dependency of the turbulent energy dissipation and the particle diameter.

7.7.3   Simulation of the Droplet Size at Different Rotational Speeds

Based on the previous presented Matlab graphs, the combined model of Martínez-Bazán et al. (1999a,b) and Prince & Blanch (1990) is further investigated. The Batchelor constant in the model of Martínez-Bazán et al. (1999) was adjusted to result in a stable droplet size corresponding to the experimental data for the system toluene/water of Steinmetz (2007). The adjustment was done only for the case of 300 rpm and the obtained Batchelor constant of 30 is used for further CFD simulations at 200, 250, and 350 rpm. The results of the simulations using the simulation tool OpenFOAM and FLUENT using the OPOSPM for the calculation of the droplet size and is shown in Figure 7.29. In addition, the simulation results using FLUENT with the QMOM are compared to the experimental data. It can be observed that the modified breakage model in combination with the coalescence model of Prince & Blanch (1990) can predict the droplet size for different rotational speeds. At 350 rpm (2.2 mm droplet size), the deviation of the models increases slightly due to slight differences in the energy dissipation.
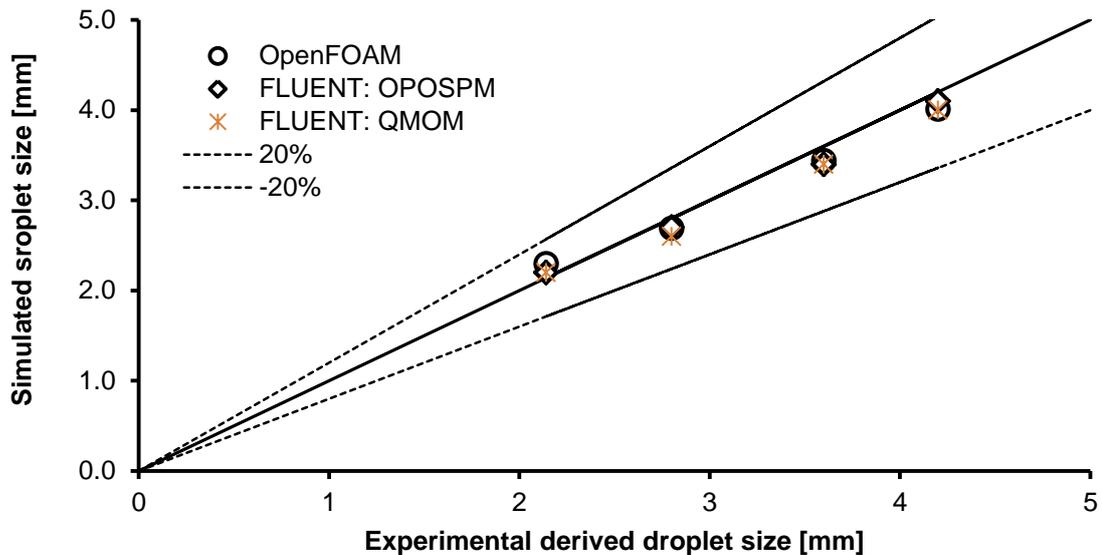
Figure 7.29: Simulated droplet size using an adjusted model compared to experimental data of Steinmetz (2007).

A further optimization of the coalescence and breakage parameters can be obtained by the inverse population balance modelling. An example is given in Jildeh et al. (2012b), where the correlation of the average energy dissipation in a single compartment is derived from CFD simulations and used in a one dimensional population balance simulation of an RDC column to determine the breakage and coalescence parameters for the model of Coulaloglou & Tavlarides (1977). The optimized parameters were then used for the three dimensional CFD simulation of the column including breakage and coalescence. The results of the droplet size simulation were in good agreement to experimental data. Compared to the one dimensional simulation, the three dimensional simulation allows further investigations of local phenomena as e.g. swirl structures or accumulations of dispersed phase.

7.8   Scale-up from a Kühni DN32 Column to a Kühni DN60 Column

The efficiency of the extraction columns depends, despite of the boundary conditions, on the local flow phenomena. During scale-up, the geometrical design of the extraction column internals may change as it is the case from the Kühni miniplant DN32 column to the Kühni DN60 column. The main geometrical details are shown in Table 10. In addition, the DN60 stirrer is mounted with a ferrule to the shaft leading to a non-symmetric design between of the upper part of the column to the lower part. The velocity vectors in axial and radial directions are shown in Figure 7.30 for both columns. In the Kühni miniplant column, four vortexes can be seen, two above the stirrer and two underneath the stirrer. In the DN60 column, two vortexes can be seen

on the right hand side of the column, one above and one underneath the stator. On the left hand side, the vortex structure is destroyed due to the interactions with the round baffle and the interaction with the dispersed phase. In addition, the vortex structure above and underneath the stator shows a higher deviation to each other compared to the ones generated in the Kühni miniplant column.

Table 10: Used column designs for simulations

Column	DN32	DN60
Diameter	32 mm	60 mm
Compartment Height	28 mm	40 mm
Stirrer diameter	20 mm	40 mm
Stirrer type	6 baffles	4 baffles
Shaft diameter	5 mm	10 mm

Kühni miniplant (DN32)   Kühni DN60
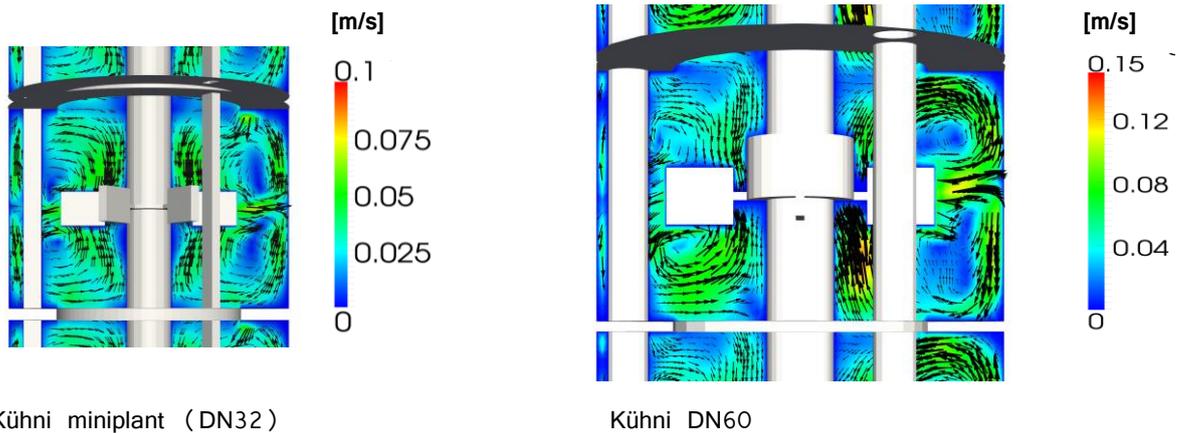
Figure 7.30: Flow field inside the Kühni miniplant (DN32) column and Kühni DN60 column at a flow rate of 5 m³/(m²h) per phase and 200 rpm (toluene/water).

7.9 Geometry Variations

Main modifications concerning the compartment height and the free cross sectional area of the stator were experimentally and numerically done by Kolb (2005) and Steinmetz (2007). The new CFD-PBM code, in combination with the automated mesh generation, now allows the investigation of different geometries including the consideration of local droplet size changes. In a first step, the compartment height of the Kühni miniplant column is reduced and increased by 5 mm leading to compartment heights of 23 mm and 33 mm respectively. In the elongated compartment height, the circular swirl structure is deformed to an ellipsoid swirl structure leading to a low circular velocity underneath the stators (Figure 7.31). In the reduced compartment

height, the swirl structure is compressed. High upward and downward directed velocities are observed close to the column wall. The high velocities close to the stators, compared to the increased compartment height, leads to a lower accumulation of dispersed phase underneath the stators （Figure 7.32）.

23 mm   33 mm
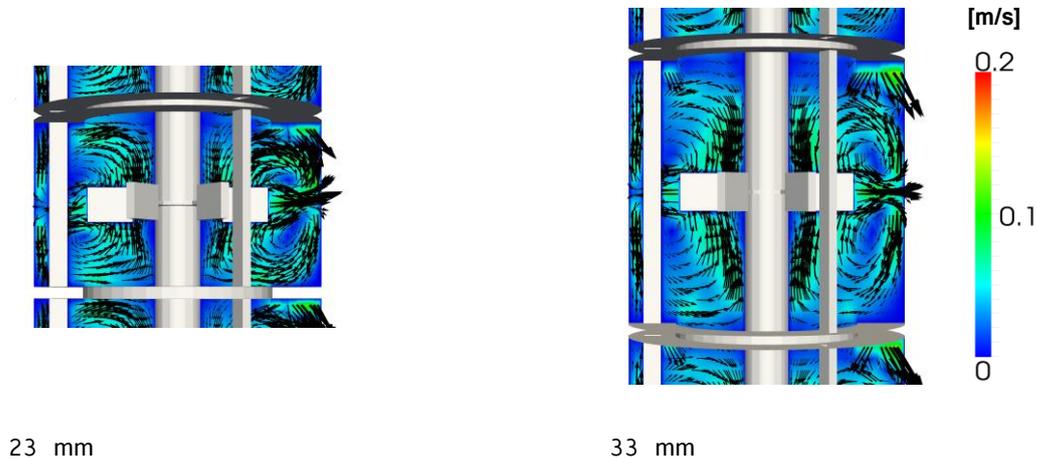
Figure 7.31: Velocity fields inside the modified Kühni DN32 columns at 300 rpm. Velocity in ms^{-1}.

23 mm   33 mm
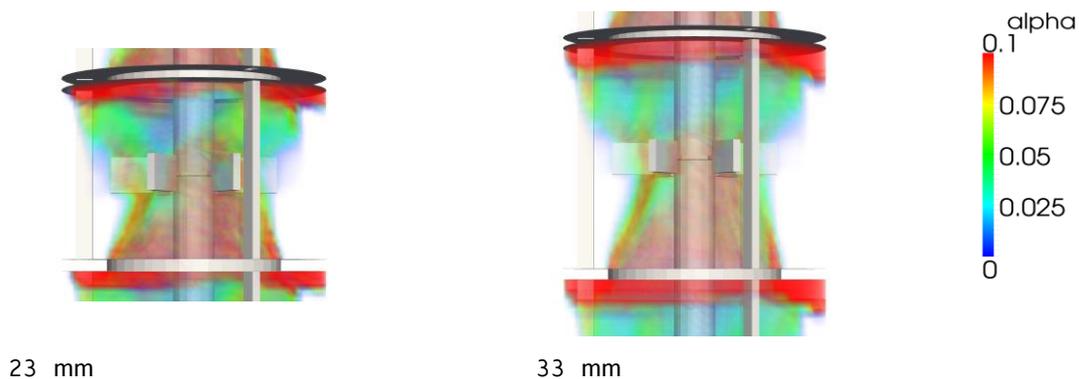
Figure 7.32: Phase fraction distribution inside the modified Kühni DN32 columns at 300 rpm.

However, the dispersed phase is mainly distributed in the upper part of the compartment due to the impact of the stirrer. A geometrical optimization of the stirrer position may induce a higher distribution of the dispersed phase in the lower part of the compartments and to higher mass transfer due to a higher interfacial area.

An eight compartment section of the Kühni miniplant column is generated using presented the toolbox where the stirrer position is set to one third of the compartment height. The column is simulated using the optimized mixed model for breakage and coalescence to account for changes in the droplet size. The velocity above the stirrer and underneath the stirrer is similar to the original design. In the modified design, the vortex structure is compressed underneath the stirrer, where the vortexes become larger above the stirrer （Figure 7.33）. The resulting phase fraction

distribution is compared to the standard geometry in Figure 7.34 as an iso-value plot. The dispersed phase is distributed in both simulations at the stirrer level. The reduction of the stirrer position to one third of the compartment height leads to a higher dispersion in the lower compartment area. Concerning the droplet size, an overall smaller droplet size can be observed in the new geometrical design (Figure 7.35). The combination of a higher phase fraction with lower droplet sizes (higher interfacial area) indicates an increase of mass transfer by using the modified column design. But, the compressed swirl structure inhibits the rise of the dispersed phase and will lead to an earlier flooding point.
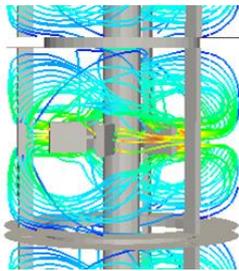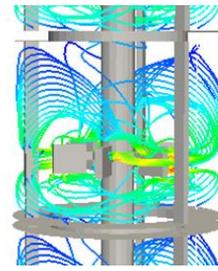
DN32 Original   DN32 Modified

Figure 7.33: Velocity field inside the Kühni DN32 column (left) and the modified Kühni DN32 column with stirrer level at 1/3 of the compartment height (right).
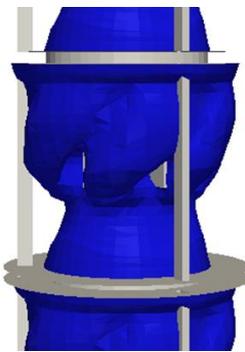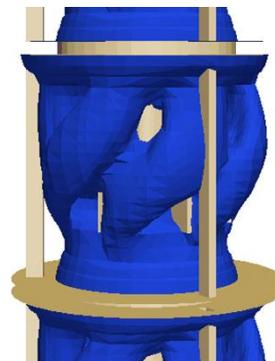
DN32 Original   DN32 Modified

Figure 7.34: Phase fraction inside the Kühni DN32 column (left) and the modified Kühni DN32 column with stirrer level at 1/3 of the compartment height (right).
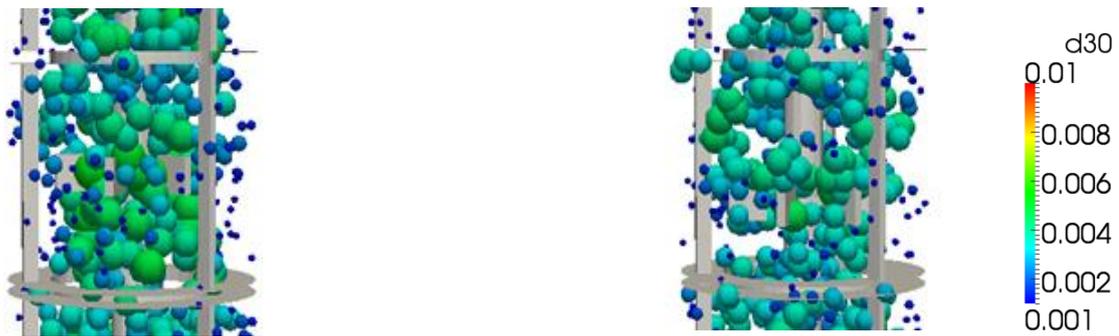
DN32 Original   DN32 Modified

Figure 7.35: Droplet size inside the Kühni DN32 column (left) and the modified Kühni DN32 column with stirrer level at 1/3 of the compartment height (right).

7.10 Mass Transfer Simulations of a Full RDC Column using FLUENT

The liquid-liquid extraction column hydrodynamics were widely investigated for an RDC with the use of computational fluid dynamics (CFD) (Modes & Bart, 2001, Drumm, 2010). Main researchers focused on the determination of the flow field and hydrodynamic parameters. A two-fluid model is mainly used for the calculation, due to the fact that the numerical effort compared to other models as the volume of fluid model (VOF) is low and allows the simulation of large scale columns and reactors. The droplet itself is not resolved and only accounted by a parameter and even so, the complex droplet interactions cannot be resolved. In the past, droplet population balance modelling allowed the consideration of droplet breakage and droplet coalescence by introducing additional transport equations for each section of droplet sizes (class method) or additional moments for the calculation of the droplet size (d_{30}, d_{32}). A good estimation of the droplet size could be obtained by the determination of coalescence and breakage parameters for the coalescence and breakage terms. A first simulation of a pilot plant extraction column was done by Drumm et al. (2010) and resulted in a good prediction of the droplet size with a simplified one group model, the one primary one secondary particle method (OPOSPM).

The main point in the determination of the efficiency of the extraction column, the mass transfer, was neglected until now for the three dimensional simulation of liquid-liquid columns. Mass transfer combined with CFD simulations were mainly performed for stirred vessels (Laakonen, 2006, Gimbun et al., 2009), where mass transfer is described by the two-film theory. A wide experimental investigation of mass transfer in liquid-liquid extraction columns was performed by Garthe (2006), who investigated the concentration profile, the droplet size and the phase fraction along the column height of a pilot plant column with different internals (RDC, Kühni, PSE, PESP). The simplest column geometry for modelling is the RDC geometry, that basically can be modelled as a two dimensional rotational symmetrical case and compared to the other

column geometries, dramatically decreases the numerical effort. Two different liquid-liquid systems were used by Garthe (2006) that were recommended by the European Federation of Chemical Engineering (Mísek et al., 1984): toluene/water/acetone as a system with a high interfacial tension and butyl acetate/acetone/water as a system with low interfacial tension.

A combined simulation of the hydrodynamics, droplet size and mass transfer enables the engineer to draw conclusions about the efficiency of the investigated liquid-liquid extraction column. The used CFD/OPOSPM code is further extended by two species transport equations, one for each phase:

$$\frac{\partial \alpha \rho_i Y_i}{\partial t} + \nabla \cdot \left(\alpha \rho_i Y_i U_\varphi \right) = \alpha \rho_i \nabla D \nabla Y_i + \rho_t S_m \qquad \textbf{(7.7)}$$

The diffusion D is given by the laminar diffusion coefficient and the turbulent diffusion:

$$D = D_{diff} + \frac{\mu_t}{Sc_t} \qquad \textbf{(7.8)}$$

where the turbulent Schmidt number Sc_t is set to 0.7 (Konstantinov & Kuznechikov, 1974). The transferred mass between the phases is accounted by the source term on the right hand side of the equation. The source term is based on the two film theory and includes the local diameter of the droplet as well as the local phase fraction:

$$A = \frac{6\alpha}{d_{30}} \qquad \textbf{(7.9)}$$

In addition, the densities of the mixture are calculated for each phase:

$$\rho_i = \rho_{i,0} \cdot (1 - Y_i) + \rho_t \cdot Y_i \qquad \textbf{(7.10)}$$

In addition, the interfacial tension is accounted by the EFCE equation (Mísek et al., 1984) for the system toluene/acetone/water:

$$\sigma = 0.001 \cdot \left(\frac{sa0 + sa1 \cdot sa + sa2 \cdot (sa)^2 + sa3 \cdot (sa)^3}{1 - sa4 \cdot Y_c \cdot sf} \right) \qquad \textbf{(7.11)}$$

with

$$sa = Y_c \cdot sf - sxp \qquad \textbf{(7.12)}$$

The change in viscosity can also be accounted by the mixture viscosity given in Eqn. 7.13 or any other known correlation.

$$\mu_i = \mu_{i,0} \cdot (1 - Y_i) + \mu_t \cdot Y_i \qquad\qquad\qquad \textbf{(7.13)}$$

A coupling with PBM leads to a further improvement of the simulation accuracy by a continuous exchange of the hydrodynamics parameters（velocity, phase fraction）, the liquid-liquid properties（interfacial tension, viscosities, densities）and the concentration in each phase（Figure 7.36）.
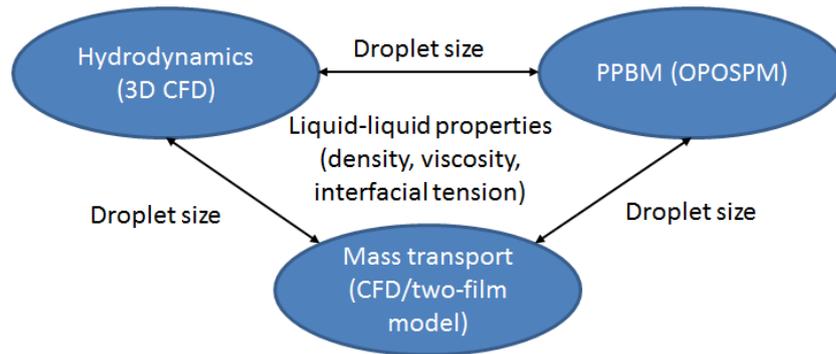
Figure 7.36: Continuous exchange between the hydrodynamics, PPBM and mass transfer influencing the liquid-liquid properties.

7.10.1   Comparison Between the Mass Transfer Models

In a first step, the different mass transfer coefficient models were compared in a test case for constant droplet size along the column height. The simulations were performed using the commercial CFD code FLUENT 12.0 and the mass transfer equations were implemented as user defined functions. The dimensions of the used RDC column represent the dimensions of the pilot plant column, which was experimentally investigated by Garthe（2006）. Due to the rotational symmetry, the column can be represented by a two dimensional mesh.

Table 11: Principle dimensions of the RDC column used by Garthe (2006).

Dimension	Symbol	Value
Column height	H	4400 mm
Column diameter	D_c	80 mm
Active height	H_a	2650 mm
Compartment height	H_c	50 mm
Stirrer Diameter	D_R	45 mm
Free inner stator area	φ	40%
Diameter shaft	D_S	10 mm

7.10.1.1. Mesh Generation

The numerical grid was built using the pre-processor GAMBIT and consists of 46 896 numerical hexagonal cells with a cell spacing of two millimetres. The shaft and the stirrers are defined by a rotating velocity boundary condition of 200 rpm. The column stators and column walls are defined by the wall boundary condition. At the bottom of the column, the boundary condition is set to the velocity inlet boundary condition for the dispersed and continuous phase and at the top of the column, a pressure boundary condition was chosen. The volumetric flow rate of the continuous phase is set to 40 l/h and the flow rate of the dispersed phase is 48 l/h. Garthe (2006) measured for the specific conditions a droplet size of 3.1 mm at the first measurement position, a droplet size of 3.0 mm at the second position and a droplet size of 2.6 mm at the third position. The average measured phase fraction was 7.1%. Due to the constant droplet size over the column height, the droplet size was set to a constant value of 3 mm. The concentration of the continuous phase inside the column was set to the concentration of the continuous phase inlet boundary (5.68%). The concentration of the dispersed phase inside the column was set to zero. The concentration of the dispersed phase at the inlet was set to the measured value (0.10%) of Garthe (2006). The concentrations at the outlet of the column were set to zero gradient by the use of a UDF.

A single compartment is depicted in Figure 7.37. For the comparison of the mass transfer model and the long expected simulation time, the mesh was not further refined which may result to slight deviations in hydrodynamics. Five measurement positions are defined according to the measurement positions chosen by Garthe (2006) for later comparison of the results.
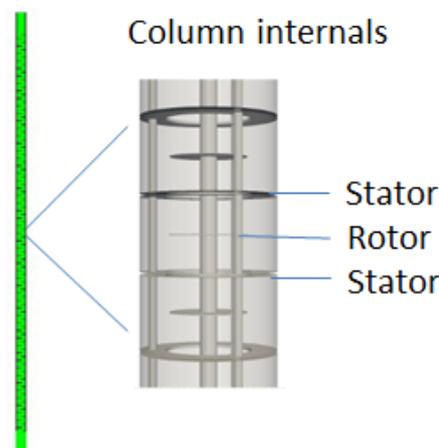
Figure 7.37: Mesh showing a single compartment of the investigated RDC DN150 column.

7.10.1.2.   Simulation Results

The simulations were performed for 5000 seconds using a time step of 0.01 seconds using
the mass transfer coefficient combinations. First, Kumar & Hartland (1996) for the dispersed and
continuous phase mass transfer coefficient. The second model combination consists of the model
of Kronig & Brink (1950) for the continuous phase mass transfer coefficient and Pilhofer &
Mewes (1979) for the dispersed phase mass transfer coefficient. The fourth and fifth combination
is given by the models of Kronig & Brink (1950) & Laddha (1974) and the combination of
Garner & Tayeban (1960) & Laddha (1974), respectively.

The simulation results of the average phase fraction in the active height of the column are
compared to the experimental value of Garthe (2006) in Table 12. Due to the use of a
constant droplet size of 3 mm, the phase fraction between the simulations is only dependent on
the change in density and viscosity. Hence, also from the simulation with the different mass
transfer models, the simulations show a good accordance to each other where the simulated
phase fraction is around 4% higher than the experimental value.

Table 12: Average phase fraction of dispersed phase in the active column height.

	Meas.	Laddah / Kronig & Brink	Pilhofer & Mewes / Kronig & Brink	Kumar & Hartland	Laddah/ Garner & Tayeban
Phase fraction	7.1%	7.45%	7.44%	7.44%	7.43%

The concentration profiles along the column height are compared to the experimental results of
Garthe (2006) in Table 13 for the continuous and in Table 14 for the dispersed phase. The
highest mass transfer can be observed using the overall mass transfer model combination from
Laddah and Pilhofer & Mewes. The second highest mass transfer is observed by using the
combination of Laddah and Garner & Tayeban followed by the model combination of Pilhofer &
Mewes and Kronig & Brink. However, the concentration deviation at the outlets of each
simulation is in the range of the measurement accuracy.

Table 13: Acetone concentrations in the continuous phase along the column height compared to experimental values of Garthe (2006).

	Meas.	Laddah / Kronig & Brink	Pilhofer & Mewes / Kronig & Brink	Kumar & Hartland	Laddah/ Garner & Tayeban
Top	5.68	5.66	5.68	5.67	5.67
Pos. 3	5.38	5.26	4.88	5.13	5.1
Pos. 2	4.86	4.50	4.07	4.37	4.3
Pos. 1	2.99	2.76	2.29	2.86	2.59
Bottom	1.92	1.2	1.81	1.95	1.63

Table 14: Acetone concentrations in the dispersed phase along the column height compared to experimental values of Garthe **(2006).**

	Meas.	Laddah / Kronig & Brink	Pilhofer & Mewes / Kronig & Brink	Kumar & Hartland	Laddah/ Garner & Tayeban
Top	3.95	4.50	4.26	3.82	4.32
Pos. 3	3.62	4.10	3.47	3.25	3.75
Pos. 2	3.06	3.40	2.66	2.50	2.97
Pos. 1	1.52	1.66	0.87	1.01	1.26
Bottom	0.1	0.1	0.1	0.1	0.1

Further FLUENT simulations at different boundary conditions in combination with population balance modelling were published in Hlawitschka & Bart (2012b) and Jildeh et al. (2012b). The resulting phase fraction, velocity field and droplet size of a combined CFD/PBM mass transfer simulation is depicted in Figure 7.38. Due to the tremendous increase in computational cells by using more complex column as it is the case for the Kühni miniplant column, the use of the OpenSource Code OpenFOAM in combination with a high performance cluster is necessary.
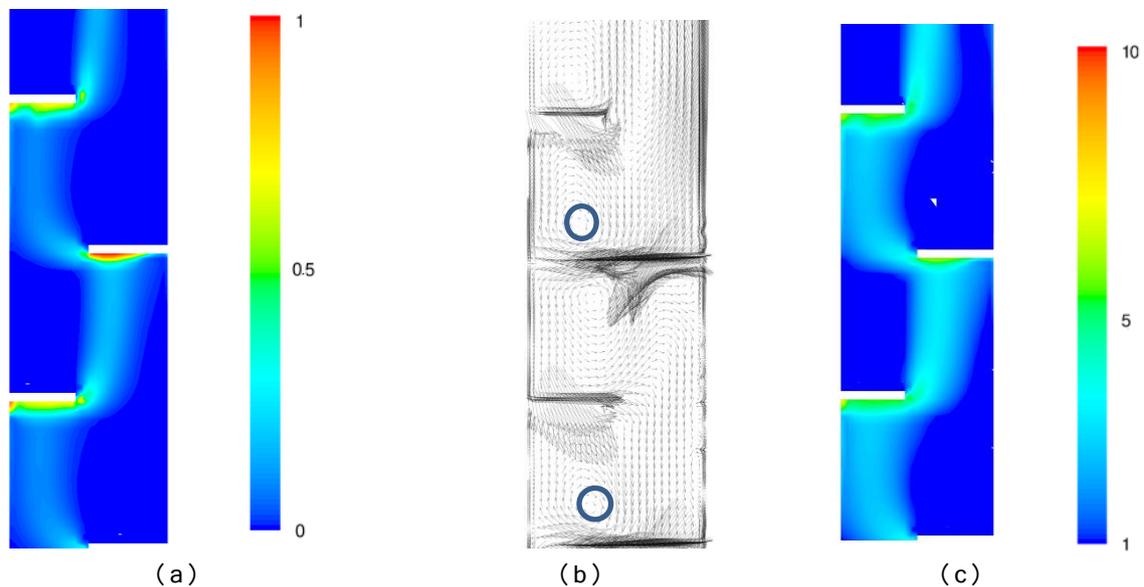
Figure 7.38:   CFD simulations at the top of the extraction column for: (a) phase fraction (–), (b) continuous phase velocity (m/s) and (c) droplet size (mm) (Jildeh et al., 2012b**).**

7.10.2 Computational Time Including PBM for Complex Mass Transfer Simulations

The presented simulated hydrodynamics in combination with population balance modelling showed a good agreement to measurements and can help to improve the layout of liquid-liquid extraction columns. However, the efficiency of a stirred extraction column is essentially characterized by the mass transfer, which has an impact on the fluid properties as viscosity, density and interfacial tension and hence influences the hydrodynamics and droplet size inside the column. This highly coupled system can only be accurately solved by combining the hydrodynamic equations to droplet population balance modelling and mass transfer. Therefore, first simulations using the commercial CFD code FLUENT were done. For more complex cases as the Kühni miniplant column, a deeper study of the computational time is required.

From a computational point of view, the required computational resources rises due to additional equations and a dramatically increased time to steady state compared to a single hydrodynamics calculations. A first estimate of the required computing time can be met on the basis of the results of Drumm (2010) who investigated different population balance models for the simulation of a full pilot plant RDC column using the two dimensional rotational symmetry as simplification. The simulations were performed with the simulation tool FLUENT (v6). Using the pure hydrodynamics simulations, a single time step required 32 seconds on a single core 3GHz processor. For the simulation with the QMOM for accounting the changing droplet size along the column height, the required computational time was doubled (64 seconds) compared to the pure hydrodynamics simulations (Figure 7.39). The highest computational time could be observed using the class method with (160 seconds). A reduction of the computational time could be reached using the one group model OPOSPM, where only a slight increase of the computational time compared to the hydrodynamics simulation could be observed (34 seconds). For the steady state of the hydrodynamics simulations, 4000 time steps at a time step size of 0.05 seconds were simulated which resulting in a required computational time of 36 hours for the pure hydrodynamics simulations. For mass transfer, approximately 20 minutes have to be simulated for the convergence of mass transfer resulting in a computational time of at least 8.8 days without accounting droplet size and mass transfer equations. For complex three dimensional cases, as the Kühni miniplant extraction column, the required number of mesh cells further increases. In the case of a five compartment section with in- and outflow zones, the used mesh size was 500 000 cells. The simulations were performed with FLUENT (v12) on a quad core AMD Phenom II X4 965 processor with 2.8Gb DDR2 RAM. The results show a decrease of the computational time from 140 s per time step using the QMOM to 84 s using the OPOSPM. The pure hydrodynamics simulation requires 80 s per time step, which is only four seconds less than using the one group population balance model for accounting the droplet interactions. A further

reduction of the simulation time could be achieved by using the presented OpenSource code on the cluster of the University of Kaiserslautern. The use of the OpenSource code in combination with the used hexagonal mesh generated by the own developed GUI allowed the simulations of full of mini plant and pilot plant columns using parallelization.
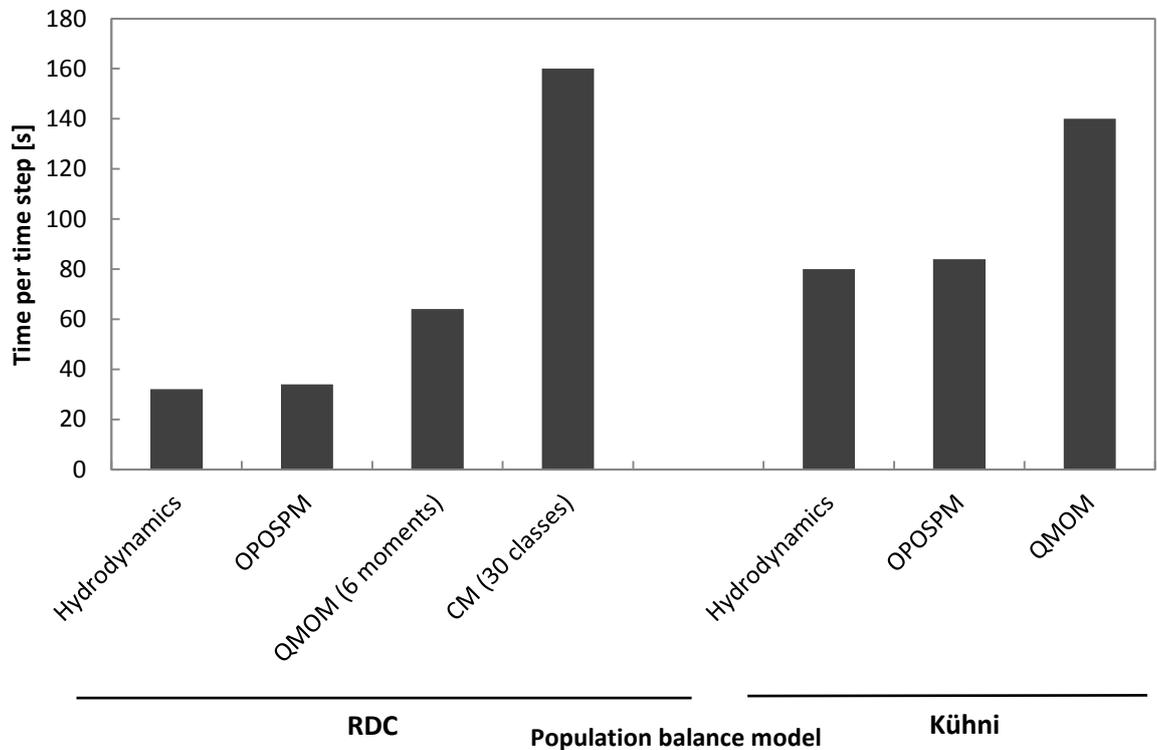
Figure 7.39: Computational time required for the simulation of the RDC column and the Kühni column using different population balance models.

7.11 Simulation of a Full Kühni Miniplant Column

For the mass transfer simulation of a Kühni miniplant extraction column, the OpenSource based CFD/PBM code was extended by the presented mass transfer equations. However, due to the low concentrations, the change in viscosity is neglected in the further simulations and accounted by a constant value. The simulated column consists of 50 repeating compartments and two zones which are used as the inflow and outflow zones and was generated using the presented m4 script. The boundary conditions for the simulation of the Kühni miniplant column correspond to the experimental work. The flow rate was set to 6 l/h dispersed phase (toluene) and 5 l/h continuous phase (water). The rotational speed of the stirrer is set to 200 rpm. Turbulence is accounted by the mixture $k-\varepsilon$ turbulence model. The concentration in the dispersed phase is set to zero at the bottom of the column and the concentration of acetone in the continuous phase is set to 5-wt% at the top of the column. The change in droplet size is accounted by the use of the mixed model, where the Batchelor constant in the breakage model

was set to 30. For the calculation of the overall mass transfer coefficient, a combination of the model from Kronig & Brink (1950) for the continuous phase mass transfer coefficient and the model from Handlos & Baron (1957) for the dispersed phase mass transfer coefficient is used to determine the overall mass transfer coefficient.

The concentration profile of the continuous and dispersed phase obtained from the simulation is shown in Figure 7.40. The concentration profiles are non-linear along the column height where the continuous phase concentration decreases from the top of the column to the bottom of the column and the dispersed phase concentration increases from the bottom of the column to the top of the column.
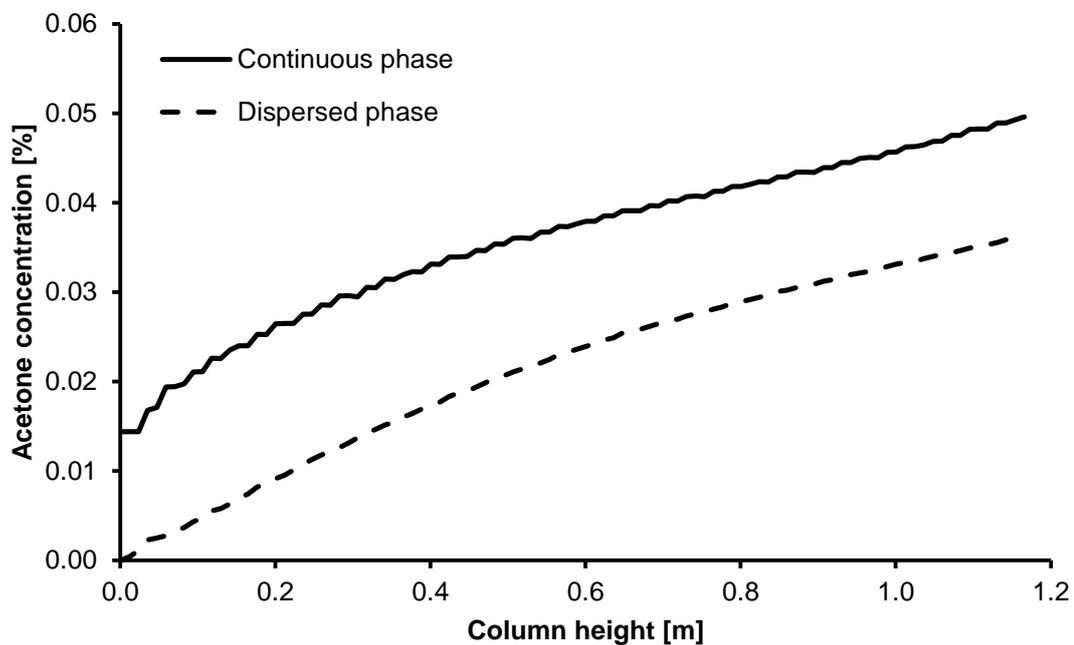
Figure 7.40: Simulated acetone concentration in the continuous and dispersed phase along the column height.

Due to the mass transfer of acetone from the continuous to the dispersed phase, the interfacial tension between the two phases changes. In this case, a decrease of the interfacial tension can be observed from the bottom of the column to the top of the column leading to a change of coalescence and breakage kernels (Figure 7.41). The density of the continuous phase increases from the column top to the bottom of the column, where only a slight change of the dispersed phase density can be observed due to the similarity of the toluene and acetone densities (Figure 7.42).
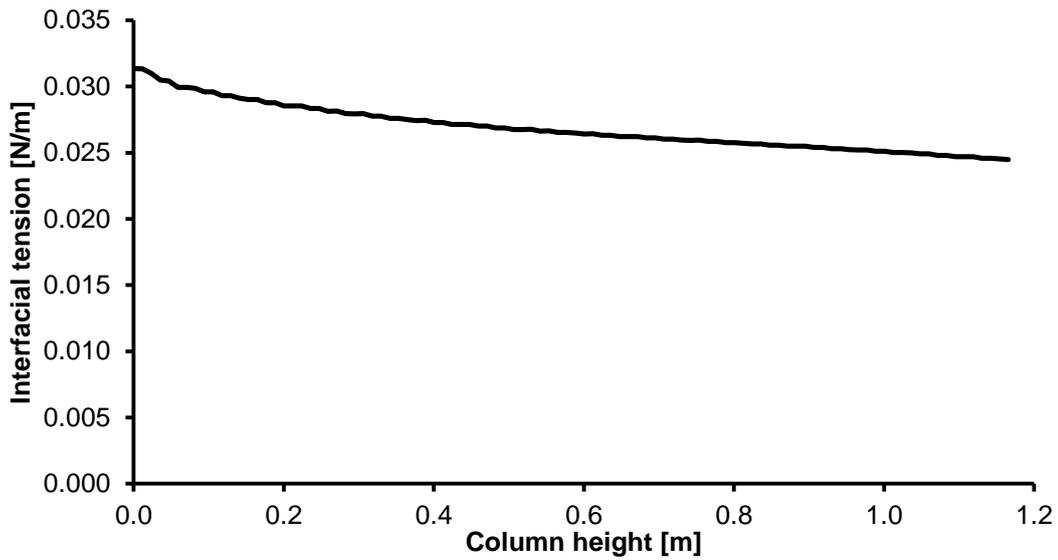
Figure 7.41: Interfacial tension between the aqueous phase (water/acetone) and the organic phase (toluene/acetone) along the column height of the DN32 miniplant column.
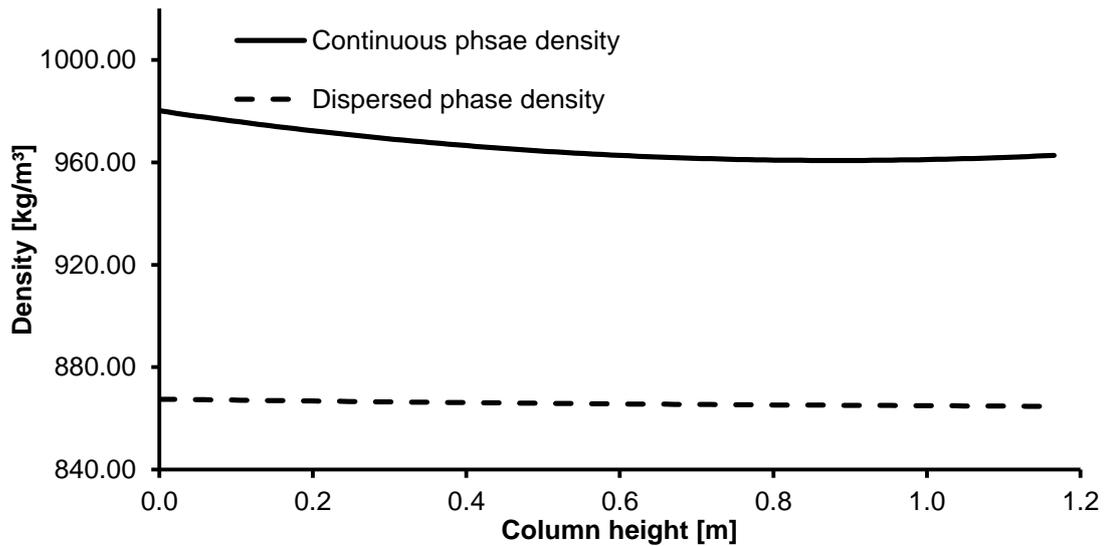
Figure 7.42: The change in phase density along the column height of DN32 miniplant column.

In addition, the droplet size development is shown along the column height for the position (0.01, 0.0, column height (H)) in Figure 7.43. The droplet size increases due to accumulation underneath the stators and decreases due to energy input of the stirrer in each compartment. To reduce the fluctuations in the figure, the droplet size was averaged for each compartment. The simulated outlet droplet size (3.80 mm) fits to the measured droplet size at the outlet (3.85 mm) where for the specific location of (0.01, 0.0, H) a slightly higher average droplet size (4.3 mm) is predicted then the one obtained by the measurement (3.85 mm).
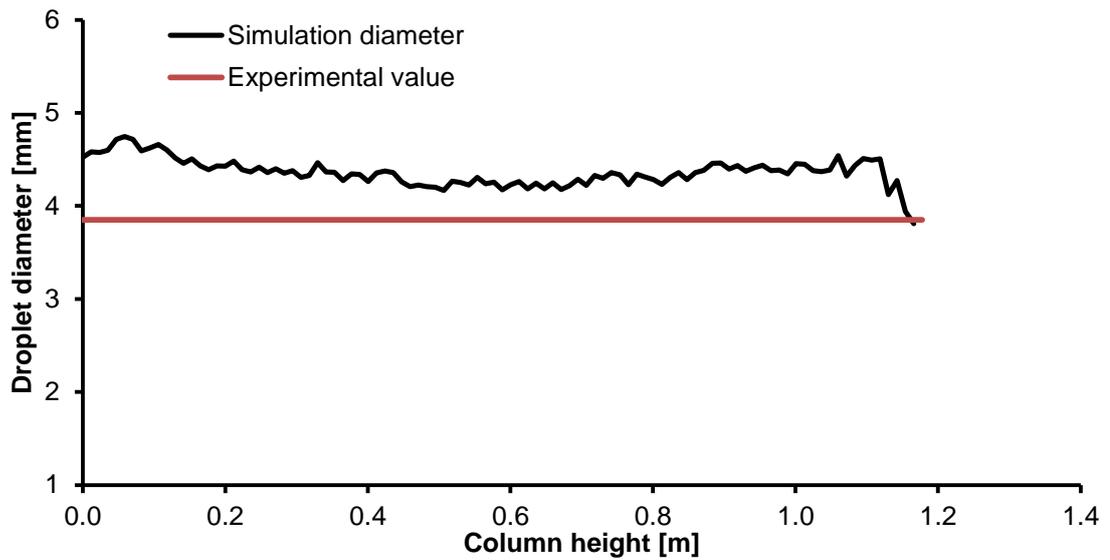
Figure 7.43: Droplet size along the column height at position (0.01, 0.0, H) compared to the average droplet size measured at the top of the column.

The resulting mass transfer is finally compared to own experimental results in Figure 7.44. The simulation results of the dispersed and continuous phase depicts the experimental results in good agreement accounting the standard deviation of the mass transfer correlations of 30% to experimental data.
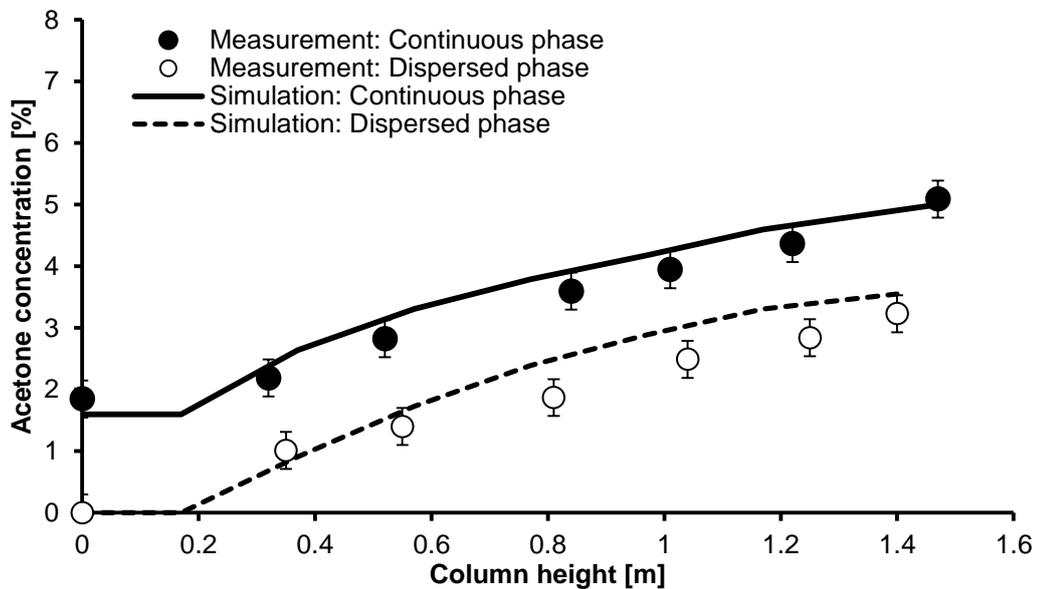
Figure 7.44: Simulated acetone concentration compared to the measured acetone concentration along the column height.

7.12 From 3D to 1D Simulation

The complex interactions of the droplets and the hydrodynamics (backmixing, wall effects, etc.) made a design and layout of liquid-liquid extraction columns a challenging task. For 1D axial dispersion models combined with population balance modelling, an set of experimental correlations (e.g. axial dispersion coefficient, energy dissipation, droplet rise velocity) are required to account for these interactions and to obtain an accurate result of the concentration profile along the column height.

In contrast to this, this worked proved that a 3D-CFD is able to predict these correlations for different column designs. A combination of 3D-CFD and 1D-CFD seems to be straight forward to reduce experimental effort for the 1D simulation and on the hand to reduce the computational time for mass transfer simulation. The concept of this multi-scale modelling is depicted in Figure 7.45 and is presented in Bart et al. (2013).
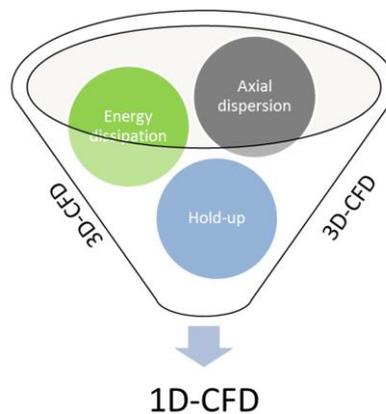
Figure 7.45: From 3D simulation to 1D simulation using numerically determined correlations.

As an example, the result of the mass transfer simulation using the 1D simulation tool PPBLAB (Attarakih et al., 2012) is shown in Figure 7.46. As boundary conditions, a total flow rate of 18.7 m³/m²/h was chosen at a rotational speed of 200 rpm. The simulation thereby uses the correlations for axial dispersion coefficient of the dispersed and continuous phase, which were determined by 3D CFD simulations in this work. In addition, the used energy dissipation correlation was validated using the 3D simulation. Hence, a perfect fit of the acetone concentration in the continuous and dispersed phase could be observed compared to own measurements. In addition, the mass transfer simulation using the 1D simulation tool was performed within minutes, where the CFD required still weeks to reach steady-state. On the other hand, the CFD/PBM/mass transfer simulation gives local information about the hydrodynamics, droplet size and their influences to the mass transfer. Further results at different boundary conditions are reported in Bart et al. (2013).
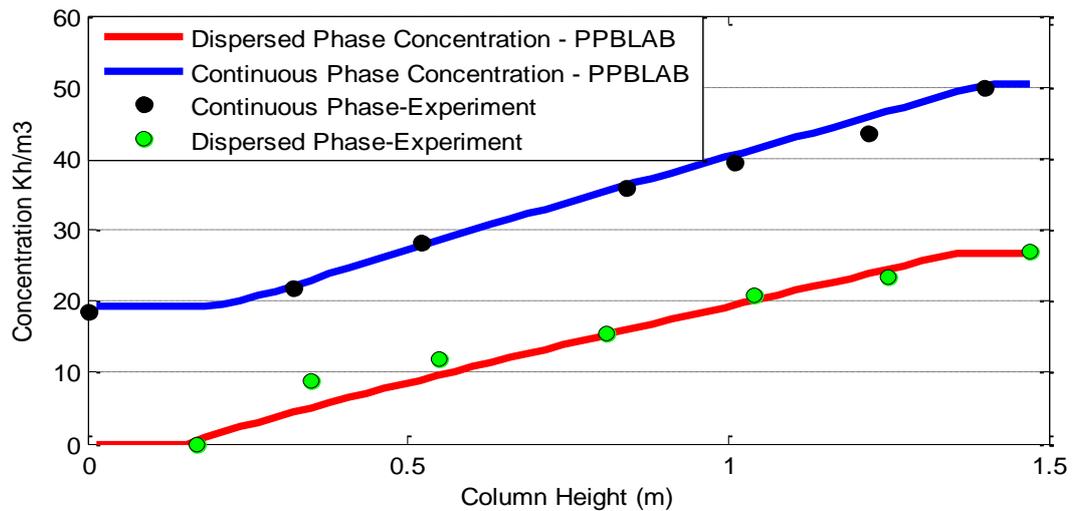
Figure 7.46: Comparison between the measured concentration profile and the PPBLAB simulation for 200 rpm and a throughput of 18.7 m³/m²/h (Bart & Hlawitschka et al., 2013).

7.13   Multiple Discrete Phases Modelling – SQMOM

The energy input in liquid-liquid extraction columns generates a homogenous droplet size close to the stable droplet diameter. Accumulation underneath the stators resulting in a generation of larger droplets and satellite droplets generated by droplet breakage events lead to polydispersity of the droplets (Figure 7.47).
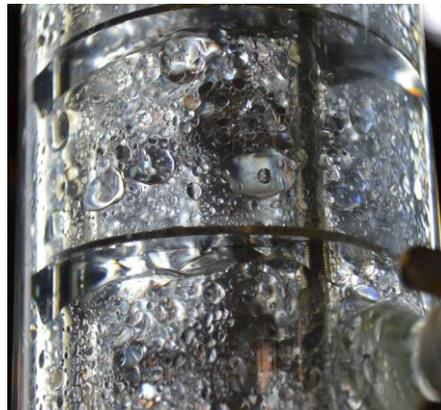
Figure 7.47: Polydispersity due to accumulation of droplets underneath the stators resulting in new droplet dispersion and droplet rise.

The SQMOM developed by Attarakih et al. (2009a) is an efficient method to account for droplet size changes between two and more droplet sizes calculated in each cell. In combination with the OpenSource CFD tool, the higher computational effort of the model can be compensated by increased computational resources.

The twoPhaseEulerPimpleFoam code was extended based on the multiphaseTransport and multiphaseTurbulence libraries (Chevalier, 2010) which allow the simulation of more than one Eulerian dispersed phase. The SQMOM implementation in OpenFOAM strictly follows the implementations done by Drumm (2010) into the commercial CFD code FLUENT. The rectangular test case is simulated for a constant droplet size of 2 mm using only one primary particle and two secondary particles. The result of the simulation at a constant breakage rate of 0.05 1/s perfectly fits to the analytical solution given in Eqn. 7.5 (Figure 7.48).

In a next step, two primary particles are used to simulate the droplet size at constant breakage. The used particles have a size of 2 mm and 4 mm and interact due to a constant breakage rate of 0.05 1/s. The phase fraction is set to 0.05 at the start of the simulation for each phase. Due to the interaction between the primary particles, the phase fraction of larger droplet size (phase 2) decreases with time, where the phase fraction of the primary phase increases (Figure 7.49). However, the overall phase fraction is conserved by the solver, where the sum of alpha is constant over time.
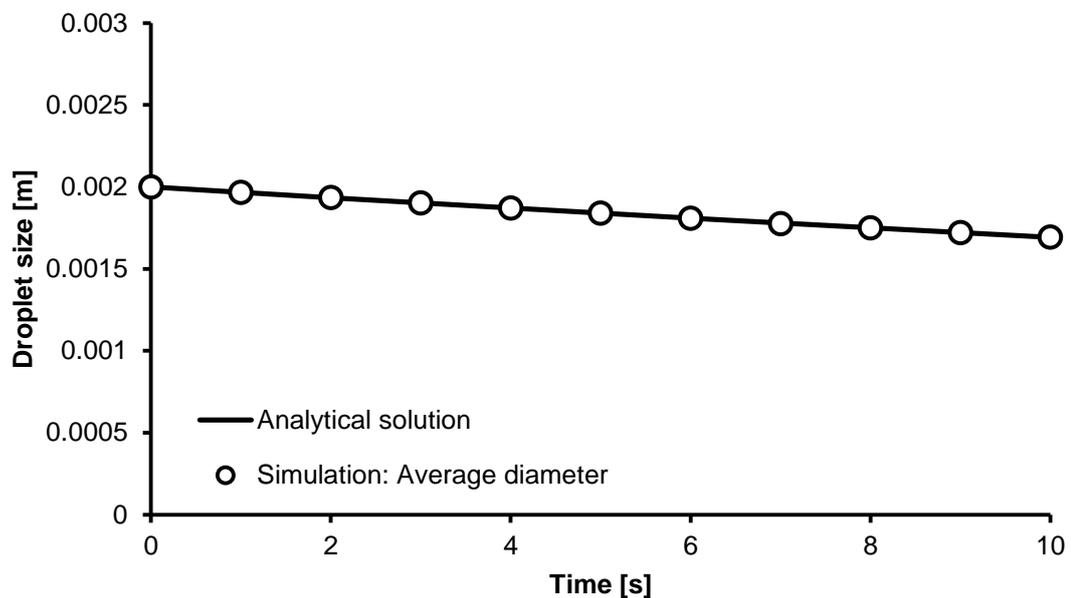
Figure 7.48: Droplet size development using only one primary particle at a constant breakage rate of 0.05 1/s.
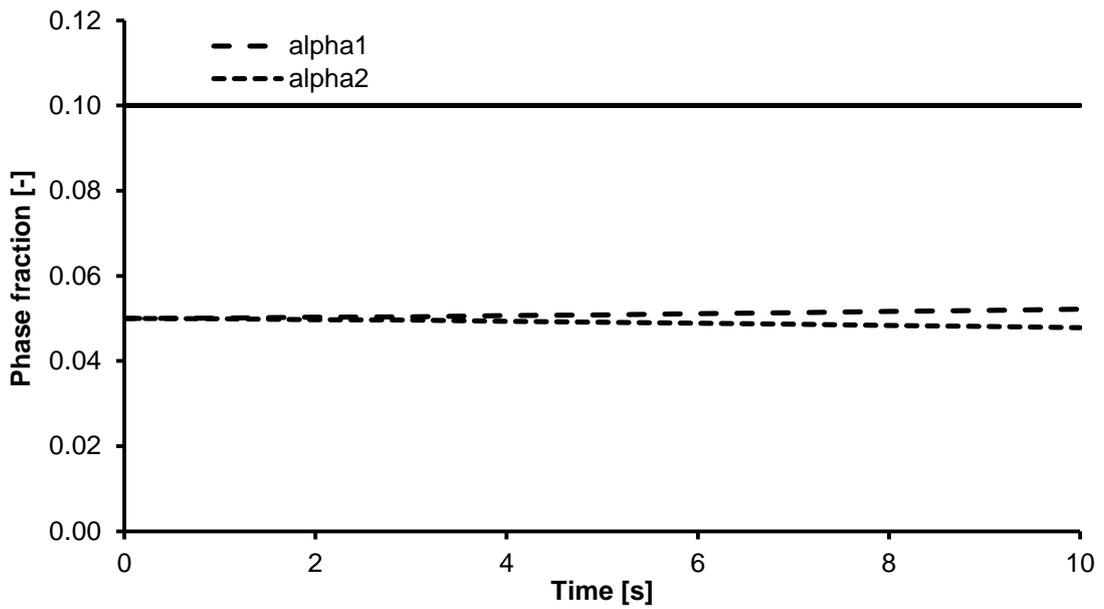
Figure 7.49: Development of the phase fraction due to interactions between the primary particles.

The droplet size of each phase decreases over time (Figure 7.50). The average droplet size follows the trend of the analytical solution by increasing the resolution of the distribution compared to the OPOSPM. Also at higher breakage rates of 0.2 1/s, the simulation fits to the analytical result Figure 7.51.
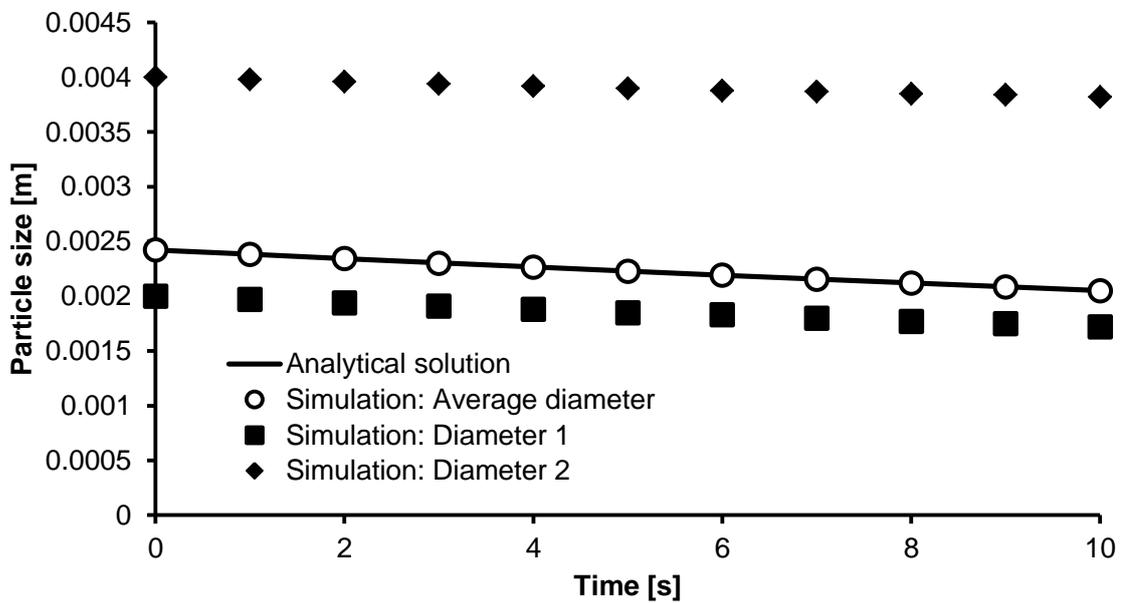
Figure 7.50: Droplet size (d30) development due to the constant breakage kernel of 0.05 1/s in each class and comparison of the average droplet size to the analytical solution.
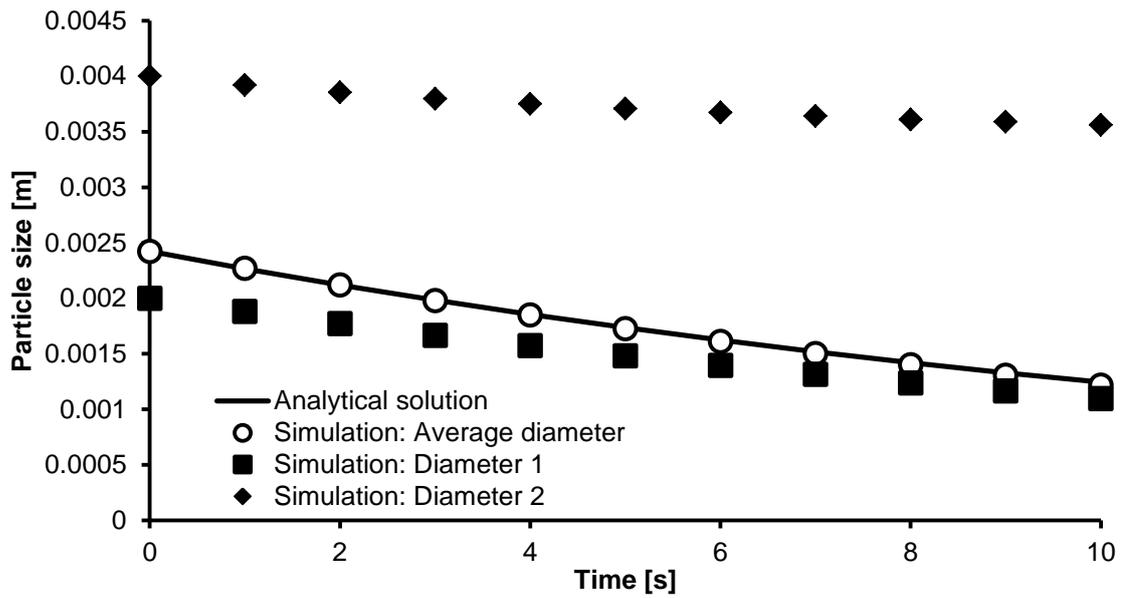
Figure 7.51: Droplet size (d30) development due to the constant breakage rate of 0.2 1/s in each class and comparison of the average droplet size to the analytical solution.

The result at a constant source term of 1E-8 is shown in Figure 7.52. The sizes of each class increases by time. The average diameter is in good agreement with the analytical solution, where slightly higher values can be observed.
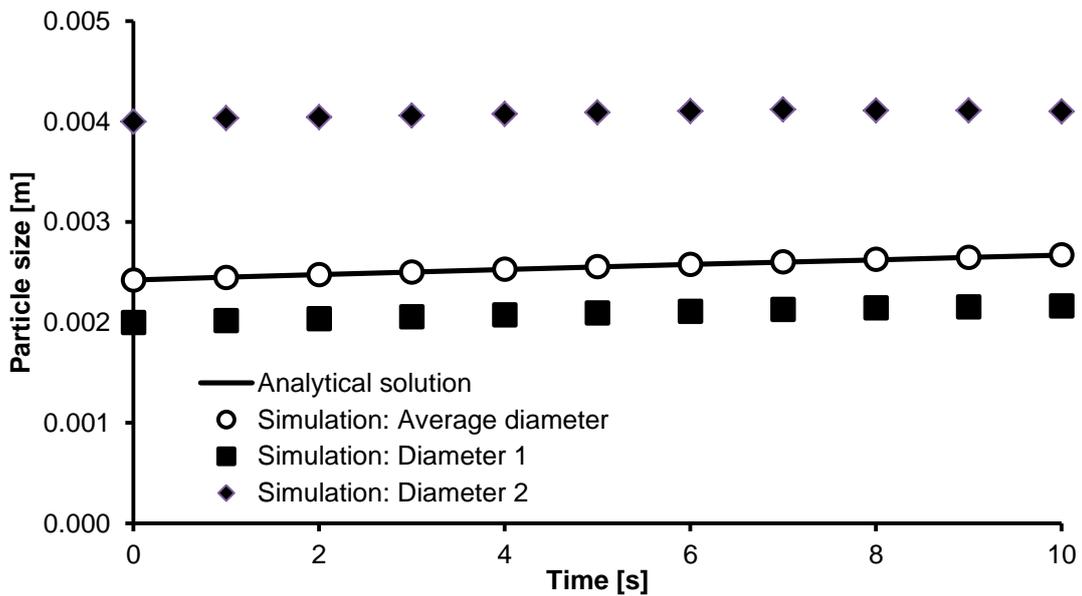
Figure 7.52: Droplet size (d30) development due to the constant coalescence kernel of $1E^{-8}$ m^3/s in each class and comparison of the average droplet size to the analytical solution.

In a next step, the OpenSource CFD/SQMOM solver is compared to FLUENT/QMOM simulations performed by Drumm (2010).

7.13.1   Simulation of an RDC Column using the SQMOM-Three Fluid Model

The use of multi-fluid models in combination with CFD enhances the accuracy of the simulation, especially when a wide droplet size distribution is present. To show the differences in flow behaviour between smaller droplets and larger droplets in extraction columns, a five compartment section is simulated using the three fluid model in combination with SQMOM. The droplet size at the inlet is set to 2 mm and 4 mm. A constant breakage rate of 0.2 1/s with binary breakage is used. The hydrodynamics boundary conditions are a stirring speed of 150 rpm and flow rates of 50 l/h continuous phase and 100 l/h dispersed phase. The volumetric flow rate ratio between the phases is set to 1. As turbulence model, the k-ε-mixture model is used. The interactions between the continuous phase and each dispersed phase and is coupled separately. It can be seen from Figure 7.53, that the smaller droplet size show a higher distribution inside the compartment then the phase with larger droplets. Also the phase fraction of the smaller droplet size phase is higher resulting from a lower droplet rise velocity and hence a longer retention time of the droplets inside the column.

Phase fraction of dispersed phase 1

Phase fraction of dispersed phase 2

Droplet size of dispersed phase 1

Droplet size of dispersed phase 2
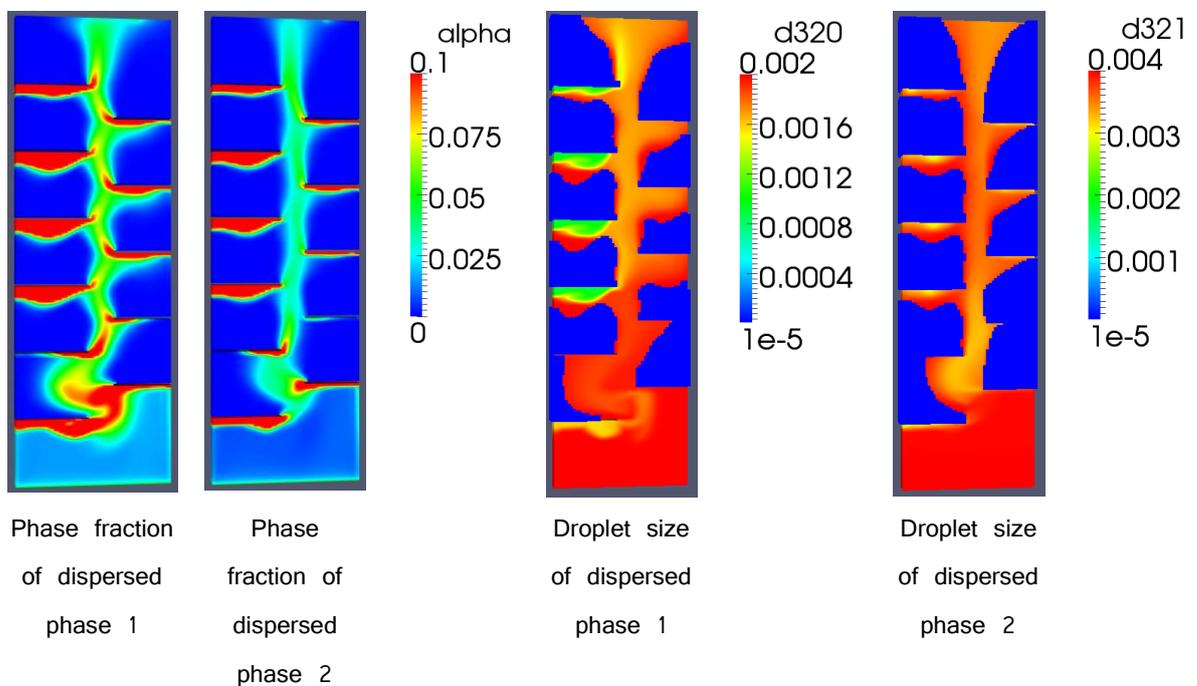
Figure 7.53: Phase fraction and droplet size in meter of each phase in a five compartment section of an RDC DN150 column at constant breakage kernel using the SQMOM model.

8   Visualization

The visualization of Eulerian multiphase flow simulation data lacks due to the description of the phases as interpenetrating continua where the droplet size is decoupled from its position and the dispersed phase fraction. Until now, it was mainly possible to either investigate the droplet size represented by scalar values as a point source, plotted over a line, on a plane or as isosurface.

In a joint work with the Computer Graphics and HCI Group, a novel approach for visualizing Eulerian multiphase fluid simulations based on a stochastic modelling combining the information of phase fraction and droplet size was developed (Hlawitschka et al., 2011). The following description is based on the publication.

For every time step, the number of droplets N and the diameter of the droplets in each cell can be described by a homogeneous distribution function for the droplet center $[p(x),\ p(y),\ p(z)]$:

$$p(x) = \begin{cases} \dfrac{1}{x_{cellmax} - x_{cellmin}} & if\ x_{cellmin} \leq x \leq x_{cellmax} \\[2mm] \\ 0 & otherwise \end{cases}, \qquad (8.1)$$

The number of droplets N is given by the following equation:

$$\sum N \cdot V_{every\ Droplet} = \alpha \cdot V_{cell\ volume} \qquad (8.2)$$

The droplets are positioned in such a way, that overlapping droplets are not allowed. For example, a visualization of the data set from a Kühni miniplant column simulation is given in Figure 8.1 for a time sequence of the inflow of dispersed phase into the column section.

A further development to achieve a visualization of the droplet movement including breakage and coalescence determination. For the visualization of the movement of the droplets given in Figure 8.2, path-line based flow visualization is enhanced (Hlawitschka et al., 2011). Conventional path-line computation suffers by two aspects:

- Path-line hits a boundary and no longer continues.
- Path-line continuous even if a droplet vanishes.

<table>
<tr><td>a)</td><td>b)</td><td>c)</td><td>d)</td></tr>
</table>
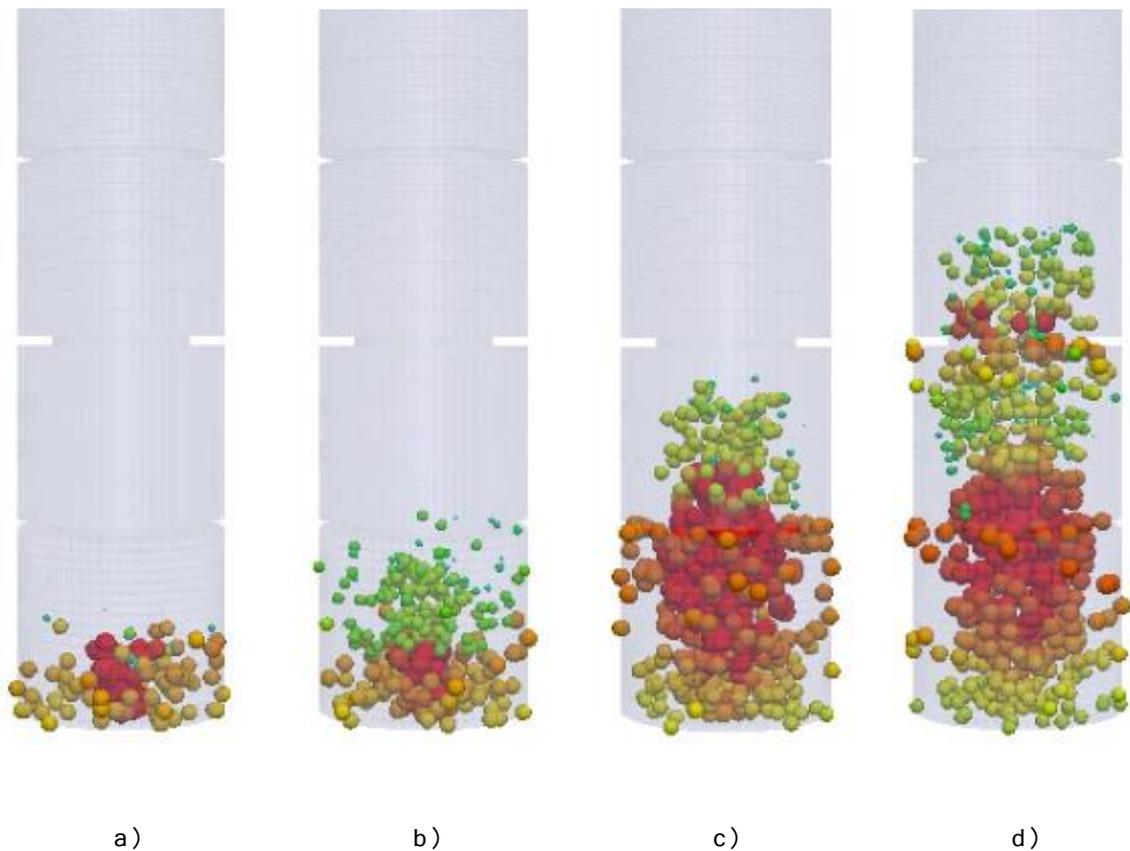
Figure 8.1:   Time sequence of droplets inside the extraction column (Chen, 2012).

Both points are counteracting the nature of the dispersed droplets in a counter-current flow. Especially the second point is important for process engineering experts, because it describes the change generation of new droplets（breakage）or loss of droplets due to coalescence are important for process engineering experts. In order to overcome these two points, the visualization of path-lines is extended by coalescence and breakage detection and a re-seeding near the boundaries：

- Re-seeding near the boundary： Interrupted path-lines close to the boundary （e.g. stirrer）start a new path-line in the neighbour of the interruption.

- Path-line termination after droplet interaction： A trace of a droplet ends after droplet coalescence or breakage to record the life span of the droplets. From this point on, new path lines can be generated to follow the path of the coalesced drop or the new daughter droplets.

The breakup detection is done using the following algorithm:

Algorithm 1: Adaptive path-line integration with breakup detection.

For each path-line do

  for $t = 0 \rightarrow t_i$ **do**

    if $d_i/d_{i+1} > \sqrt[3]{2}$ **and** $\alpha_i > \alpha_{threshhold}$

      then

        terminate current path-line integration,

        take a neighbouring point, start a new path-line

      end if

  end for

end for

---
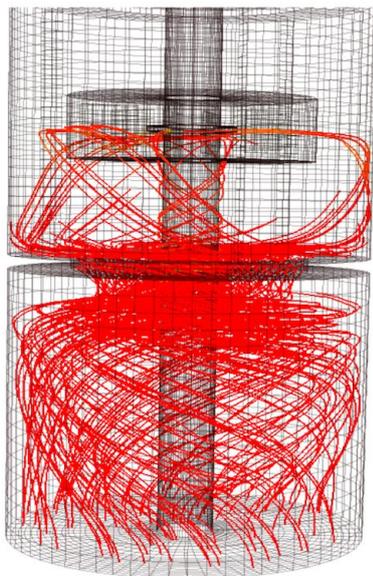
a）Straightforward path-line integration
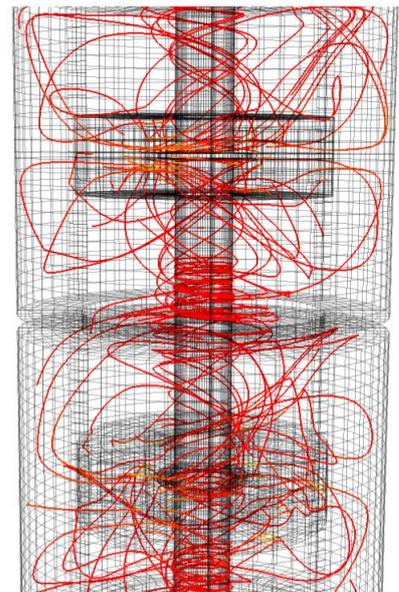
b） Path-lines with collision and bifurcation detection

Figure 8.2:   Comparison of straight forward integration method and the proposed particle reseeding method (Chen, 2012).

9   Conclusions

The design of liquid-liquid extraction columns is still based on empirical correlations for droplet velocity, energy dissipation, axial dispersion and hold-up. These correlations are geometrical dependent and only valid up to a column diameter of DN150, which makes experimental validation indispensable. Instead, Computational Fluid Dynamics simulations allow a description of the local flow field without geometrical constraints. Based on the numerical investigations of Drumm (2010) for a five compartment section of a two dimensional spartial discretized RDC column, an OpenSource CFD code was extended by population balance modelling and mass transfer equations allowing the simulation of the hydrodynamics, droplet size and mass transfer of full miniplant and pilot plant columns in a three dimensional framework (RDC DN80, Kühni DN32 and DN60).

The idea of this work was to develop a design methodology based on a combined CFD-PBM approach, which should predict the separation performance in any apparatus geometry without experimental input. Reliable "experiments in silico" (computer calculations) should give the engineer a valuable and user-friendly tool for early design studies at minimal costs.

The application of OpenSource software in this work enabled the simulation of complex geometries using high performance computing. The use of m4-scripts allow a mesh generation of different column layouts of full miniplant and pilot plant columns within minutes, which was only possible within hours at the beginning of this work. The setup of the simulations and the definition of the column geometry was further facilitated by a graphical user interface.

An Euler-Euler code was modified to fulfil the requirements for the existing two-phase liquid-liquid flow. The simulated hydrodynamics of different column designs were compared to own experimental and literature data. The results using the OpenSource code were in the range of the commercial CFD code FLUENT and compared to the experimental results, the OpenSource code showed even a better prediction of the flow field compared to the commercial CFD code. Breakage and coalescence heavily dependent on the turbulent energy dissipation inside the compartment. The used energy model for the OpenSource simulation was in good agreement to the commercial CFD code FLUENT. Furthermore, a good agreement between the experimental results and the correlations given in literature could be found. The local phase fraction at steady state was experimentally investigated by a LIF method. A deviation of the Kumar & Hartland (1995) correlation for the phase fraction and the measured phase fraction could be observed close to the flooding point. However, for rotational speeds below the flooding point, the correlation showed a good agreement to the experimental data. Instead, the performed CFD simulations could predict the phase fraction close to the flooding point. The axial dispersion coefficient of the continuous and dispersed phase was investigated using a Lagrangian solver

based on the steady state Euler-Euler flow fields. The simulated axial dispersion coefficient could predict the experimental results and also fitted to literature correlations. For the dispersed phase dispersion coefficient, only the correlation of Bauer & Widmer (1977) was in the range of the CFD results.

Based on the measurements and simulations, it has been shown, that the droplet size has an influence on the phase fraction and on the hydrodynamics in the liquid-liquid extraction column and therefore requires a consideration by population balance modelling. A one group model was combined with the validated CFD code and successfully tested against several numerical test cases. Simulations of modified column geometries were done, which indicate a better column performance by setting the stirrer to one third of the column height to improve the dispersion of the dispersed phase and to improve the final surface area of the droplets.

First simulations using the commercial CFD code FLUENT combined with mass transfer equations, based on the two-film theory, could predict the concentration profile along the column height of a pilot plant RDC column. For the simulation of complex geometries, the mass transfer equations were combined with the presented OpenSource CFD-population balance code. The simulation of a Kühni miniplant column indicated a good prediction of the concentration and droplet size along the column height. An application of the gained correlations as an input for one dimensional mass transfer simulations leaded to a perfect fit of the numerical obtained concentration profiles to experimental data at varied boundary conditions. The computational time to gain information about the concentration profile at steady state, can thereby be further decreased to minutes.

In conclusion, CFD combined with population balance modelling and mass transfer equations lead to a full description of liquid-liquid extraction columns and provides a huge step into the direction of a virtual laboratory. The presented user-friendly toolbox allows a generation of different geometrical designs within minutes and combined with the CFD/PBM/mass transfer code a description of the column performance. Yet, rotational speed independent coalescence and breakage parameters could only be found by inverse determination based on single swarm experiments. The whole tool can also be used for a computer aided scale-up of extraction columns and thereby is an efficient tool to investigate local phenomena and theirs dependencies on the column efficiency. The effect of hardly investigated systems on the hydrodynamics can be studied previous to the first operation for saving time, money and resources. Harmful systems can be studied without any risk for the environment and workers. Concerning mass transfer simulations, the used mass transfer coefficient models were investigated in this work for well-studied standard EFCE test systems. Further studies are required for more complex systems, including reactive liquid-liquid extraction systems. Polydispersed systems occurring in large scaled columns influence the accuracy of the one group model. The presented implementation of the SQMOM is able to overcome the problem of a one group model and therefore was implemented

in the CFD code. A first validation of the population balance code led to a good agreement compared to pure numerical analytics.

Further, in cooperation with the HCI Group of the University of Kaiserslautern, the visualization of Euler-Euler data sets was improved. Instead of the visualization of a single data set, the phase fraction and droplet size were combined to allow a realistic visualization of the droplet size and position. In a second part, a visualization of the droplet movement including breakage and coalescence determination was achieved, which gives the engineer the possibility to investigate not only the points and with high and low influence to the droplet size, but also the way of droplets to these points.

10 Outlook

The use of CFD for the layout of liquid-liquid extraction columns has been shown. A further improvement of the code in respect to coalescence and breakage as well as mass transfer models with less dependency on experimental parameters will lead to a better prediction of the hydrodynamics and the droplet size. The existing coalescence and breakage kernels are subject to previous single droplet or swarm experimental investigations. The kernels are still based on adjustable parameters for each chemical system due to a high influence of surfactants and impurities influencing the especially the coalescence of droplets. The parameters in this work were found based on a simple inverse problem solving in Matlab for several known droplet size distributions at the outlet. The inverse problem solving was enhanced for liquid-liquid by using 1D-CFD simulations (Jildeh et al., 2012a). A reasonable agreement could be found by using the optimized kernels from 1D for the 3D simulations (Jildeh et al., 2012b). A direct implementation of the inverse problem solving based on local experimental data into CFD will further improve the simulation results.

For the hydrodynamics, a better description of the wetting and coalescence by wetting behaviour is required to describe accumulation underneath the stator by CFD. A combination of the presented OpenFOAM/SQMOM solver with multivariate mass transfer equations leads to a better prediction of multivariate dispersed systems (e.g. reactive systems). With increasing computational resources, Euler-Langrange simulations should come into focus of computational investigations to keep the information of specific particle positions, particle interactions, particle agglomeration and particle concentration. The combination of different scales of simulation ranging from molecular modelling for the determination of diffusion coefficients, simulating the interfacial mass transfer for gaining advanced two film theory equations and finally the presented simulations of whole columns leads to a computational lab in the future, which is suitable to predict the performance of multiphase columns without the effort of experimental studies.

The visualization techniques need to be extended to provide more information about droplet deformation and droplet movement (residence time). An integration of mass transfer information will further provide information to identify locations with high and low mass transfer efficiency and will facilitate the optimization of the column design.

Besides the application of population balance modelling and mass transfer equations for liquid-liquid systems, the code can be transferred to account for gas-liquid, solid-liquid or solid-gas systems. Specific limitations as pressure differences on the air bubbles or limiting solid concentrations must be accounted for by additional equations.

11 Appendix

11.1 Dispersed phase – Velocity and Droplet Size

The hydrodynamics of dispersed phase system were hardly investigated inside liquid extraction columns. A PDA system is used to overcome this lack and provide principle data of the local droplet size above and underneath the stirrer and of the axial velocity at corresponding positions. The droplet size underneath the stirrer is higher than the one measured above the stirrer (Figure 10.1). Nevertheless, the measured values are far below the one obtained by e.g. Steinmetz (2007) resulting from a change of the measurement system. Steinmetz used an optical system to analyze the droplet size which was limited by a minimum droplet size of one millimeter. The occurrence of small satellite droplets circulating for a longer time in a single compartment than the larger droplets shifts the measured droplet size of the PDA system to smaller droplet sizes. The dispersed phase velocity obtained by simulations for different droplet sizes is further compared to the results of the PDA measurements (Figure 10.2). The experiments show a high deviation from each single experiment resulting from the previously discussed droplet accumulation underneath the stator rings and subsequent droplet rise. However, with the determined droplet size as input for the simulations, the axial velocity of the droplets could be predicted underneath the stirrer, where above the stirrer, the velocity of the simulations is higher than the average velocity obtained from the measurements but at least in the range of deviation of the single measurement series. The simulations are based on the multi reference frame (MRF) to simulate the stirring using a fixed mesh. To account for the rotor-stator interactions in the simulations, the simulated velocity is averaged using six specific points following the Laser of the PDA measurement.

An increased measurement time of the single experimental series and traversing the PDA throughout the whole compartment will increase the accuracy of the experimental results in the future. From simulation point of view, the use of a sliding reference frame allows a direct comparison of the droplet velocity at a specific location with the experimental results. Also the use of a multi-fluid model allows the simulation of different droplet sizes in a single numerical cell which comes closer to the experimental distribution of the droplet size.
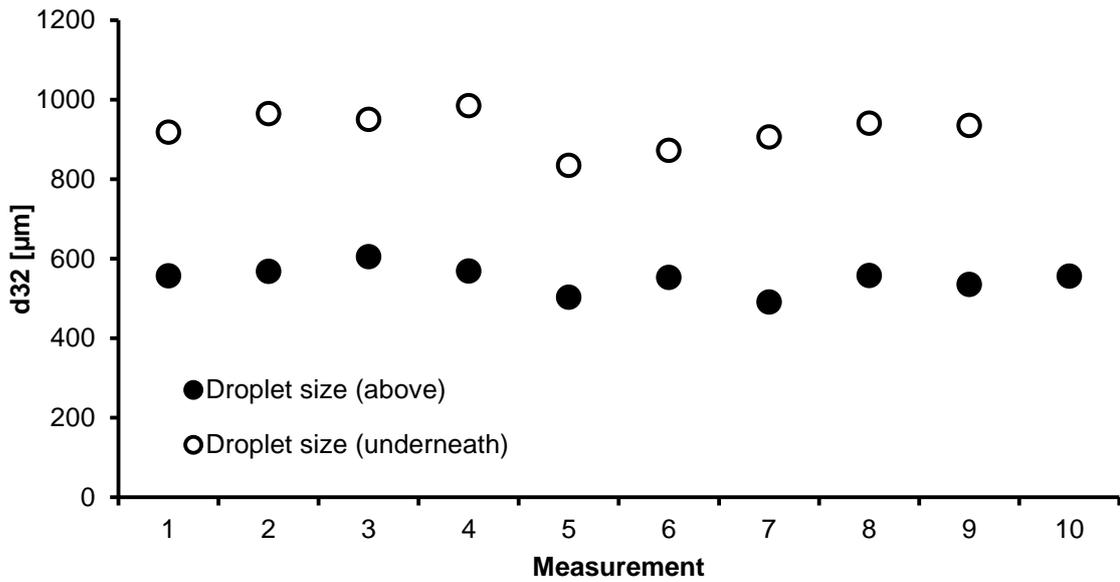
Figure 10.1: Measured droplet size above and underneath the stirrer at 6 l/h per phase and 200 rpm. System: toluene/water.
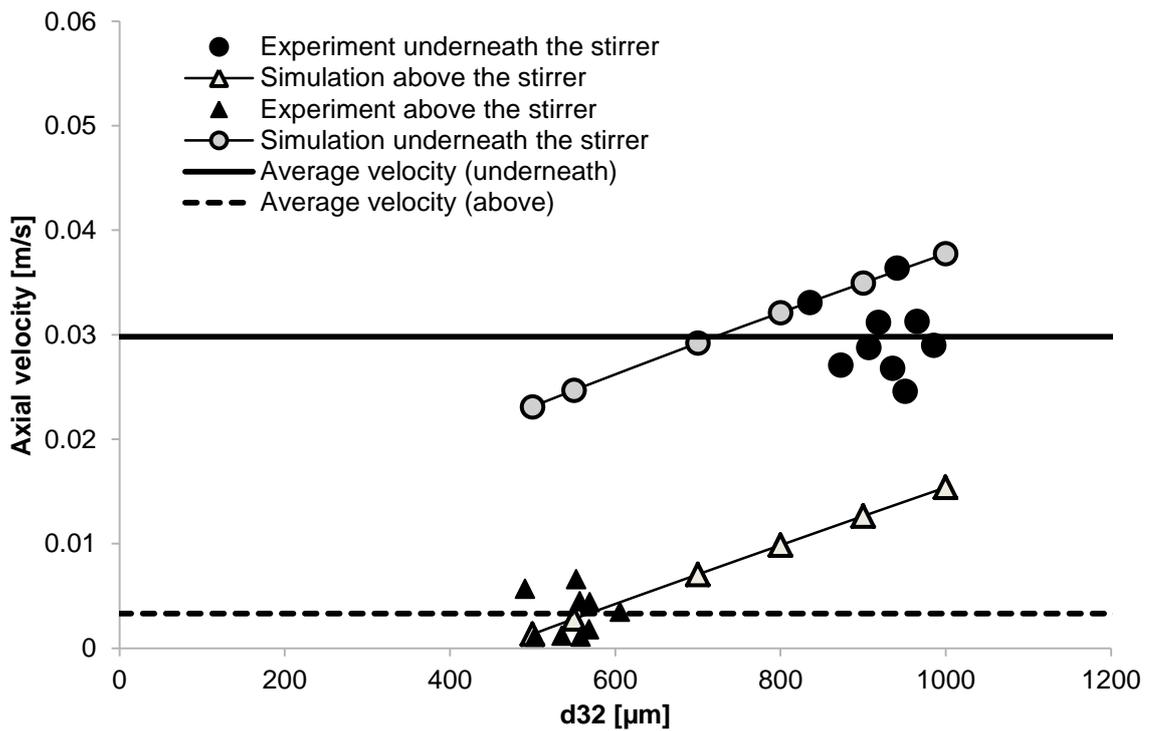
Figure 10.2: Simulated velocities in axial direction compared to the measured velocities in dependence on the droplet size above and underneath the stirrer at 6 l/h per phase and 200 rpm. System: toluene/water.

11.2 A New Multi-Phase Solver

The OpenFOAM release 2.1.0 included an official release of an multi-phase solver based on the Eulerian modelling. The release enables engineers to extend the multi-phase modelling on a common base. The solver comes with a large eddy simulation to account for turbulence. For the use of population balance modelling, it is necessary to know the turbulent energy dissipation. Hence the large eddy simulation was replaced in this work by the standard k-ε-model. A transport equation for the mixture temperature is added to the code for a first test to account for the temperature transport in reactive systems (e.g. bubble columns).

$$\frac{\partial T}{\partial t} + \nabla \cdot \left(T U_\varphi \right) - \nabla D \nabla\, T = S_m \qquad (10.1)$$

The diffusion term D is given by:

$$D = \frac{\kappa}{\rho c_p} + \frac{\nu_t}{Pr_t} \qquad (10.2)$$

A further extend of the temperature equation is necessary to account for the temperature transport of each phase. The OPOSP method is coupled with the dispersed phase to account for the droplet-droplet interactions and a back coupling with the hydrodynamics. An implementation of the SQMOM will account for the droplet interactions between several dispersed phases (classes).

11.3 Liquid-liquid Properties

Table 15: Properties of the used fluorescence for LIF measurements.

Liquid	Density [kg/m³]	Viscosity [mPas]	Interfacial tension [mN/m]
Water	998.8	1.00	74
Toluene	866.0	0.60	34
N-butyl acetate	879.0	0.74	14
N-heptane	679.9	0.41	–
Glycerine	1220	1412	–

Table 16: Iso-optical systems for used for laser measurements.

Liquid/Liquid system	Composition [wt-%]	Density [kg/m³]	Viscosity [m²/s]	Refractive Index
Water/glycerine	44/56	1098	$3.28 \cdot 10^{-6}$	1.38
Water/CaCl$_2$	70/30	1317	$2.06 \cdot 10^{-6}$	1.40

Table 17: Interfacial tension of the iso-optical systems at 25°C.

Liquid/Liquid system	Interfacial tension [mN/m]
Water/glycerine/n-heptane	25

Table 18: Properties of the used fluorescence for LIF measurements.

	Elemental formula	Wavelength	Solubility in water
Rhodamine 6G	$C_{28}H_{31}ClN_2O_3$	$\lambda_{max} = 527 - 533$	30 g/l at 20°C

Table 19: Principle geometrical data of used internals.

	Kühni DN32	Kühni DN60	Garthe DN80 (Kühni)	Garthe DN80 (RDC)
Column diameter	32 mm	60 mm	80 mm	80 mm
Compartment height	28 mm	40 mm	50 mm	50 mm
Stirrer diameter	20 mm	40 mm	45 mm	45 mm
Shaft diameter	5 mm	10 mm	10 mm	10 mm
Height of the blade	4.5 mm	7.5 mm	7 mm	1.5 mm
No. of stirrer blades	6	4	6	6
Free cross-sectional area	40%	31%	40%	40%
Streambreakers	Flat	Cylindrical	Cylindrical	Cylindrical

11.4 Transient and Steady State Measurements of the DN32 Column

The following results were obtained during the student research project of Matthias Platz.

$$y = 546.67x$$
$$R^2 = 0.9994$$

● Acetone in water

—— Linear (Acetone in water)
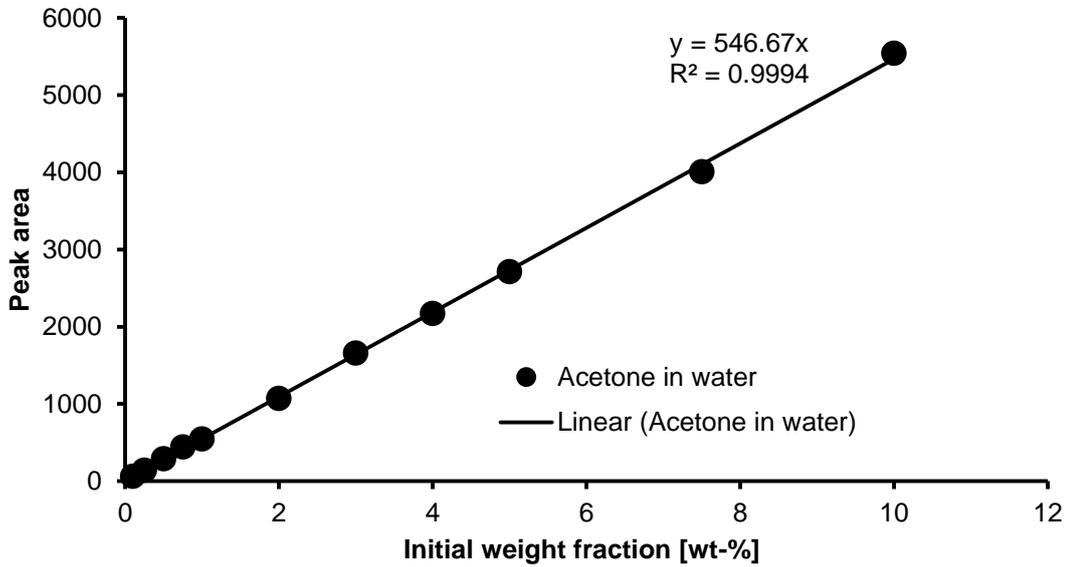
Figure 10.3: GC calibration curve for acetone in water.

$$y = 493.03x$$
$$R^2 = 0.9996$$

● Acetone in toluene

—— Linear (Acetone in toluene)
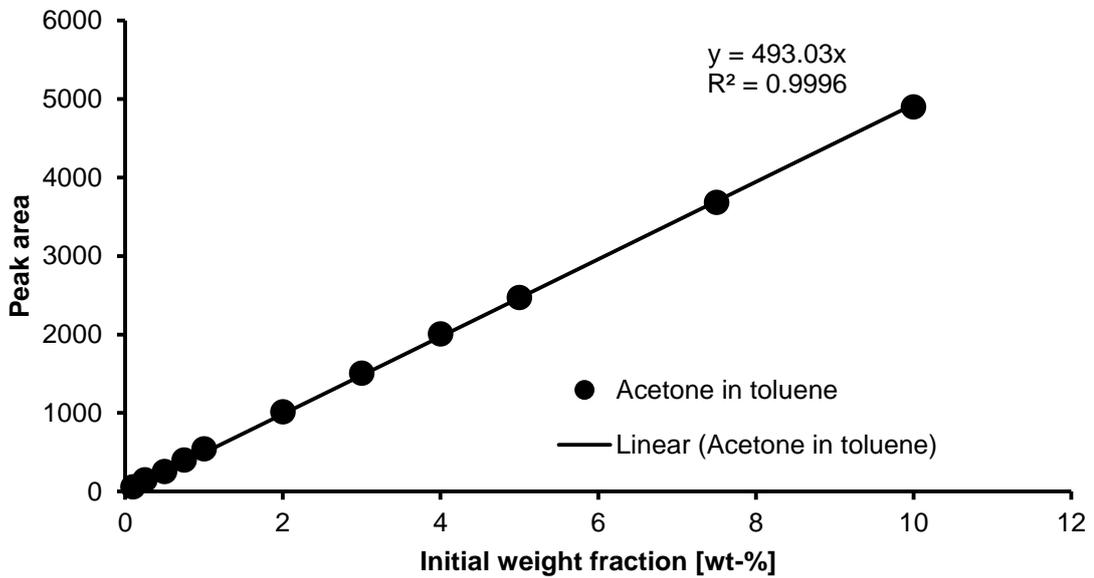
Figure 10.4: GC calibration curve for acetone in toluene.

Table 20: Concentration profiles of the continuous phase at 5 l/h continuous phase (water/acetone) and 6 l/h dispersed phase (toluene) at 200 rpm.

Time [min]	Phase	Bottom	1. Position	2. Position	3. Position	4. Position	5. Position	Top
		Location of the sampling point [mm]						
		0	320	520	840	1010	1220	1470
40	Aqueous	1.77	2.08	2.73	3.53	3.89	4.32	
50	Aqueous	1.89	2.24	2.93	3.73	4.08	4.41	
60	Aqueous	1.93	2.31	2.99	3.75	4.05	4.45	
70	Aqueous	1.85	2.21	2.87	3.70	3.99	4.39	
80	Aqueous	1.79	2.13	2.80	3.58	3.93	4.32	
90	Aqueous	1.76	2.11	2.82	3.57	3.93	4.43	
100	Aqueous	1.76	2.12	2.79	3.58	3.89	4.35	
Average		1.82	2.17	2.85	3.63	3.97	4.38	5.00

Table 21: Concentration profiles of the dispersed phase at 5 l/h continuous phase (water/acetone) and 6 l/h dispersed phase (toluene) at 200 rpm.

Time [min]	Phase	Bottom	1. Position	2. Position	3. Position	4. Position	5. Position	Top
		Location of the sampling point [mm]						
		0	0	320	520	840	1010	1220
40	Organic		1.16	1.35	1.81	2.30	2.85	3.20
50	Organic		0.98	1.45	1.93	2.71	2.94	3.28
60	Organic		0.99	1.51	2.00	2.65	2.98	3.29
70	Organic		0.95	1.41	1.85	2.48	2.79	3.26
80	Organic		0.92	1.44	1.85	2.45	2.78	3.21
90	Organic		0.88	1.39	1.83	2.45	2.82	3.22
100	Organic		0.81	1.22	1.83	2.37	2.76	3.18
Average		0	1.40	0.96	1.40	1.87	2.49	2.84

Table 22: Hold−up of the dispersed phase at 5 l/h continuous phase (water/acetone) and 6 l/h dispersed phase (toluene) at 200 rpm.

Time [min]	40	50	60	70	80	90	100
Hold-up [%]	6.5	6.9	7.5	7.9	7.2	6.9	7.1

Table 23: Concentration profiles of the continuous phase at 5 l/h continuous phase (water/acetone) and 6 l/h dispersed phase (toluene) at 250 rpm.

Time [min]	Phase	Bottom	1. Position	2. Position	3. Position	4. Position	5. Position	Top
				Location of the sampling point [mm]				
		0	320	520	840	1010	1220	1470
40	Aqueous	1.55	1.91	2.61	3.57	3.84	4.29	
50	Aqueous	1.51	1.85	2.58	3.46	3.70	4.28	
60	Aqueous	1.48	1.85	2.55	3.51	3.82	4.30	
70	Aqueous	1.46	1.80	2.47	3.43	3.78	4.28	
80	Aqueous	1.36	1.70	2.38	3.34	3.66	4.21	
90	Aqueous	1.26	1.55	2.19	3.18	3.56	4.09	
Average		1.43	1.78	2.46	3.42	3.73	4.24	4.95

Table 24: Concentration profiles of the dispersed phase at 5 l/h continuous phase (water/acetone) and 6 l/h dispersed phase (toluene) at 250 rpm.

Time [min]	Phase	Bottom	1. Position	2. Position	3. Position	4. Position	5. Position	Top
				Location of the sampling point [mm]				
		0	350	550	810	1040	1250	1470
40	Organic		1.20	1.92	2.12	2.71	3.12	3.40
50	Organic		1.16	1.65	2.06	2.62	3.05	3.41
60	Organic		1.16	1.55	2.01	2.57	3.05	3.43
70	Organic		1.02	1.52	1.98	2.51	2.99	3.38
80	Organic		0.81	1.50	1.87	2.45	2.93	3.32
90	Organic		0.89	1.38	2.77	2.27	1.74	3.29
Average		0	1.59	1.04	1.59	2.14	2.52	2.81

Table 25: Hold-up of the dispersed phase at 5 l/h continuous phase (water/acetone) and 6 l/h dispersed phase (toluene) at 250 rpm.

Time [min]	40	50	60	70	80	90
Hold-up [%]	8.9	7.8	7.6	7.0	7.9	8.2

Table 26: Concentration profiles of the continuous phase at 6.7 l/h continuous phase (water/acetone) and 8.2 l/h dispersed phase (toluene) at 150 rpm.

Time [min]	Phase	Bottom	1. Position	2. Position	3. Position	4. Position	5. Position	Top
				Location of the sampling point [mm]				
		0	320	520	840	1010	1220	1470
40	Aqueous	2.06	2.66	3.28	4.01	4.20	4.63	
50	Aqueous	2.26	2.63	3.32	4.03	4.21	4.64	
60	Aqueous	0.00	2.59	3.12	3.78	4.11	4.44	
70	Aqueous	2.15	2.50	3.20	3.89	4.23	4.49	
80	Aqueous	2.25	2.65	3.28	3.81	4.14	4.50	
90	Aqueous	2.35	2.35	3.25	4.05	4.32	4.59	
100	Aqueous	2.33	2.73	3.30	3.90	4.21	4.61	
Average		1.91	2.59	3.25	3.92	4.20	4.56	5.19

Table 27: Concentration profiles of the dispersed phase at 6.7 l/h continuous phase (water/acetone) and 8.2 l/h dispersed phase (toluene) at 150 rpm.

Time [min]	Phase	Bottom	1. Position	2. Position	3. Position	4. Position	5. Position	Top
				Location of the sampling point [mm]				
		0	350	550	810	1040	1250	1470
40	Organic		1.14	1.50	1.98	2.40	2.69	2.98
50	Organic		1.09	1.54	1.88	2.40	2.65	3.01
60	Organic		1.08	1.42	1.90	2.38	2.61	2.99
70	Organic		1.11	1.43	1.86	2.40	2.58	3.02
80	Organic		1.13	1.33	1.83	2.53	2.67	2.97
90	Organic		1.01	1.42	1.80	2.43	2.64	3.00
100	Organic		1.08	1.40	1.86	2.40	2.67	2.96
Average		0	1.09	1.43	1.87	2.42	2.64	2.99

Table 28: Hold-up of the dispersed phase at 6.7 l/h continuous phase (water/acetone) and 8.2 l/h dispersed phase (toluene) at 150 rpm.

Time [min]	40	50	60	70	80	90	100
Hold-up [%]	7.5	7.7	7.1	7.7	7.7	7.6	7.4

Table 29: Concentration profiles of the continuous phase at 6.7 l/h continuous phase (water/acetone) and 8.2 l/h dispersed phase (toluene) at 200 rpm.

Time [min]	Phase	Bottom	1. Position	2. Position	3. Position	4. Position	5. Position	Top
		Location of the sampling point [mm]						
		0	320	520	840	1010	1220	1470
40	Aqueous	1.90	2.46	2.97	3.84	4.15	4.42	
50	Aqueous	1.84	2.32	2.97	3.72	3.96	4.48	
60	Aqueous	1.78	2.22	2.86	3.61	3.91	4.33	
70	Aqueous	1.79	2.26	2.87	3.61	4.01	4.41	
80	Aqueous	1.76	2.21	2.97	3.69	4.02	4.51	
90	Aqueous	1.75	1.75	2.98	3.76	4.00	4.50	
100	Aqueous	1.72	2.28	2.94	3.71	3.98	4.27	
Average		1.80	2.22	2.94	3.71	4.00	4.42	5.19

Table 30: Concentration profiles of the dispersed phase at 6.7 l/h continuous phase (water/acetone) and 8.2 l/h dispersed phase (toluene) at 200 rpm.

Time [min]	Phase	Bottom	1. Position	2. Position	3. Position	4. Position	5. Position	Top
		Location of the sampling point [mm]						
		0	350	550	810	1040	1250	1470
40	Organic		1.23	1.47	1.94	2.55	2.80	3.03
50	Organic		1.00	1.44	1.86	2.58	2.83	3.04
60	Organic		0.95	1.29	1.70	2.48	2.72	3.02
70	Organic		0.90	1.34	1.76	2.42	2.73	2.92
80	Organic		0.94	1.34	1.76	2.30	2.71	3.01
90	Organic		0.89	1.36	1.78	2.19	2.54	3.08
100	Organic		0.79	1.30	1.56	2.26	2.67	3.01
Average		0	0.96	1.36	1.77	2.40	2.72	3.02

Table 31: Hold-up of the dispersed phase at 6.7 l/h continuous phase (water/acetone) and 8.2 l/h dispersed phase (toluene) at 200 rpm.

Time [min]	40	50	60	70	80	90	100
Hold-up [%]	7.6	7.3	7.5	8.4	8.4	7.8	7.9

11.5 Transient and Steady State Measurements of the DN60 Column

The following results were obtained during the student research project of Sven Müller.

By plotting the data, an exponential decrease of the acetone concentration in the continuous phase could be observed from the inlet at the top of the column to the outlet at the bottom which can be referred to accumulation of both phases in the measuring volume. However, the concentration in the continuous phase decreased compared to the DN32 results. However, also the concentration of acetone in the dispersed phase decreased at the outlet. A reason for this could be found in the accumulation of dispersed phase underneath the stator. A the layer thickness of the accumulation increased compared to the DN32 results resulting in transport of new droplets to the accumulation, droplet accumulation and a further transport of newly generated droplet from this accumulation. The retention time of the droplet in the accumulation increases thereby the axial dispersion of the dispersed phase. The given average value is referred to the measurements starting from 40 minutes.

Table 32: Concentration profiles of the continuous phase at 17.52 l/h continuous phase (water/acetone) and 21.02 l/h dispersed phase (toluene) at 200 rpm.

Time [min]	Phase	Bottom	1. Position	2. Position	3. Position	4. Position	5. Position	Top
		Location of the sampling point [mm]						
		0	359	724	1089	1454	1819	2269
5	Aqueous	0.20	2.38	4.54	5.06	5.10	5.17	5.04
15	Aqueous	2.00	0.86	1.52	2.44	3.53	4.49	
25	Aqueous	2.22	0.52	1.08	1.84	2.87	3.91	
40	Aqueous	1.18	0.28	0.68	1.57	2.09	3.02	
55	Aqueous	0.25	0.24	0.59	1.07	1.90	3.05	
70	Aqueous	0.25	0.41	0.98	1.57	2.36	3.73	
85	Aqueous	0.24	0.22	0.52	1.02	1.66	2.75	
Average		0.4	0.29	0.69	1.31	2.01	3.14	5.04

Table 33: Concentration profiles of the dispersed phase at 17.52 l/h continuous phase (water/acetone) and 21.02 l/h dispersed phase (toluene) at 200 rpm.

Time [min]	Phase	Bottom	1. Position	2. Position	3. Position	4. Position	5. Position	Top
		Location of the sampling point [mm]						
		0	494	859	1224	1589	1954	2269
5	Organic		2.69	3.84	3.48	4.09	3.76	4.02
15	Organic		0.99	2.12	2.21	2.71	3.20	3.75
25	Organic		0.57	1.38	1.37	2.10	2.40	3.29
40	Organic		0.26	0.89	0.89	1.54	2.17	3.05
55	Organic		0.20	0.72	0.72	1.39	2.32	3.18
70	Organic		0.25	0.69	0.84	1.82	2.74	3.28
85	Organic		0.17	0.54	0.67	1.32	2.32	3.09
Average		0	0.22	0.71	0.78	1.52	2.39	3.15

Table 34: Concentration profiles of the continuous phase at 17.52 l/h continuous phase (water/acetone) and 21.02 l/h dispersed phase (toluene) at 175 rpm.

Time [min]	Phase	Bottom	1. Position	2. Position	3. Position	4. Position	5. Position	Top
		Location of the sampling point [mm]						
		0	359	724	1089	1454	1819	2269
5	Aqueous	0.28	2.28	3.89	4.67	4.90	5.07	5.14
15	Aqueous	2.62	1.25	2.27	3.15	3.95	4.51	
25	Aqueous	1.58	0.71	1.31	1.93	2.84	3.57	
40	Aqueous	1.17	0.53	1.00	1.56	2.42	3.27	
55	Aqueous	0.78	0.39	0.76	1.22	1.95	2.89	
70	Aqueous	0.48	0.48	0.90	1.35	2.07	3.11	
85	Aqueous	0.42	0.41	0.92	1.54	2.46	3.49	
100	Aqueous	0.41	0.47	0.92	1.45	2.18	3.37	
Average		0.65	0.46	0.90	1.42	2.22	3.23	5.14

Table 35: Concentration profiles of the dispersed phase at 17.52 l/h continuous phase (water/acetone) and 21.02 l/h dispersed phase (toluene) at 175 rpm.

Time [min]	Phase	Bottom	1. Position	2. Position	3. Position	4. Position	5. Position	Top
		Location of the sampling point [mm]						
		0	494	859	1224	1589	1954	2269
5	Organic	0	2.04	3.14	3.63	3.89	3.73	4.01
15	Organic		0.91	1.92	2.36	2.90	3.31	3.75
25	Organic		0.48	1.12	-	2.04	2.64	3.25
40	Organic		0.32	-	1.12	1.71	2.44	2.97
55	Organic		0.23	0.71	-	1.35	2.25	2.92
70	Organic		0.20	0.64	0.93	1.50	2.47	3.04
85	Organic		0.24	0.72	1.09	1.60	2.23	2.94
100	Organic		0.19	0.67	0.95	1.53	2.47	3.03
Average		0	0.24	0.68	1.02	1.54	2.37	2.98

Table 36: Concentration profiles of the continuous phase at 17.52 l/h continuous phase (water/acetone) and 21.02 l/h dispersed phase (toluene) at 100 rpm.

Time [min]	Phase	Bottom	1. Position	2. Position	3. Position	4. Position	5. Position	Top
		Location of the sampling point [mm]						
		0	359	724	1089	1454	1819	2269
5	Aqueous	4.39	2.95	3.78	4.24	4.59	4.74	4.94
15	Aqueous	3.88	1.99	2.67	3.29	3.94	4.41	
25	Aqueous	2.11	1.48	2.07	2.57	3.14	3.79	
35	Aqueous	1.33	1.17	1.78	2.32	3.13	3.61	
50	Aqueous	1.15	1.14	1.78	2.38	3.05	3.79	
65	Aqueous	1.08	1.05	1.66	2.22	2.96	3.79	
80	Aqueous	1.01	0.98	1.56	2.16	2.74	3.74	
95	Aqueous	0.95	1.01	1.60	2.25	2.93	3.77	
Average		1.11	1.07	1.68	2.27	2.96	3.74	4.94

Table 37: Concentration profiles of the dispersed phase at 17.52 l/h continuous phase (water/acetone) and 21.02 l/h dispersed phase (toluene) at 100 rpm.

Time [min]	Phase	Bottom	1. Position	2. Position	3. Position	4. Position	5. Position	Top
		Location of the sampling point [mm]						
		0	494	859	1224	1589	1954	2269
5	Organic	0	1.52	2.49	2.71	3.12	3.20	3.46
15	Organic		0.87	1.87	1.99	2.56	2.74	3.10
25	Organic		0.50	1.40	-	1.86	2.32	2.71
35	Organic		0.44		1.23	1.78	2.08	2.51
50	Organic		0.36	1.08	1.21	2.78	2.18	2.60
65	Organic		0.32	0.99	1.17	1.65	2.09	2.57
80	Organic		0.29	0.90	1.04	1.55	2.07	2.59
95	Organic		0.30	0.86	1.10	1.51	2.12	2.69
Average		0	0.34	0.95	1.15	1.85	2.11	2.59

Table 38: Measured average droplet sizes at the outlet of the DN60 column are shown in the following table for different rotational speeds.

Rotational speed [rpm]	100	125	150	175	200	225
Droplet size [mm]	2.73	2.66	2.32	2.45	1.90	1.87

The following figures transient measurement with step change from 100 rpm to 150 rpm and back to 125 rpm at 75 minutes and 145 minutes respectively.
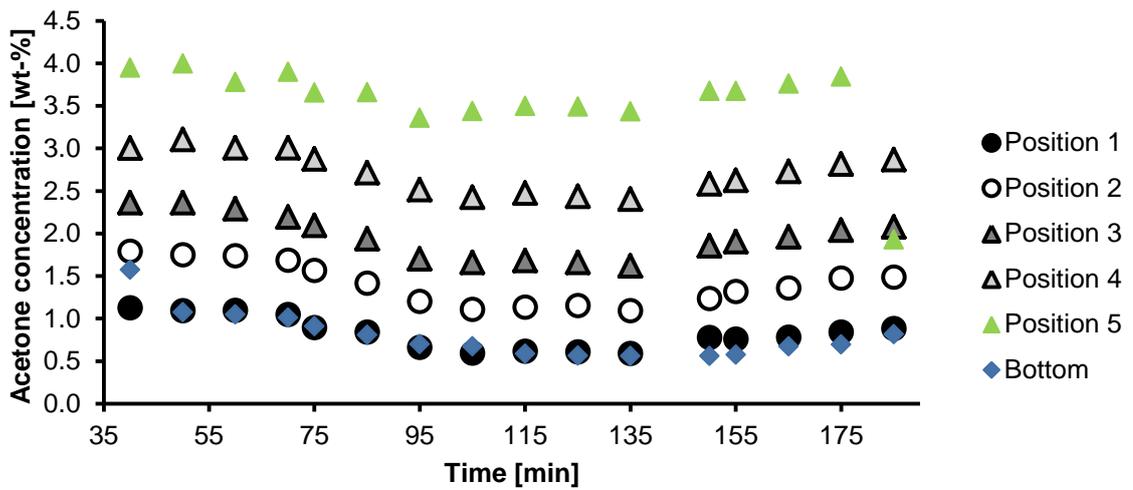
Figure 10.5: Acetone concentration in the continuous phase.
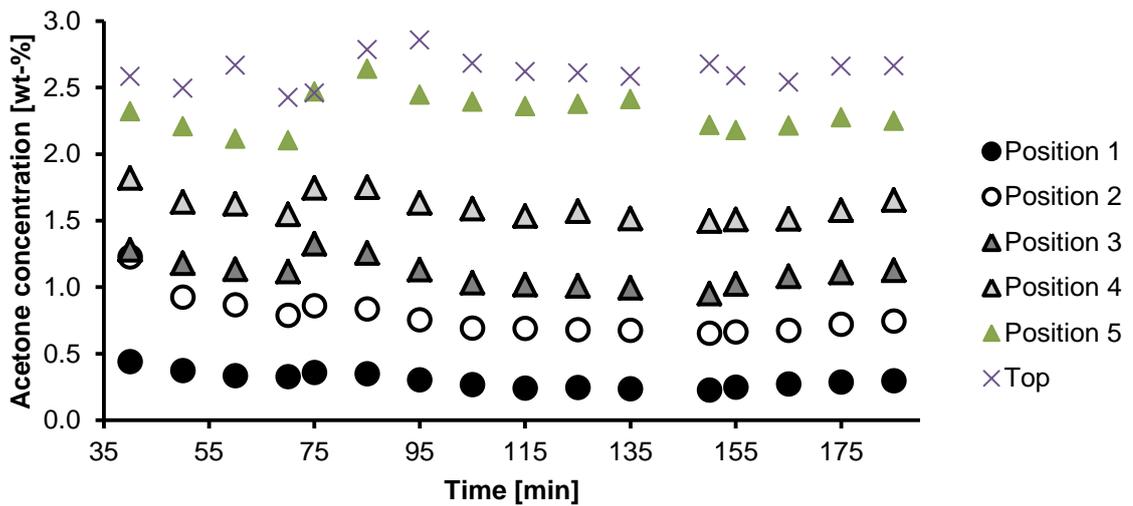
Figure 10.6: Acetone concentration in the dispersed phase.

The change in rotational speed results in first in an increased hold-up which decreases again by time to the steady state value for the corresponding rotational speed. However, the hold-up depends on the droplet size. With increasing rotational speed, smaller droplets can be observed.
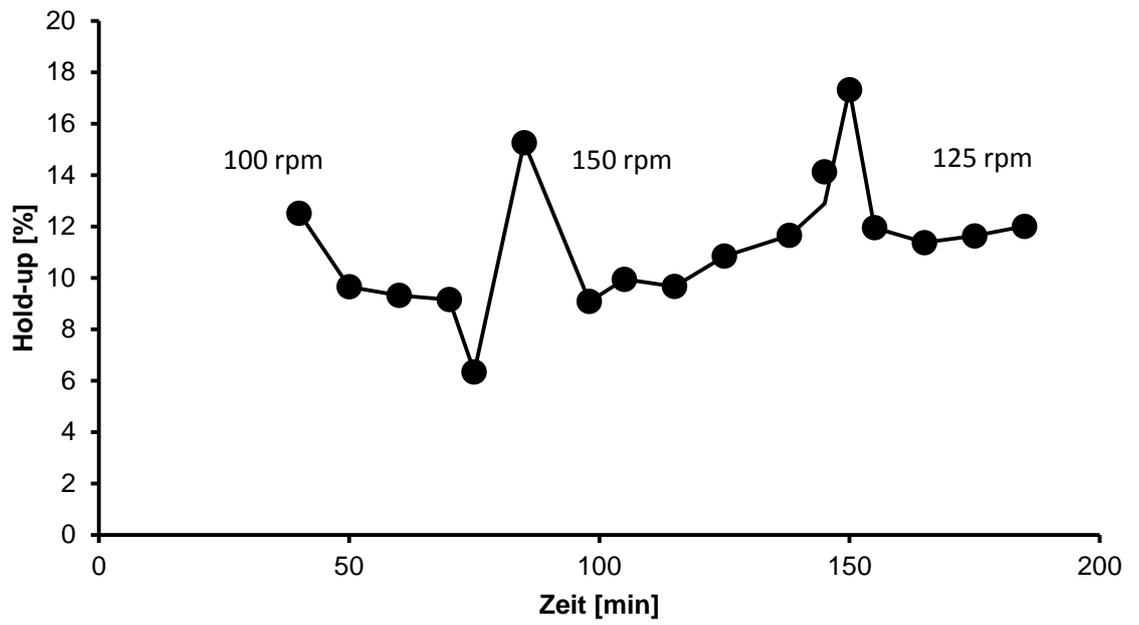
Figure 10.7: Hold‑up profile for the transient measurement including step change.
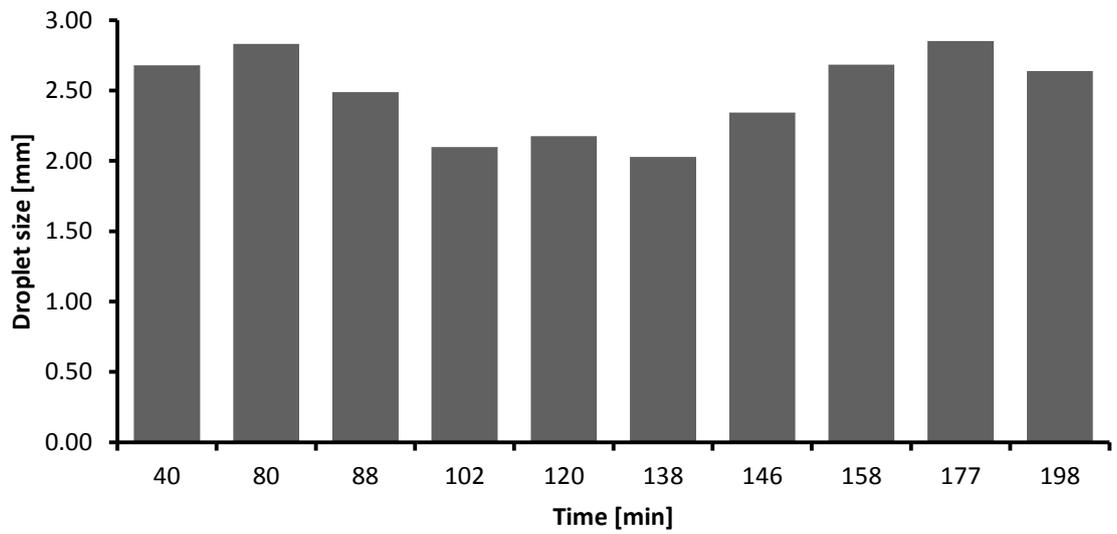
Figure 10.8: Droplet size for the transient measurement including step change.

Literature

Alekseenko, S.V., Bilsky, A.V., Dulin, V.M. & Markovich, D.M., 2007. Experimental Study of an Impinging Jet with Different Swirl Rates. *Int. J. Heat Mass Transfer* 28(6), pp. 1340-59.

Andersson, R. & Andersson, B., 2006. On the Breakup of Fluid Particles in Turbulent Flows. *AIChE J.* 52(6), pp. 2020-30.

Ataki, A., 2006. *Wetting of Structured Packing Elements – CFD and Experiment*. Dissertation. Kaiserslautern, Germany: University of Kaiserslautern.

Attarakih, M., Al-Zyod, S., Abu-Khader, M. & Bart, H.-J., 2012. PPBLAB: A New Multivariate Population Balance Environment for Particulate System Modelling and Simulation. *Procedia Eng.* 42, pp. 1445-62.

Attarakih, M.M., Bart, H.-J., Steinmetz, T., Dietzen, M. & Faqir, N.M., 2008. LLECMOD: A Bivariate Population Balance Simulation Tool for Liquid-Liquid Extraction Columns. *Open Chem. Eng. J.* 2, pp. 10-34.

Attarakih, M.M., Drumm, C. & Bart, H.-J., 2009a. Solution of the Population Balance Equation using the Sectional Quadrature Method of Moments (SQMOM). *Chem. Eng. Sci.* 64, pp. 742-52.

Attarakih, M. et al., 2009. Solution of the Population Balance Equation using the One Primary and One Secondary Particle Method (OPOSPM). In Jezowski, J. & Thullie, J., eds. *19th European Symposium on Computer Aided Process Engineering – Escape19.*, 2009. Elsevier.

Attarakih, M., Jaradat, M., Hlawitschka, M., Bart, H.-J. & Kuhnert, J., 2011. Integral Formulation of the Population Balance Equation using the Cumulative QMOM. *Comput. Aided Chem. Eng.* 29, pp. 81-85.

Aufderheide, E., 1985. *Hydrodynamische Untersuchungen an Pulsierten Siebbodenextraktionskolonnen*. Dissertation. Clausthal, Germany: Technical University of Clausthal.

Backhurst, J.R..H.J.H., Richardson, J.F. & Coulson, J.M., 1999. *Chemical Engineering Volume 1: Fluid Flow, Heat Transfer and Mass Transfer*. 6th ed. Oxford: Butterworth-Heinemann.

Baerns, M. et al., 2006. *Technische Chemie*. Weinheim: Wiley-VCH Verlag GmbH und Co. KgaA.

Bart, H.-J., Hlawitschka, M.W., Attarakih, M., Alzyood, S. & Platz, M., 2013. Mass Transfer and Population Balance Modeling using 3D-CFD. In *Proceeding of 5th International*

Conference on Population Balance Modelling, September11-13, 2013. Bangalore, India, 2013.

Batterham, R.J.J., Hall, S. & Barton, G., 1981. Pelletizing Kinetics and Simulation for Full-Scale Balling Circuits. *Proc. 3rd Int. Symp. Agg.*.

Bauer, R., 1976. *Die Längsvermischung beider Phasen in einer gerührten Fest-Flüssig-Extraktionskolonne*. Dissertation. ETH Zürich, Zürich.

Bauer, R. & Widmer, F., 1977. Die Längsvermischung beider Phasen einer gerührten Fest-Flüssig-Extraktionskolonne. *Verfahrenstechnik*

Bäumler, K., Wegener, M., Paschedag, A.R. & Bänsch, E., 2010. Drop Rise Velocities and Fluid Dynamic Behavior in Standard Test Systems for Liquid/Liquid Extraction – Experimental and Numerical Investigations. *Chem. Eng. Sci.* 66, pp. 426-39. DOI:10.1016/j.ces.2010.11.009.

Bertakis, E. et al., 2010. Validated Simulation of Droplet Sedimentation with Finite-Element and Level-Set Methods. *Chem. Eng. Sci.* 65(6), pp. 2037-51.

Bibaud, R.E. & Treybal, R.E., 1966. Axial Mixing and Extraction in a Mechanically Agitated Liquid Extraction Tower. *AIChe J.* 12(3), pp. 472-77.

Brauer, H., 1971. *Grundlagen der Einpasen- und Mehrphasenströmungen*. Aarau: Sauerländer.

Breysee, J., Bühlmann, U. & Godfrey, J.C., 1983. Axial Mixing Characteristics of Industrial and Pilot Scale Kühni Columns. *AIChe Symposium Series* 80(238), pp. 94-101.

Chen, F., 2012. *The Simulation and Visualization of Multi-Phase Fluid*. Dissertation. TU Kaiserslautern, Kaiserslautern, Germany.

Chevalier, T., 2010. *Simulation of a Rotating Disc Contactor Using a CFD-PBM Coupling*. Diploma Thesis. Kaiserslautern, Germany: University of Kaiserslautern.

Chhabra, R.P. & Bangun, J., 1997. Wall Effects on the Terminal Velocity of Small Drops in Newtonian and Non-Newtonian Fluids. *Can. J. of Chem. Eng.* 75, pp. 817-22.

Clift, R., Grace, J.R. & Weber, M.E., 1978. *Bubbles, Drops and Particles*. New York: Academic Press.

Coulaloglou, C.A. & Tavlarides, L.L., 1977. Description of Interaction Processes in Agitated Liquid-Liquid Dispersions. *Chem. Eng. Sci.* 32(11), pp. 1289-97.

Danckwerts, P.V., 1951. Significance of Liquid Film Coefficients in Gas Absorption. *Ind. Eng. Chem.* 43, pp. 1460-67.

Danckwerts, P.V., 1953. Continuous Flow Systems. Distribution of Residence Times. *Chem. Eng. Sci.* 2(195), pp. 1-13.

Deshpande, K.B. & Zimmerman, W.B., 2006. Simulation of Interfacial Mass Transfer by Droplet Dynamics Using the Level Set Method. *Chem. Eng. Sci.* 61(19), pp. 6486-98.

Dijkhuizen, W., van Sint Annaland, M. & Kuipers, H., 2005. Numerical Invesitgation of Closures for Interface Forces in Dispersed Flows using 3D Front Tracking Model. In STINTEF/NTNU, ed. *Proceedings of the 4th International Conference on CFD in Oil and Gas*. Trondheim, Norway, 2005.

Drumm, C., 2010. *Coupling of Computational Fluid Dynamics and Population Balance Modelling for Liquid-Liquid Extraction*. Dissertation. Kaiserslautern, Germany: University of Kaiserslautern.

Drumm, C., Attarakih, M.M. & Bart, H.-J., 2009. Coupling of CFD with DPBM for an RDC Extractor. *Chem. Eng. Sci.* 64, pp. 721-32.

Drumm, C., Attarakih, M., Hlawitschka, M.W. & Bart, H.-J., 2010. One-Group Reduced Population Balance Model for CFD Simulation of a Pilot-Plant Extraction Column. *Ind. Eng. Chem. Res.* 49(7), pp. 3442-51.

Durmm, C. & Bart, H.-J., 2006. Hydrodynamics in a RDC Extractor: Single and Two-Phase PIV Measurements and CFD Simulations. *Chem. Eng. Technol.* 29(11), pp. 1297-302.

Fei, W.Y., Wang, Y.D. & Wan, Y.K., 2000. Physical Modelling and Numerical Simulation of Velocity Fields in Rotating Disc Contactor via CFD Simulation and LDV Measurement. *Chem. Eng. J.* 78(2-3), pp. 131-39.

Feller, W., 1968. *An Introduction to Propability Theory and its Applications*. 3rd ed. New York: John Wiley and Sons.

Fischer, E.A., 1973. *Hydrodynamik und Stoffaustausch in einer Flüssig-Flüssig-Rührextraktionskolonne*. Zürich: Juris Druck + Verlag Zürich.

Fluent, 2005. *FLUENT 6.2 User's Guide*. Lebanon, NH 03766: Fluent Inc.

Garner, F.H. & Tayeban, M., 1960. The Importance of the Wake in Mass Transfer from Both Continuous and Dispersed Phase Systems. *An. Real. Soc. Espan. Fis. Quim. (Madrid)* 56(5), pp. 479-90.

Garthe, D., 2006. *Fluiddynamics and Mass Transfer of Single Particles and Swarms of Particles in Extraction Columns*. Dissertation. Munich: Lehrstuhl für Fluidverfahrenstechnik.

Ghaniyari-Benis, S., Hedayat, N., Ziyari, A., Kazemzadeh, M. & Shafiee, M., 2009. Three-Dimensional Simulation of Hydrodynamics in a Rotating Disc Contactor using Computational Fluid Dynamics. *Chem. Eng. Technol.* 32(1), pp. 93-102.

Gimbun, J., Rielly, C.D. & Nagy, Z.K., 2009. Modelling of Mass Transfer in Gas-Liquid Stirred Tanks Agitated by Rushton Turbine and CD-6 Impeller: A Scale-Up Study. *Chem. Eng. Res. Des.* 87(4), pp. 437-51.

Goldmann, G., 1986. *Ermittlung und Interpretation von Kennlinienfeldern einer gerührten Extraktionskolonne*. Dissertation. Munich, Germany: TU München.

Gomes, L.N., Guimares, M.L., Regueiras, P.F.R., Stichlmair, J. & Cruz Pinto, J.J., 2006. Simulated and Experimental Dispersed-Phase Breakage and Coalescence Behavior in a Kühni Liquid-Liquid Extraction Column Steady State. *Ind. Eng. Chem. Res.* 11, pp. 3955-68.

Gourdon, C., Casamatta, G. & Muratet, G., 1994. Population Balance Based Modelling. In J.C. Godfrey & M.J. Slater, eds. *Liquid-Liquid Extraction Equipment*. New York: John Wiley & Sons. pp.141-226.

Grace, J.R., Wairegi, T. & Nguyen, T.H., 1976. Shapes and Velocities of Single Drops and Bubbles Moving Freely Through Immiscible Liquids. *Chem. Eng. Res. Des.* 54, pp. 167-73.

Gurker, T. & Marr, R., 2009. Aufbau und Vermessung einer 150 mm Labor RDC Kolonne und Vergleich mittels CFD. *Chem. Ing. Tech.* 81(8), p. 1090.

Handlos, A.E. & Baron, T., 1957. Mass and Heat Transfer from Drops in Liquid-Liquid Extraction. *AIChE J.* 3(1).

Hanson, C., 1971. *Recent Advances in Liquid-Liquid Extraction*. Oxford: Pergamon Press.

Heertjes, P.M., Holve, W.A. & Talsma, H., 1954. Mass Transfer Between Isobutanol and Water in a Spray Column. *Chem. Eng. Sci.* 3(3), pp. 122-42.

Henschke, M., 2003. *Auslegung pulsierter Siebboden-Extraktionskolonnen*. Professorial Dissertation. Aachen, Germany: RTWH Aachen.

Henschke, M., Waheed, A. & Pfennig, A., 2000. Wandeinfluss auf die Sedimentationsgeschwindigkeit von Kugeln. *Chem. Ing. Tech.* 72(11), pp. 1376-80.

Higbie, R., 1935. The Rate of Absorption of a Pure Gas into a still Liquid during short Periods of Exposure. *Tran. Am. Inst. Chem. Eng.* 31, pp. 365-89.

Hill, P.J. & Ng, K.M., 1995. New Discretization Procedure for the Breakage Equation. *AIChE J.* 41(5), pp. 1204-16.

Hirt, C.W. & Nichols, B.D., 1981. Volume of Fluid (VOF) Method for the Dynamics of Free Boundaries. *J. Comput. Phys.* 39, pp. 201-25.

Hlawitschka, M.W. & Bart, H.-J., 2012a. Determination of Local Velocity, Energy Dissipation and Phase Fraction with LIF- and PIV-Measurement in a Kühni Miniplant Extraction Column. *Chem. Eng. Sci.* 69(1), pp. 138-45.

Hlawitschka, M.W. & Bart, H.-J., 2012b. CFD-Mass Transfer Simulation of an RDC Column. In K.A. Karimi & R. Srinivasan, eds. *Proceedings of the 11th International Symposium on Process System Engineering, 15-19 July*. Singapore. pp.920-25.

Hlawitschka, M.W., Chen, F. & Bart, H.-J., 2011. CFD Simulation und verbesserte Datenauswertung einer Extraktionskolonne vom Typ Kühni. In Balle, F., Marheineke, N., Kienle, F., Schmidt, K. & Tschauder, N., eds. *Proceedings of the 1st Young*

*Researcher Symposium by Center for Mathematical and Computational Modelling (CM)²
(YRS2011)*. Kaiserslautern, Germany, February 15, 2011.

Hlawitschka, M.W., Chen, F., Bart, H.-J. & Hamann, B., 2011. CFD Simulation of Liquid-Liquid
Extraction Columns and Visualization of Eulerian Datasets., 2011. OASICS Schloss
Dagstuhl – Leibniz-Zentrum für Informatik, Dagstuhl Publishing Germany.

Hounslow, M.J., Ryall, R.L. & Marshall, V.R., 1988. A Disretized Population Balance for
Nucleation, Growth, and Aggregation. *AIChE J.* 34(11), pp. 1821-32.

Hulburt, H.M. & Katz, S., 1964. Some Problems in Particle Technology. *Chem. Eng. Sci.* 19,
pp. 555-74.

Issa, R., 1985. Solution of the Implicitly Discretized Fluid Flow Equations by Operator Splitting.
J. Comp. Phys. 62, pp. 40-65.

Jaradat, M.M., Attarakih, M.M., Steinmetz, T. & Bart, H.-J., 2012. LLECMOD: A Bivariate
Population Balance Simulation Tool for Pulsed Liquid-Liquid Extraction Columns. *Open
Chem. Eng. J.* 6, pp. 8-31.

Jildeh, H., Attarakih, M. & Bart, H.-J., 2012a. Inverse Populationsbilanzen bei
Extraktionskolonnen. *Chem. Ing. Tech.* 84(8), pp. 1228-29.

Jildeh, H.B., Hlawitschka, M.W., Attarakih, M. & Bart, H.-J., 2012b. Solution of Inverse
Problem with the One Primary and One Secondary Particle Model (OPOSPM) Coupled
with Computational Fluid Dynamics (CFD). *Procedia Eng.* pp. 1692-710.

Johnson, C.R. & Hansen, C.D., 2005. *The Visualization Handbook*. Amsterdam: Elsevier
Academic Press.

Kalem, M., Buchbender, F. & Pfennig, A., 2011. Simulation of Hydrodynamics in RDC extraction
columns using the Simulation Tool "ReDrop". *Chem. Eng. Res. Des.* 83(7), pp. 1-
14.

Kalide, W., 1990. *Einführung in die technische Strömungslehre*. 7th ed. München: Fachbuchverlag
Leipzig.

Klee, A. & Treybal, R.E., 1956. Rate of Rise or Fall of Liquid Drops. *AIChE J.* 92(4), pp.
444-47.

Kolb, P., 2005. *Hydrodynamik und Stoffaustausch in einem gerührten Miniplantextraktor der Bauart
Kühni*. Dissertation. TU Kaiserslautern, Germany.

Konstantinov, E.N. & Kuznechikov, V.A., 1974. Numercial Experiment on Mass Transfer in Binary
Mixtures Using the Mathematical Model of Convective Diffusion for Turbulent Flow of
Gas in a Tube. *J. Eng. Phys. Thermophys.* 27(5), pp. 1321-25.

Krizan, P., 1987. *Analyse des dynamischen Verhaltens disperser Mehrphasensysteme bei
ausgeprägter Großraumströmung am Beispiel einer Gegenstrom-Blasensäule*. Dissertation.
Munich, Germany: Technische Universität München.

Kronig, R. & Brink, J.C., 1950. On the Theory of Extraction from Falling Droplets. *Appl. Sci. Res.* A2, pp. 142-54.

Kumar, A., 1985. *Hydrodynamics and Mass Transfer in Kühni Extractors*. Dissertation. Zürich, Swiss: ETH Zürich.

Kumar, A. & Hartland, S., 1983. Correlation for Drop Size in Liquid/Liquid Spray Columns. *Chem. Eng. Commun.* 31(1), pp. 193-207.

Kumar, A. & Hartland, S., 1995. A Unified Correlation for the Prediction of Dispersed-Phase Hold-Up in Liquid-Liquid Extraction Columns. *Ind. Eng. Chem. Res.* 34(11), pp. 3925-40.

Kumar, A. & Hartland, S., 1996. Unified Correlations for the Prediction of Drop Size in Liquid-Liquid Extraction Columns. *Ind. Eng. Chem. Res.* 35(8), pp. 2682-95.

Kumar, A. & Hartland, S., 1999. Correlations for Prediction of Mass Transfer Coefficients in Singel Drop Systems and Liquid-Liquid Extraction Columns. *Trans IChemE* 77(Part A), pp. 372-84.

Kumar, S. & Ramkrishna, D., 1996. On the Solution of Population Balance Equations by Discretiization – II. A Moving Pivot Technique. *Chem. Engng. Sci.* 8, pp. 1333-42.

Kumar, S. & Ramkrishna, D., 1996. On the Solution of Population Balance Equations by Discretization – I. A Fixed Pivot technique. *Chem. Engng. Sci.* 8, pp. 1311-32.

Laakonen, M., 2006. *Development and Validation of Mass Transfer Models for the Design of Agitated Gas-Liquid Reactors*. Dissertation. Espoo Finland: Helsinki University.

Laddha, G.S., 1974. *Transport Phenomena in Liquid Extraction*. New Delhi: Tata McGraw-Hill Publ. Co.

Langmuir, I., 1908. The Velocity of Reactions in Gases Moving Through Heated Vessels and the Effect of Convection and Diffusion. *Z. Phys. Chem.* 61, pp. 422-36.

Launder, B.E. & Spalding, D.B., 1974. The Numerical Computation of Turbulent Flows. *Comput. Meth. Appl. Mech. Eng.* 3(2), pp. 269-89.

Levenspiel, O. & Smith, W.K., 1957. Notes on Diffusion-Type Model for the Longitudanal Mixing of Fluids in Flow. *Chem. Eng. Sci.* 6 (4), pp. 227-35.

Lewis, W.K. & Whitman, W.G., 1924. Principles of gas adsorption. *Ind. Eng. Chem.* 16(12), pp. 1215-20.

Litster, J.D. & Hounslow, M.J., 1995. Adjustable Discretized Population Balance for Growth and Aggregation. *AIChE J.* 41(3), pp. 591-603.

Liu, L., Matar, O.K., Perez de Ortiz, E.S. & Hewitt, G.F., 2005. Experimental Investigation of Phase Inversion in a Stirred Vessel using LIF. *Chem. Eng. Sci.* 60(1), pp. 85-94.

Lohrengel, B., 2007. *Einführung in die thermischen Trennverfahren: Trennung von Gas-, Dampf- und Flüssigkeitsgemischen*. München: Oldenbourg Wissenschaftsverlag GmbH.

Luo, H. & Svendsen, H.F., 1996. Theoretical Model for Drop and Bubble Breakup in Turbulent Dispersions. *AIChE J.* 42(5), pp. 1225-33.

Maaß, S., Gäbler, A., Zaccone, A., Paschedag, A.R. & Kraume, M., 2007. Experimental Investigations and Modelling of Breakage Phenomena in Stirred Liquid/Liquid Systems. *Chem. Eng. Res. Des.* 85(A5), pp. 703-09.

Marchisio, D.L., Pikturna, J.T., Fox, R.O. & Vigil, R.D., 2003. Quadrature Method of Moments for Population-Balance Equations. *AIChE J.* 49(5), pp. 1266-76.

Marchisio, D.L., Vigil, R.D. & Fox, R.F., 2003. Implementation of the Quadrature Method of Moments in CFD Codes for Aggregation-Breakage Problems. *Chem. Eng. Sci.* 58(15), pp. 3337-51.

Martínez-Bazán, C., Montañés, J.L. & Lasheras, J.C., 1999a. On the Break-Up of an Air Bubble Injected into a Fully Developed Turbulent Flow. Part I: Break-Up Frequency. *J. Fluid Mech.* 401, pp. 157-82.

Martínez-Bazán, C., Montañés, J.L. & Lasheras, J.C., 1999b. On the Break-Up of an Air Bubble Injected into a Fully Developed Turbulent Flow. Part II. Size PDF of the resulting Daughter Bubbles. *J. Fluid Mech.* 401, pp. 183-207.

McGraw, R., 1997. Description of Aerosol Dynamics by the Quadrature Method of Moments. *Aerosol Sci. and Technol.* 27(2), pp. 255-65.

Mersmann, A., 1986. *Stoffübertragung*. Berlin: Springer.

Misek, T., 1974. *Berechnung von Kontaktoren mit Längsvermischung*. Aarau: Sauerländer AG.

Mísek, T., Berger, R. & Schröter, J., 1984. *Standard test systems for liquid extraction / EuropeaFederation of Chemical Engineering Working Party on Distillation, Absorption and Extraction.* 2nd ed. Warwickshire: Rugby.

Misek, T. & Rod, V., 1971. *Calculation of Contactors with Longitudinal Mixing*. Oxford: Pergamom Pr.

Miyauchi, T., Mitsutake, H. & Harase, I., 1966. Longitudinal Dispersion in Rotating Impeller Types of Contactors. *AIChe J.* 12(3), pp. 508-13.

Modes, G., 2000. *Grundsätzliche Studie zur Populationsdynamik einer Extraktionskolonne auf Basis von Einzeltropfenuntersuchungen*. Aachen: Shaker Verlag.

Modes, G. & Bart, H.-J., 2001. CFD Simulation of Nonideal Dispersed Phase Flow in Stirred Extraction Columns. *Chemical Eng. Technol.* 24(12), pp. 1242-45.

Morsi, S.A. & Alexander, A.J., 1972. An Investigation of Particle Trajectories in Two-Phase Flow Systems. *J. Fluid Mech.* 55(2), pp. 193-208.

Newman, A.B., 1931. The Drying of Porous Solids. *AIChE J.* 27, pp. 203-20.

Nikuradse, J., 1933. *Strömungsgesetze in rauhen Rohren*. 361st ed. VDI-Forschungsheft.

Nopens, I. & Vanrolleghem, P.A., 2006. Comparison of Discretization Methods to Solve a Population Balance Model of Activated Sludge Flocculation Including Aggregation and Breakage. *Math. Comput. Modell. Dyn. Syst.* 12(5), pp. 441-54.

Oseen, C.W., 1910. Über die Stokessche Formel und über die verwandte Aufgabe in der Hydrodynamik. *Arkiv Mat. Astron. Fys.* 6(29), p. 20.

Paschedag, A.R., 2004. *CFD in der Verfahrenstechnik: Allgemeine Grundlagen und mehrphasige Anwendungen*. Weinheim: WILEY-VCH Verlag GmbH & Co. KGaA.

Patankar, S.V. & Spalding, D.B., 1972. A Calculation Procedure for Heat, Mass and Momentum Transfer in Three-Dimensional Parabolic Flows. *Int. J. Heat Mass Transfer* 15(10), pp. 1787-806.

Paul, E.L., Atiemo-Obeng, V. & Kresta, S.M., 2004. *Handbook of Industrial Mixing: Science and Practice*. New Jersey, USA: John Wiley and Sons.

Petera, J. & Weatherley, L.R., 2001. Modelling of Mass Transfer from Falling Droplets. *Chem. Eng. Sci.* 56(16), pp. 4929-47.

Pilhofer, T. & Mewes, D., 1979. *Siebbodenextraktionskolonnen*. Weinheim: VCH.

Pratt, H.R.C. & Hanson, C., 1982. *Selection, Pilot Testing And Scale-up of Commercial Extractors. In: Lo, T. C., Baird, M. H. I., Hanson, C. (Hrsg.), Handbook of Solvent Extraction*. New York, USA: John Wiley & Sons.

Prince, M.J. & Blanch, H.W., 1990. Bubble Coalesence and Break-Up in Air Sparged Bubble Columns. *AIChE J.* 36(10), pp. 1485-99.

Qi, M., 1992. *Untersuchungen zum Stoffaustausch am Einzeltropfen in flüssigkeitspulsierten Siebboden-Extraktionskolonnen*. Dissertation. Clausthal, Germany: Technical University of Clausthal.

Ramkrishna, D., 2000. *Population Balances*. San Diego: Academic Press.

Rieger, R., Weiss, C., Wigley, G., Bart, H.-J. & Marr, R., 1996. Investigating the Process of Liquid-Liquid Extraction by Means of Computational Fluid Dynamics. *Comput. Chem. Eng.* 20(12), pp. 1467-75.

Rod, V., 1968. Longitudinal Mixing in the Dispersed Phase in Rotating Disc Extractors. *Coll. Czech. Chem. Commun.* 33(9), pp. 2855-61.

Rydberg, J., Musikas, C. & Choppin, G.R., 1992. *Principles and Practice of Solvent Exraction*. New York: Marcel Dekker.

Sattler, K., 1988. *Thermische Trennverfahren: Grundlagen, Auslegung, Apparate*. Weinheim, Germany: VCH Verlagsgesellschaft mbH.

Schade, H. & Kunz, E., 1989. *Strömungslehre*. 2nd ed. New York: Walter de Gruyter.

Schiller, L. & Naumann, Z., 1935. A Drag Coefficient Correlation. *Z. Ver. Dtsch. Ing.* (77), p. 318.

Schmidt, R., 1988. Anlagen und Apparate für die Destillation, Rektifikation, Sorption, Permeation, Extraktion, Achema Berichte. *Chem. Ing. Tech.* 60(12), pp. 956-65.

Schmidt, S.A., 2006. *Populationsdynamische Simulation gerührter Extraktionskolonnen auf der Basis von Einzeltropfen- und Tropfenschwarmuntersuchungen*. Aachen, Germany: Shaker Verlag.

Sigloch, H., 2007. *Technische Fluidmechanik*. 6th ed. Heidelberg, New York: Springer Berlin.

Simon, M., 2004. *Koaleszenz von Tropfen und Tropfenschwärmen*. Dissertation. Kaiserslautern, Germany: University of Kaiserslautern.

Slater, M.J., 1994. Rate Coefficients in Liquid-Liquid Extraction Systems. In J.C. Godfrey & M.J. Slater, eds. *Liquid-Liquid Extraction Equipment*. New York: Eds. John Wiley and Sons. pp.47-94.

Sommerfeld, M., 2001. Validation of a Stochastic Lagrangian Modelling Approach for Inter-Particle Collisions in Homogeneous Isotropic Turbulence. *Int. J. Multiphase Flow* 27(10), pp. 1829-59.

Steiner, L., 1988. *Rechnerische Erfassung der Arbeitsweise von Flüssig-Flüssig Extraktionskolonnen*. Düsseldorf, Germany: VDI-Verlag.

Steinmetz, T., 2007. *Tropfenpopulationsbilanzgestütztes Auslegungsverfahren zur Skalierung einer gerührten Miniplant-Extraktionskolonne*. Düsseldorf: VDI Verlag GmbH.

Stermerding, S., Lumb, E.C. & Lips, J., 1963. Axiale Vermischung in einer Drehscheiben-Extraktionskolonne. *Chem. Ing. Techn.* 35(12), pp. 844-50.

Stieß, M., 1995. *Mechanische Verfahrenstechnik 1*. 2nd ed. Heidelberg: Springer-Verlag.

Stokes, G.G., 1851. On the Effect of the Internal Friction of Fluids on the Motion of Pendulums. *Cambridge Philos. Trans.* 9, pp. 8-106.

Tomiyama, A., Zun, I., Sou, A. & Sakaguchi, T., 1993. Numerical Analysis of Bubble Motion with the VOF Method. *Nucl. Eng. Des.* 141(1-2), pp. 69-82.

Treybal, R.E., 1963. *Liquid Extraction*. New York: McGraw Hill.

Tu, J., Yeoh, G.H. & Liu, C., 2007. *Computational Fluid Dynamics: A Practical Approach*. Amsterdam: Butterworth Heinemann.

Valentas, K.J. & Amundson, N.R., 1966. Breakage and Coalescence in Dispersed Phase Systems. *Ind. Eng. Chem. Fundam.* 5(4), pp. 533-42.

Valentas, K.J., Bilois, O. & Amundson, A.R., 1966. Analysis of Breakage in Dispersed Phase Systems. *Ind. Eng. Chem. Fundam.* 5(2), p. 271.

van Doormal, J.P. & Raithby, G.D., 1984. Enhancements of the SIMPLE Method for Predicting Incompressible Fluid Flows. *Numer. Heat Transfer* 7(2), pp. 147-63.

Vignes, A., 1965. Hydrodynamique des dispersions - mouvement d'un globule dans un fluide immobile et infini. *Genie Chim.* 93, pp. 129-42.

Vikhansky, A. & Kraft, M., 2004. Modelling of a RDC using a combined CFD-population balance approach. *Chem. Eng. Sci.* 59(13), pp. 2597-606.

Waheed, M.A., Henschke, M. & Pfennig, A., 2004. Simulating Sedimentation of Liquid Drops. *Int. J. Numer. Methods Eng.* 59(14), pp. 1821-37.

Wang, F. & Mao, Z.-S., 2005. Numerical and Experimental Investigation of Liquid-Liquid Two-Phase Flow in Stirred Tanks. *Ind. Eng. Chem. Res.* 55(15), pp. 5776-87.

Watanabe, T. & Ebihara, K., 2003. Numerical Simulation of Coalescence and Breakup of Rising Droplets. *Computer & Fluids* 32(6), pp. 823-34.

Weisbach, J., 1845. *Lehrbuch der Ingenieur- und Maschinen-Mechanik, Vol. 1. Theoretische Mechanik*. Braunschweig: Vieweg und Sohn.

Weiss, C. & Bart, H.-J., 1993. Calculation of Flow Patterns in an RDC Based on Computational Fluid-Dynamic Methods. In LOGSDAIL, D.H. & Slater, M.J. *Solvent Extraction in the Process Industry*. London: Elsevier Applied Science. pp.1191-97.

Yakhot, V., Thangam, S., Gatski, T.B., Orszag, S.A. & Speziale, C.G., 1991. Development of Turbulence Models for Shear Flows by a Double Expansion Technique. *NASA Contractor Report 187611*

Yeoh, G.H. & Tu, J., 2009. *Computational Techniques for Multiphase Flows*. Amsterdam: Elsevier Science.

Yeung, P.K. & Zhou, Y., 1997. Universality of the Kolmogorov Constant in Numerical Simulations of Turbulence. *Phys. Rev. E* 56(2), pp. 1746-52.

You, X.Y. & Xiao, X., 2005. Simulation of the Three-Dimensional Two-Phases Flow in Stirred Extraction Columns by Lagrangian-Eulerian Method. *Chem. Biochem. Eng. Q.* 19(1), pp. 1-11.

Zamponi, G., 1996. *Das dynamische Verhalten einer gerührten Solventextraktionskolonne*. Dissertation. Munich, Germany: Technical University of Munich.

Supervised student thesis

It gives me a pleasure in acknowledging the support of my students during my thesis work. I consider it an honor to work with:

J. Herkelrath (2013): „Tropfenverhalten in einer gerührten Extraktionskolonne: Experimentelle Untersuchung und Simulation", Studienarbeit.

D. Seiberth (2013): „Aufbau, Inbetriebnahme und Simulation einer Venturizelle zur Untersuchung von Einzelphänomenen und Blasen-Blaseninteraktionen", Studienarbeit.

J. Delfs (2012): „Rückgewinnung von Essigsäure aus dem Extraktionsmittelgemisch Trioctylamin-Tributylphosphat mittels Vakuumdestillation in einer Kurzwegdestillationsanlage", Studienarbeit.

S. Müller (2012): „Bestimmung des Stoffaustauschs in einer Kühni Pilotkolonne bei unterschiedlichen Rührerpositionen", Diplomarbeit.

D. Mähser (2012): „Validierung eines CFD Codes und Optimierung einer Extraktionskolonne mit dem OpenSource Tool OpenFOAM", Studienarbeit.

A. Frings (2012): „Bestimmung von hydrodynamischen Kenngrößen einer Extraktionskolonne mit CFD", Studienarbeit.

A. Dernbecher (2012): „Bestimmung der axialen Dispersion in gerührten Extraktionskolonnen mit CFD", Diplomarbeit.

A. Weber, S. Roßbach (2012):
„CFD-Simulation von Extraktionskolonnen mit OpenFOAM", Projektarbeit.

K. Hagelauer: „Erstellung einer Benutzeroberfläche zur Simulation extraktiver Strömungsprozesse in einer Kühni- oder einer RDC-Kolonne mit OpenFOAM", Studienarbeit.

S. Müller (2012): "Experimentelle Untersuchung des Hold-up mit einem PIV System", Studienarbeit.

M. Platz (2012): „Bestimmung des Stoffaustauschs in einer Kühni Miniplant Kolonne", Studienarbeit.

P. Müller, F. Höfler, A. Grimm (2011):
„Simulation einer Extraktionskolonne mit einem OpenSource CFD Code", Projektarbeit.

Y. Gao (2011): „Kameragestütze Tropfenzerfallsexperimente an gerührten Extraktionskolonnen am Beispiel einer Kühni DN32 Kolonne", Studienarbeit.

You Bin Xu (2011): „Simulation von Massentransfer in einer RDC Kolonne", Studienarbeit, Masterarbeit.

M. Rachid (2011): „Validierung eines OpenFOAM CFD Codes zur Simulation einer RDC Extraktionskolonne", Diplomarbeit.

P. Müller (2010): „Bestimmung der Hydrodynamik in gerührten Miniplant-Extraktionskolonnen mit OpenFOAM", Studienarbeit.

T. Chevalier (2010): „Simulation of a Rotating Disc Contactor using a CFD-PBM Coupling", Diplomarbeit in Kooperation mit der University of Cambridge.

I. Kamga (2010): „Untersuchung des Phasenanteils in Extraktionskolonnen mittels LIF", Studienarbeit.

C. Dreiser (2010): „Geometrische Optimierung einer strukturierten Stoffaustauschpackung unter Berücksichtigung numerischer Strömungssimulation", Diplomarbeit.

Curriculum Vitae

Diplom-Ingenieur
Mark W. Hlawitschka

Employment

01/2009-10/2013	Scientific Assistant, PhD Student
	University Kaiserslautern
	Chair of Separation Science and Technology (Prof. H.-J. Bart)

Studies

10/2003 – 11/2008	Process Engineering (Verfahrenstechnik)
	University Kaiserslautern
	Degree: Diplom, Master of Science
11/2007 – 04/2008	Internship at BASF SONATRACH PropanChem S.A., Spain
10/2002 – 10/2003	Distance Learning during civilian service: Electrical Engineering and Mechanical Engineering
	University Kaiserslautern